Studies on Triphenylamine-Based Organic Functional Materials

Masashi Uebe

2018

Preface

American architect, Louis Henry Sullivan coined the famous phrase, “form ever follows function.”

The remarkable progress of modern synthetic methodology provided great impetus for constructing unprecedented organic molecules with complicated structures. Furthermore, the last few decades have witnessed a rapid development of computer hard- and software, and therefore, computational studies offer powerful complement to experimental studies. These circumstances enable us to design and create an organic molecular system having a bespoke function, and the advantage of organic molecules has been widely accepted in materials science. This is exactly the situation that molecular architecture ever follows function.

Triphenylamine (TPA) based compounds are an important class of molecular materials in organic electronics because of their donor ability and high stability in oxidized states. In this thesis, the author explored the possibility of creating intriguing functional molecular systems by focusing on three kinds of novel TPA-based compounds. The first one is to study the TPA-introduced oligoacenes that can be considered to be new redox-active semiconductive materials facilitating device fabrications by using wet process. The second one is to investigate the light-emitting TPA-based compounds based on new molecular designs. The third one is to develop the TPA-based mixed-valence compounds as useful model systems appropriate for controlling and understanding of intramolecular charge/spin transfer mechanisms. The author hopes that the studies in this thesis will contribute to deeper understanding of functional organic molecular systems and further development of materials science.

Acknowledgments

The present thesis is the summary of the author's studies from 2012 to 2018 at the Department of Molecular Engineering, Graduate School of Engineering, Kyoto University under the supervision of Professor Kazuyoshi Tanaka and Associate Professor Akihiro Ito.

First, the author would like to express his deepest gratitude to Professor Kazuyoshi Tanaka for his valuable suggestions, helpful discussions, and continuous encouragement through the course of his studies. He also expresses his deepest thanks to Associate Professor Akihiro Ito, whose precise guidance, stimulating suggestions, and fruitful discussions were indispensable for the completion of the present thesis. He has always encouraged the author throughout the work.

He also expresses his appreciation to Associate Professor Tohru Sato for his valuable comments, discussion and collaboration. He wishes to thank Dr. Hiroyuki Fueno for his kind advices on the computational methods. The author expresses his acknowledgments to Professor Tatsuhisa Kato (Kyoto University) for his kind help in the ESR measurements. He also wishes to thank Dr. Tetsuo Iwanaga (Okayama University of Science) for his collaboration. He would like to thank Dr. Hiroyasu Sato and Dr. Takashi Matsumoto (Rigaku Corporation) for his kind help in the X-ray crystallographic analyses. He would like to acknowledge Dr. Karin Nishimura for the mass spectroscopy. The author heartily thanks Dr. Sakamaki and Dr. Ryohei Kurata for their continuous encouragement, kind advice and collaborations. He is indebted to Mr. Hiroshi Ishikawa, Mr. Yuichiro Kameoka, Mr. Kazuki Takahashi, Mr. Tatsuya Kazama, Mr. Kensuke

Kaneda and Mr. Kenji Kawashima for their collaborations. He is grateful to Mr. Shin Omae, Mr. Soichiro Yano, Mr. Aira Ohnishi, Mr. Akiyoshi Ooba, Mr. Tatsuya Hirano, Mr. Tetsuya Kawamoto, and Mr. Shinya Fukuzaki for their kind helps on performing his work. He also thanks other members of the research group of Professor Kazuyoshi Tanaka laboratory, and the secretary, Ms. Miya Kitao.

The author is grateful to the Research Fellowship of the Japan Society for the Promotion of Science for Young Scientists for financial support.

Finally, the author would like to express his sincere gratitude to his parents Shuichi Uebe and Atsuko Uebe, his sister Rika Uebe and his grand parent the late Hirozo Uebe for their continuous support, understanding, and encouragement.

Masashi Uebe

Kyoto, 2018

Contents

Part 2

Optical Properties of Triphenylamine-Based Functional Materials

Part 3

Charge/Spin Transfer Mechanisms of Triphenylamine-Based Functional Materials

* * * * *

General Introduction

To date, electronic and optoelectronic devices using organic materials as organic light-emitting diodes (OLEDs), organic photovoltaic devices (OPVs), organic field effect transistors (OFETs) and so on, have recently received a great deal of attention. The devices using organic materials are attractive because they can take advantage of organic materials such as lightweight, low cost, and flexibility. Particularly, π-electron systems are pivotal compounds in the organic electronic devices. In organic electronics, triphenylamine derivatives which are embedded nitrogen atom into π-electron systems have been regarded as very important hole-transport materials from the viewpoints of fundamental physical organic chemistry, because they have low oxidation potential and can generate the relatively highly stable oxidized species by electrochemical and chemical oxidation.[1,2] Furthermore, triphenylamine derivatives are expected to be hopeful materials of the organic spintronics devices.[3]

Until the 1990, copper-catalyzed Ullman coupling reaction[4,5] had been the most

effective method to synthesize aromatic amines. However, the Ullman type reaction requires harsh reaction conditions and results in unsatisfactory yields because of by-products. On the other hand, the recent progress of research on the Buchwald-Hartwig palladium coupling amination reactions has enabled us to readily synthesize various kinds of triphenylamine derivatives.[6,7] It is well known that triphenylamine derivatives show various electronic properties depending on their molecular structures. For example, phenylenediamine is considered to be the simplest system of the aromatic amine with the two redox-active nitrogen atoms. There exist three structural isomers for phenylenediamine derivatives: *ortho*-, *meta*-, and *para*-isomers. The substitution pattern is the crucial factor determining the electronic interaction between the two redox-active amino groups, along with the distance between the redox sites.[8] As shown in Figure 1, the numbers of covalent bonds between the amino groups in the each structural isomer are three (*ortho*), four (*meta*) and five (*para*). However, the electronic coupling[9] of the radical cation species become the stronger for *ortho*- and *para*-isomers than for *meta*-isomer.

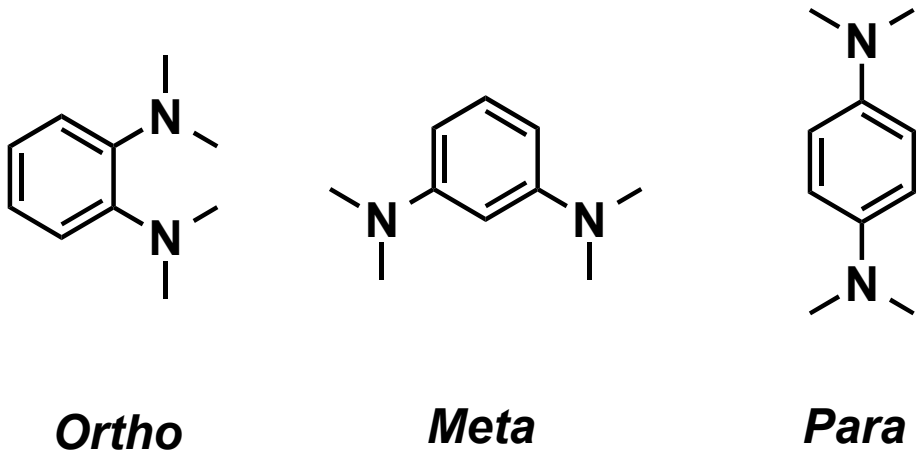

Figure 1. The structural isomers of phenylenediamines.

Generally, *ortho*- and *para*-phenylene units are known as Kekulé molecule. *Ortho*- and *para*-phenylenediamine can generate chemically and thermally stable radical cation bearing a positive charge and an unpaired electron spin all over the molecules, corresponding to a class-III mixed-valence system according to Robin and Day (Figure 2).[8,10] Particularly, tetramethyl-*para*-phenylenediamine (TMPD) referred to as "Wurster's Blue" and can be readily converted into the stable semiquinone radical cation and the stable closed-shell quinone dication by successive one-electron oxidations.[11] Therefore, the use of this type of radical as a spin-bearing unit is persistent to the exploitation of novel high-spin organic molecules.[12,13]

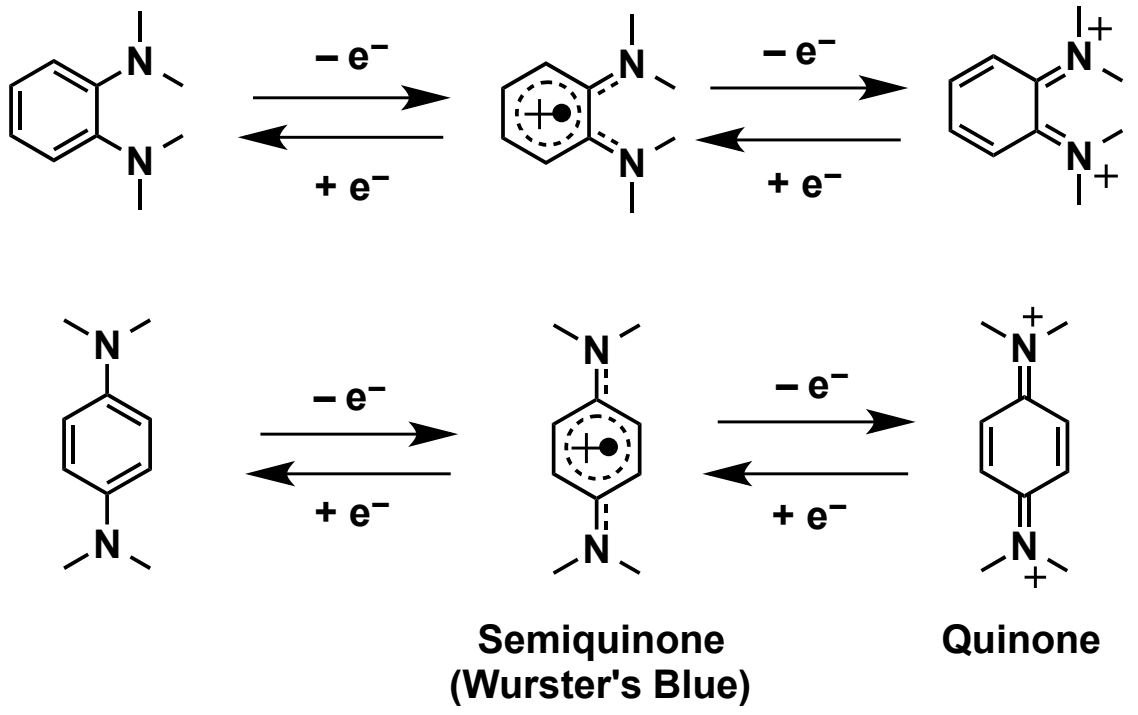

Figure 2. Two-stage redox systems of *ortho*- and *para*-phenylenediamine.

On the other hand, *meta*-phenylene unit is known as non-Kekulé molecule (Figure 3). The radical cation of *meta*-phenylenediamine has hopping electron transfer process unlike *ortho*- and *para*-phenylenediamine because it cannot draw the semiquinoid structure. According to the Longuet-Higgins theory[14] and Hund's rule, the dication of *meta*-phenylenediamine has the ground state in which each of the two degenerate non-bonding molecular orbitals (NBMOs) are occupied with one electron. *Meta*-phenyenediamine derivatives are interesting compounds because they form high-spin states which are verified by ESR measurement.[15,16]

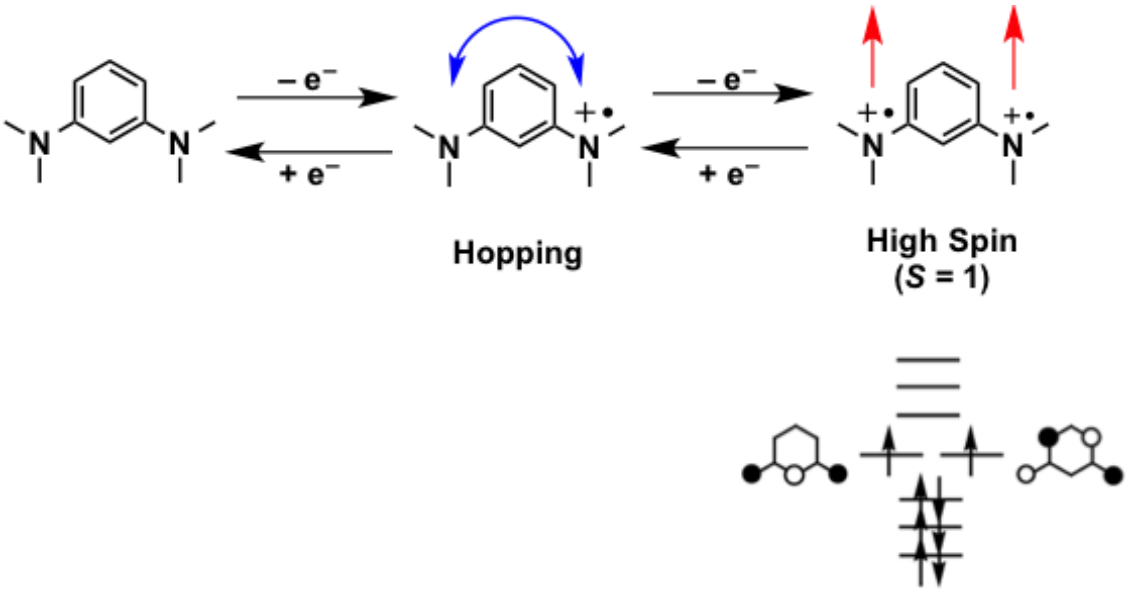

Figure 3. Redox system of *meta*-phenylenediamine.

Moreover, polyaniline can be seen as triphenylamine-based polymer. Polyaniline is one of the most popular examples of organic conductive polymers.[17,18] Its electronic, optical, and magnetic properties have been applied to various materials such as rechargeable lithium-polyaniline batteries[19] and hole-transporting layer in

electroluminescence devices[20,21] and it has been attractive in organic electronics because it is lightweight, conductivity, flexibility, low cost and simple synthetic method by chemical[22] and electrochemical[23,24] oxidation. For example, poly(*para*-aniline) exhibited their conductivities upon protonic acid doping (Figure 4).[25,26] Thus it is very interesting to examine the charge or spin distribution of the oxidized species of poly(*para*-aniline). On the other hand, poly(*meta*-aniline) can be regarded as the precursor of the typical high-spin non-Keculé organic polymer (Figure 4).[27-29]

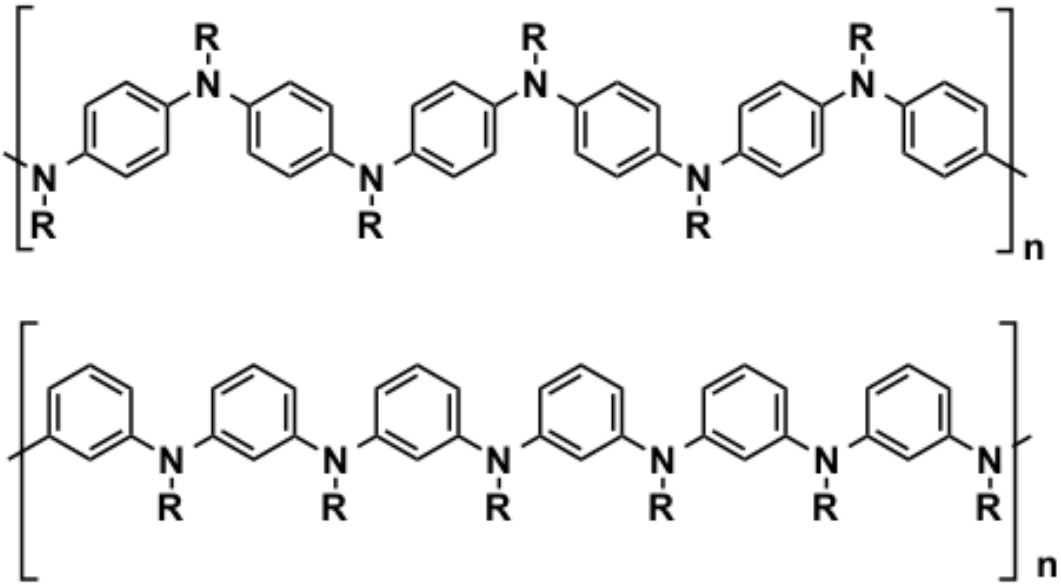

Figure 4. The structures of poly(*para*-aniline) and poly(*meta*-aniline).

In the course of the characterization of the electronic states of polyaniline, a variety of aniline oligomers of controlled chain length have been prepared and investigated as model molecules.[30-34] Among them, the above mentioned phenylenediamine derivatives are the simplest dyad models for polyaniline (Figure 1). For example, to examine what extent is an unpaired electron delocalized within polyaniline, the simplest

Hückel calculations and ESR studies on the radical cations of oligoaniline manifested that the generated spin was confined to the central *para*-phenyenediamine moiety and spin delocalization took place only to a small extent.[35] The flexibility of the linear structure resulted in spin or charge localization. In contrast to the spin confinement for the radical cation of the linear oligomer, macrocyclic aza[1_6]*para*-cyclophane were synthesized and the DFT calculation and ESR analysis of this molecule showed delocalized spin distribution for the cyclic structure.[36] The rigid molecular framework and periodic boundary condition by cyclization resulted in charge or spin delocalization on entire molecule. And then, it seems simple that high spin oligomers or polymers connecting the ferromagnetic coupler *meta*-phenylenediamine are generated by oxidation, but it was found difficult to realize such high spin system because of the instability of their polycationic states.[37] One effective remedy to increase the stability of the polycationic states is to incorporate the *para*-phenylenediamine units into a molecular framework and to connect the amino groups by the *meta*- and *para*-phenylene units alternatively (Figure 5). The linear *meta*-*para*-oligoaniline derivatives have been prepared and investigated the electronic and magnetic states. However, in the simple linear polymers, it was found that the observed spin states after the multi-electron oxidations were at most the triplet states, and the higher spin states have been not detected. This was probably because of the inherent flexibility of the structures and the effect of the spin defects. Accordingly, to control the spin state, cyclization is one way to rigidly constrain the molecular structure because molecular motion and structure distortion perturbs the spin alignment.[38] Tetraaza[1.1.1.1]*m,p,m,p*-cyclophene is a simple example of a macrocycle high spin molecule which exhibited a triplet state in the ESR and SQUID measurements.[39,40,41] Furthermore, the ladder-type[42] and

star-shape[43] high spin molecules which have this tetraazacyclophane moiety have been reported. These macrocyclic aromatic amine have planarity with two-dimensional structure and the extension of macrocyclic aromatic amines toward the three-dimensional systems have been prepared and investigated in their characteristic electronic and magnetic properties.[44] In this way, by properly designing the molecular structures, the electronic states of aromatic amines can be controlled.

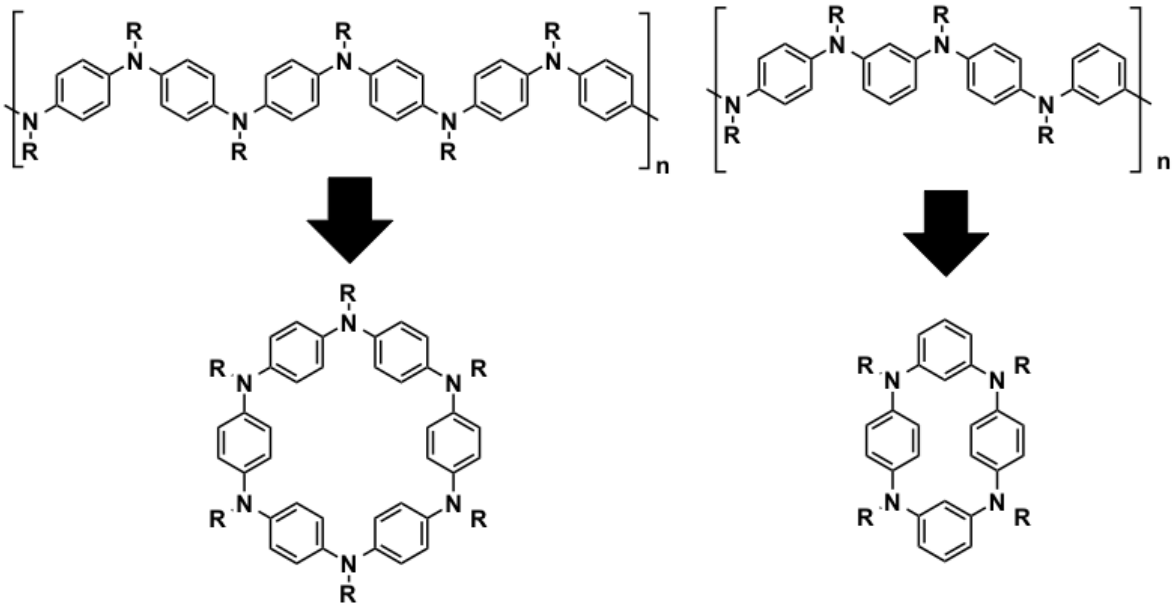

Figure 5. Macrocyclization scheme of polyaniline.

Survey of this thesis

In this thesis, the author presents the synthesis and electronic properties of triphenylamine-based functional materials that have unique structures. He aimed to realize various electronic characters by modulating the molecular structures. And he investigated the electronic properties of these molecules by means of UV-vis-NIR and photoluminescence spectroscopic, electrochemical, X-ray crystallographic, ESR, and magnetic susceptibility measurements as well as DFT calculations.

Part 1 deals with the electronic structures of triphenylamine-based acene materials. In Chapter 1, the electronic structures, and photochemical stability of radical cations of oligoacenes in solution under ambient light and air conditions were investigated. The author selected anthracene, tetracene, and pentacene derivatives with moderately bulky mesityl (Mes) substituents. The reason of this choice stems from (i) steric protection of the highly reactive carbon centers of the acenes, (ii) improvement of poor solubility of the unsubstituted acenes in common organic solvents, and (iii) perpendicularity between the π-faces of the acene moiety and the Mes-groups, which retains the electronic structures (in particular, the frontier orbitals) of the acene moiety.

In Chapter 2, the author investigated how the difference in the *N*-substituent identity influences the electronic structures of the oxidized species of hitherto sporadically studied 9,10-diaminoanthracenes. To do the comparative study on the electronic structures of oxidized states of 9,10-diaminoanthracenes, the author have carried out a complementary series of measurements such as cyclic voltammetry, spectroelectrochemistry, and ESR spectroscopy, and furthermore, performed density functional theory (DFT) calculations.

In Chapter 3, the author prepared a new derivative of hexaaza[1_6]paracyclophane in

which *para*-phenylenes are alternately replaced by 9,10-anthrylenes. The impact on overall π-conjugation as well as conformational change of the macrocycle was investigated. The charge and spin distribution of the macrocycle was elucidated by means of electrochemical, spectroelectrochemical, ESR spectroscopic, and SQUID magnetometric methods. In particular, the triradical trication was successfully isolated as an air-stable salt, and moreover, its structure was disclosed by X-ray analysis.

In Chapter 4, the synthesis of 5,12-diaminotetracenes was reported as a new class of redox-active tetracene and their electronic properties. For a comparative study of the electronic structures of the oxidized states of diaminotetracenes, the author has carried out cyclic voltammetry, spectroelectrochemistry, ESR and fluorescence spectroscopy, and furthermore, have performed density functional theory (DFT) calculations. It was revealed that the difference in the *N*-substituent patterns of oligoacenes and the oligoacene moiety caused the different redox behaviors.

In Chapter 5, the author newly prepared 6,13-diaminosubstituted pentacenes as a new class of redox-active pentacene derivatives and investigated their electronic properties. Pentacene has attracted growing interest as benchmark semiconductive materials for organic thin film transistors, and to improve its poor solubility in common organic solvents and its chemical instability in solution when exposed to light and air, various kinds of functionalized pentacenes have been reported so far. The stability in various condition and solubility in common organic solvents of diaminopentacenes was investigated and the electronic structures of their neutral and oxidized species were elucidated by means of electrochemical and spectral measurements, and DFT calculations.

Part 2 deals with the optical properties of triphenyl-amine based functional materials.

In Chapter 1, given that light-emitting efficiency of non-fluorescent molecules can be enhanced by general guiding principles, many more options become available for exploitation of new fluorescent molecules. As an example of typical non-fluorescent molecules, triphenylamine are designated, and their excited states undergo nonradiative decay with internal conversion and vibrational relaxation. For the fluorescence enhancement of non-fluorescent triphenylamine, the author newly prepared singly, doubly, and triply carborane-substituted triphenylamines and investigated these molecules from electrochemical and spectrochemical measurments, and DFT calculations.

In Chapter 2, the author synthesized new donor-acceptor compounds that have electron-donating amino groups and electron-accepting boryl groups on the 9,10-anthracene as central π-bridging unit. These compounds are predicted that they have solid-state fluorescence by preventing the concentration quenching because they have perpendicular structure due to steric effect of anthracene. These compounds were characterized by analysis of crystal structure and cyclic voltammetry, ESR and UV/vis absorption, fluorescence spectroscopy.

In Chapter 3, the author envisioned that two *para*-phenylene-bridged B-π-N embedded diazadibora[1_4]*m*,*p*,*m*,*p*-cyclophanes would have been intriguing to elucidate how the B-π-N orientation patterns affect their (opto)electronic properties. The one macrocycle has the two B-π-N units in anti-parallel fashion, thus leading to a potential quadrupolar molecule, whereas the other macrocycle in parallel fashion. In addition, the author also prepared the remaining isomer, which contains two *meta*-phenylene-bridged B-π-N units, to characterize the effect of *meta*-phenylene-bridging in the B-π-N unit. Herein the author reported the (opto)electronic and structural characteristics of these

ambipolar π-conjugated B-π-N macrocycles.

Part 3 deals with the charge/spin transfer mechanisms of triphenylamine-based functional materials. In Chapter 1, in conjunction with the so-called toroidal delocalization/conjugation of charge/spin in radical cations of redox-active hexaarylbenzene derivatives, where the through-space charge delocalization is supposed to be realized through six arene units attached to the central benzene ring in a paddlewheel-like fashion, the bis(triphenylamines) (BTAs) bridged by *ortho*-phenylene linker also serves as an optimal dyad model compound of hexaarylbenzene derivatives to estimate the contribution of the through-bond and through-space interaction. In addition, as an antipode of the π-conjugated through-bond interaction via *ortho*-phenylene linker, the σ-conjugated through-bond interaction via *ortho*-carborane cluster, if it does exist, is intriguing. The BTAs bridged by *ortho*-phenylene and *ortho*-carborane linkers have similar geometrical arrangements on the two nitrogen redox centers, although the orientation of the two NC_3 planes differs between the two compounds. As such, radical cations of these compounds are attractive analogs for exemplifying a segregation of covalent and noncovalent pathways in the IV-CT process. The author investigated the mixed-valence states of these molecules from electrochemical, spectrochemical and ESR measurements, as well as DFT calculations.

Finally, in Chapter 2, *meta*- and *para*-phenylene-bridged BTA and *meta*- and *para*-phenylenediamine are very interesting mixed-valence compounds. By cyclic voltammetry, UV-vis-NIR and ESR spectroscopy, and DFT calculations, the author investigated the impact by difference of bridging unit on intramolecular charge or spin transfer.

In this thesis, the author investigated the electronic properties of

triphenylamine-based acene materials, optical properties of triphenylamine-based material and intramolecular electron transfer mechanisms of triphenylamine-based materials. These molecules have their unique electronic properties originating from their structures. The findings in this thesis have demonstrated that the organic materials with various electronic properties can be created by properly designing the molecular structures. The author hopes that the present thesis can contribute to development of the physical organic chemistry, and the concept in this thesis will be helpful in creating new materials.

Reference

[1] Y. Shirota, H. Kageyama, *Chem. Rev.* **2007**, *107*, 953-1010.

[2] C. H. Teh, R. Daik, E. L. Lim, C. C. Yap, M. A. Ibrahim, N. A. Ludin, K. Sopian, M. A. M. Teridi, *J. Mater. Chem. A* **2016**, *4*, 15788-15822.

[3] S. A. Wolf, D. D. Awschalom, R. A. Buhrman, J. M. Daughton, S. v. Molnár, M. L. Roukes, A. Y. Chtchellkanova, D. M. Treger, *Science* **2001**, *294*, 1488-1495.

[4] F. Ullman. *Chem. Ber.* **1903**, *36*, 2389-2391.

[5] S. V. Ley, A. W. Thomas, *Angew. Chem. Int. Ed.*, **2003**, *42*, 5400-5409.

[6] D. S. Surry, S. L. Buchwald, *Angew. Chem. Int. Ed*. **2008**, *47*, 6338-6361.

[7] a) J. F. Hartwig, *Nature* **2008**, *455*, 314-322; b) J. F. Hartwig, *Acc. Chem. Res*. **2008**, *41*, 1534-1544.

[8] A. Heckmann, C. Lambert, *Angew. Chem. Int. Ed.* **2012**, *51*, 326-392.

[9] N. S. Hush, *Coord. Chem. Rev.* **1985**, *64*, 135-137.

[10] J. Hankache, O. S. Wenger, *Chem. Rev.* **2011**, *111*, 5138-5178.

[11] K. Deuchert, S. Hünig, *Angew. Chem. Int. Ed. Engl.* **1978**, *17*, 875-886.

[12] a) M. M. Wienk, R. A. J. Janssen, *Chem. Commun.* **1996**, 267-268; b) M. M. Wienk, R. A. J. Janssen, *J. Am. Chem. Soc.* **1996**, *118*, 10626-10628; c) M. M. Wienk, R. A. J. Janssen, *J. Am. Chem. Soc.* **1997**, *119*, 4492-4501.

[13] a) K. R. Stickley, T. D. Selby, S. C. Blackstock, *J. Org. Chem.* **1997**, *62*, 448-449; b) T. D. Selby, S. C. Blackstock, *J. Am. Chem. Soc.* **1999**, *121*, 7152-7153.

[14] H. C. Longuet-Higgins, *J. Chem. Phys.* **1950**, *18*, 265-274.

[15] M. Yano, Y. Ishida, K. Aoyama, M. Tatsumi, K. Sato, D. Shiomi, A. Ichimura, T. Takui, *Synth. Met.* **2003**, *137*, 1275-1276.

[16] K. Sato, M. Yano, M. Furuichi, D. Shiomi, K. Aoyama, T. Takui, K. Abe, K. Itoh, A.

Higuchi, K. Katsuma, Y. Shirota, *Tetrahedron Lett.* **1997**, *119*, 6607-6613.

[17] A. G. MacDiarmid, *Angew. Chem. Int. Ed.* **2001**, *40*, 2581-2590.

[18] A. J. Heeger, *Angew. Chem. Int. Ed*. **2001**, *40*, 2511-2611.

[19] a) A. G. MacDiarmid, S. -L. Mu, N. L. D. Somasiri, W. Wu, *Mol. Cryst. Liq. Cryst*. **1985**, *121*, 187-190; b) R. B. Kaner, A. G. Macdiarmid, *Sci, Am*, **1988**, *258*, 106-108.

[20] T. Kobayashi, H. Yoneyama, H. Tamura, *J. Electroanal. Chem.* **1984**, *161*, 419-423.

[21] P. Novak, K. Mueller, K. S. V. Santhanam, O. Haas, *Chem. Rev.* **1997**, *97*, 207-281.

[22] M. Abe, A. Ohtani, Y. Umemoto, S. Akizuki, M. Ezoe, H. Higuchi, K. Nakamoto, A. Okuno, Y. Noda, *J. Chem. Soc., Chem Commun.* **1989**, 1736-1738.

[23] a) T. Mizoguchi, R. N. Adams, *J. Am. Chem. Soc.* **1962**, *84*, 2058-2061; b) D. M. Mohilner, R. N. Adams, W. J. Argersinger, *J. Am. Chem. Soc.* **1962**, *84*, 3618-3622.

[24] A. F. Diaz, J. A. Logan, *J. Electroanal. Chem.* **1980**, *111*, 111-114.

[25] E. M. Geniés,A. Boyle, M. Lapkowdki, C. Tsintavis, *Synth. Met.* **1990**, *36*, 139-182.

[26] G. Cric-Marjarnovic, *Synth. Met.* **2013**, *177*, 1-47.

[27] K. Yoshizawa, A. Tanaka, K. Tanaka, T. Yamabe, *Polym. J.* **1992**, *24*, 857-864.

[28] M. Baumgarten, K. Müllen, N. Tyutyukov, G. Madjarova, *Chem. Phys*, **1993**, *169*, 81-84.

[29] G. Madjarova, M. Baumgarten, K. Müllen, N. Tyutyulkov, *Macromol. Theory Simul.* **1994**, *3*, 803-815.

[30] A. G. MacDiarmid, Y. Zhou, J. Feng, *Synth. Met.* **1999**, *100*, 131-140.

[31] J. Honzl, M. Tlustakova, *J. Polymer Sci.* **1968**, *C22*, 451-462.

[32] L.W. Shacklette, J. F. Wolf, S. Gould, R.H. Baughman, *J. Chem. Phys.* **1988**, *88*, 3955-3961.

[33] F. L. Lu, R. Wudl, M. Nowak, A. J. Heeger, *J. Am. Chem. Soc*. **1986**, *108*, 8311-8313.

[34] J. P. Sadighi, R. A. Singer, S. L. Buchwald, *J. Am. Chem. Soc.* **1998**, *120*, 4960-4976.

[35] B. Grossmann, J. heinze, T. Moll, C. Palivan, S. Ivan, G. Gescheidt, *J. Phys. Chem. B* **2004**, *108*, 4669-4672.

[36] A. Ito, Y. Yokoyama, R. Aihara, K. Fukui, S. Eguchi, K. Shizu, T. Sato, K. Tanaka, *Angew. Chem. Int. Ed.* **2010**, *49*, 8205-8208.

[37] K. R. Stickly, S. C. Blackstock, *Tetrahedron Lett.* **1995**, *36*, 1585-1588.

[38] A. Ito, *J. Mater. Chem. C* **2016**, *4*, 4614-4625.

[39] a) A. Ito, Y. Ono, K. Tanaka, *Angew. Chem. Int. Ed.* **2000**, *39*, 1072-1075; a) R. Kurata, D. Sakamaki, A. Ito, *Org. Lett.* **2017**, *19*, 3115-3118.

[40] S. I. Lakshmi, K. V. Lakshmi, J. F. Hartwig, *Org. Lett.* **1999**, *1*, 2057-2060.

[41] M. Xu, C. Yi, C. -J. Yang, J. -H. Wang, Y. -Z. Liu, B. Xie, X. -C. Gao, P. Wang, D. -C. Zou, *Thin Solid Films* **2008**, *516*, 7720-7726.

[42] X. Z. Yan, J. Pawlas, T. Goodson, J. F. Hartwig, *J. Am. Chem. Soc.* **2005**, *127*, 9105-9116.

[43] D. Sakamaki, A. Ito, K. Furukawa, T. Kato, K. Tanaka, *Chem. Commun.* **2009**, *30*, 4524-4526.

[44] a) D. Sakamaki, A. Ito, K. Tanaka, K. Furukawa, T. Kato, M. Shiro, *Angew. Chem. Int. Ed.* **2012**, *51*, 8281-8285; b) Y. Yokoyama, D. Sakamaki, A. Ito, K. Tanaka, M. Shiro, *Angew. Chem. Int. Ed.* **2012**, *51*, 9403-9406; c) D. Sakamaki, A. Ito, K. Furukawa, T. Kato, M. Shiro, K. Tanaka, *Angew. Chem. Int. Ed.* **2012**, *51*, 12776-12781.

Part 1

Electronic Structures of Triphenylamine-Based Acene Materials

Introduction

Polycyclic aromatic hydrocarborns (PAHs) are defined as a group of compounds that consist of several annulated aromatic rings.[1] PAHs can be regarded as fragments of the graphene and the electronic states is determined by the shape of the molecule. Particularly, acenes that are PAH made up linearly fused benzene and described by the fewest localized Clar resonant sextets per number of aromatic rings[2] have long been the subject of intense study due to the unique electronic properties associated with their π-bond topology.[3-5] One of the most appealing points of oligoacences is that they will have a smaller HOMO-LUMO energy gap as acene length is increased. It has been predicted that acenes as small as heptacene may possesses a singlet diradical ground state due to small HOMO-LUMO energy gap.[6] Moreover, oligoacenes have strong two-dimensional electronic interactions in the solid state. Therefore, oligoacenes are the

focus of recent major research activities of chemists, physicists, and materials scientists, because of their application in organic field-effect transistors (OFETs). However, unfortunately, increasing acene length tends to also lead to significantly decreased stability and solubility. Particularly, oligoacenes longer than pentacene are known to readily undergo photoinduced degradation in the solution phase, and their chemical instability under ambient light and air conditions is still unsatisfactory for device fabrication by using wet process. Substitution with bulky substituents to protect kinetically photoactive carbon sites, as seen in the most popular example, 6,13-bis(triisopropyl-silylethynyl)pentacene (TIPS-Pentacene), is one of the remedies to overcome this difficulty.[7] And TIPS-hexacene and heptacene have been isolated as crystalline solid.[8] The non-substituted longer acene nonacene and decacene have been reported as isolation in a matrix and on-surface synthesis.[9,10,11]

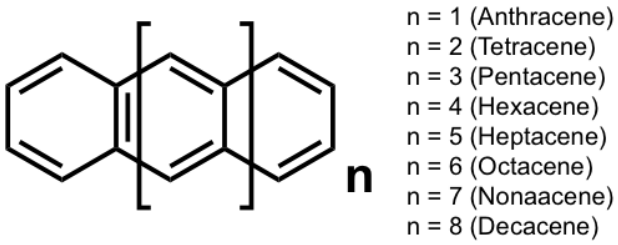

Figure 1. The structures of Oligoacenes

In Chapter 1, acenes: anthracene, tetracene, and pentacene, with moderately bulky mesityl substituents were prepared and investigated the electronic states in their neutral and radical cation species. The radical cations of them revealed that their photochemical stability in solution under ambient light and air conditions is comparable to that of the corresponding neutral state, thus indicating the possibility of persistent acene radical

cations.

In Chapter 2-5, aminoacenes: anthracene, tetracene, and pentacene, and their macrocyclic derivatives were prepared and investigated the electronic states of neutral and oxidized species. Aminoacenes revealed that they have higher stability and solubility than non-substituted acene due to substitution by bulky amino groups. The author investigated that the difference in the *N*-substituent patterns of oligoacenes and the oligoacene moiety caused the different redox behaviors by means of electrochemistry, absorption and ESR spectroscopy, as well as DFT calculations.

References

[1] M. D. Watson, A. Fechtenkötter, K. Müllen, *Chem. Rev.* **2001**, *101*, 1267-1300.

[2] Y. Ruiz-Morales, *J. Phys. Chem. A* **2002**, *106*, 11283-11308.

[3] M. Bendikov, F. Wudl, D. F. Perepichka, *Chem. Rev.* **2004**, *104*, 4891-4945.

[4] J. E. Anthony, *Chem. Rev.* **2006**, *106*, 5028-5048.

[5] J. E. Anthony, *Angew. Chem. Int. Ed.* **2008**, *47*, 452-483.

[6] M. Bendikov, H. M. Duong, K. Starkey, K. N. Houk, E. A. Carter, F. Wudl, *J. Am. Chem. Soc.* **2004**, *126*, 7416-7417.

[7] J. E. Anthony, J. S. Brooks, D. L. Eaton, S. R. Parkin, *J. Am. Chem. Soc*. **2001**, *123*, 9482–9483.

[8] M. M. Payne, S. A. Odom, S. R. Parkin, J. E. Anthony, *Org. Lett.* **2004**, *6*, 3325-3328.

[9] C. Tönshoff, H. F. Bettinger, *Angew. Chem. Int. Ed.* **2010**, *49*, 4125-4128.

[10] R. Zuzak, R. Dorel, M. Krawiec, B. Such, M. Kolmer, M. Szymonski, A. M. Echavarren, S. Godlewski, *ACS Nano*, **2017**, *11*, 9321-9329.

[11] J. Krüger, F. Carcía, F. Eisenhut, D. Skidin, J. M. Alonso, E. Guitián, D. Pérez, G. Cuniberti, F. Moresco, D. Pêna, *Angew. Chem. Int. Ed.* **2017**, *56*, 11945-11948.

Chapter 1

Mesityl-Substituted Acene Radical Cations: Decent Stability Comparable to Their Neutral States under Ambient Light and Air Conditions

1.1 Introduction

Lower acenes, such as anthracene, tetracene, and pentacene, and their functionalized derivatives have been thoroughly studied so far and widely utilized for a variety of applications in moleculer electronics.[1–3] Although they are indeed robust in comparison with the case where oligoacenes longer than pentacene are known to readily undergo photoinduced degradation in the solution phase, their chemical instability under ambient light and air conditions is still unsatisfactory for device fabrication by using wet process. Substitution with bulky substituents to protect kinetically photoactive carbon sites, as seen in the most popular example, 6,13-bis(triisopropyl-silylethynyl)pentacene or TIPS-pentacene,[4] is one of the remedies to overcome this difficulty.

As an exceptional but intriguing case, Einholz and Bettinger reported that dicationic

species of oligoacenes including higher acenes like hexacene and heptacene are easily formed in concentrated sulfuric acid, and their dications in sulfuric acid solution are persistent in the absence of water and oxygen.[5] They inferred from this observation that higher oligoacenes as formal 4n+2 Hückel aromatic compounds, no matter how long, possessing only one Clar's aromatic sextet[6,7] are of diradical character, and two-electron oxidation to the dications results in a more stabilized 4n π-electron system having two aromatic sextets (Scheme 1.1a). If that is the case, one-electron oxidation of acenes can also lead to stable 4n + 1 π-electron systems, as is depicted in Scheme 1.1b. We report herein the electronic structures, and photochemical stability of radical cations of synthetically readily accessible acenes: anthracene, tetracene, and pentacene, in solution under ambient light and air conditions. For the present study, the author has selected anthracene, tetracene, and pentacene derivatives with moderately bulky mesityl (Mes) substituents, that is, **1** to **3** (Scheme 1.1c). The reason of this choice stems from (i) steric protection of the highly reactive carbon centers of the acenes, (ii) improvement of poor solubility of the unsubstituted acenes in common organic solvents, and (iii) perpendicularity between the π-faces of the acene moiety and the Mes-groups, which retains the electronic structures (in particular, the frontier orbitals) of the acene moiety (Figure 1.1).

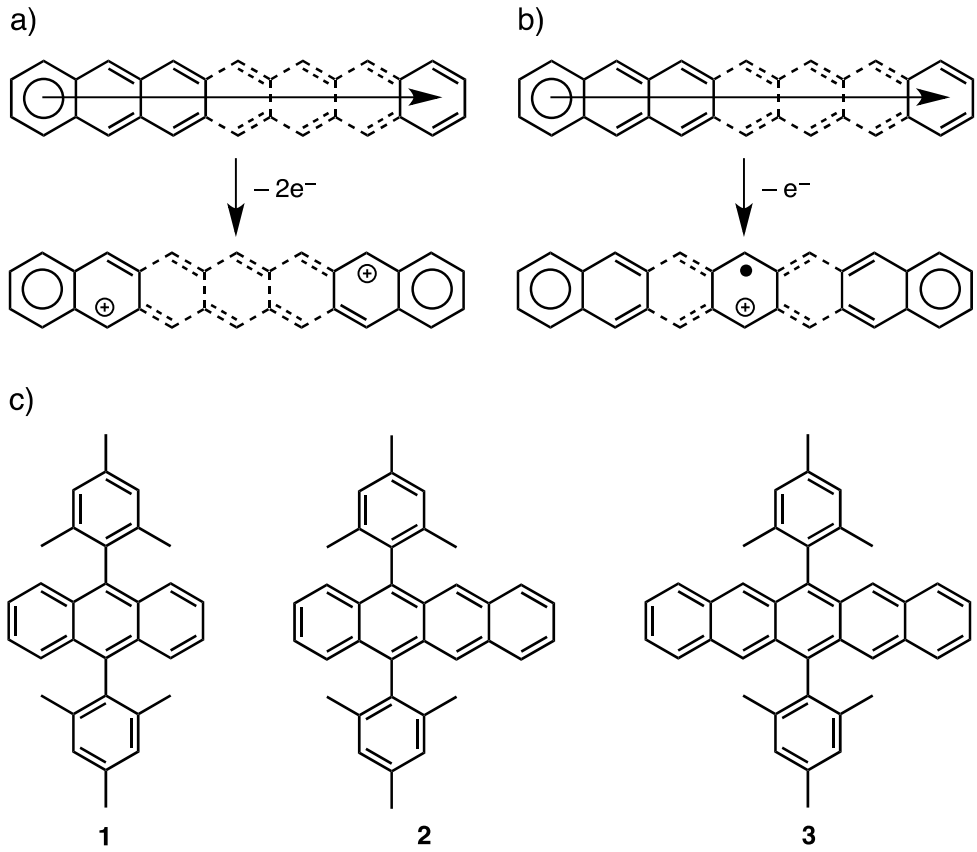

Scheme 1.1. (a) From neutral acene to acene dication with two Clar sextets; (b) from neutral acene to acene radical cation with two Clar sextets; (c) 9,10-dimesitylanthracene **1**, 5,12-dimesityltetracene **2**, and 6,13-dimesitylpentacene **3**.

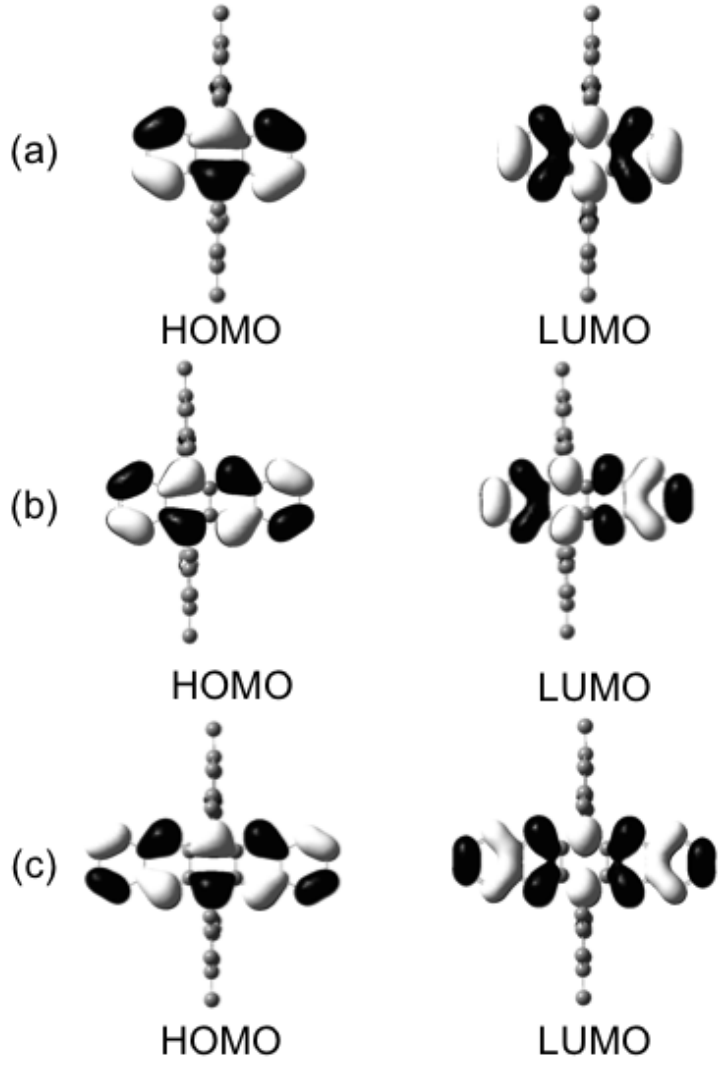

Figure 1.1. Frontier Kohn-Sham orbital profiles for the ground state of (a) **1**, (b) **2**, and (c) **3** at the B3LYP/6-31G* level of theory.

1.2 Experimental Section

1.2.1 Synthesis

All the purchased reagents were of standard quality, and used without further purification. All the purchased solvents were purified, dried, and degassed by standard procedures. Column chromatography was performed with silica gel (Kanto Chemical Co., Inc., silica gel 60N, spherical neutral). Elemental analyses were performed by

Center for Organic Elemental Microanalysis, Kyoto University. ^{1}H and ^{13}C NMR spectra were measured by a JEOL JNM-AL400 FT-NMR spectrometer. Chemical shifts of NMR spectra are determined relative to internal tetramethylsilane (TMS) standard (δ), and are given in parts per million (ppm). UV-Vis-NIR absorption spectra were obtained with a Perkin-Elmer Lambda 950 spectrometer. High resolution (HR) atmospheric pressure chemical ionization (APCI) mass spectra were acquired using a Thermo Fischer EXACTIVE mass spectrometer.

5, 12-Dimesityltetracene (**2**) : A solution of mesitylmagnesium bromide was slowly added to a solution of 5,12-naphthacenequinone (2 mmol, 516.5 mg) in THF (10 mL) at 0 °C under argon atmosphere. Then, the reaction mixture was allowed to warm to room temperature and stirred for 2 days. 1M HCl (15 mL) and $SnCl_2$ (8 mmol, 1.805 g) was added in one portion and stirred for 4 h. The resulting solution was extracted with ethyl acetate, washed with water, and then dried over $NaSO_4$. After evaporation, the crude product was purified with column chromatography on silica gel (*n*-hexane:CH_2Cl_2 = 1:9). Compound **2** was further purified by recrystallization from hexane/toluene as orange solid (586.8 mg, 63.1%); ^{1}H NMR (400 MHz, acetone-d_6) δ 8.21 (s, 2H), 7.85 (dd, 2H), 7.47 (dd, 2H), 7.35 (dd, 2H), 7.33 (dd, 2H), 7.22 (s, 4H), 2.50 (s, 6H), 1.76 (s, 12H); ^{13}C NMR (100 MHz, $CDCl_3$): δ 137.9, 137.2, 135.5, 135.2, 131.5, 129.3, 128.8, 128.6, 128.5, 126.6, 125.2, 125.0, 124.9, 21.2, 19.9 ; APCI HRMS: *m*/*z* calcd for $C_{36}H_{32}$: 465.2577 $[M+H]^+$; found 465.2577; elemental analysis (%) calcd for $C_{36}H_{32}$: C, 93.05; H, 6.95; found: C, 92.55; H, 7.12.

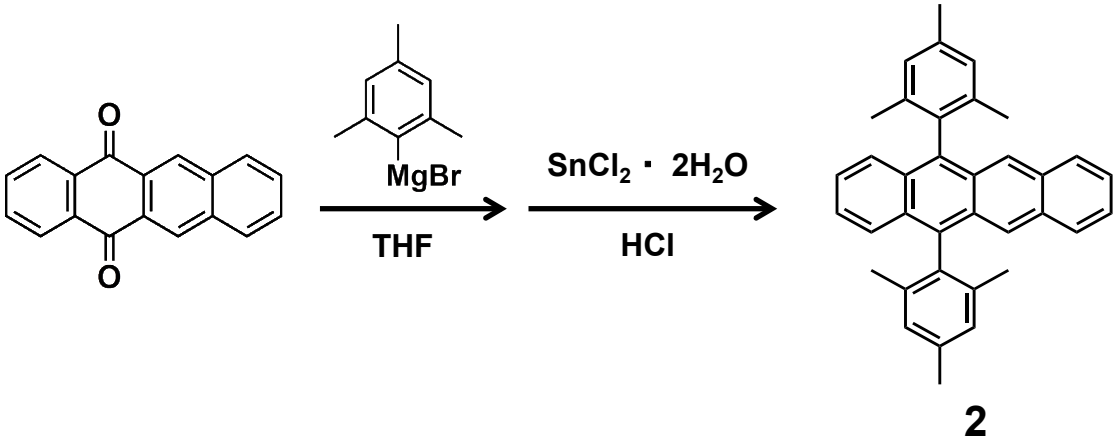

Scheme 1.2. Synthesis of compound **2**.

1.2.2 DFT Calculations

Quantum chemical calculations were performed with using a hybrid Hartree–Fock/density functional theory (HF/DFT) method (B3LYP).[8] Full geometrical optimization for the ground S_0 state of **1**, **2**, **3**, $\mathbf{1}^{\bullet+}$, $\mathbf{2}^{\bullet+}$, and $\mathbf{3}^{\bullet+}$ was carried out and furthermore, their local minimum structures were confirmed by performing subsequent frequency analyses. Excitation energies were examined on the basis of time-dependent density functional theory (TD-DFT)[9] by using the (U)B3LYP/6-31G* optimized structures. All the computations employed the 6-31G* basis set.[10] All these computational approaches are implemented in Gaussian 09 package of ab initio MO calculation.[11]

1.2.3 Electrochemical Measurements

The redox properties were evaluated by cyclic voltammetry (CV) and differential pulse voltammetry (DPV) in CH_2Cl_2 solution at 298 K with 0.1 M tetra-*n*-butylammonium tetrafluoroborate ($TBABF_4$) as supporting electrolyte (scan rate

100 mV s^{-1}) using an ALS/chi Electrochemical Analyzer model 612A. A three-electrode assembly was used, which was equipped with a platinum disk (2 mm^2) and a platinum wire as the working and counter electrodes, respectively, and Ag/0.01 M $AgNO_3$ (acetonitrile) was used as the reference electrode. The redox potential were referenced against a ferrocene/ferrocenium ($Fc^{0/+}$) redox potential measured in the same electrolytic solution.

1.2.4 Spectroelectrochemical Measurements

Spectroelectrochemical measurements were carried out with a custom-made optically transparent thin-layer electrochemical (OTTLE) cell (light pass length = 1 mm) equipped with a platinum mesh and a platinum coil as the working and counter electrodes, respectively, and Ag/0.01 M $AgNO_3$ (acetonitrile) was used as the reference electrode. The potential was applied with an ALS/chi Electrochemical Analyzer model 612A.

1.2.5 ESR Measurements

Cw-ESR Spectra were recorded on a JEOL JES-TE200 X-band ESR spectrometer, in which temperature was controlled by a JEOL ES-DVT3 variable-temperature unit in the range of 193-293 K. An Mn^{2+}/MnO solid solution was used as a reference.

1.2.6 Photophysical Measurements

Fluorescence spectra were recorded on an absolute photoluminescence quantum yield measurement system (HAMAMATSU Quantaurus-QY).

1.3 Results and Discussion

The preparation of Mes-substituted acenes, **1** and **3**, has already been reported,[12,13] and 5,12-dimesityltetracene **2** was newly prepared in 63% yield by treating mesitylmagnesium bromide with 5,12-naphthacenedione, followed by reduction of the resulting Mes-substituted magnesium alcoholate compound with $SnCl_2$–HCl. The absolute fluorescence quantum yields of **1**, **2**, and **3** in *n*-hexane were 0.78, 0.59, and 0.10, respectively (Figure 1.2).

(a) (b)

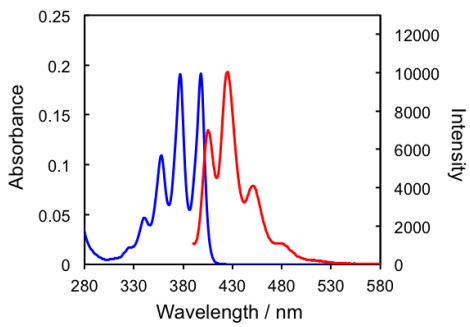

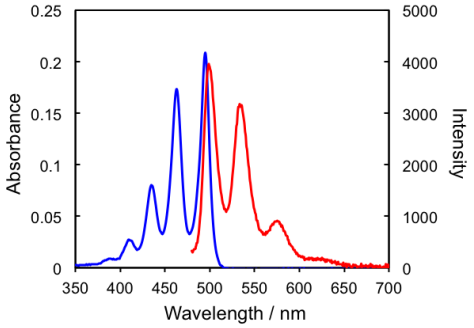

(c)

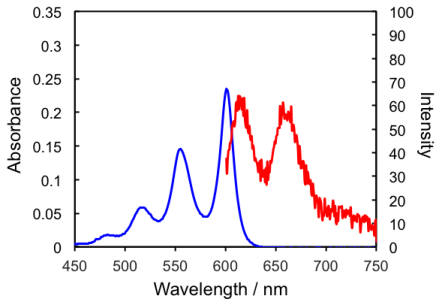

(d)

Figure 1.2. Absorption and fluorescence spectra of (a) **1**, (b) **2**, and (c) **3** in CH_2Cl_2 at 1×10^{-5} M, and (d) photograph of the CH_2Cl_2 solution of compounds **1**–**3** with UV irradiation at 365 nm.

Prior to discussion on the oxidized species of **1**-**3**, their redox properties are summarized on the basis of cyclic voltammetry (CV). For comparison, we remeasured the redox potentials of **1** and **3**, together with those of newly prepared **2**, on the same conditions. The CV for **1**-**3** revealed single reversible oxidation waves (**1**: $E_{1/2}^{ox}$ = +0.77 V; **2**: $E_{1/2}^{ox}$ = +0.47 V; **3**: $E_{1/2}^{ox}$ = +0.23 V (**3**) vs $Fc^{0/+}$) in CH_2Cl_2 and single reversible reduction waves (**1**: $E_{1/2}^{red}$ = –2.64 V; **2**: $E_{1/2}^{red}$ = –2.21 V; **3**: $E_{1/2}^{red}$ = –1.94 V vs $Fc^{0/+}$) in THF. The substitution of Mes-groups resulted, to some extent, in the low oxidation potentials as compared with those of the related compounds. The electrochemical HOMO-LUMO gaps ($\Delta E_{gap} = E_{1/2}^{ox} - E_{1/2}^{red}$) for **1**-**3** were estimated to be 3.41, 2.68, and 2.17 eV, respectively, and were in good accordance with the DFT-computed HOMO-LUMO gaps (B3LYP/6-31G*, **1**: 3.47 eV; **2**: 2.71 eV; **3**: 2.15 eV). Thus it suggests that the radical cations of **1**-**3** would be easily accessible by chemical oxidation.

To explore the electronic states for the oxidized species of **1**-**3**, we recorded the optical absorption spectral change during electrochemical oxidation of **1**-**3** in CH_2Cl_2 (Figure 1.3) and the observed spectral features were assigned by the time-dependent DFT calculations (TD-DFT: (U)B3LYP/6-31G*), as shown in Figures 1.4–1.6. The substitution of Mes-groups resulted in the bathochromic shift of the lowest energy bands of anthracene, tetracene, and pentacene as compared with those of the related compounds. For 9,10-dimesitylanthracene **1**, the lowest energy band possessing its associated vibrational structure at 3.12 eV (398 nm), corresponding to the HOMO-LUMO transition of the anthracene core, was gradually changed into new bands at 1.79 eV (689 nm) and 2.89 eV (430 nm) with an isosbestic point at 3.06 eV (406 nm) on going from **1** to $\mathbf{1}^{\bullet+}$. A similar spectral change was also observed for the

electrochemical oxidation from **2** to $\mathbf{2}^{\bullet+}$: the lowest energy vibronic band at 2.51 eV (495 nm) due to the HOMO-LUMO transition of the tetracene core was changed into new bands at 1.40 eV (884 nm) and 1.61 eV (768 nm) with an isosbestic point at 3.06 eV (405 nm). In the electrochemical oxidation from **3** to $\mathbf{3}^{\bullet+}$, the lowest energy vibronic band at 2.06 eV (601 nm) originating from the HOMO-LUMO transition of the pentacene core was replaced by new bands 1.04 eV (1194 nm), 1.31 eV (947 nm), and 1.48 eV (836 nm), which are similar to those in the absorption spectra of $\mathbf{3}^{\bullet+}$ observed by the oxidative titration with $SbCl_5$.[13] The origin of the observed lowest energy transitions for $\mathbf{1}^{\bullet+}$ and $\mathbf{2}^{\bullet+}$ was mainly assigned to the transition from β(HOMO-4) to β(LUMO), where both orbitals are localized on the acene core of **1** and **2** (Figures 1.4b and 1.5b). Differently, for $\mathbf{3}^{\bullet+}$ the lowest energy transition was predominantly from α(HOMO) to α(LUMO), and thus the transition from β(HOMO) to β(LUMO), corresponding to the lowest energy transition for $\mathbf{1}^{\bullet+}$ and $\mathbf{2}^{\bullet+}$, was attributed to the next lowest energy transition (Figure 1.6b). Hence, the weak vibronic band at 1.04 eV was characterized by a small HOMO-LUMO gap of $\mathbf{3}^{\bullet+}$.

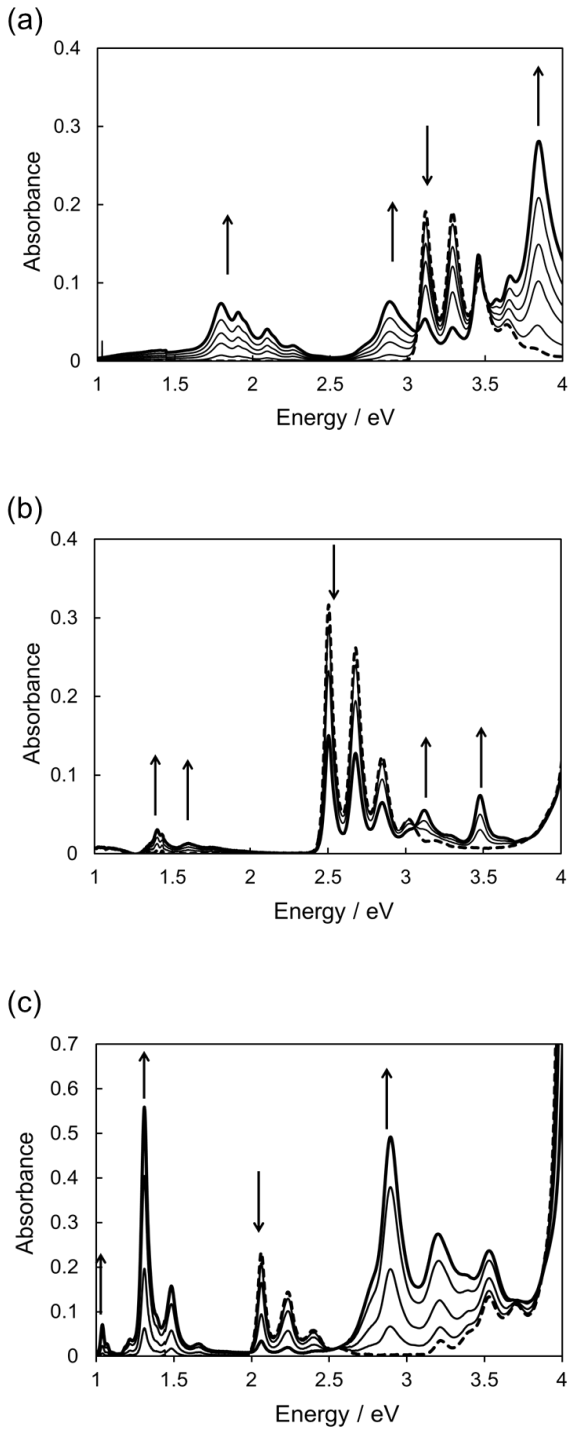

Figure 1.3. UV/Vis-NIR optical absorption spectral change during the stepwise electrochemical oxidation (a) from **1** (broken line) to $\mathbf{1}^{\bullet+}$ (bold line), (b) from **2** (broken line) to $\mathbf{2}^{\bullet+}$ (bold line), and (c) from **3** (broken line) to $\mathbf{3}^{\bullet+}$ (bold line), in CH_2Cl_2 with 0.1 M *n*-Bu_4NBF_4 at 298 K.

(a)

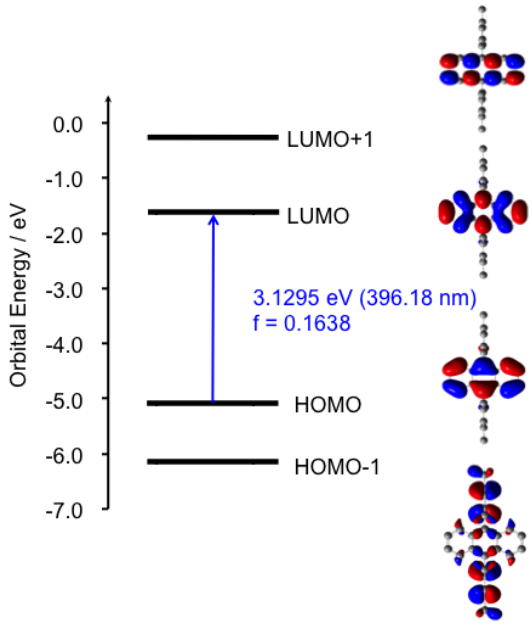

(b)

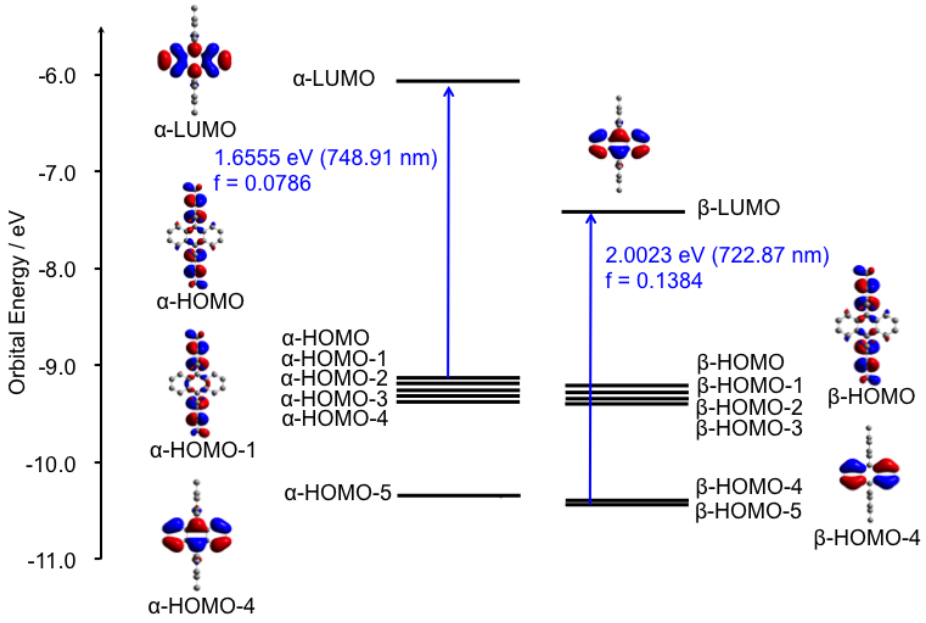

Figure 1.4. Frontier Kohn-Sham orbital energy levels for the ground state of (a) **1** and (b) $\mathbf{1}^{\bullet+}$ at (U)B3LYP/6-31G* level of theory. The arrows represent the major contributions related to the lowest energy optical absorption bands observed experimentally for $\mathbf{1}^{\bullet+}$ on the basis of TD-DFT calculations.

(a)

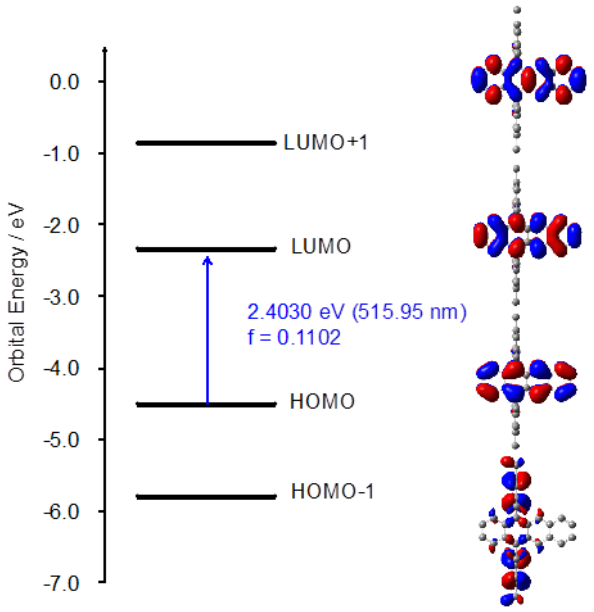

(b)

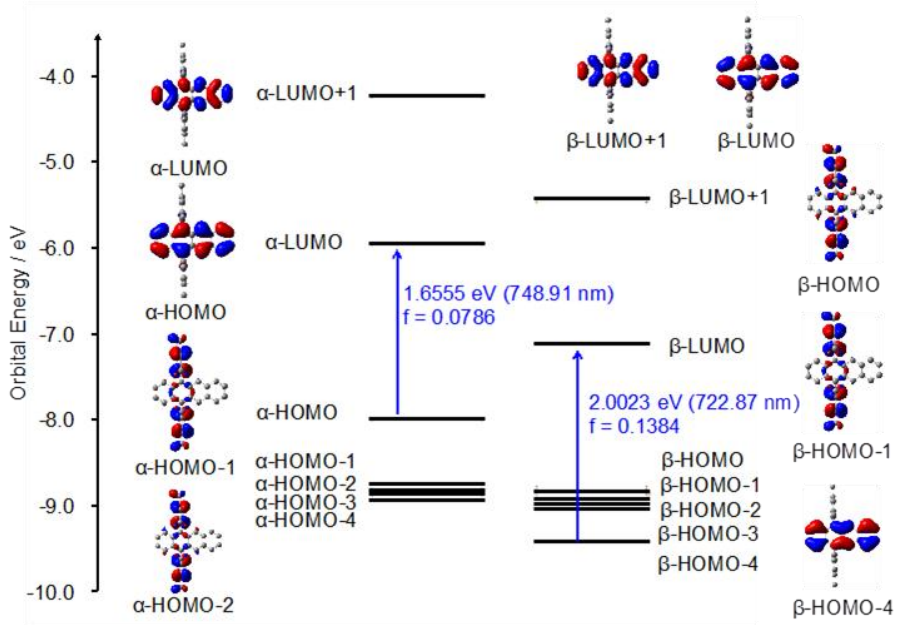

Figure 1.5. Frontier Kohn-Sham orbital energy levels for the ground state of (a) **2** and (b) $\mathbf{2}^{\bullet+}$ at (U)B3LYP/6-31G* level of theory. The arrows represent the major contributions related to the lowest energy optical absorption bands observed experimentally for $\mathbf{2}^{\bullet+}$ on the basis of TD-DFT calculations.

(a)

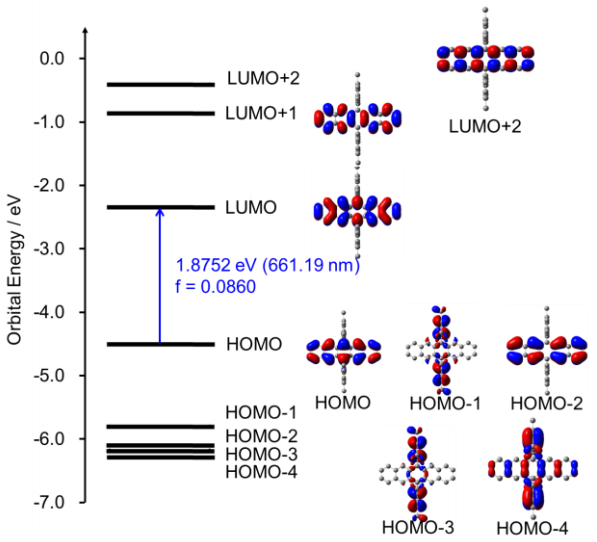

(b)

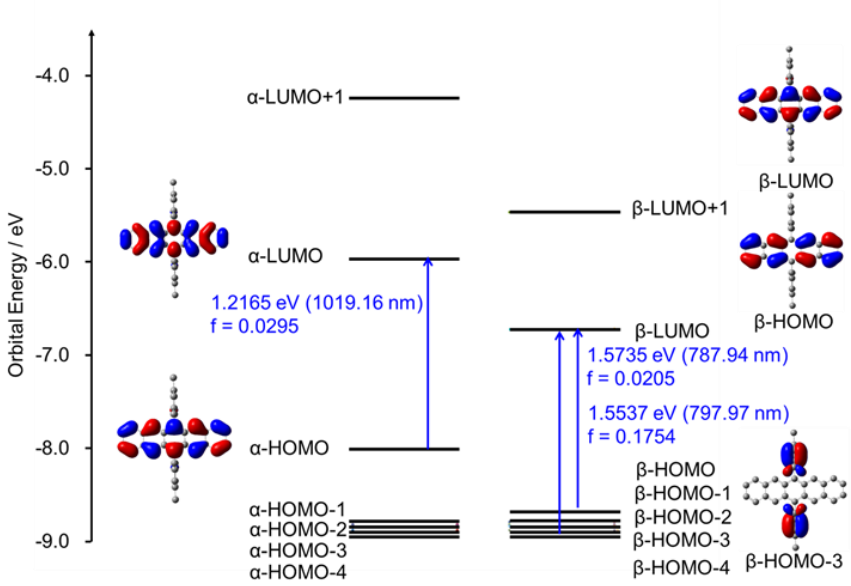

Figure 1.6. Frontier Kohn-Sham orbital energy levels for the ground state of (a) **3** and (b) $\mathbf{3}^{\bullet+}$ at (U)B3LYP/6-31G* level of theory. The arrows represent the major contributions related to the lowest energy optical absorption bands observed experimentally for $\mathbf{3}^{\bullet+}$ on the basis of TD-DFT calculations.

The electrochemical measurements on **1**–**3** indicated that radical cations can be formed by chemical oxidation reactions; the compounds **2** and **3** were oxidized with 1 equiv of $AgSbF_6$ in CH_2Cl_2 at room temperature, whereas oxidation of **1** with the same oxidant went wrong probably due to the higher oxidation potential of **1**; finally the generation of radical cation $\mathbf{1}^{\bullet+}$ was achieved by treatment with excess $SbCl_5$, however, the neutral **1** were completely recovered by dilution of the CH_2Cl_2 solution containing $\mathbf{1}^{\bullet+}$ with CH_2Cl_2. The ESR spectra of $\mathbf{1}^{\bullet+}$, $\mathbf{2}^{\bullet+}$, and $\mathbf{3}^{\bullet+}$ in CH_2Cl_2 solution[14] at 298 K are shown in Figure 1.7, together with the simulated spectra. For $\mathbf{1}^{\bullet+}$, although the observed spectrum was low-resolved at 298 K, clear hyperfine interactions with two nonequivalent hydrogen nuclei originating from the anthracene core and with four identical hydrogen nuclei of Mes groups were observed at 193K (Figure 1.8a), and the hyperfine coupling constants (hfccs) were determined to be 0.25 (4H), 0.12 (4H), and 0.06 mT (4H) by the digital simulation, and the contributions from the negligible hydrogen nuclei were incorporated in the line width of the spectral simulation (0.2 mT) (Figure 1.7a). In the case of Mes-substituted tetracene **2** and pentacene **3**, one-electron oxidation leads to the more resolved ESR spectra at 298 K (Figures 1.7b and 1.7c), and the signal patterns of which were attributed to hyperfine interaction with five and three nonequivalent hydrogen nuclei (the simulated hfccs: 0.500 (2H), 0.185 (2H), 0.160 (2H), 0.100 (2H), and 0.080 mT (2H) for $\mathbf{2}^{\bullet+}$; 0.35 (4H), 0.10 (4H), and 0.05 mT (4H) for $\mathbf{3}^{\bullet+}$) and the contributions from the negligible hydrogen nuclei were incorporated in the line width of the spectral simulation (0.085 mT for $\mathbf{2}^{\bullet+}$; 0.065 mT for $\mathbf{3}^{\bullet+}$). The determined hfccs were in good correlation with the previous data on the radical cations of tetracene, pentacene, and their derivatives,[15–19] which were generated in concentrated sulfuric acid and so on (Figure 1.9). The spectral shape of $\mathbf{1}^{\bullet+}$, $\mathbf{2}^{\bullet+}$, and $\mathbf{3}^{\bullet+}$ remained unchanged

in the measured temperature range from 20 to –80℃; however, the resolutions were improved with decreasing temperature (Figure 1.8).

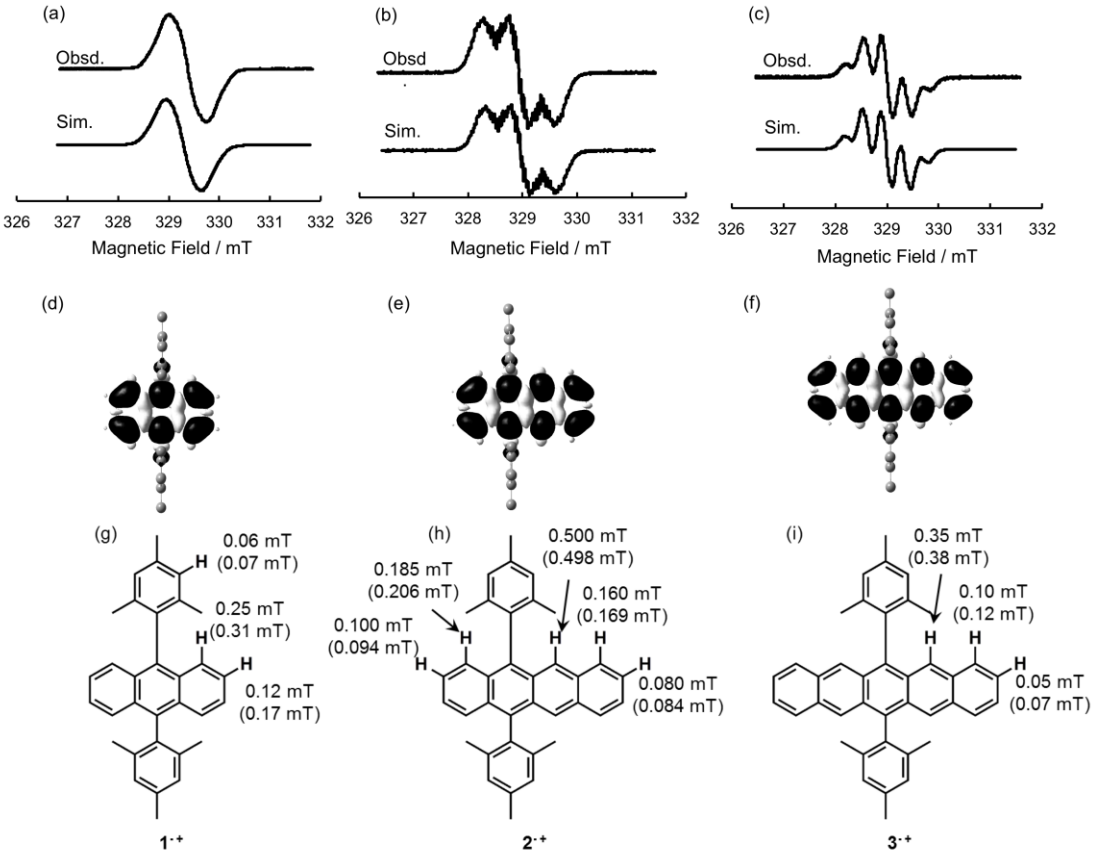

Figure 1.7. Observed and simulated X-band ESR spectra of (a) $\mathbf{1}^{\bullet+}$ (0.1 mM in CH_2Cl_2), (b) $\mathbf{2}^{\bullet+}$ (1.0 mM in CH_2Cl_2), and (c) $\mathbf{3}^{\bullet+}$ (0.1 mM in CH_2Cl_2) in CH_2Cl_2 at 293 K; the DFT-computed spin density distributions of (d) $\mathbf{1}^{\bullet+}$, (e) $\mathbf{2}^{\bullet+}$, and (f) $\mathbf{3}^{\bullet+}$ (UB3LYP/6-31G*); the simulated ^{1}H hfcc values (and the DFT-computed values (UB3LYP/6-31G*) are in parentheses) for (g) $\mathbf{1}^{\bullet+}$, (h) $\mathbf{2}^{\bullet+}$, and (i) $\mathbf{3}^{\bullet+}$.

(a)

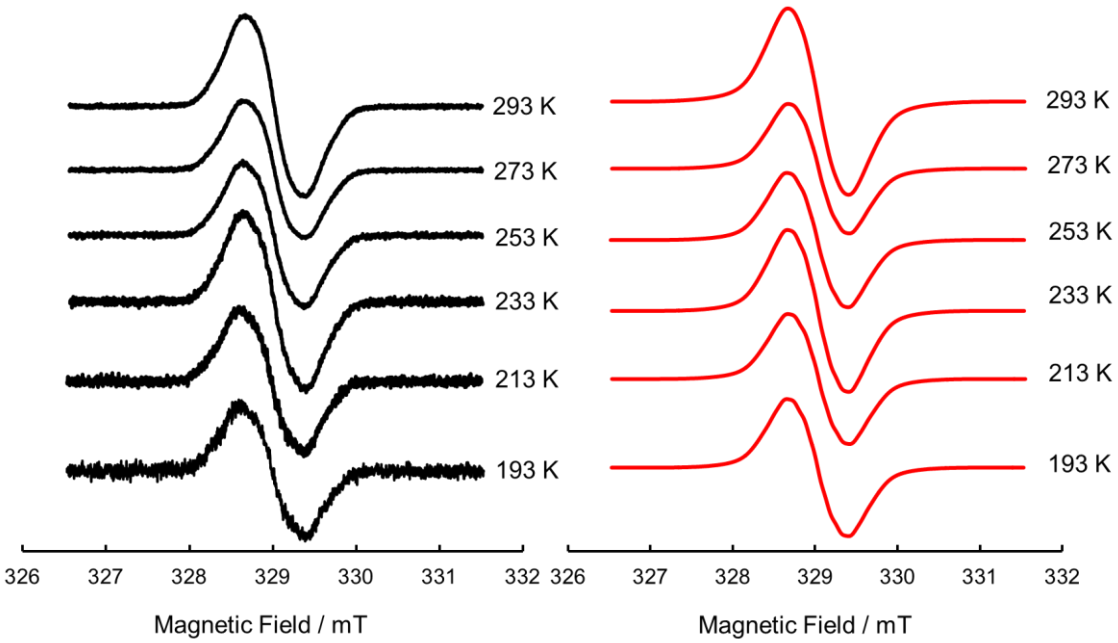
293 K
273 K
253 K
233 K
213 K
193 K
326
327
328
329
330
331
332
Magnetic Field / mT
293 K
273 K
253 K
233 K
213 K
193 K
326
327
328
329
330
331
332
Magnetic Field / mT

(b)

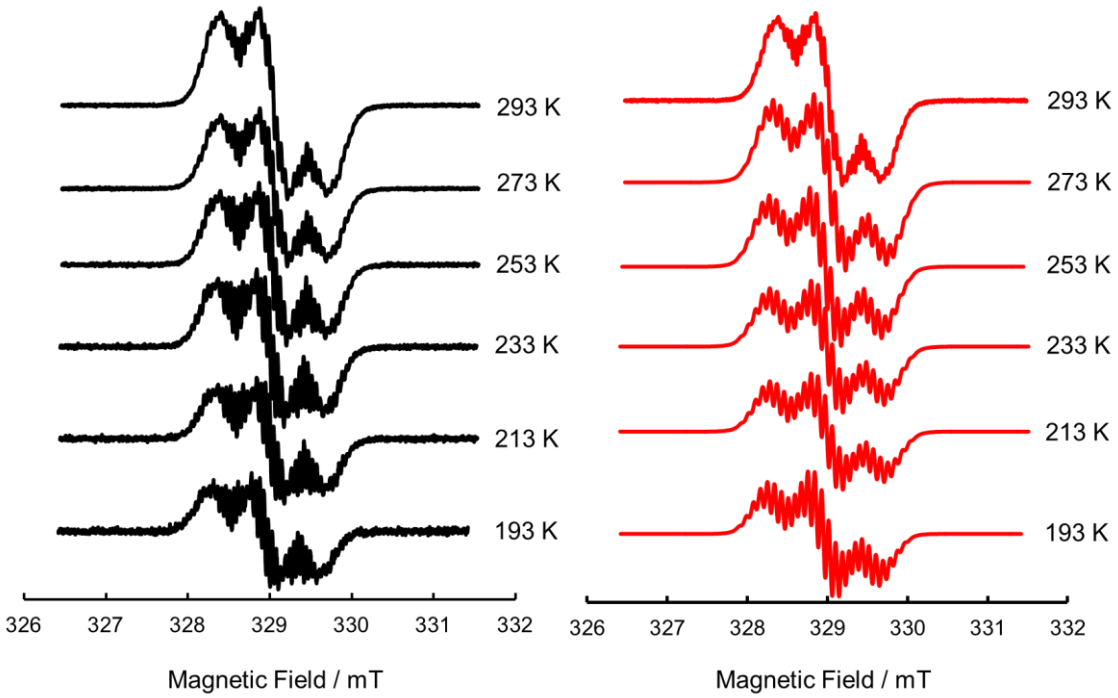
293 K
273 K
253 K
233 K
213 K
193 K
326
327
328
329
330
331
332
Magnetic Field / mT
293 K
273 K
253 K
233 K
213 K
193 K
326
327
328
329
330
331
332
Magnetic Field / mT

(c)

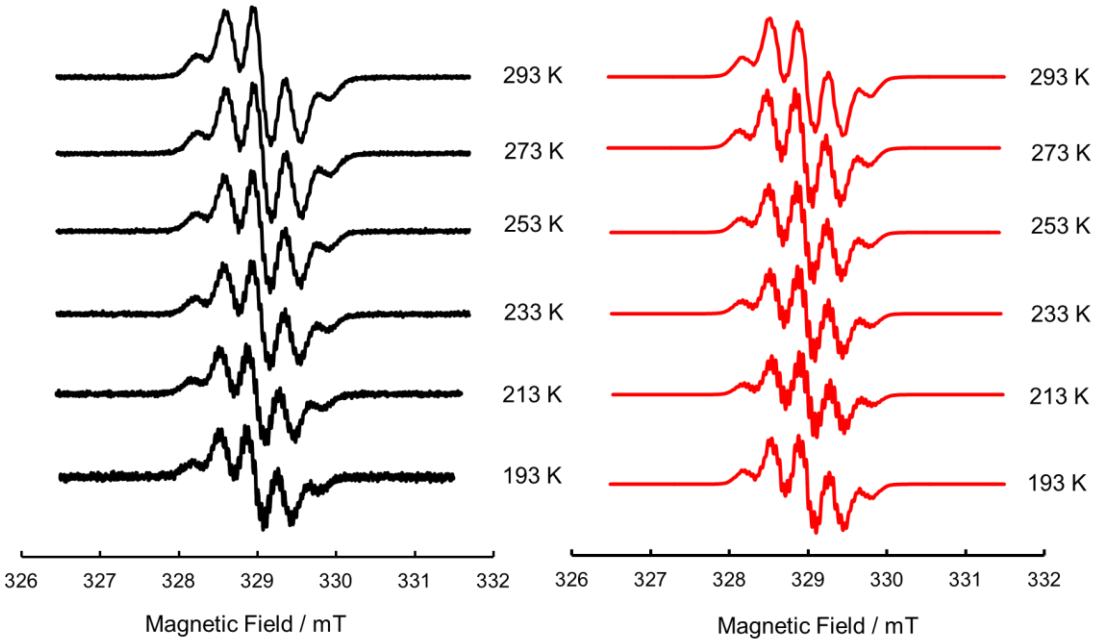

Figure 1.8. Temperature-dependence of the observed (black) and simulated (red) X-band ESR spectra of (a) $\mathbf{1}^{\bullet+}$, (b) $\mathbf{2}^{\bullet+}$, and (c) $\mathbf{3}^{\bullet+}$.

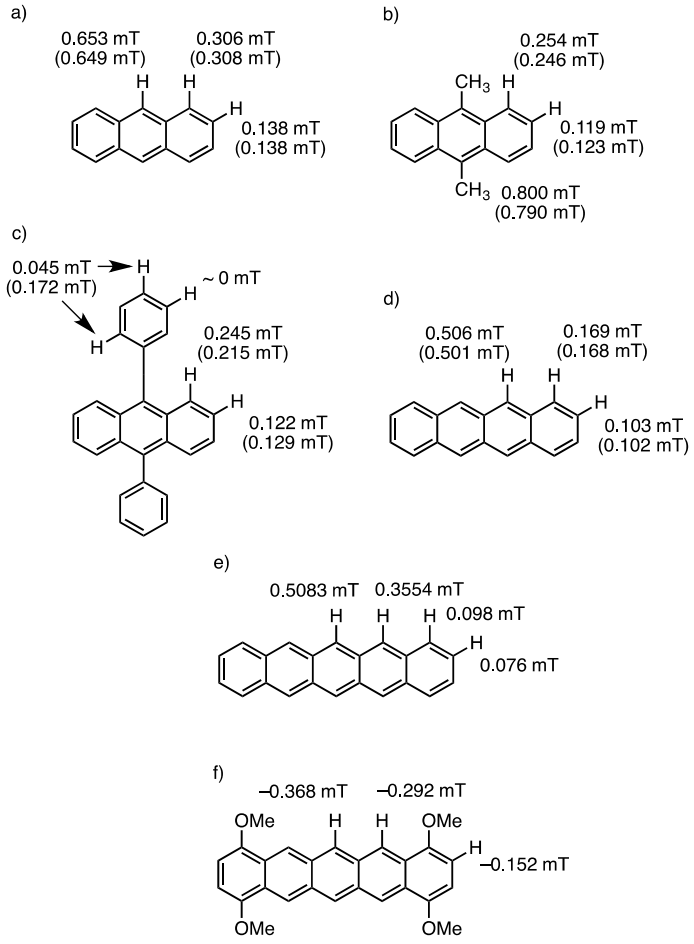

Figure 1.9. Reported ^{1}H hfcc values for radical cations of the related acene compounds: a) measured in conc. H_2SO_4 (in CH_2Cl_2 by oxidation with $SbCl_5$ in parentheses), see Ref. 18; b) measured in conc. H_2SO_4 (in CH_2Cl_2 by oxidation with $SbCl_5$ in parentheses), see Refs. 18 and 15a; c) measured in conc. H_2SO_4 (in CH_3CN by electrochemical oxidation in the presence of tetraethylammonium perchlorate in parentheses), see Refs. 17 and 16; d) measured in conc. H_2SO_4 (in CH_2Cl_2 by oxidation with $SbCl_5$ in parentheses), see Ref. 18; e) measured in liq. SO_2 by oxidation with a stoichiometric amount of BF_3), see Ref. 19; f) measured in trifluoroacetic acid, see Ref. 20.

As has been recently pointed out by Yeates and coworkers, the photochemical stability of TIPS-pentacene in solution was found to be concentration- and solvent-dependent.[21] To check the photo-stability of the acene radical cations $\mathbf{1}^{\bullet+}$ – $\mathbf{3}^{\bullet+}$ in air-equilibrated solvent under ambient light, the author herein chose 1.0×10^{-4} M[22] solutions in CH_2Cl_2 at room temperature, on the grounds that the oxidation reactions prefer in the chlorinated hydrocarbon solvents. The half-life times ($\tau_{1/2}$) for the neutral species of **1**–**3** and their radical cations were estimated from the normalized absorbance–time profiles $A(t)/A(0)$ at the lowest energy absorption bands, which are characteristic of the acene cores, as a function of the irradiation time. First of all, the half-lives of **1**–**3** in minutes were determined to be 3135, 979, and 482, respectively. For comparison, the half-life for TIPS-pentacene was reported to be about 500 min under ambient light and air conditions similar to the present conditions.[23] The decay profiles of $\mathbf{1}^{\bullet+}$–$\mathbf{3}^{\bullet+}$ in the air-equilibrated CH_2Cl_2 solution were shown in Figure 1.10, and the estimated half-lives of the radical cations in minutes, 1414 ($\mathbf{1}^{\bullet+}$), 63 ($\mathbf{2}^{\bullet+}$), and 292 ($\mathbf{3}^{\bullet+}$), were on the same order as those of the corresponding neutral species, beyond the expectations. Additionally, the decrease of half-lives of $\mathbf{1}^{\bullet+}$–$\mathbf{3}^{\bullet+}$ were observed to a greater or lesser extent in the concentrated solution at 1.0×10^{-3} M; 666 ($\mathbf{1}^{\bullet+}$), 42 ($\mathbf{2}^{\bullet+}$), and 220 ($\mathbf{3}^{\bullet+}$) minutes.[24] It should be noted, however, that the stability of Mes-substituted pentacene radical cation ($\mathbf{3}^{\bullet+}$) is comparatively maintained even at higher concentration. The relative instability of $\mathbf{2}^{\bullet+}$ is probably due to halfway protection of 6- and 11-positions of tetracene core where the spin density is concentrated. Such decent stabilities of the Mes-substitued acene radical cations comparable to their neutral states under ambient light and air conditions are probably reflected in the generation of two aromatic sextets shown in Scheme 1.1b,[25] as is

supported by the NICS(0) values computed for **1**–**3**, and $\mathbf{1}^{\bullet+}$–$\mathbf{3}^{\bullet+}$.[26] The present results open the way to persistent acene radical cations, and lead to multi-spin molecular systems based on acene radical cations as spin-bearing units. Unfortunately, we could not isolate the single crystals of the present radical cations; however, elaborate substituents promises realization of isolable acene radical cations.

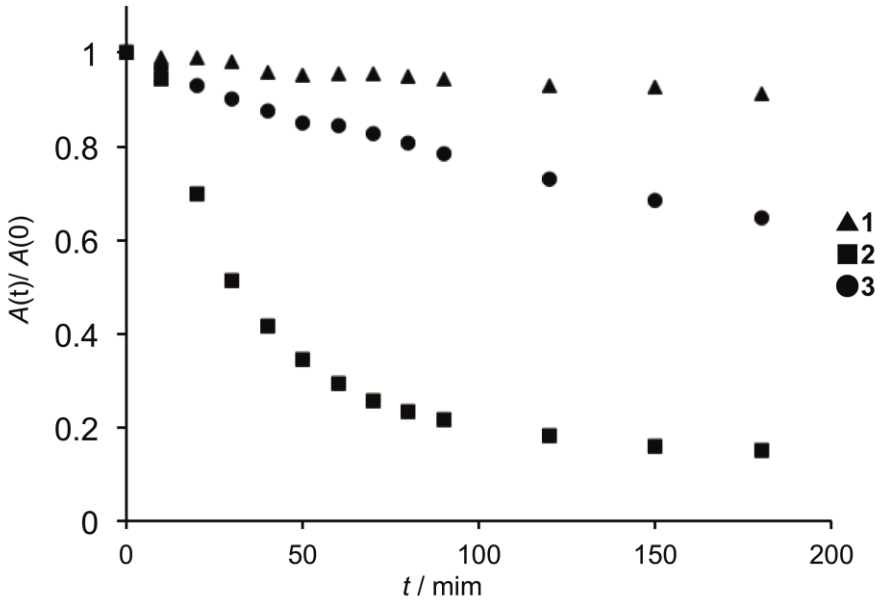

Figure 1.10. Decay profiles of $\mathbf{1}^{\bullet+}$ (▲), $\mathbf{2}^{\bullet+}$ (■), and $\mathbf{3}^{\bullet+}$ (●) for 1.0×10^{-4} M solutions in CH_2Cl_2 at room temperature under ambient light and air conditions.

1.4 Conclusion

The electronic structures, and photochemical stability of radical cations of synthetically readily accessible acenes: anthracene, tetracene, and pentacene, in solution under ambient light and air conditions were reported in this chapter. Radical cations of synthetically readily accessible acenes: anthracene, tetracene, and pentacene, with moderately bulky mesityl substituents revealed that their photochemical stability in solution under ambient light and air conditions is comparable to that of the corresponding neutral state, thus indicating the possibility of persistent acene radical cations.

1.5 References

[1] a) K. Deuchert, S. Hünig, *Angew. Chem. Int. Ed.* **1978**, *17*, 875-886; b) M. Bendikov, F. Wudl, D. F. Perepichka, *Chem. Rev*. **2004**, *104*, 4891–4946.

[2] J. E. Anthony, *Chem. Rev*. **2006**, *106*, 5028–5048.

[3] J. E. Anthony, *Angew. Chem. Int. Ed*. **2008**, *47*, 452–483.

[4] J. E. Anthony, J. S. Brooks, D. L. Eaton, S. R. Parkin, *J. Am. Chem. Soc*. **2001**, *123*, 9482–9483.

[5] R. Einholz, H. F. Bettinger, *Angew. Chem. Int. Ed.* **2013**, *52*, 9818-9820.

[6] E. Clar, *The Aromatic Sextet*, Wiley, New York, **1972**.

[7] M. Solà, *Front. Chem*. **2013**, *1*, 22.

[8] K. Ragavachari, *Theor. Chem. Acc*. **2000**, *103*, 361-363 and references cited therein.

[9] A. Dreuw, M. Head-Gordon, *Chem. Rev*. **2005**, *105*, 4009-4037.

[10] W. J. Hehre, L. Radom, P.v. R. Schleyer, J. A. Pople, *Ab Initio Molecular Orbital Theory*, Wiley, New York, **1986**.

[11] M. J. Frisch, *et al*., Gaussian 09 (Revision C.01), Gaussian, Inc., Wallingford CT, **2010**.

[12] C. Hoffend, M. Diefenbach, E. Januszewski, M. Bolte, H.-W. Lerner, M. C. Holthausen, M. Wagner, *Dalton Trans.* **2013**, *42*, 13826-13837.

[13] X. Shi, W. Kueh, B. Zheng, K. -W. Huang, C. Chi, *Angew. Chem. Int. Ed.* **2015**, *54*, 14412-14416.

[14] The samples for ESR measurements were degassed by three freeze-pump-thaw cycles, and then charged with high purity nitrogen gas (99.9999%) before sealing. The concentrations of the radical species in CH_2Cl_2 were determined so as to obtain the highest-resolution hyperfine ESR spectra.

[15] a) J. R Bolton, A. Carrington, A. D. McLachlan, *Mol. Phys*. **1962**, *5*, 31-41; b) J. R. Bolton, G. K. Fraenkel, *J. Phys. Chem*. **1964**, *40*, 3307-3320.

[16] R. E. Sioda, W. S. Koski, *J. Am. Chem. Soc*. **1965**, *87*, 5573-5575.

[17] L. O. Wheeler, K. S. V. Santhanam, A. J. Bard, *J. Phys. Chem*. **1966**, *70*, 404-406.

[18] I. C. Lewis, L. S. Singer, *J. Chem. Phys.* **1965**, *43*, 2712-2727.

[19] J. R. Bolton, *J. Chem. Phys*. **1967**, *46*, 408-409.

[20] A. R. Wartini, H. A. Staab, F. A. Neugebauer, *Eur. J. Org. Chem*. **1998**, 1161-1170.

[21] L. Abu-Sen, J. J. Morrison, A. B. Horn, S. G. Yeates, *Adv. Optical Mater*. **2014**, *2*, 636-640.

[22] According to ref. 21, the half-life of TIPS-pentacene increases with increasing concentration of the solution; particularly in the chlorinated solvents such as CH_2Cl_2, a substantial increase in half-life takes place at around 1.0×10^{-4} M.

[23] I. Kaur, W. Jia, R. P. Kopreski, S. Selvarasah, M. R. Dokmeci, C. Pramanik, N. E. McGruer, G. P. Miller, *J. Am. Chem. Soc*. **2008**, *130*, 16274-16286.

[24] The trend of the half-lives for the acene radical cations was opposite to that of the half-life for the neutral TIPS-pentacene: above concentrations of around 2×10^{-4} M, the half-life of TIPS-pentacene was observed to increase up to the solubility limit, probably because of insusceptibility to O_2 activation due to partial aggregation of TIPS-pentacene (ref. 21). The discrepancy between the half-lives for the neutral and cationic states of acenes might be ascribed to the difference of their spin states.

[25] The photochemical stability of $\mathbf{1}^{\bullet+}$ – $\mathbf{3}^{\bullet+}$ might closely relate to the half-life increase by introduction of stable neutral radical substituents to pentacene: Y. Kawanaka, A. Shimizu, T. Shinada, R. Tanaka, Y. Teki, *Angew. Chem. Int. Ed*. **2013**, *52*, 6643-6647.

[26] a) P. v. R. Schleyer, C. Maerker, A. Dransfeld, H. Jiao, N. J. R. v. E. Hommes, *J.*

Am. Chem. Soc. **1996**, *118*, 6317-6318; b) P. v. R. Schleyer, M. Manoharan, H. Jiao, F. Stahl, *Org. Lett*. **2001**, *3*, 3643-3646.

Chapter 2

9,10–Diaminoanthracenes Revisited: The Influence of *N*-Substituents on their Electronic States

2.1 Introduction

Two-stage redox systems where their redox-active end groups are located outside a central arene π-system that has an aromatic character in the fully reduced state are classified into the Wurster-type, and one of the representative examples, *N*,*N*,*N'*,*N'*-tetramethyl-*p*-phenylenediamine (**TMPD**) is well-known for the precursor of the stable radical cation, Wurster's Blue (Figure 2.1a).[1] When the central arene π-system in **TMPD** is replaced by extended π-systems such as polycyclic aromatic hydrocarbons, the question of whether such a Wurster-type-like redox system retains the two-stage redox property is of great interest. In this sense, it has already been reported that 9,10-bis(*N*,*N*-dimethylamino)anthracene **1** (Figure 2.1c) showed only one two-electron oxidation process with a distinctive cyclic voltammogram, whereas **TMPD** undergoes typical two reversible one-electron oxidation processes to form the

semiquinoid radical cation and quinoid dication.[2] The observed electrochemical behavior was explained by the large structural change into a butterfly-like structure during the two-electron oxidation process, in which the central six-membered ring is folded along the C9–C10 line (Figure 2.1b).[2,3]

On the other hand, 9,10-bis(*N*,*N*-di(*p*-anisyl)amino)anthracene **3** has been prepared to examine the electronic coupling in tetraanisylarylenediamine mixed-valence systems.[4] In contrast to **1**, the diamine **3** displayed two reversible one-electron oxidation processes with a very small redox potential splitting,[4] thus strongly suggesting no significant structural changes during the electrochemical oxidation. More recently, the dication of **3** has been reported to be in a spin-singlet in the ground state with a small singlet-triplet energy gap, thus leading to its diradical character due to its thermally accessible excited spin-triplet state, and furthermore, the X-ray structural analysis revealed that $\mathbf{3}^{2+}$ did not adopt the folding butterfly-like structure and the planarity of the anthrylene moiety was preserved.[5]

These findings strongly suggest that the difference in the *N*-substituent patterns of 9,10-diaminoanthracenes causes the different redox behaviors (Figure 2.1b). Herein the author reports how the difference in the *N*-substituent identity influences the electronic structures of the oxidized species of hitherto sporadically studied 9,10-diaminoanthracenes, **1** and **3**, and additionally **2**, where two of four methyl groups in **1** are replaced by anisyl groups, has been newly prepared (Figure 2.1c). To do the comparative study on the electronic structures of oxidized states of **1**–**3**, we have carried out a complementary series of measurements such as cyclic voltammetry, spectroelectrochemistry, and ESR spectroscopy, and furthermore, performed density functional theory (DFT) calculations.

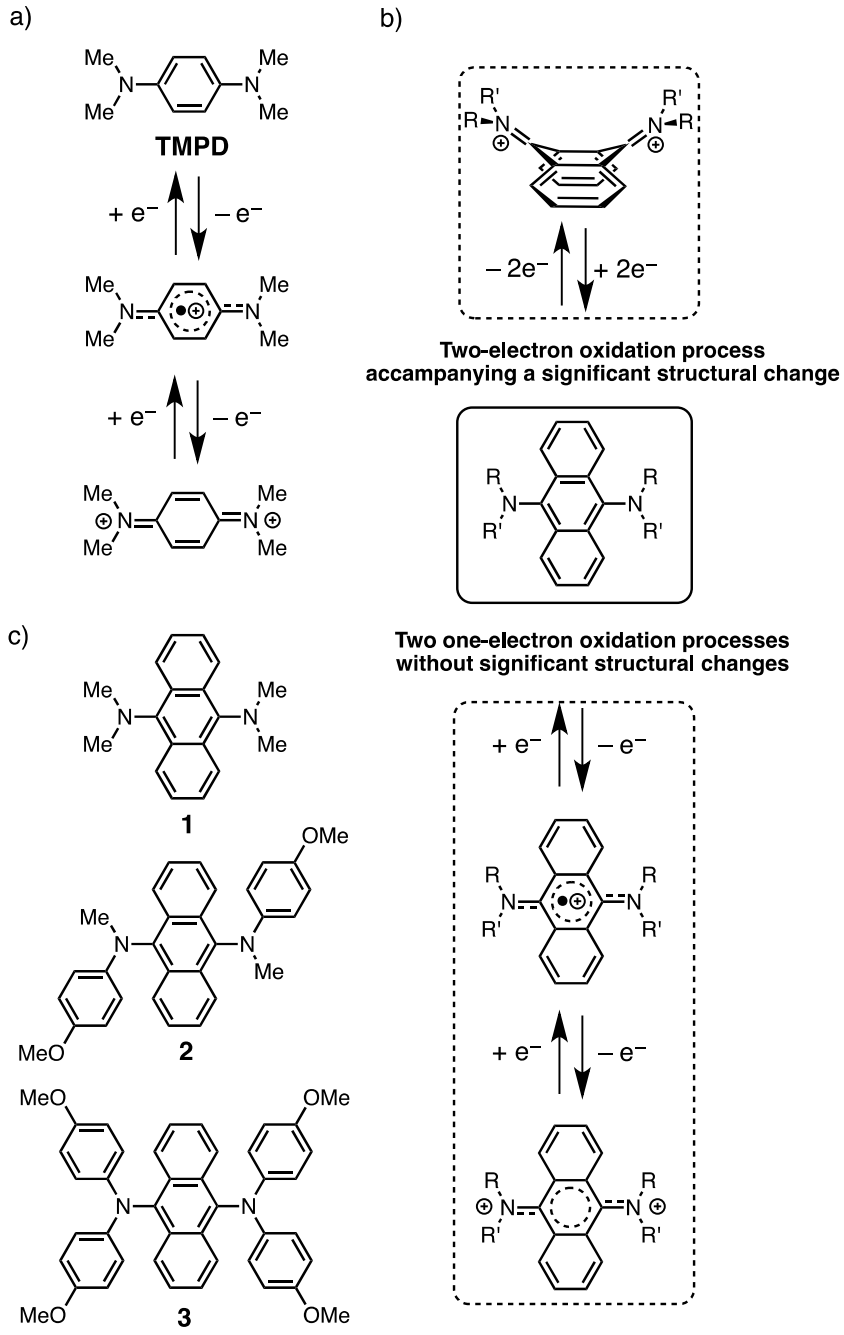

Figure 2.1. a) *N*,*N*,*N'*,*N'*-tetramethyl-*p*-phenylenediamine (**TMPD**) as an exemplary two-stage Wurster-type redox system, b) two directions of redox processes for 9,10-diaminoanthracenes, and c) a series of 9,10-diaminoanthracenes **1**–**3**, where the methyl groups as *N*-substituents of **1** are replaced by the anisyl groups.

2.2 Experimental Section

2.2.1 Synthesis

All starting materials and reagents of standard quality were purchased from Tokyo Chemical Industry Co., Ltd. (Tokyo, Japan), and used without further purification. Compounds **1** and **3** was prepared by following the reported method.[4,6] Toluene was purchased from Kanto Chemical Co., Inc. (Tokyo, Japan), and purified by the GlassContour solvent purification system. Dichloromethane was purchased from Nacalai Tesque Inc. (Kyoto, Japan), and refluxed over and then distilled from calcium hydride under argon before use. Column chromatography was carried out with silica gel (Kanto Chemical Co., Inc., silica gel 60N, spherical neutral). ^{1}H and ^{13}C NMR spectra were measured by a JEOL JNM-AL400 FT-NMR spectrometer. Chemical shifts of NMR spectra are determined relative to internal tetramethylsilane (TMS) standard (δ), and are given in parts per million (ppm). High resolution (HR) electrospray ionization (ESI) mass spectra were recorded using a mass spectrometer (Thermo Fisher EXACTIVE). Elemental analyses were performed by Center for Organic Elemental Microanalysis, Kyoto University.

Synthesis of 9,10-Bis(*N*-*p*-anisyl-*N*-methylamino)anthracene (**2**): A mixture of N-p-anisyl-*N*-methylamine (274.4 mg, 2 mmol), 9,10-dibromoanthracene (336.0 mg, 1 mmol), NaOtBu (288.3 mg, 3 mmol), $Pd(dba)_2$ (27.5 mg, 0.05 mmol), and $P(tBu)_3HBF_4$ (29 mg, 0.1 mmol) in toluene (30 mL) was refluxed under an Ar atmosphere for 24 h. The resulting mixture was cooled down to room temperature and washed with brine. The organic layer was separated and dried over Na_2SO_4. After evaporation of the solvent, the crude product was chromatographed on silica gel (CH_2Cl_2/*n*-hexane = 1:1

(v/v) as eluent) to afford **2** as a yellow solid (213.0 mg, 47.5%); m.p. 293 ℃; ^{1}H NMR (400 MHz, $CDCl_3$): δ = 3.52, 3.56 (s, (~3 + ~3)H), 3.72, 3.73 (s, (~3 + ~3)H), 6.46, 6.49 (d, J = 8.8 Hz, (~2 + ~2)H), 6.75, 6.78 (d, J = 8.8 Hz, (~2 + ~2)H), 7.40 (m, 4H), 7.97 ppm (m, 4H); ^{13}C NMR (100 MHz, $CDCl_3$): δ = 39.64, 39.85, 55.57, 112.67, 114.86, 114.89, 124.91, 126.25, 131.13, 131.18, 139.19, 144.65, 144.72, 151.25, 151.28 ppm; HRMS (ESI): m/z calcd for $C_{30}H_{28}N_2O_2$: 448.2145 $[M]^+$; found 448.2143; Anal calcd for $C_{30}H_{28}N_2O_2$: C, 80.33; H, 6.29; N, 6.25. Found: C, 80.25; H, 6.50; N, 5.85.

2.2.2 DFT Calculations

Quantum chemical calculations were performed with using a hybrid Hartree–Fock/density functional theory (HF/DFT) method ((U)B3LYP).[7] Full geometrical optimization of **1**, **2**, **3**, $\mathbf{1}^{\bullet+}$, $\mathbf{2}^{\bullet+}$, $\mathbf{3}^{\bullet+}$, $\mathbf{1}^{2+}$, $\mathbf{2}^{2+}$, and $\mathbf{3}^{2+}$ were carried out, and furthermore, their local minimum structures were confirmed by performing subsequent frequency analyses. Excitation energies were examined on the basis of the time-dependent density functional method (TD-DFT)[8] by using the (U)B3LYP/6-31G* optimized structures. NICS (nuclear independent chemical shift) values of **2** and $\mathbf{2}^{2+}$ (GIAO/HF/6-311+G*//B3LYP/6-31G*) were computed at the center of the plane (NICS(0)) defined by the peripheral six-membered ring of the anthrylene moiety of **2** and butterfly-like $\mathbf{2}^{2+}$, the geometries of which were re-optimized at the B3LYP/6-31G* level of theory. The NICS value of benzene at the center of the six-membered ring was calculated to –9.4 at the same level of calculation. All the computations employed the 6-31G* basis set.[9] All these computational approaches are implemented in Gaussian 09 package of ab initio MO calculation.[10]

2.2.3 Electrochemical Measurements

The redox properties were evaluated by cyclic voltammetry (CV) and differential pulse voltammetry (DPV) in CH_2Cl_2 solution at 298 K with 0.1 M tetra-*n*-butylammonium tetrafluoroborate ($TBABF_4$) as supporting electrolyte (scan rate 100 mV s^{-1}) using an ALS/chi Electrochemical Analyzer model 612A. A three-electrode assembly was used, which was equipped with a platinum disk (2 mm^2) and a platinum wire as the working and counter electrodes, respectively, and Ag/0.01 M $AgNO_3$ (acetonitrile) was used as the reference electrode. The redox potential were referenced against a ferrocene/ferrocenium ($Fc^{0/+}$) redox potential measured in the same electrolytic solution.

2.2.4 Spectroelectrochemical Measurements

Spectroelectrochemical measurements were carried out with a custom-made optically transparent thin-layer electrochemical (OTTLE) cell (light pass length = 1 mm) equipped with a platinum mesh and a platinum coil as the working and counter electrodes, respectively, and Ag/0.01 M $AgNO_3$ (acetonitrile) was used as the reference electrode. The potential was applied with an ALS/chi Electrochemical Analyzer model 612A.

2.2.5 ESR Measurements

ESR spectra were recorded on a JEOL JES-TE200 X-band ESR spectrometer, in which temperature was controlled by a JEOL ES-DVT3 variable-temperature unit in the range of 193-293 K. A Mn^{2+}/MnO solid solution was used a reference.

2.3 Results and Discussion

2.3.1. Molecular and electronic structures in the neutral state

Syntheses of **1**[6] and **3**[4] have already been reported, and *N*-anisyl-*N*-methyl-substituted 9,10-diaminoanthracene **2** was newly obtained from 9,10-dibromoanthracene and *N*-methyl-4-methoxyaniline by using the Buchwald-Hartwig amination reaction[11,12] similar to **3**. From the X-ray crystallographic determination, the two dianisylamino groups of **3** adopts an eclipsed conformation, and the torsional angle of the dianisylamino group with respect to the 9,10-anthrylene moiety ranges around 72˚ to 74˚, in good agreement with the B3LYP/6-31G** results.[4] Such a large torsional angle indicates the steric congestion between 9,10-anthrylene moiety and the substituted amino groups. In contrast to **1** and **3**, indeed, the ^{1}H NMR spectrum in toluene at room temperature revealed the existence of two conformational isomers of **2**, cisoid and transoid ones (Figure 2.2c). These conformational isomers probably originate from the restricted rotation of amino-substitutents around the 9,10-anthrylene π-face due to the steric congestion. To investigate the conformational change between the two isomers, the author carried out the variable temperature ^{1}H NMR measurements in toluene-d_8 in the temperature range from 293 K to 363 K (Figure 2.2). All the signals corresponding to the methyl, methoxy, and the peripheral phenyl groups of the two isomers gradually broadened with increasing temperature, and finally coalesced into four broad signals at 353 K, indicating the free rotation of the amino groups. As a consequence, the activation energy for the cisoid-transoid conformational change ($\Delta G^{\ddagger}$) was estimated as 18.1 kcal mol^{-1},[13] which is comparable to the rotational barrier for amides (10–20 kcal mol^{-1}).[14] Note that the restricted rotation of amino substitutents has also been detected for the

recently reported 6,13-diaminopentacene derivative **4**, and the estimated activation energy for **4** ($\Delta G^{\ddagger}$ = 17.6 kcal mol^{-1})[15] is comparable to that for **2**.

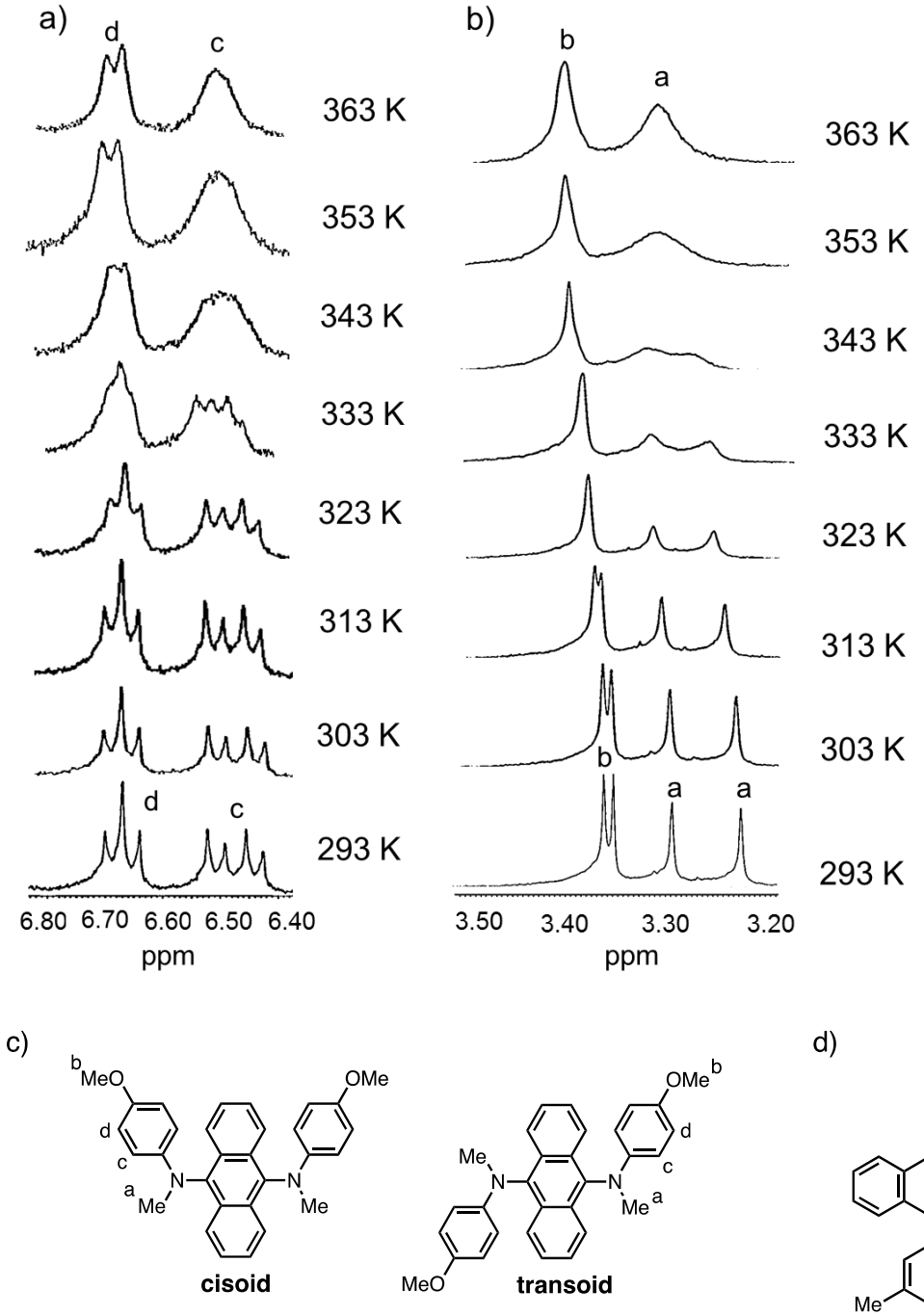

Figure 2.2. Temperature dependence of ^{1}H NMR spectrum of **2** in toluene-d_8; (a) in the aromatic region and (b) in the aliphatic region; c) the cisoid and transoid conformational isomers of **2**; d) 6,13-bis(*N*-*p*-tolyl-*N*-methylamino)pentacene **4**.

To gain insight into the electronic structures of compounds **1**–**3** in their neutral states, the quantum chemical calculations were conducted for **1**–**3** at the B3LYP/6-31G* level of density functional theory (DFT). The optimized geometrical parameters characterizing the molecular structures of **1**, **2**, and **3** are shown in Figure 2.8. Figure 2.3 shows the Kohn-Sham MO energy diagrams in the frontier orbital region for the optimized **1**, **2**, and **3**. As has been pointed out in the case of compound **3**,[4] the HOMO and the energetically neighboring occupied orbitals can be roughly classified into (i) amine-localized, (ii) anthrylene-localized, and (iii) delocalized molecular orbitals according to their relative distributions on the molecular structure, and there exist significant differences in energetic ordering of the above-mentioned three kinds of orbitals for **1**, **2** and **3**. As will be described later, the relative orderings of these occupied orbitals play a crucial role in the structural changes observed in the oxidized states of **1**–**3**.

In the fully *N*-methylated 9,10-diaminoanthracene **1**, both the HOMO and LUMO are localized on the 9,10-anthrylene moiety, thus corresponding to the HOMO and LUMO of anthracene itself, and a pair of nearly degenerate amine-localized molecular orbitals, HOMO-1 and HOMO-2, which are formed by in-phase and out-of-phase combinations of nitrogen-centered 2p AOs on two amino groups, are energetically lower than the anthrylene-localized HOMO (Figure 2.3a). On the other hand, in the partially *N*-methylated 9,10-diaminoanthracene **2**, in-phase and out-of-phase orbital interactions between the HOMO of anthracene itself and the two nitrogen-centered 2p AOs lead to the HOMO and HOMO-2 of delocalized type, while the LUMO is regarded as the anthrylene-localized one (Figure 2.3b). Despite of the delocalized character, the HOMO of **2** markedly retains the shape of the anthracene HOMO. In contrast to compounds **1**

and **2**, the HOMO and HOMO-1 of **3** are of amine-localized character, although the HOMO is still, to some extent, smeared out over the entire molecule (Figure 2.3c). The DFT calculations demonstrate that these differences arise from changes in both the shape and the ordering of the HOMO and the energetically neighboring occupied orbitals due to different orbital interactions between the anthrylene moiety and the substituted amino groups with different *N*-substituents.

The observed lowest energy bands for **1**–**3** were confirmed by TD-DFT calculations for **1**, **2**, and **3**. Calculated vertical excitation energies and oscillator strengths are listed in Table 1. The first excitation corresponds to the excitation to the first singlet excited state ($S_0 \rightarrow S_1$), and the $S_0 \rightarrow S_1$ electronic transition is mainly described by the one-electron excitation from the HOMO to the anthrylene-localized LUMO (Figure 2.3).

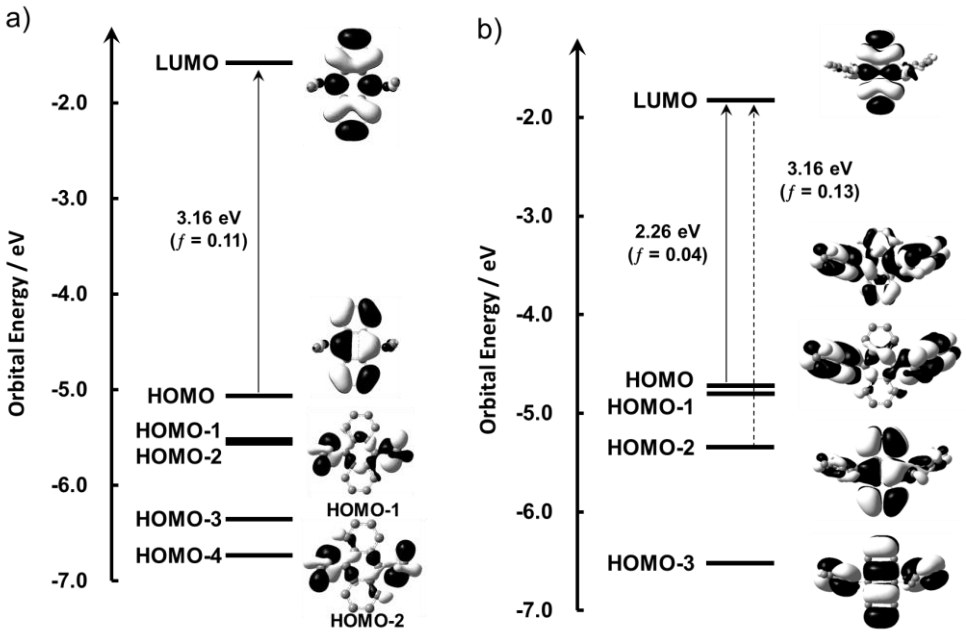

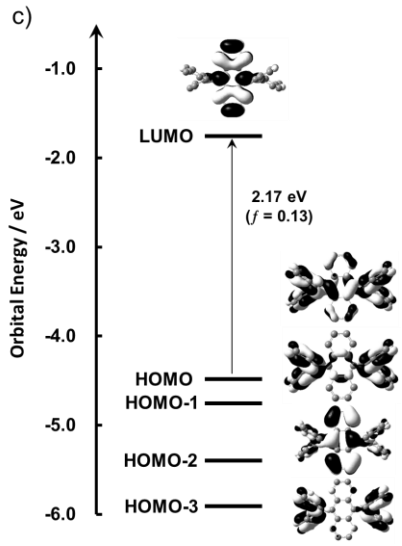

Figure 2.3. Frontier Kohn-Sham orbital energy levels for the ground state of a) **1**, b) **2**, and c) **3** at the B3LYP/6-31G* level of theory. The solid and broken arrows represent the major contributions related to the lowest and next lowest energy optical absorption bands observed experimentally for **1**–**3**.

Table 2.1. TD-DFT//B3LYP/6-31G* vertical excitation energies calculated for **1**, **2**, and **3** related to the lowest energy optical absorption bands observed experimentally for **1**–**3**.

Compound	$h\nu$ (f)[a] [eV]	Major contribution[b]
1	3.16 (0.11)	H → L
2	2.26 (0.04)	H → L
	3.16 (0.13)	H–2 → L
3	2.17 (0.13)	H → L

[a] Oscillator strength (f) values are given in parentheses. [b] HOMO and LUMO are abbreviated as H and L, respectively.

2.3.2. Molecular and electronic structures in the oxidized state

Prior to discussion on the oxidized states of compounds **1**–**3**, their redox properties are organized on the basis of cyclic voltammetry measurements. For comparison, we re-measured electrochemical behaviors of **1** and **3**, together with newly prepared **2**, in the same conditions, and properly, the present behaviors for **1** and **3** are almost the same as those reported previously. The voltammograms obtained for **1**–**3** in CH_2Cl_2 are depicted in Figure 2.4. It should be noted here that the observed voltammogarms for **1** and **2** differ considerably from that for **3**. The fully and partially *N*-methylated 9,10-diaminoanthracens **1** and **2** exhibited a single oxidation peak [–0.18 and +0.17 V versus $Fc^{0/+}$ for **1** and **2**, respectively] and a single reduction peak [–0.59 and –0.22 V versus $Fc^{0/+}$ for **1** and **2**, respectively] on the return sweep with very large anodic/cathodic peak potential separation [ΔE = 0.41 and 0.39 V for **1** and **2**, respectively], as has already been reported by Evans and co-workers.[2] These characteristic voltammograms are explainable by two-electron oxidation process which undergoes a considerable structural change between the neutral and dicationic states,[2,3,16] and thus, it is apparent that compounds **1** and **2** generate deformed dicationic species without an one-electron oxidation process. On the other hand, the fully *N*-anisyl-substituted 9.10-diaminoanthracene **3** showed one quasi-reversible oxidation process. A closer inspection by the differential pulse voltammetry (DPV) and the simulation of the observed DPV clarified that the observed voltammogram consists of successive two reversible one-electron oxidations with a very small potential splitting [ΔE = 0.06 V] for the first and second oxidation processes [E_1 = +0.19 and E_2 = +0.25 V versus $Fc^{0/+}$], as has been reported previously.[4] The observed differences in the redox behaviors among **1**, **2**, and **3** were reminiscent of the *N*-substituent dependency on the

redox properties for 6,13-diaminopentacenes: only fully-*N*-anisyl-substituted 6,13-diaminopentacene displayed the same quasi-reversible cyclic voltammogram as **3**.[17] What has to be noticed here is that the different redox behavior of **3** is no guarantee of suppression of the structural change of **3** upon oxidation, as has been demonstrated by the case of the fully-*N*-anisyl-substituted 6,13-diaminopentacene.[17] Hence the author must check the absorption spectral change of compounds **1**–**3** during oxidation process.

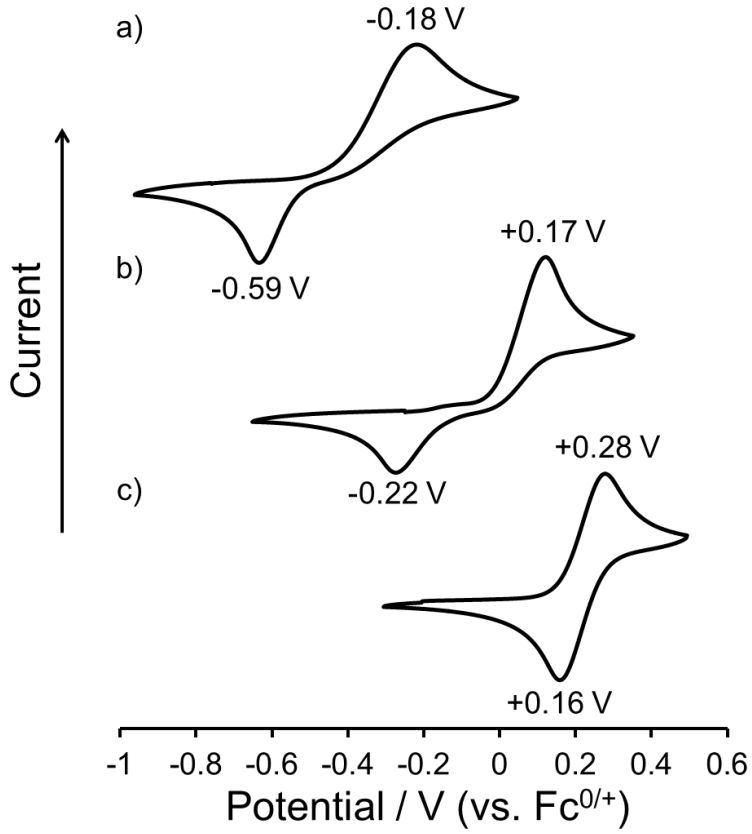

Figure 2.4. Cyclic voltammograms of a) **1**, b) **2**, and c) **3** in CH_2Cl_2 at 298 K, measured with 0.1 M *n*-Bu_4NBF_4 as the supporting electrolyte at a scan rate of 100 mV s^{-1}.

To ascertain the electronic states for the oxidized species of **1**–**3**, we recorded the change in the optical absorption spectra during electrochemical oxidation of **1**–**3** in CH_2Cl_2 (Figure 2.5). For the fully *N*-methylated 9,10-diaminoanthracene **1**, the lowest energy band with a vibrational fine structure at 3.10 eV (400 nm), corresponding to the HOMO-LUMO transition localized on the anthrylene moiety of **1**, was gradually changed into a new structure-less band at 3.99 eV (311 nm) with an isosbestic point at 3.57 eV (347 nm) during the oxidation process from **1** to $\mathbf{1}^{2+}$ (Figure 2.5a), thus indicating no generation of radical cationic species of **1**. A similar, but a little complicated, spectral change was also observed for the electrochemical oxidation of the partially *N*-methylated 9,10-diaminoanthracene **2** (Figure 2.5b): a series of lowest energy bands at 2.70, 3.22, 3.37, and 3.77 eV (459, 385, 368, and 329 nm) were changed into a series of new bands originating from the generation of $\mathbf{2}^{2+}$ at 2.81, 3.59, and 4.49 eV (441, 345, and 276 nm), with several isosbestic points at 2.77, 3.15, 3.45, 3.69, 3.95, and 4.64 eV (448, 394, 359, 336, 314, and 267 nm), bypassing the generation of radical cation $\mathbf{2}^{\bullet +}$. In contrast, the spectral change of **3** upon the electrochemical oxidation clearly exhibited a two-step change, thus indicating the generation of radical cation $\mathbf{3}^{\bullet +}$. In the first oxidation process from **3** to $\mathbf{3}^{\bullet +}$, a lowest energy band newly appeared at 0.64 eV (1936 nm), together with the next lowest band at 1.63 eV (762 nm) (Figure 2.5c). As has already been reported,[4] the lowest energy band was assigned to a charge-resonance (CR) band originating from the class III or the borderline class III/class II mixed-valence (MV) state[18] of $\mathbf{3}^{\bullet +}$. In fact, the observed CR transition energy was in good agreement with that calculated by TD-DFT for the UB3LYP/6-31G** optimized symmetrical structure of $\mathbf{3}^{\bullet +}$ (0.71 eV[4]) [0.74 eV for TD-DFT/6-31G*//UB3LYP/6-31G* calculation of $\mathbf{3}^{\bullet +}$; corresponding to the transition

from β–HOMO to β–LUMO (Figure 2.6)]. In the second oxidation process from $\mathbf{3}^{\bullet+}$ to $\mathbf{3}^{2+}$, the lowest energy band at 0.64 eV gradually disappeared, whereas the next lowest energy band at 1.63 eV continued to grow up until the complete oxidation into $\mathbf{3}^{2+}$ and the intensity reached up to about twice that of $\mathbf{3}^{\bullet+}$ (Figure 2.5d), again strongly supporting that the observed band at 0.64 eV corresponds to the mixed-valence band of $\mathbf{3}^{\bullet+}$.

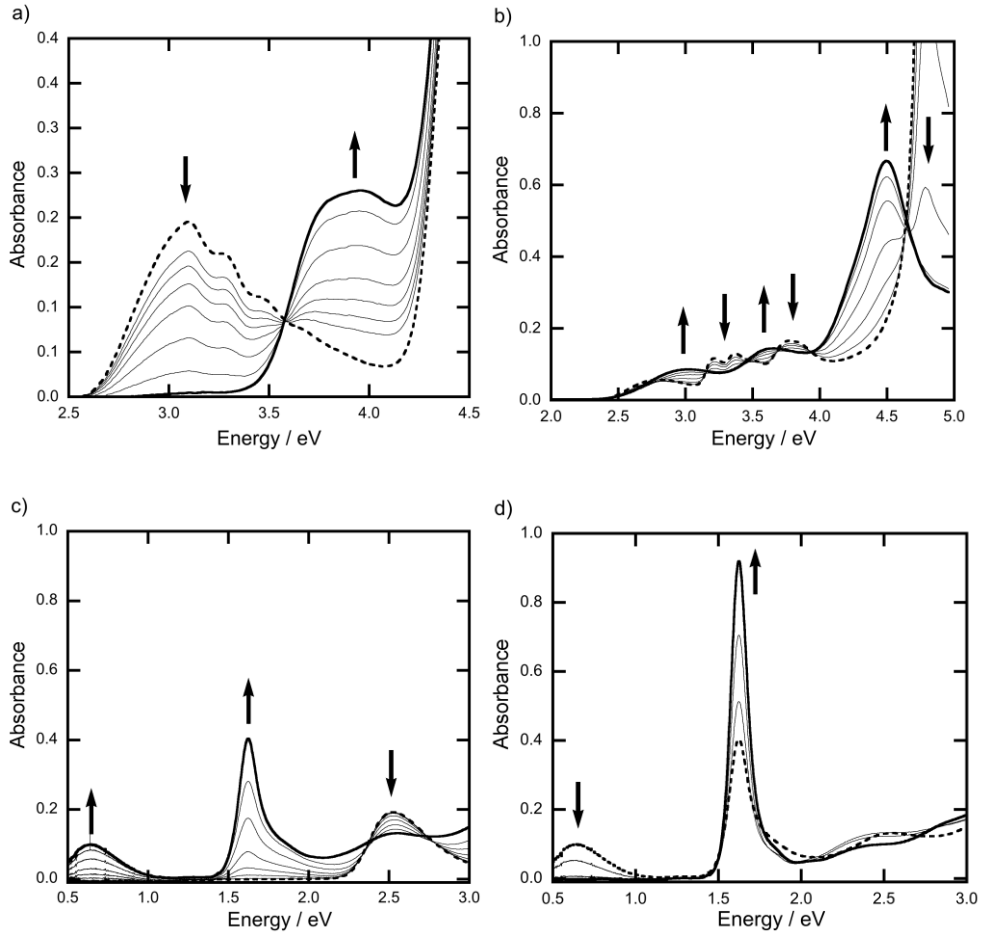

Figure 2.5. UV/Vis-NIR optical absorption spectra of the stepwise electrochemical oxidation a) from **1** (broken line) to $\mathbf{1}^{2+}$ (bold line), b) from **2** (broken line) to $\mathbf{2}^{2+}$ (bold line), c) from **3** (broken line) to $\mathbf{3}^{\bullet+}$ (bold line), and d) from $\mathbf{3}^{\bullet+}$ (broken line) to $\mathbf{3}^{2+}$ (bold line), in CH_2Cl_2 with 0.1 M *n*-Bu_4NBF_4 at 298 K.

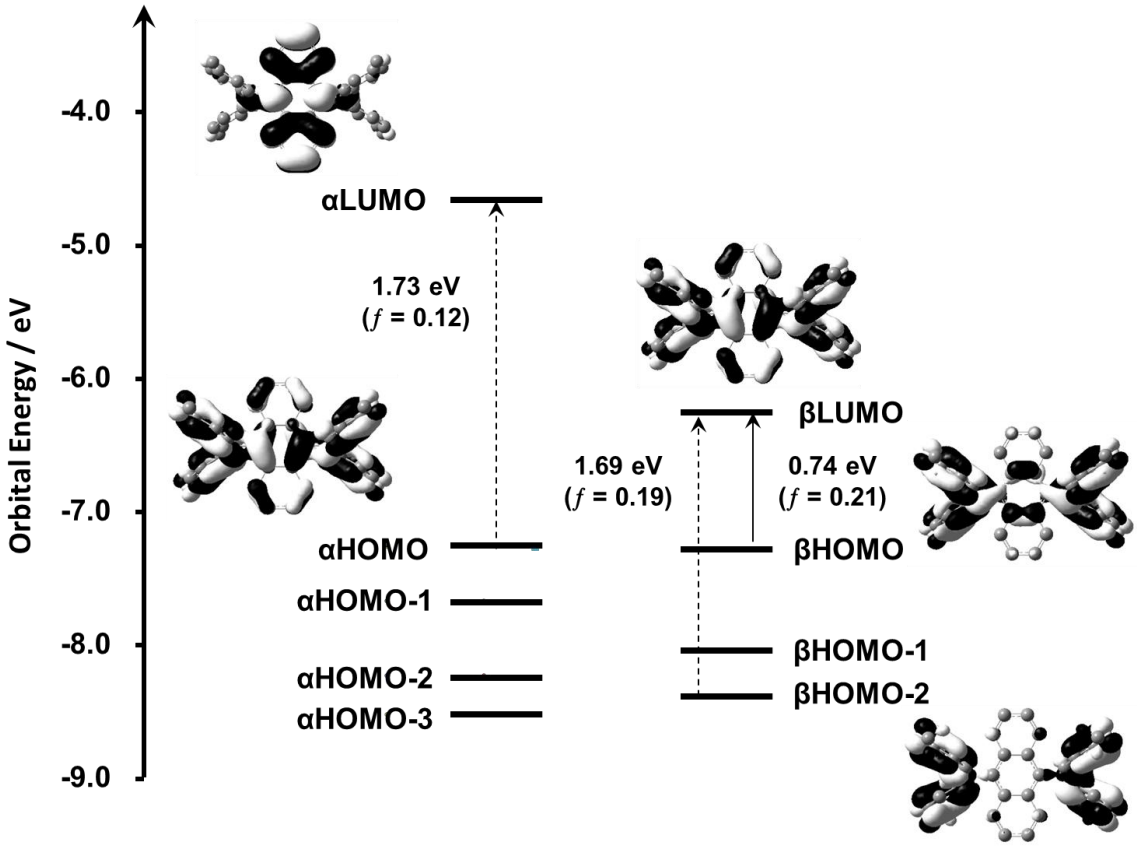

Figure 2.6. Frontier Kohn-Sham orbital energy levels for the ground state of $\mathbf{3}^{\bullet+}$ at the UB3LYP/6-31G* level of theory. The solid and broken arrows represent the major contributions related to the lowest and next lowest energy optical absorption bands observed experimentally for $\mathbf{3}^{\bullet+}$.

To understand these spectroscopic observations for the oxidized states of **1**–**3**, we carried out DFT calculations. The ground state structures for the oxidized species of **1**–**3** were first optimized. Although the radical cations of **1** and **2** were not observed experimentally, we can determine theoretically the optimized structures of $\mathbf{1}^{\bullet+}$ and $\mathbf{2}^{\bullet+}$, including that of $\mathbf{3}^{\bullet+}$. As can be seen from Figure 2.7a, for all three compounds, the most energetically stable structure was found to adopt a planar structure with a fully aromatic

anthracene moiety. In addition, it was predicted that, for $\mathbf{1}^{\bullet+}$, the butterfly-like structure, in which the central six-membered ring in the anthrylene moiety is folded along C9–C10 line, lies 0.93 kcal mol^{-1} above the planar structure.[19] Herein, note that the author was not able to find any local minima corresponding to the butterfly-like structures of both $\mathbf{2}^{\bullet+}$ and $\mathbf{3}^{\bullet+}$. On the other hand, the energetically most stable structure for $\mathbf{3}^{2+}$ takes the planar structure, while those for $\mathbf{1}^{2+}$ and $\mathbf{2}^{2+}$ the butterfly-like structure, in good accordance with the experimental observations (Figure 2.7b). In conjunction with the folding deformation of the anthrylene moiety (the bend angles 138.9° and 134.8° for $\mathbf{1}^{2+}$ and $\mathbf{2}^{2+}$, respectively (Figure 2.8b)), the C–C bonds around C9 and C10 are considerably elongated from 1.414 and 1.410 Å for $\mathbf{1}^{2+}$ and $\mathbf{2}^{2+}$, respectively, to 1.481 and 1.477 Å for $\mathbf{1}^{2+}$ and $\mathbf{2}^{2+}$, respectively (Figure 2.8a). On the other hand, the conspicuous geometrical changes are not seen throughout all the oxidized states of **3** (Figure 2.8), thus indicating a clear difference from the diamagnetic quinoid dication of **TMPD**, and therefore, the low-lying excited triplet state of $\mathbf{3}^{2+}$ was observed in the solid state.[5] More interestingly, the butterfly-like structure were not found for $\mathbf{3}^{2+}$, while the planar structure for $\mathbf{2}^{2+}$ lies 5.9 kcal mol^{-1} above the butterfly-like one. In addition, the author could not find any local minima corresponding to the planar structure of $\mathbf{1}^{2+}$.

The difference in the ground-state structures for $\mathbf{1}^{2+}$, $\mathbf{2}^{2+}$, and $\mathbf{3}^{2+}$ can be seen explicitly in the frontier molecular orbitals (Figure 2.9): in $\mathbf{1}^{2+}$ and $\mathbf{2}^{2+}$ with the butterfly-like structure, the MOs containing both in-phase and out-of-phase combinations of nitrogen-centered 2p AOs on two amino groups become unoccupied (LUMO and LUMO+1 for $\mathbf{1}^{2+}$ and $\mathbf{2}^{2+}$), whereas the corresponding amine-localized MOs for $\mathbf{3}^{2+}$ with the planar structure are HOMO and LUMO. The structural change associated with the oxidation process of oligoacenes is in general qualitatively

explainable by Clar's aromatic π-sextet rule, where the contribution of the Kekulé resonance structure with the largest number of disjoint aromatic π-sextets, that is, benzene-like moieties is decisive of characterization of properties of polycyclic aromatic hydrocarbons (PAHs).[20] Two-electron oxidation of 9,10-diaminoanthracene with only one migrating π-sextet loses a π-bond, and thus, this situation can be compensated by the structural change, in which the central six-membered ring is folded along the C9–C10 line, so as to form an extra π-sextet (Figure 2.10).[21] As has already been described on the characteristics of the MOs for neutral species of **1**–**3**, the two-electron oxidation for **1** and **2** with the HOMO of anthrylene-localized character inevitably leads to such a structural change according to the Clar's rule. On the other hand, the oxidation for **3** with the HOMO of amine-localized character does not significantly affect the π-conjugated structure of the anthrylene moiety itself, so that the oxidized species of **3** retains the planar structure with radical centers localized mainly on the dianisylamino groups. The same can be said of the compounds **1**–**3**.

The observed lowest energy bands for $\mathbf{1}^{2+}$–$\mathbf{3}^{2+}$ were confirmed by TD-DFT calculations by using the optimized geometries for the butterfly-like structured $\mathbf{1}^{2+}$ and $\mathbf{2}^{2+}$, and for the planar structured $\mathbf{3}^{2+}$. Calculated vertical excitation energies and oscillator strengths are listed in Table 2.2. The lowest energy transitions for $\mathbf{2}^{2+}$ and $\mathbf{3}^{2+}$ are mainly described by the one-electron excitation from the HOMO to the LUMO [the *N*-phenyl-localized HOMO and HOMO–1 to the delocalized LUMO for $\mathbf{2}^{2+}$, and the amine-localized HOMO to the amine-localized LUMO for $\mathbf{3}^{2+}$], whereas that for $\mathbf{1}^{2+}$ corresponds to two kinds of contribution from both the delocalized HOMO-3 to the delocalized LUMO and the anthrylene-localized HOMO to the delocalized LUMO+1 (Figure 2.9).

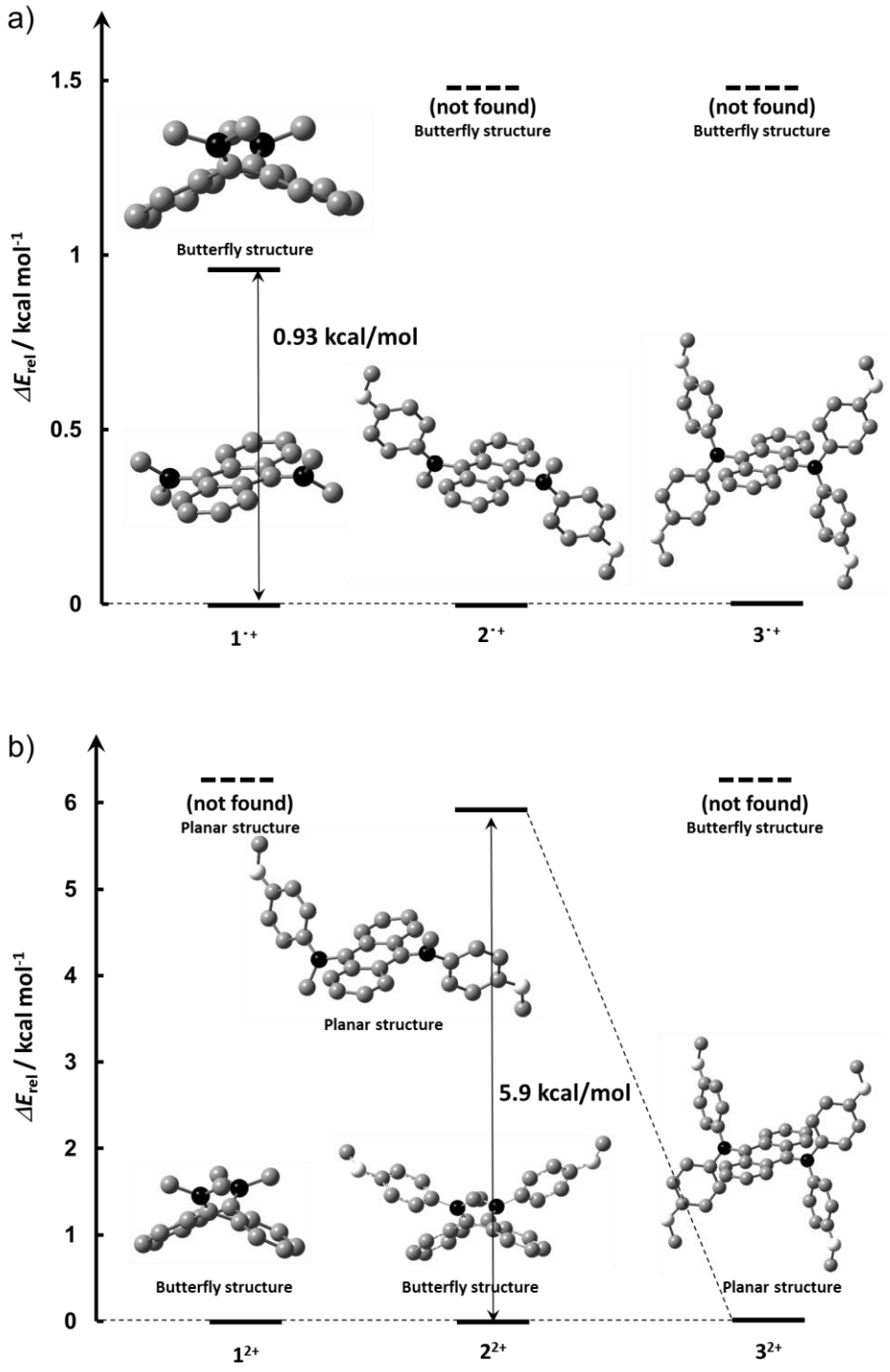

Figure 2.7. Relative energies (ΔE_{rel}) of a) $\mathbf{1}^{\bullet+}$, $\mathbf{2}^{\bullet+}$, and $\mathbf{3}^{\bullet+}$ in relation to planar structure and b) $\mathbf{1}^{2+}$, $\mathbf{2}^{2+}$, and $\mathbf{3}^{2+}$ in relation to butterfly structure.

(a)

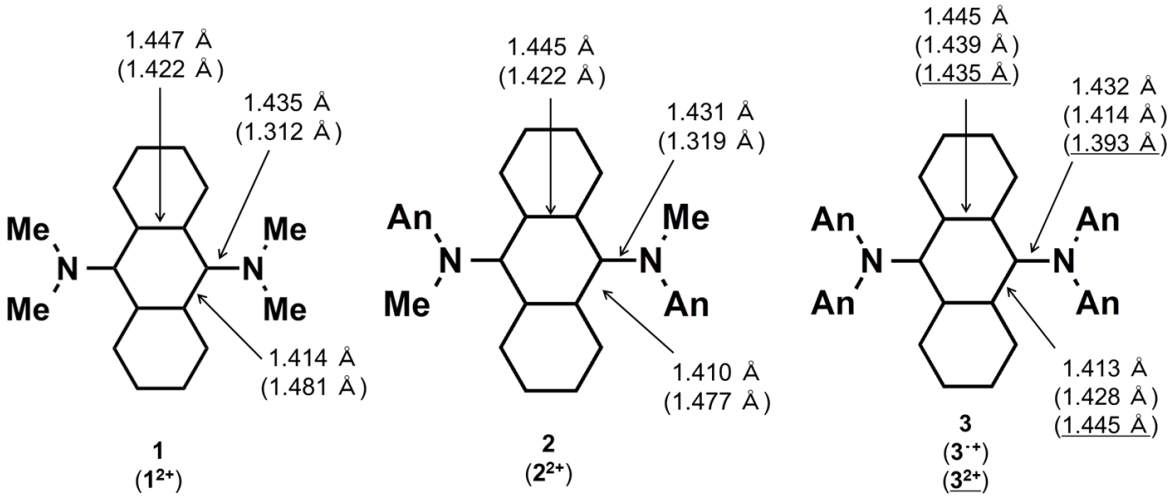

(b)

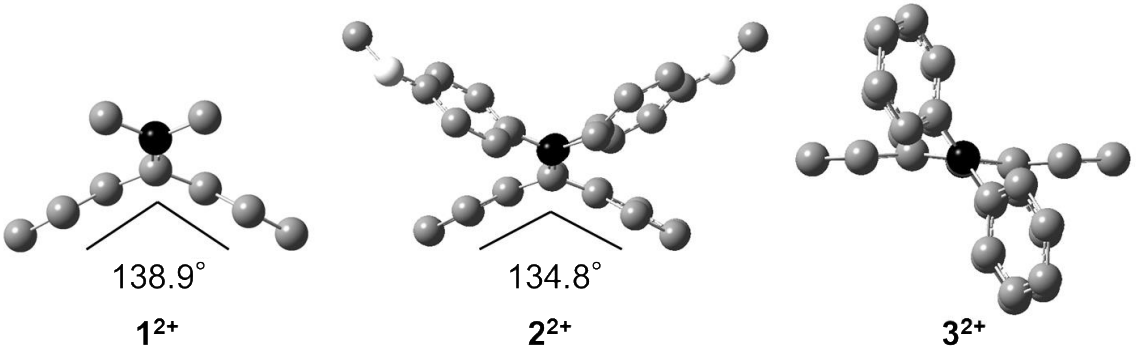

Figure 2.8. Selected geometrical parameters of the B3LYP/6-31G* optimized structures for neutral, radical cation, and dication of **1**, **2**, and **3**: (a) the bond lengths; (b) the bend angles of the anthrylene moiety (each view is shown along the short axis of anthrylene moiety).

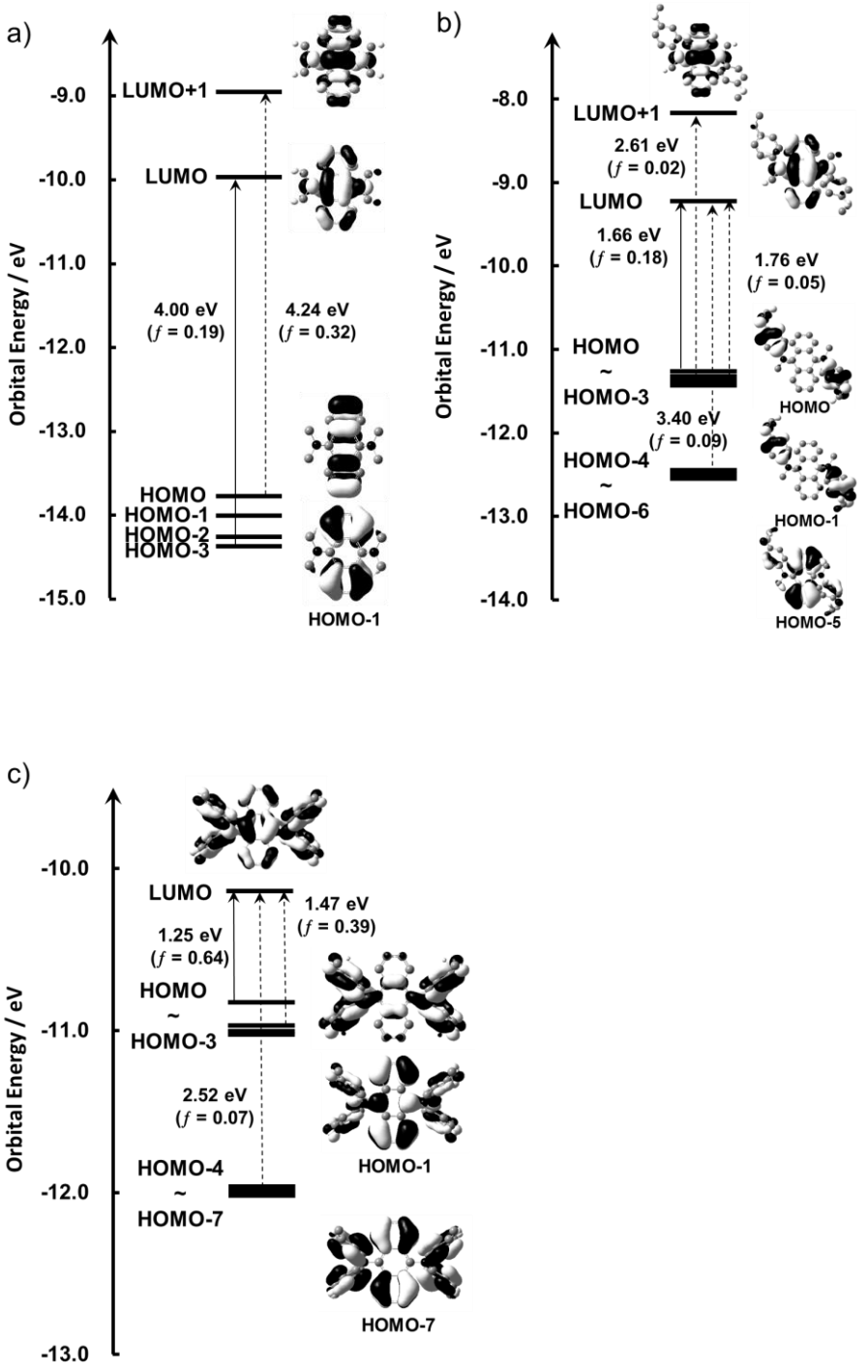

Figure 2.9. Frontier Kohn-Sham orbital energy levels for the ground state of a) $\mathbf{1}^{2+}$, b) $\mathbf{2}^{2+}$, and c) $\mathbf{3}^{2+}$ at the B3LYP/6-31G* level of theory. The solid and broken arrows represent the major contributions related to the lowest and next lowest energy optical absorption bands observed experimentally for $\mathbf{1}^{2+}$–$\mathbf{3}^{2+}$.

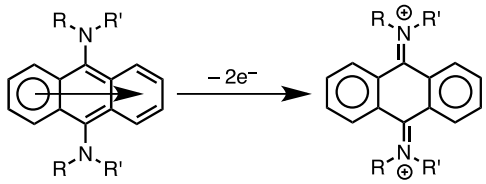

Figure 2.10. 9,10-Diaminoanthracene with only one migrating aromatic π-sextet. Two-electron oxidation leads to two aromatic π-sextets accompanying a butterfly-like deformation.

Table 2.2. TD-DFT//B3LYP/6-31G* vertical excitation energies calculated for $\mathbf{1}^{2+}$, $\mathbf{2}^{2+}$, and $\mathbf{3}^{2+}$ related to the lowest energy optical absorption bands observed experimentally for $\mathbf{1}^{2+}$–$\mathbf{3}^{2+}$.

Compound	$h\nu$ (f)[a] [eV]	Major contribution[b]
$\mathbf{1}^{2+}$	4.00 (0.19)	H–3 → L
	4.24 (0.32)	H → L+1
$\mathbf{2}^{2+}$	1.66 (0.18)	H → L
	1.76 (0.05)	H–1 → L
	2.61 (0.02)	H → L+1
	3.40 (0.09)	H–5 → L
$\mathbf{3}^{2+}$	1.25 (0.64)	H → L
	1.47 (0.39)	H–1 → L
	2.52 (0.07)	H–7 → L

[a] Oscillator strength (f) values are given in parentheses. [b] HOMO and LUMO are abbreviated as H and L, respectively.

2.3.3. Characterization of dication of 2 by NMR spectroscopy

The author has confirmed that chemically oxidized dications of **1** and **2** were ESR-silent in CH_2Cl_2, in consistent with the above-mentioned spectroelectrochemical and the DFT results. This observation, in turn, indicates the possibility of characterizing $\mathbf{1}^{2+}$ and $\mathbf{2}^{2+}$ by the NMR measurements. However, the orange color due to the freshly prepared $\mathbf{1}^{2+}$ disappeared immediately in CH_2Cl_2 at room temperature, thus indicating chemical instability of $\mathbf{1}^{2+}$ under ambient conditions. In contrast, ^{1}H NMR spectrum of $\mathbf{2}^{2+}$, which was generated with an excess of $AgSbF_6$ in $CDCl_3$, was measurable at 293 K (Figure 2.11). As seen in Figure 2.2, in the neutral state, **2** adopts both the cisoid and transoid isomers. Remarkably, the spectrum for $\mathbf{2}^{2+}$ showed the presence of only one isomer, though both cisoid and transoid isomers can be assumed also for the butterfly conformation of $\mathbf{2}^{2+}$ (Figure 2.12). The geometry optimization of dication structure $\mathbf{2}^{2+}$ at the B3LYP/6-31G* level of theory indicated that the transoid isomer was stable by 0.41 kcal mol^{-1}, as compared with the cisoid isomer, thus supporting the present ^{1}H NMR data. Note that the energy difference between the two conformational isomers optimized at the same level of theory for neutral state of **2** was estimated to be only 0.02 kcal mol^{-1}. More interestingly, pronounced signal shifts caused by the oxidation into $\mathbf{2}^{2+}$, in particular, the downfield shifts of the signals corresponding to the protons at the anthrylene moiety relative to the corresponding signals of **2** attest for an increase in aromaticity for outer six-membered rings in the anthrylene moiety owing to the large structural change into the butterfly-like conformation of **2**. The observed deshielding of the protons attached to the anthrylene moiety was also supported by the NICS(0) values computed for **2** and the butterfly-like $\mathbf{2}^{2+}$ (GIAO/HF/6-311+G*//B3LYP/6-31G*):[22] the NICS value for the anthrylene outer rings of **2** changes from –7.7 to –9.0 during the

course of oxidation from **2** to 2^{2+}, thus leading to the observed downfield shifts in ^{1}H NMR spectrum. The change into the more negative NICS value associated with the oxidation of **2** is totally consistent with the Clar's rule, as has been discussed before. Taken together, the NMR spectroscopic investigations provide strong evidence that the dication $\mathbf{2}^{2+}$ adopts the butterfly-like folded structure with a closed-shell structure.

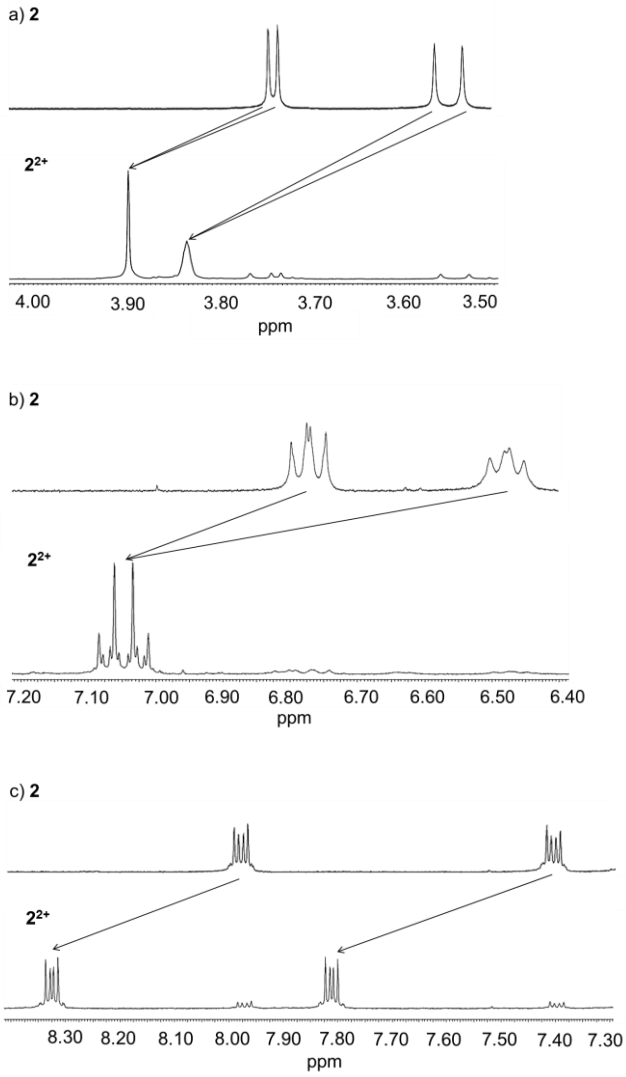

Figure 2.11. Comparison of ^{1}H NMR spectra of **2** and $\mathbf{2}^{2+}$ in $CDCl_3$ at room temperature; a) in the aliphatic region, b) in the aromatic region corresponding to *N*-anisyl moiety, and c) in the aromatic region corresponding to anthrylene moiety.

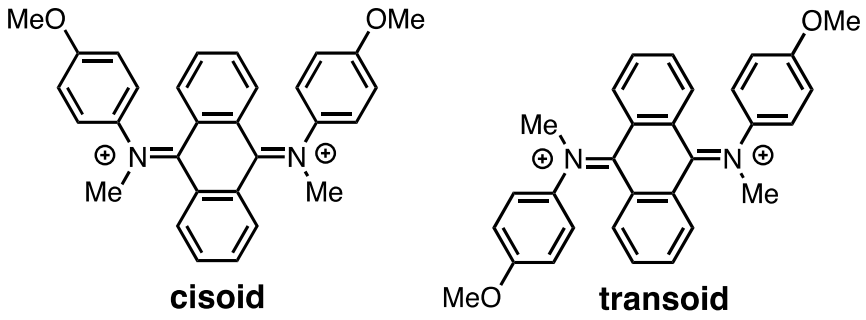

Figure 2.12. Cisoid and transoid conformational isomers of $\mathbf{2}^{2+}$.

2.3.4. Characterization of radical cation and dication of 3 by solution ESR spectroscopy

In accordance with the electrochemical and spectroelectrochemical studies, we could not detect the existence of radical cation for **1** and **2**: when treated by less than one equiv of $AgSbF_6$ in CH_2Cl_2, the resulting oxidized species were found to be ESR-silent. On the other hand, the ESR spectrum of $\mathbf{3}^{\bullet+}$ was successfully observed by the chemical oxidation of **3** with 0.5 equiv of $AgSbF_6$ in CH_2Cl_2 at 293 K (Figure 2.13a). The optimum simulation of the observed five-line spectrum gave the following hyperfine coupling constants: $|a_N|$ = 0.45 mT (2N), $|a_{H_A}|$ = 0.15 mT (4H), $|a_{H_B}|$ = 0.075 mT (4H), and the contributions from the negligible hydrogen nuclei were incorporated in the line width of the spectral simulation (0.15 mT) (Figure 2.13b), with reference to the DFT-computed spin density distribution for the optimized planar structure of $\mathbf{3}^{\bullet+}$ (Figure 2.13c). In addition, the spectral shape for $\mathbf{3}^{\bullet+}$ remained unchanged in the temperature range from 20 to –80˚C, again indicating the possibility of class III or the borderline class III/class II MV state of $\mathbf{3}^{\bullet+}$.[18] Turning finally to the dication of **3**, the solution of $\mathbf{3}^{2+}$ turned out to be ESR-silent in accordance with the previous results. Note that, in

contrast to the solution ESR result, the powder sample of $\mathbf{3}^{2+}$ displayed a typical fine-structured ESR spectrum for an excited triplet state with a small singlet–triplet energy gap (ΔE_{S-T} = –1.4 kcal mol^{-1}).[5] Moreover, the planarity of anthrylene moiety was elucidated by the single-crystal X-ray crystallography. Overall, it was demonstrated that dianisylamino-substituted anthracene **3** retains planarity of the anthrylene moiety during the course of oxidation going from neutral **3** to dication $\mathbf{3}^{2+}$.

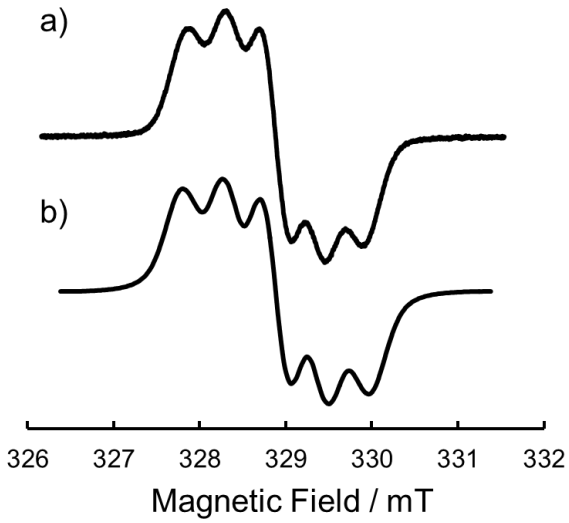

c)

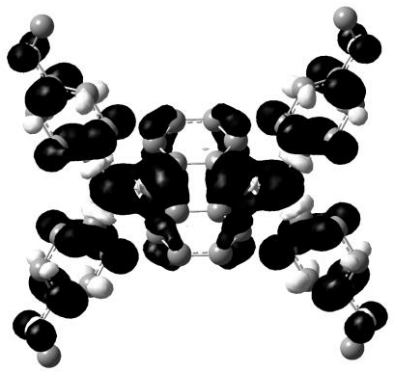

d)

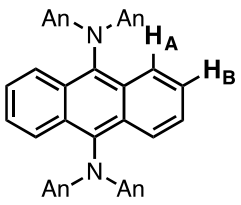

Figure 2.13. a) Observed X-band ESR spectrum of $\mathbf{3}^{\bullet+}$ recorded in CH_2Cl_2 at 293 K, b) the simulated ESR spectrum, c) the DFT-computed spin density distribution of $\mathbf{3}^{\bullet+}$ (UB3LYP/6-31G*), and d) the designation of hydrogen nuclei on the anthrylene moiety, H_A and H_B.

2.4 Conclusion

The author has shown that the influence of *N*-substituents on the electronic states for the neutral and oxidized species of 9,10-diaminoanthracenes. In accordance with an increase in the number of *N*-anisyl-substituents, the frontier MOs of 9,10-diaminoanthracenes changed from the anthrylene-localized type to the amine-localized type. This tendency finally determines whether the significant structural change into the butterfly-like structure takes place in their oxidized species. The fully and partially *N*-alkylated 9,10-diaminoanthracens **1** and **2** underwent the folding structural change along C9–C10 line in their dicationic state bypassing the generation of radical cation. Fortunately, the stability of $\mathbf{2}^{2+}$ afforded the NMR measurements to provide additional corroborative evidence that the dication of **2** adopts the diamagnetic butterfly-like structure in accordance with the computed NICS values, as is predicted qualitatively by the Clar's aromatic π-sextet rule. In contrast, the fully *N*-anisyl-substituted 9,10-diaminoanthracene **3** exhibited two-stage redox property with a very small oxidation potential splitting, indicating no significant structural changes throughout all the oxidation processes. The ESR measurements demonstrated that the radical cation of **3** is classified into the class III or the borderline class III/class II mixed-valence state, thus retaining planarity of the anthrylene moiety.

2.5 References

[1] K. Deuchert, S. Hünig, *Angew. Chem. Int. Ed. Engl*. **1978**, *17*, 875-886.

[2] K. Hu, D. H. Evans, *J. Electroanal. Chem*. **1997**, *423*, 29-35.

[3] a) N. E. Gruhn, N. A. Macías-Ruvalcaba, D. H. Evans, *J. Phys. Chem. A* **2006**, *110*, 5650-5655; b) N. A. Macías-Ruvalcaba, D. H. Evans, *Chem. Eur. J*. **2007**, *13*, 4386-4395.

[4] C. Lambert, C. Risko, V. Coropceanu, J. Schelter, S. Amthor, N. E. Gruhn, J. C. Durivage, J.-L. Brédas, *J. Am. Chem. Soc*. **2005**, *127*, 8508-8516.

[5] Y. Su, X. Wang, Y. Li, Y. Song, Y. Sui, X. Wang, *Angew. Chem. Int. Ed*. **2015**, *54*, 1634-1637.

[6] Y. Chung, B. F. Duerr, T. A. McKelvey, P. Nanjappan, A. W. Czarnik, *J. Org. Chem*. **1989**, *54*, 1018-1032.

[7] K. Raghavachari, *Theor. Chem. Acc*. **2000**, *103*, 361-363 and references cited therein.

[8] a) R. Bauernschmitt, R. Ahlrichs, *Chem. Phys. Lett*. **1996**, *256*, 454-464; b) M. E. Casida, C. Jamorski, K. C. Casida, D. R. Salahub, *J. Chem. Phys*. **1998**, *108*, 4439-4449; c) R. E. Stratmann, G. E. Scuseria, M. J. Frisch, *J. Chem. Phys*. **1998**, *109*, 8218-8224.

[9] W. J. Hehre, L. Radom, P. v. R. Schleyer, J. A. Pople, *Ab Initio Molecular Orbital Theory*, Wiley, New York, **1986**.

[10] M. J. Frisch, G. W. Trucks, H. B. Schlegel, G. E. Scuseria, M. A. Robb, J. R. Cheeseman, G. Scalmani, V. Barone, B. Mennucci, G. A. Petersson, H. Nakatsuji, M. Caricato, X. Li, H. P. Hratchian, A. F. Izmaylov, J. Bloino, G. Zheng, J. L. Sonnenberg, M. Hada, M. Ehara, K. Toyota, R. Fukuda, J. Hasegawa, M. Ishida, T. Nakajima, Y.

Honda, O. Kitao, H. Nakai, T. Vreven, J. A. Montgomery, Jr., J. E. Peralta, F. Ogliaro, M. Bearpark, J. J. Heyd, E. Brothers, K. N. Kudin, V. N. Staroverov, T. Keith, R. Kobayashi, J. Normand, K. Raghavachari, A. Rendell, J. C. Burant, S. S. Iyengar, J. Tomasi, M. Cossi, N. Rega, J. M. Millam, M. Klene, J. E. Knox, J. B. Cross, V. Bakken, C. Adamo, J. Jaramillo, R. Gomperts, R. E. Stratmann, O. Yazyev, A. J. Austin, R. Cammi, C. Pomelli, J. W. Ochterski, R. L. Martin, K. Morokuma, V. G. Zakrzewski, G. A. Voth, P. Salvador, J. J. Dannenberg, S. Dapprich, A. D. Daniels, O. Farkas, J. B. Foresman, J. V. Ortiz, J. Cioslowski, and D. J. Fox, Gaussian 09, Revision C.01, Gaussian, Inc., Wallingford CT, **2010**.

[11] D. S. Surry, S. L. Buchwald, *Angew. Chem. Int. Ed*. **2008**, *47*, 6338-6361.

[12] a) J. F. Hartwig, *Nature* **2008**, *455*, 314-322; b) J. F. Hartwig, *Acc. Chem. Res*. **2008**, *41*, 1534-1544.

[13] J. Sandström, *Dynamic NMR Spectroscopy*, Academic Press, New York, **1982**.

[14] W. E. Stewart, T. H. Siddall, III, *Chem. Rev*. **1970**, *70*, 517-551.

[15] Temperature dependence of the methyl signal of *N*-tolyl groups in ^{1}H NMR spectrum of **4** in toluene-d_8 were used for estimation of the $\Delta G^{\ddagger}$ value.

[16] The digital simulation of the observed CV for **1** was in good agreement with the reported results (see reference [2]).

[17] A. Ito, M. Uebe, K. Takahashi, H. Ishikawa, D. Sakamaki, H. Sato, T. Matsumoto, K. Tanaka, *Chem. Eur. J*. **2016**, *22*, 2165-2170.

[18] a) J. Hankache, O. S. Wenger, *Chem. Rev*. **2011**, *111*, 5138-5178; b) A. Heckmann, C. Lambert, *Angew. Chem. Int. Ed.* **2012**, *51*, 326-392.

[19] At the (U)B3LYP/6-31G** level of theory, similar results were also obtained for **1** (see reference [3a]), but the relative energy difference was not reported.

[20] E. Clar, *The Aromatic Sextet*, Wiley, New York, **1972**.

[21] M. Solà, *Front. Chem*. **2013**, *1*, 22.

[22] a) P. v. R. Schleyer, C. Maerker, A. Dransfeld, H. Jiao, N. J. R. v. E. Hommes, *J. Am. Chem. Soc*. **1996**, *118*, 6317-6318; b) P. v. R. Schleyer, M. Manoharan, H. Jiao, F. Stahl, *Org. Lett*. **2001**, *3*, 3643-3646.

Chapter 3

Isolable Triradical Trication of Hexaaza[1_6]paracyclophane with Embedded 9,10-Anthrylenes: A Frustrated 3-Spin System

3.1 Introduction

Delocalization or localization of spin and/or charge in π-conjugated molecular systems has been a fascinating problem in fundamental chemistry as well as materials chemistry.[1] In particular, comparative studies between the corresponding doped linear and cyclic oligomers as models for conducting polymers have attracted much attention as exemplified by the studies on oligothiophenes[2,3] and oligoparaphenylenes.[4,5] In 2010, we reported the first synthesis of hexaaza[1_6]paracyclophane **1**, as a cyclic hexamer of polyaniline, in which all six nitrogen centers are connected with *para*-phenylene units (Figure 3.1). The mono-oxidized species of **1** showed a multiplet hyperfine-structured ESR spectrum, which is indicative of delocalization of the spin and charge over the entire macrocyclic molecular backbone,[6] whereas the spin and charge

localization was confirmed for the radical cations of the corresponding linear oligoanilines.[7] In addition, the multi-redox activity and shape-persistency of (poly)macrocyclic oligoarylamines are expected to expand the possibility of hole- and spin-containing scaffolds for molecule-based electronics due to.[8]

In this chapter, the author reports a new derivative of hexaaza[1_6]paracyclophane, **2a** and **2b** (Figure 3.1), in which *para*-phenylenes are alternately replaced by 9,10-anthrylenes as a modifier for overall conformational change of the macrocycles.[9] The introduction of bulky arene units should modulate the π-conjugation through macrocyclic molecular systems, whereby the oxidized states of **2** might provide intriguing spin and charge distributions.

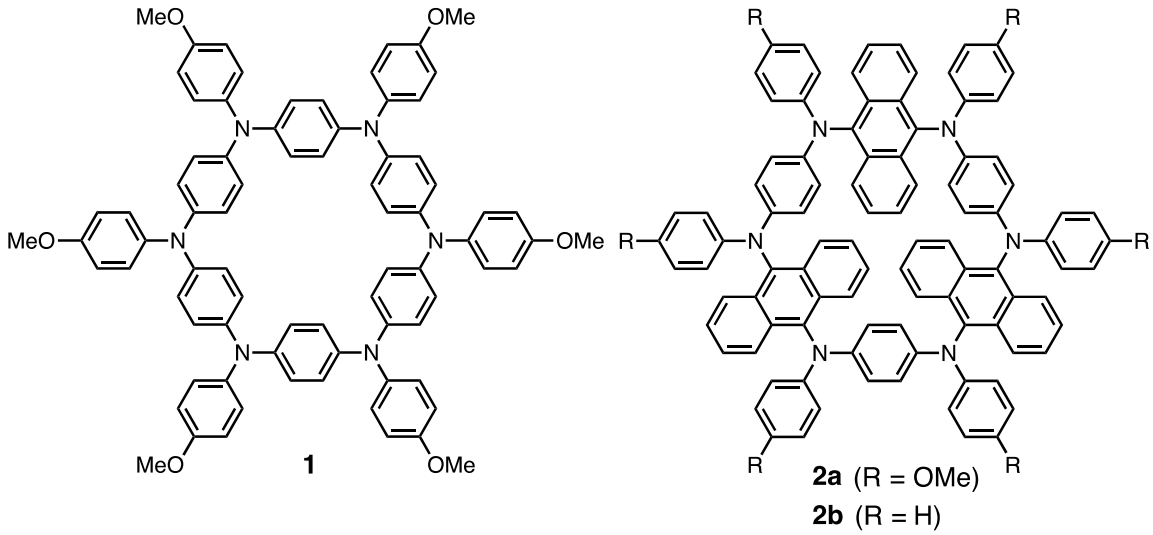

Figure 3.1. Structures of hexaaza[1_6]*para*-cyclophane **1** and its derivatives **2a** and **2b**.

3.2 Experimental Section

3.2.1 Synthesis

All the purchased reagents were of standard quality, and used without further purification. All the purchased solvents were purified, dried, and degassed by standard procedures. Column chromatography was performed with silica gel (Kanto Chemical Co., Inc., silica gel 60N, spherical neutral). Elemental analyses were performed by Center for Organic Elemental Microanalysis, Kyoto University. ^{1}H and ^{13}C NMR spectra were measured by a JEOL JNM-AL400 FT-NMR spectrometer. Chemical shifts of NMR spectra are determined relative to internal tetramethylsilane (TMS) standard (δ), and are given in parts per million (ppm). UV/Vis-NIR absorption spectra were obtained with a Perkin-Elmer Lambda 950 spectrometer.

Synthesis of 2a: To a degassed solution of 9,10-bis(*p*-methoxyphenylamino)anthracene (200 mg, 0.48 mmol) and 1,4-dibromobenzene (112 mg, 0.48 mmol) in toluene (30 mL) were added Pd(*t*-Bu$_3$P)$_2$ (24.5 mg, 0.048 mmol, 10 mol%) and NaO*t*-Bu (138 mg, 1.44 mmol). The reaction mixture was refluxed for 24 h under Ar. The solvent was removed by evaporation. The residue was dissolved in $CHCl_3$ (150 mL). The organic layer was washed with water (15 mL), and then dried over $MgSO_4$, and evaporated. The crude product was purified by chromatography on silica gel (*n*-hexane/CH_2Cl_2 = 1/1 as eluent) and followed by recrystallization from $CHCl_3$/*n*-hexane solution to give the desired compound **2a** as a red solid (32.8 mg, 14%; R_f = 0.47 (*n*-hexane/CH_2Cl_2 = 2:1)). An alternative method is as follows: a mixture of *N*,*N*'-bis(4-anisyl)-1,4-phenylenediamine (980 mg, 3.06 mmol), 9,10-dibromoanthracene (1.00 g, 2.99 mmol), Pd(dba)$_2$ (180 mg, 0.31 mmol), P(*t*-Bu)$_3$HBF$_4$ (150 mg, 0.52 mmol) and NaO*t*-Bu (1.07 g, 11.13 mmol) in

toluene (200 mL) was refluxed under an argon atmosphere for 22 h. The solvent was evaporated on a rotary evaporator. The resulting mixture was washed with brine and the organic layer was separated and dried over Na_2SO_4. After evaporation of the solvent, the crude product was chromatographed on silica gel (*n*-hexane/CH_2Cl_2 = 1/2 as eluent) and recrystallized with CH_2Cl_2/MeOH to afford **2a** (74 mg, 5%) as a red solid: mp > 300 °C; ^{1}H NMR (400MHz, $CDCl_3$); δ = 8.05 (dd, *J* = 3.2, 6.8 Hz, 12H), 7.20 (dd, *J* = 3.2, 6.8 Hz, 12H), 7.09 (d, *J* = 9.0 Hz, 12H), 6.74 (d, *J* = 9.0 Hz, 12H), 6.64 (s, 12H), 3.72 (s, 18H); ^{13}C NMR (100 MHz, $CDCl_3$) δ=154.0, 141.5, 141.3, 137.1, 131.7, 126.2, 125.1, 121.8, 119.5, 114.5, 55.5; APCI HRMS: *m/z* calcd for $C_{102}H_{79}N_6O_6$: 1483.6056 $[M+H]^+$; found 1483.6026.

Synthesis of 2b: To a degassed solution of 9,10-bis(phenylamino)anthracene (1.01 g, 2.80 mmol) and 1,4-dibromobenzene (0.66 g, 2.80 mmol) in toluene (100 mL) were added Pd(*t*-$Bu_3P)_2$ (0.54 g, 0.28 mmol, 10 mol%) and NaO*t*-Bu (81 mg, 8.40 mmol). The reaction mixture was refluxed for 24 h under Ar. The solvent was removed by evaporation. The residue was dissolved in CH_2Cl_2 (1 L). The organic layer was washed with water (500 mL), and then dried over $MgSO_4$, and evaporated. The crude product was purified by chromatography on silica gel with (*n*-hexane/CH_2Cl_2 = 1/1 as eluent) and followed by recrystallization from $CHCl_3$/*n*-hexane solution to give the desired compound **2b** as a red solid (212.4 mg, 17.5%; R_f = 0.48 (*n*-hexane/CH_2Cl_2 = 1:1)): mp 298–301˚C (decomp.); ^{1}H NMR (400MHz, $CDCl_3$); δ = 6.83 (s, 12H), 6.86 (t, *J* = 7.6 Hz, 6H), 7.07 (d, *J* = 8.4 Hz, 12H), 7.19 (t, *J* = 7.8 Hz, 12H), 7.23 (dd, *J* = 3.6, 6.8 Hz, 12H), 7.97 (dd, *J* = 3.2, 6.8 Hz, 12H); (400MHz, CD_2Cl_2); δ = 6.70 (s, 12H), 6.80 (t, *J* = 7.0 Hz, 6H), 7.00 (d, *J* = 8.4 Hz, 12H), 7.11 (t, *J* = 7.6 Hz, 12H), 7.19 (dd, *J* = 3.6, 10.5

Hz, 12H), 7.97 (dd, J = 3.3, 10.4 Hz, 12H); ^{13}C NMR (100 MHz, $CDCl_3$); δ= 119.46, 120.58, 121.15, 124.97, 126.51, 129.20, 131.63, 136.98, 141.13, 148.20; FAB HRMS: *m/z* calcd for $C_{96}H_{66}N_6$: 1302.5349 $[M]^+$; found: 1302.5144.

Synthesis of $2a^{3+}$•3$[B(C_6F_5)_4]^-$: Compound **2a** (37 mg, 0.025 mmol) was dissolved in dichloromethane (2 mL), and $Ag[B(C_6F_5)_4]$ (65 mg, 0.075 mmol) was added into the solution of **2**. The resulting solution was filtered through celite, and the filtrate was then concentrated (to about 2 mL) under vacuum. 4 mL of hexane was layered directly over the filtrate, and it was stored at around –20˚C for 1 day to afford $\mathbf{2a^{3+}•3[B(C_6F_5)_4]^-}$ (75 mg, 85%) as a dark-green solid. Crystals suitable for X-ray analyses was obtained from corresponding CH_2Cl_2/toluene solution. Anal. Calcd for $C_{174}H_{78}B_3F_{60}N_6O_6$: C, 59.36; H, 2.23; N, 2.39. Found: C, 59.50; H, 2.36; N, 2.34.

3.2.2 DFT Calculations

Quantum chemical calculations were performed with using a hybrid Hartree–Fock/density functional theory (HF/DFT) method (B3LYP).[10] Full geometrical optimization for **1**, **2a** and **2b** was carried out and furthermore, their local minimum structures were confirmed by performing subsequent frequency analyses. Excitation energies for **1** and **2** were examined on the basis of the time-dependent density functional method (TD-DFT) [11] with the same functional. All the computations employed the 6-31G* basis set.[12] All these computational approaches are implemented in Gaussian 09 package of ab initio MO calculation.[13]

3.2.3 Electrochemical Measurements

The redox properties were evaluated by cyclic voltammetry (CV) and differential pulse voltammetry (DPV) in CH_2Cl_2 solution at 298 K with 0.1 M tetra-*n*-butylammonium tetrafluoroborate ($TBABF_4$) as supporting electrolyte (scan rate 100 mV s^{-1}) using an ALS/chi Electrochemical Analyzer model 612A. A three-electrode assembly was used, which was equipped with a platinum disk (2 mm^2) and a platinum wire as the working and counter electrodes, respectively, and Ag/0.01 M $AgNO_3$ (acetonitrile) was used as the reference electrode. The redox potential were referenced against a ferrocene/ferrocenium ($Fc^{0/+}$) redox potential measured in the same electrolytic solution.

3.2.4 Spectroelectrochemical Measurements

Spectroelectrochemical measurements were carried out with a custom-made optically transparent thin-layer electrochemical (OTTLE) cell (light pass length = 1 mm) equipped with a platinum mesh and a platinum coil as the working and counter electrodes, respectively, and Ag/0.01 M $AgNO_3$ (acetonitrile) was used as the reference electrode. The potential was applied with an ALS/chi Electrochemical Analyzer model 612A.

3.2.5 ESR Measurements

ESR spectra were recorded on a JEOL JES-TE200 X-band ESR spectrometer, in which temperature was controlled by a JEOL ES-DVT3 variable-temperature unit in the range of 193-293 K. A Mn^{2+}/MnO solid solution was used a reference.

3.2.6 Magnetic Susceptibility Measurements

The magnetic susceptibility of polycrystalline samples of **2a**$^{3+}$•**3[B(C$_6$F$_5$)$_4$]**$^-$ were measured by a Quantum Design MPMS-5S SQUID magnetometer in the temperature range 2 and 300 K at a constant magnetic field of 0.1 T. The raw data were corrected for both the magnetization of the sample holder alone and the diamagnetic contribution of the sample itself. The estimation of the diamagnetic contribution was done by using the Pacault method.[14]

3.2.7 X-ray crystal structure analysis

Crystallographic data for **2a**, **2b** and **2a**$^{3+}$•**3[B(C$_6$F5)$_4$]**$^-$ were collected on a Rigaku XtaLAB mini diffractometer at 93±1 K using graphite-monochromated Mo Kα radiation (λ = 0.71075 Å) from a rotating anode operating at 50 kV and 12 mA. The structures were solved by direct method (SIR2008[20]) and refined by full-matrix least-squares procedures on F^2 (SHELXL-97[21]) (Table 3.1-3.3). The non-hydrogen atoms were refined anisotropically. All the hydrogen atoms were located on the calculated positions, and refined as a riding model. All calculations were performed using the CrystalStructure crystallographic software package (versions 4.0; Rigaku Corporation), except for the refinement, which was performed using SHELXL-97.

Table 3.1. X-ray crystallographic data for **2a**.

empirical formula	$C_{102}H_{78}N_6O_6 \bullet 6(C_6H_{12})$
formula weight	1904.58
crystal dimensions [mm]	0.180×0.060×0.050
T [K]	124±1
λ [Å]	MoKα/0.71075
crystal system	triclinic
space group	P-1 (#2)
Z	2
a [Å]	12.217(4)
b [Å]	20.357(5)
c [Å]	22.761(6)
α [°]	74.897(11)
β [°]	85.716(14)
γ [°]	85.813(13)
V [Å^3]	5442(3)
ρ_{calcd} [g cm^{-3}]	1.162
collected data	56288
unique data / R_{int}	20184/ 0.1099
no. of parameters	1468
goodness-of-fit	1.044
$R1$ ($I > 2\sigma$), $wR2$ (all reflections)	0.1084, 0.1942
residual density [e Å^{-3}]	0.62/-0.34

Table 3.2. X-ray crystallographic data for **2b**.

empirical formula	$C_{101}H_{71}Cl_{13}F_{12}N_6$
formula weight	1829.49
crystal dimensions [mm]	0.18×0.17×0.10
T [K]	123±2
λ [Å]	MoKα/0.71075
crystal system	monoclinic
space group	$P2_1/c$ (#14)
Z	4
a [Å]	24.333(5)
b [Å]	13.557(3)
c [Å]	27.189(5)
α [°]	90
β [°]	90.828(3)
γ [°]	90
V [Å^3]	8969(3)
ρ_{calcd} [g cm^{-3}]	1.355
collected data	70435
unique data / R_{int}	20132/ 0.1469
no. of parameters	1425
goodness-of-fit	1.037
$R1$ ($I > 2\sigma$), $wR2$ (all reflections)	0.1250, 0.2817
residual density [e Å^{-3}]	0.65/-0.565

Table 3.3. X-ray crystallographic data for **2a**$^{3+}$**•3[B(C$_6$F5)$_4$]**$^{-}$.

empirical formula	$C_{213.35}H_{122.46}B_3Cl_{0.88}F_{60}N_6O_7$
formula weight	4085.54
crystal dimensions [mm]	0.215×0.114×0.080
T [K]	93±1
λ [Å]	CuKα/1.54187
crystal system	monoclinic
space group	$P2_1/n$ (#14)
Z	4
a [Å]	16.31186
b [Å]	24.25840
c [Å]	46.91510
α [°]	90
β [°]	93.50400
γ [°]	90
V [Å^3]	18529.58210
ρ_{calcd} [g cm^{-3}]	1.464
collected data	99893
unique data / R_{int}	33826/ 0.0562
no. of parameters	2673
goodness-of-fit[a]	1.073
$R1$ ($I > 2\sigma$), $wR2$ (all reflections)[b]	0.1125, 0.3219
residual density [e Å^{-3}]	1.13/-0.83

3.3 Results and Discussion

The synthesis of **2a** and **2b** were readily achieved starting from the corresponding 9,10-diaminoanthracene and *p*-dibromobenzene by using a Buchwald-Hartwig reaction,[15,16] and were obtained as a red solid in a yield of 14% and 17.5%, respectively.[17] X-ray crystallographic analysis of **2a**[18] revealed that (i) the six nitrogen centers were almost in the same plane, and (ii) three phenylene units were slightly inclined at 23˚ to 35˚, whereas anthrylene units tilted 75˚ to 82˚ from the macrocyclic plane (Figure 3.2a), thus suggesting some degree of segmentation of π-conjugation through the macrocyclic molecular backbone of **2a** (Figure 3.3). In addition, no noticeable bond alternation was discerned about the N–C bonds along the macrocycle, though $N–C_{phenylene}$ bonds tend to be slightly shortened as compared to $N–C_{anthrylene}$ bonds, in conjunction with the difference in tilted angles of phenylene and anthrylene units. The similar structural features are also confirmed for unsubstituted macrocycle **2b** (Figure 3.4).[18]

a) b)

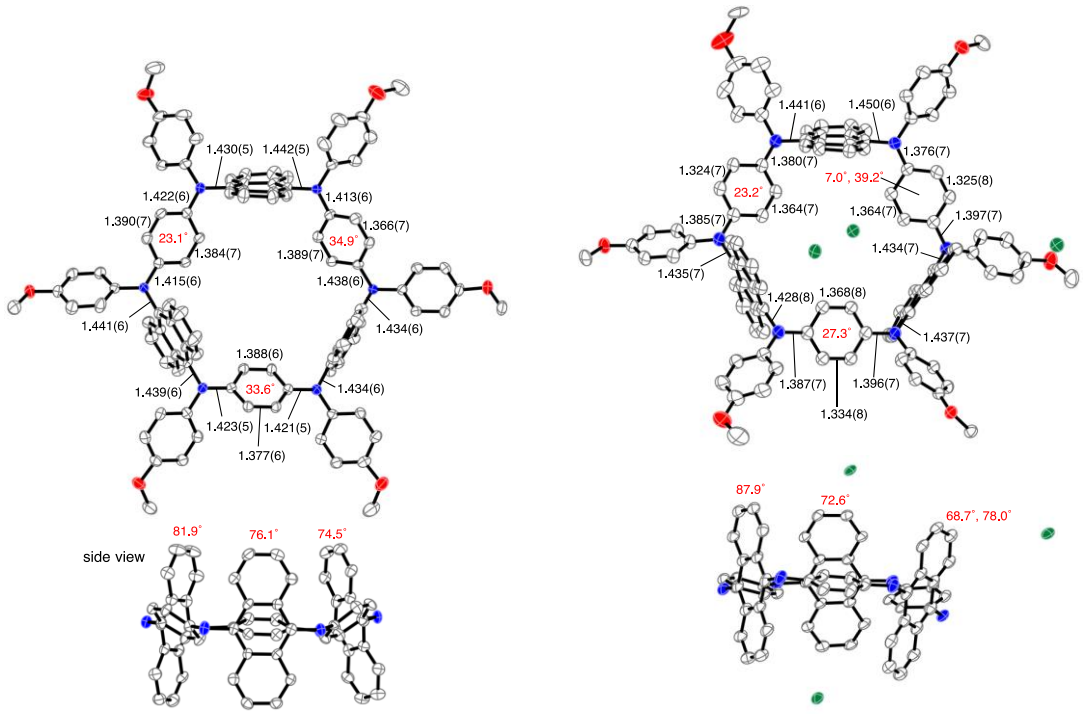

Figure 3.2. ORTEP drawings, selected bond lengths (in Å) and dihedral angles of a) **2a** and b) $\mathbf{2a}^{3+}$ in $\mathbf{2a}^{3+}\bullet\mathbf{3[B(C_6F_5)_4]}^{-}$. Thermal ellipsoids set at the 50% probability level. Hydrogen atoms are omitted for clarity; boron, nitrogen, and oxygen atoms are colored in green, blue, and red, respectively.

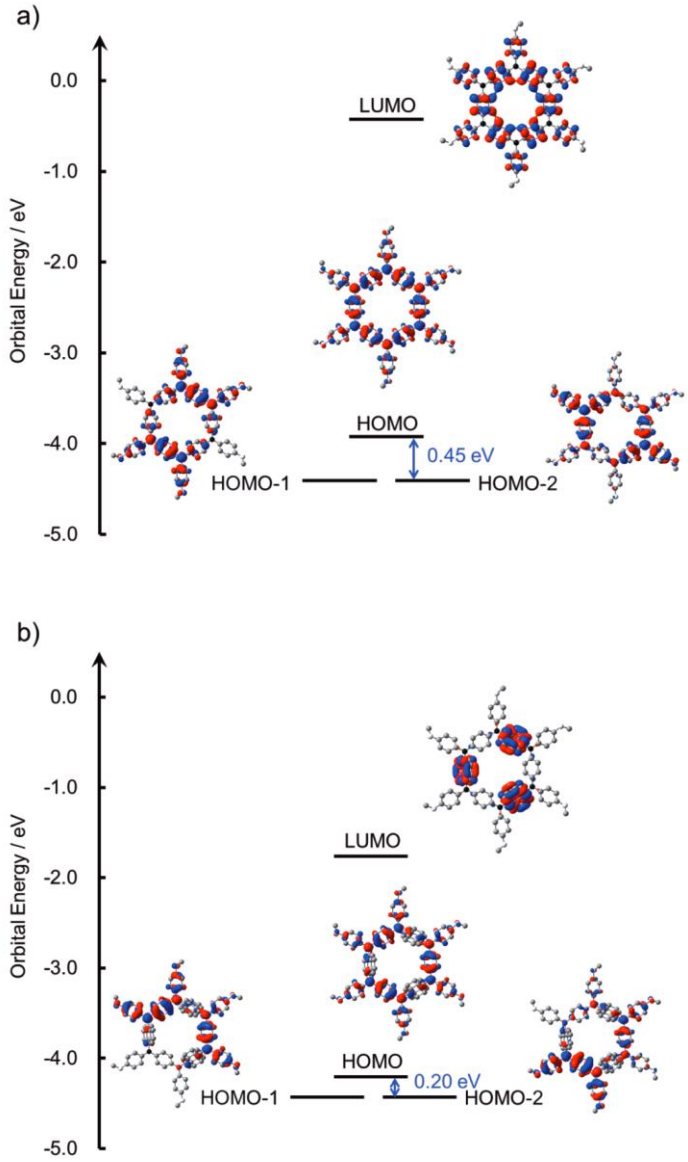

Figure 3.3. Schematic drawings of the frontier Kohn-Sham orbitals for a) **1** and b) **2a** at the B3LYP/6-31G* level of theory. In comparison with macrocycle **1**, the remarkable decrease in the orbital energy gap between the HOMO and HOMO–1 indicates that the π-conjugation through the macrocyclic molecular backbone of **2a** is weakened by introduction of the 9,10-anthrylene units, which are nearly perpendicular to the macrocyclic plane.

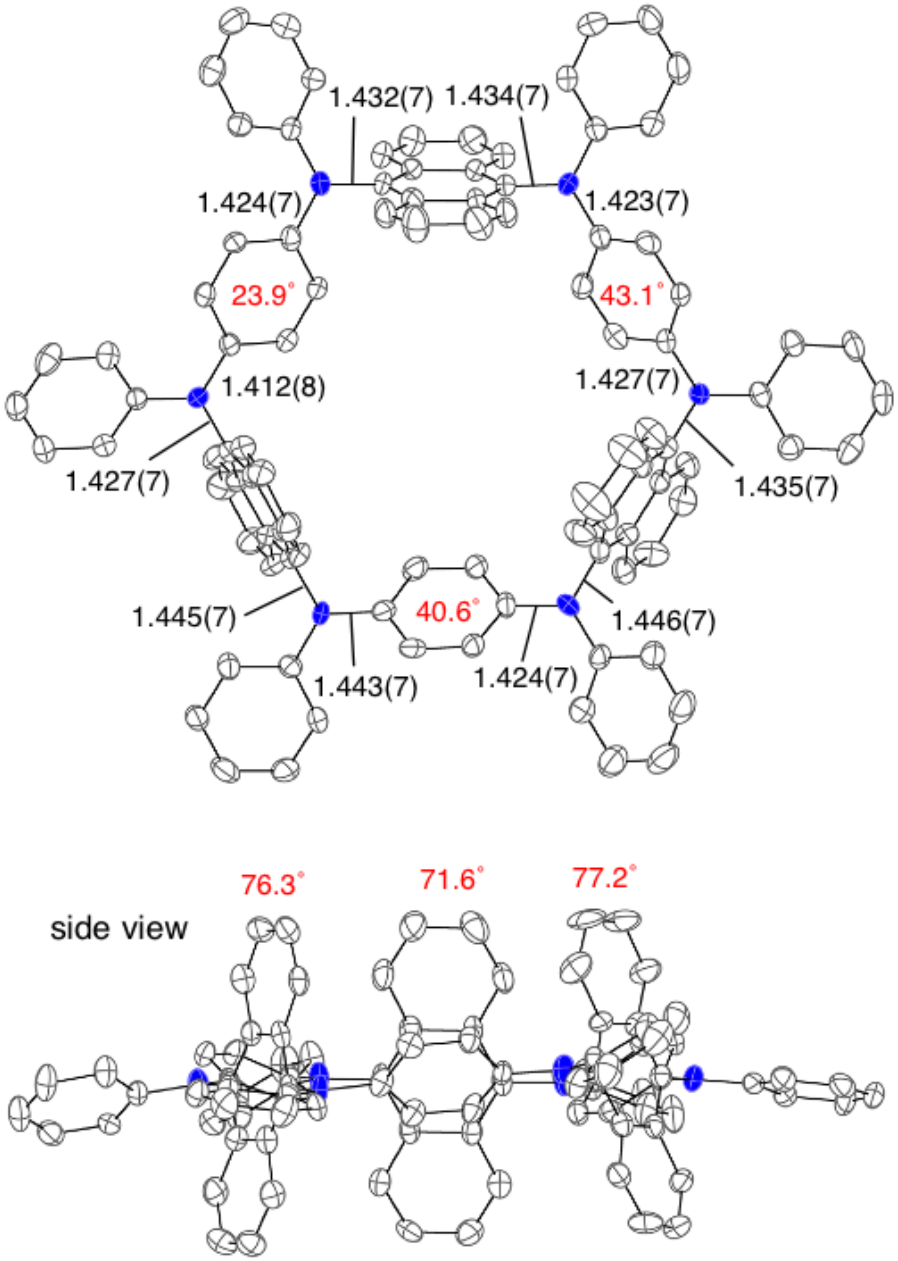

Figure 3.4. ORTEP diagrams, selected bond lengths (in Å) and dihedral angles of **2b**, as determined from X-ray structural analysis at 123(2) K. Hydrogen atoms are omitted for clarity; nitrogen atoms are colored in blue; the thermal ellipsoids are shown at the 50% probability level.

To investigate the effect of introduction of 9,10-anthrylene units, the oxidation potentials of **2a** and **2b** were measured by cyclic voltammetry (CV) and differential pulse voltammetry (DPV) in CH_2Cl_2 using nBu$_4$NBF$_4$ as an electrolyte at room temperature. As shown in Table 3.4, three reversible redox couples were observed for both **2a** and **2b**, and these redox processes were estimated to correspond to one-electron, quasi-two-electron, and quasi-three-electron transfer processes,[19] respectively, thereby indicating the macrocycle **2** is oxidizable up to hexacation in accordance with the six redox-active nitrogen centers. The first oxidation potential of **2a** was shifted to a more positive potential as compared to that of **1** (E_1 = –0.28 V), and close to the value of *N,N,N',N'*-tetraanisyl-*para*-phenylenediamine (**3**) rather than that of 9,10-bis(dianisyamino)anthracene (**4**). This observation suggests that the π-conjugation through the macrocyclic molecular backbone of **2** is weakened by introduction of the 9,10-anthrylene units, which are nearly perpendicular to the macrocyclic plane: the macrocycle **2** can be regarded as a molecular system bearing three *para*-phenylenediamine (**PD**) moieties weakly segmented by three anthrylene units. Nevertheless, the relatively large splitting between the first and second oxidation potentials ($\Delta E_{1\text{-}2}$ = 0.15 V) strongly suggests that the generated radical cation of **2** can be stabilized by spin and charge delocalization over the entire molecule via the highly-twisted anthrylene units.

Table 3.4: Redox potentials (V vs. $Fc^{0/+}$) and potential differences ($\Delta E_{1\text{-}2}$) of **1**–**4** in CH_2Cl_2 at 298 K.

	E_1	E_2	E_3	E_4	E_5	$\Delta E_{1\text{-}2}$
1 [a]	–0.28	–0.17	+0.20	+0.45	+0.72 [b]	0.11
2a	–0.10	+0.05 [b]	+0.58 [c]	—	—	0.15
2b	+0.07	+0.19 [b]	+0.64 [c]	—	—	0.12
3 [d]	–0.13	+0.35	—	—	—	0.48
4 [e]	+0.19	+0.25	—	—	—	0.06

[a] From Ref.[6]. [b] Quasi-two-electron oxidation. [c] Quasi-three-electron oxidation. [d] From Ref.[20]. [e] From Ref.[21].

Further insight into the charge distribution over the oxidized species $\mathbf{2}^{\bullet+}$ was provided by monitoring the absorption spectral change during electrochemical oxidation in CH_2Cl_2 (Figure 3.5 for **2a** and Figure 3.6 for **2b**). In the first oxidation process of **2a**, two bands appeared in the near IR region [0.60 eV (2070 nm) and 1.17 eV (1060 nm)] and continued to grow up until the oxidation to $\mathbf{2a}^{\bullet+}$ has been completed (Figure 3.5a). It should be noted here that the next-lowest-energy band at 1.17 eV closely resembles the lowest-energy band observed for the radical cation of **3**,[22] and can be considered as the charge-resonance (CR) intervalence band (IV) originating from the charge-delocalized semiquinone radical cation of the PD moiety.[23] More interstingly, the lowest-energy band at 0.60 eV is attributable to the IV charge transfer (IVCT) band between two nitrogen centers in the 9,10-diaminoanthrylene moiety, judging from a close similarity to the IVCT band observed for the radical cation of

9,10-bis(dianisylamino)anthracene.[21] This indicates that the generated charge is confined within one **PD** moiety, and furthermore, it is dynamically delocalized over the three **PD** moieties through the anthrylene as a bridging unit. During the next oxidation process from $\mathbf{2a}^{\bullet+}$ to $\mathbf{2a}^{3+}$, a continuous increase in absorbance for the CR IV band with a slight hypsochromic shift [1.29 eV (961 nm)] was detected, and the intensity reached up to almost thrice that of $\mathbf{2a}^{\bullet+}$, showing that all the **PD** moieties have positively-charged semi-quinoidal structures (Figure 3.5b). In contrast, the lowest-energy IVCT band decreased and finally disappeared, simply because the charge-transferable redox sites disappeared due to oxidation of all three **PD** moieties, thus indicating that the three charge-delocalized semiquinoid **PD** moieties are annularly being connected by the anthrylenes.

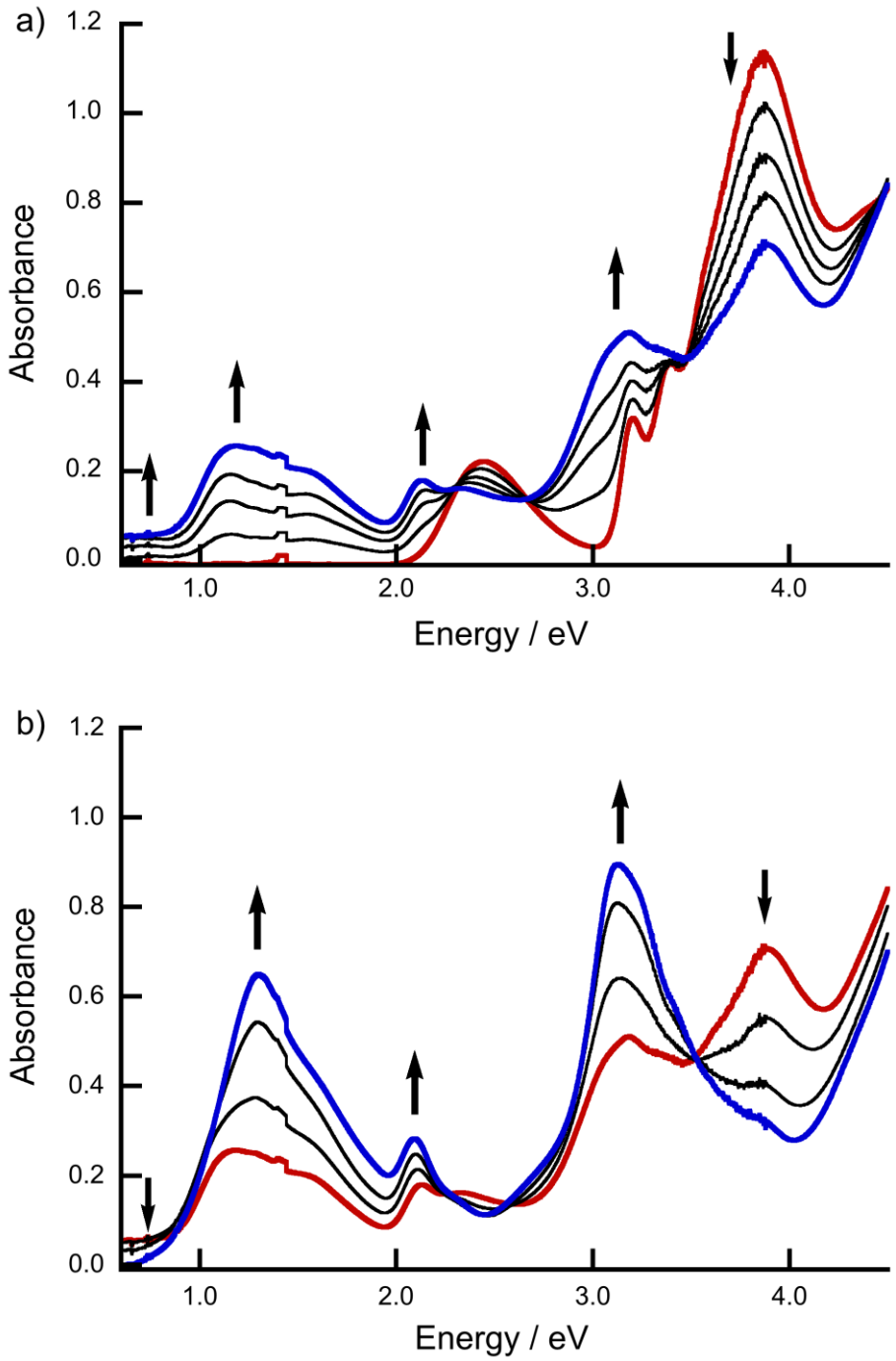

Figure 3.5. UV-vis-NIR absorption spectra of the stepwise electrochemical oxidation of **2a** in CH_2Cl_2 (at 1×10^{-4} M) with 0.1 M *n*-Bu_4NBF_4 at 298 K: a) **2a** (in red) to $\mathbf{2a}^{\bullet+}$ (in blue); b) $\mathbf{2a}^{\bullet+}$ (in red) to $\mathbf{2a}^{3+}$ (in blue).

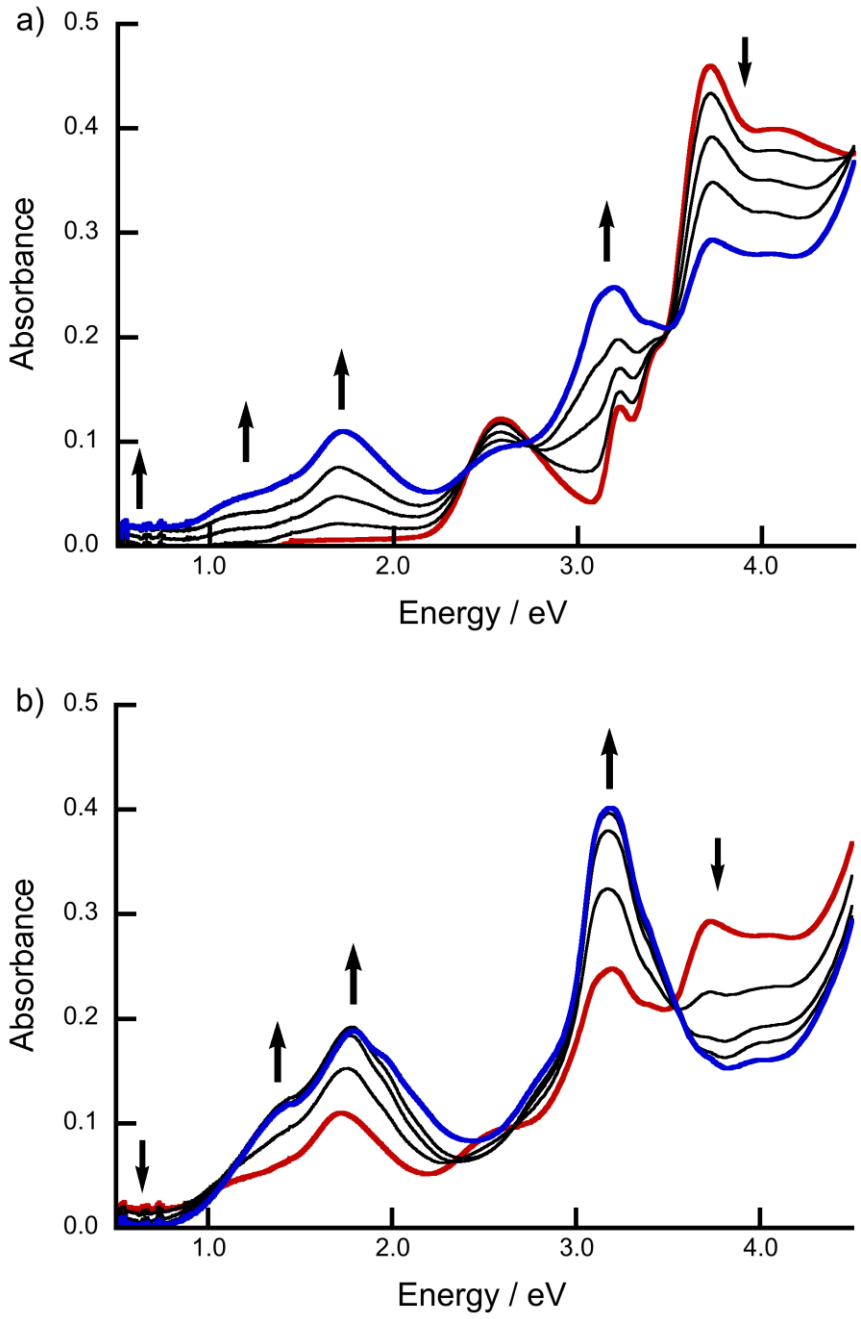

Figure 3.6. UV-vis-NIR absorption spectra of the stepwise electrochemical oxidation of **2b** in CH_2Cl_2 (at 1×10^{-4} M) with 0.1 M *n*-Bu_4NBF_4 at 298 K: a) **2b** (in red) to $\mathbf{2b}^{\bullet+}$ (in blue); b) $\mathbf{2b}^{\bullet+}$ (in red) to $\mathbf{2b}^{3+}$ (in blue).

The ESR spectrum (Figure 3.7) of the radical cation **2a**$^{\bullet+}$ generated by treating **2a** with one equiv of $Ag[B(C_6F_5)_4]$ in CH_2Cl_2 exhibited a multiplet hyperfine structure, and the spectrum was simulated only by assuming the following hyperfine coupling constants: a_N = 0.173 mT (6N) and $a_{H(\textit{para}\text{-phenylene})}$ = 0.02 mT (12H), and the contribution from the unresolved hydrogen nuclei was incorporated in the line width (0.22 mT), thus suggesting the dynamic spin delocalization over the entire molecule on the ESR time scale in spite of some degree of segmentation of π-conjugation through the macrocyclic molecular backbone in **2a**$^{\bullet+}$ due to the highly-twisted anthrylene units. This observation is consistent with the result of the spectroelectrochemical measurements (Figure 3.5a). Note that the shape of the spectrum did not change within the measured temperature range, suggesting a low barrier to thermally activated intra-annular spin transfer. Unfortunately, we could not obtain single crystals suitable for the X-ray structural analysis of **2a**$^{\bullet+}$.

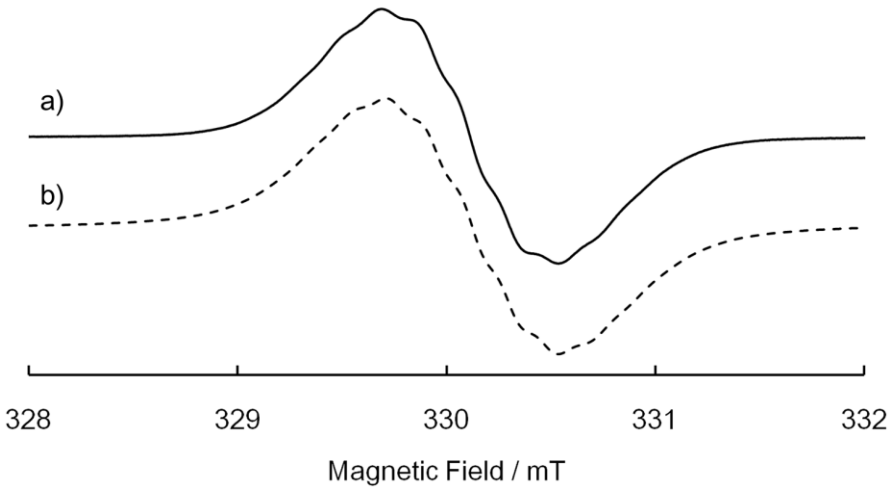

Figure 3.7. (a) Observed X-band ESR spectrum of **2a**$^{\bullet+}$ recorded in CH_2Cl_2 at 298 K. (b) Simulated ESR spectrum of **2a**$^{\bullet+}$.

In contrast to $\mathbf{2a}^{\bullet+}$, we were able to isolate crystalline material of the salt of trication, $\mathbf{2a}^{3+}\bullet\mathbf{3[B(C_6F_5)_4]}^{-}$, from the oxidation of **2a** with three equiv of $Ag[B(C_6F_5)_4]$ in CH_2Cl_2, and moreover, the isolated salts were stable under ambient conditions and can be stored under aerobic conditions at room temperature. In addition, the absorption spectrum of $\mathbf{2a}^{3+}\bullet\mathbf{3[B(C_6F_5)_4]}^{-}$ in CH_2Cl_2 solution was in good agreement with that of the electrochemically generated tricationic species of **2a**. As expected, the X-ray structural analysis revealed the clear-cut quinoidal deformation of all the **PD** moieties of $\mathbf{2a}^{3+}$ (Figure 3.2b): the averaged bond-length alternation (BLA) in phenylene rings for $\mathbf{2a}^{3+}$ is distinct (0.07 Å), whereas 0.01 Å for **2a**; in addition, the averaged bond length of $N\text{-}C_{phenylene}$ for $\mathbf{2a}^{3+}$ is shortened by 0.035 Å, as compared to that for **2a**. In contrast, significant change was not observed in the anthrylene units for both **2a** and $\mathbf{2a}^{3+}$. Thus, the macrocyclic molecular skeleton turned out to be distorted, while the six nitrogen atoms in **2a** are almost coplanar with a slight deviation (Figure 3.2a). It should be noted that two NC_3 planes are not coplanar for one of the three quinoidal **PD** moieties, where the twisted angle of the phenylene plane has two values for the two NC_3 planes (Figure 3.2b), while they are almost coplanar for the remaining two quinoidal **PD** moieties, indicating that the two quinoidal **PD** moieties adopts a similar geometrical structures. Two $[B(C_6F_5)_4]^{-}$ counter ions were located above and below the tricationic macrocycle, whereas the remaining counter ion was located far apart to some extent from $\mathbf{2a}^{3+}$. Taken together, three positive charges of $\mathbf{2a}^{3+}$ are equally pinned down to the three **PD** moieties, and each charge is delocalized over each **PD** moiety, due to the twisted anthrylenes. This picture was also verified by the DFT-computed spin density distribution of $\mathbf{2a}^{3+}$ (Figure 3.8).

(a) (b)

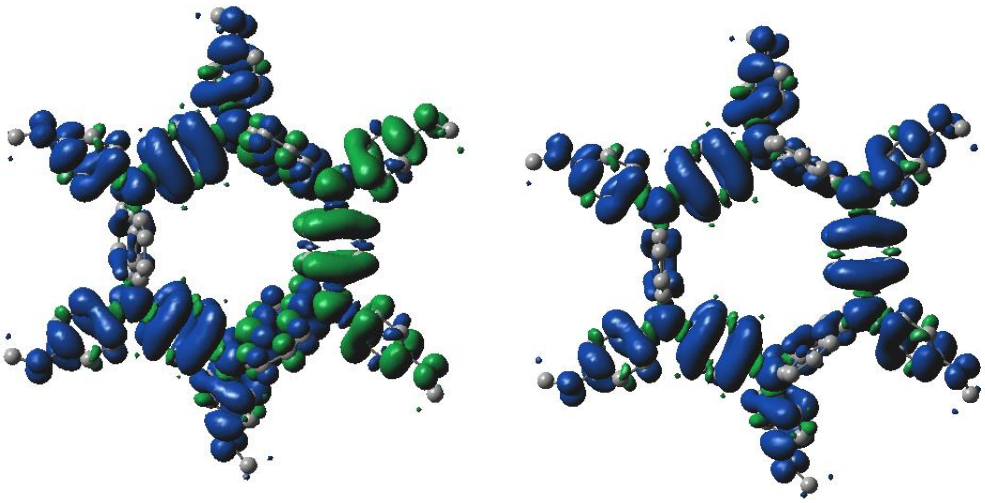

Figure 3.8. Spin density distribution of **2a**$^{3+}$; a) spin-doublet state and b) spin-quartet state (blue: positive spin, green: negative spin; spin isosurface value = 0.0004 electron/au^3; UB3LYP/6-31G*.

Judging from the molecular packing in **2a**$^{3+}$**•3[B(C$_6$F$_5$)$_4$]**$^-$ (Figure 3.9), adjacent charged macrocycles can be considered to be well separated by the counter ions and crystal solvent molecules, thereby suggesting weak intermolecular magnetic interactions. To address the intramolecular magnetic interaction between the generated three spin-centers in **2a**$^{3+}$, the temperature dependence of the molar magnetic susceptibility (χ_M) for analytically pure samples was measured by using the SQUID magnetometer. As shown in Figure 3.10a, the $\chi_M T$ value gradually decreased with decreasing temperature, and reached a nearly constant value close to a theoretical value (0.375 emu K mol^{-1}) for a single spin-1/2 per macrocyclic molecular unit at around 30 K, indicating intramolecular antiferromagnetic interaction for **2a**$^{3+}$. The X-ray structural analysis suggested an isosceles triangular 3-spin model, where three magnetically interacting

spins-1/2 are located on the apexes of an isosceles triangle with two different exchange interactions J_1 and J_2, based on the spin Hamiltonian: $H = -2J_1(S_1 \bullet S_2 + S_1 \bullet S_3) - 2J_2(S_2 \bullet S_3)$. In this model, temperature dependence of the $\chi_M T$ value can be represented as Equation (3-1),[24] where θ denotes the Weiss constant which is associated with weak intermolecular interactions:

$$\chi_M T = 0.375\left(\frac{10+\exp(-\Delta_1/k_B T)+\exp(-\Delta_2/k_B T)}{2+\exp(-\Delta_1/k_B T)+\exp(-\Delta_2/k_B T)}\right)\frac{T}{T-\theta} \qquad (3\text{-}1)$$

where $\Delta_1 = 3J_1$ and $\Delta_2 = J_1 + 2J_2$ correspond to the energy differences between the two competing doublet states and the quartet state (Figure 3.10b).[25] From the fitting to the experimental data, the best-fitted parameters were determined: $\Delta_1/k_B \cong \Delta_2/k_B = -223$ K,[26] and $\theta = -0.27$ K. This means that the present 3-spin system can be virtually considered as a regular trianglular spin system where $J_1/k_B = J_2/k_B \equiv J/k_B \simeq -74$ K, and moreover, the doublet ground state is doubly degenerate, thereby indicating the present 3-spin system is typically spin-frustrated, in conjunction with rare examples in organic polyradicals.[27]

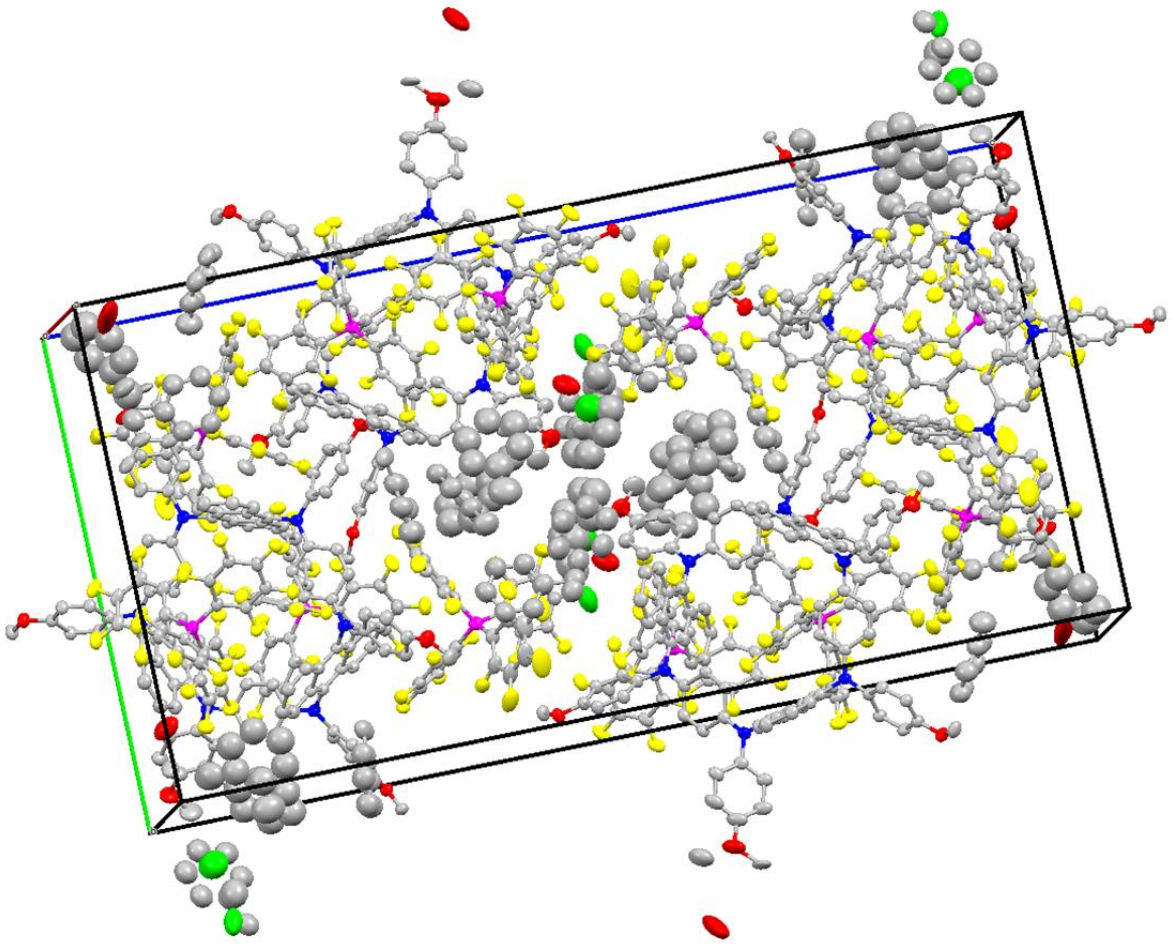

Figure 3.9. Crystal structures of (a) **3**, (b) $\mathbf{3}^{\bullet+}\bullet[B(C_6F_5)_4]^-$ and (c) $\mathbf{3}^{2+}\bullet 2[B(C_6F_5)_4]^-$, as determined from X-ray structural analyses at 93(1) K. Hydrogen atoms are omitted for clarity; boron, nitrogen, oxygen, chlorine, and fluorine atoms are colored in purple, blue, red, green, and yellow, respectively; the thermal ellipsoids are shown at the 50% probability level.

a)

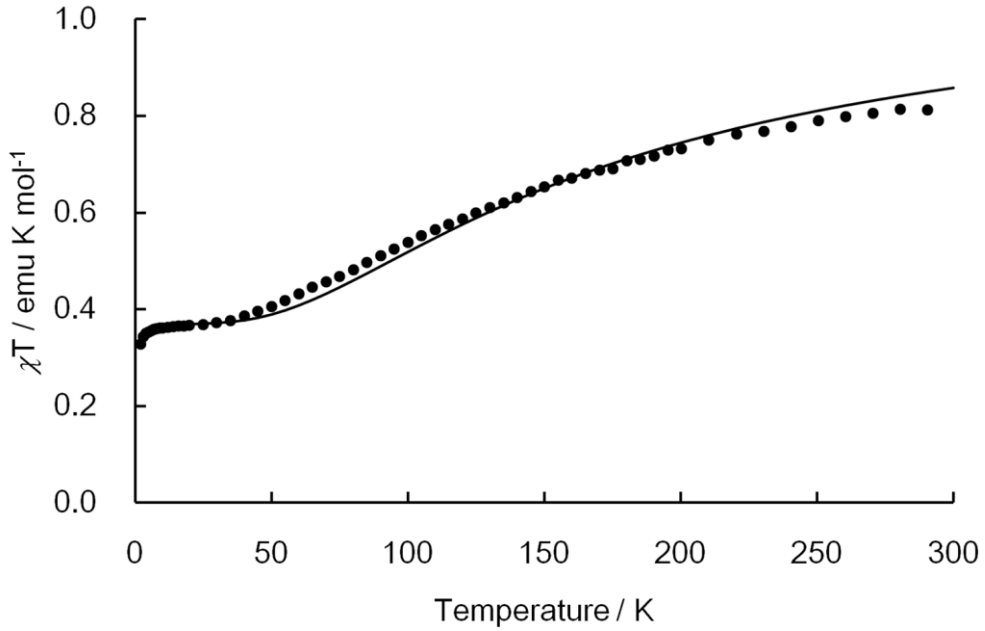

b)

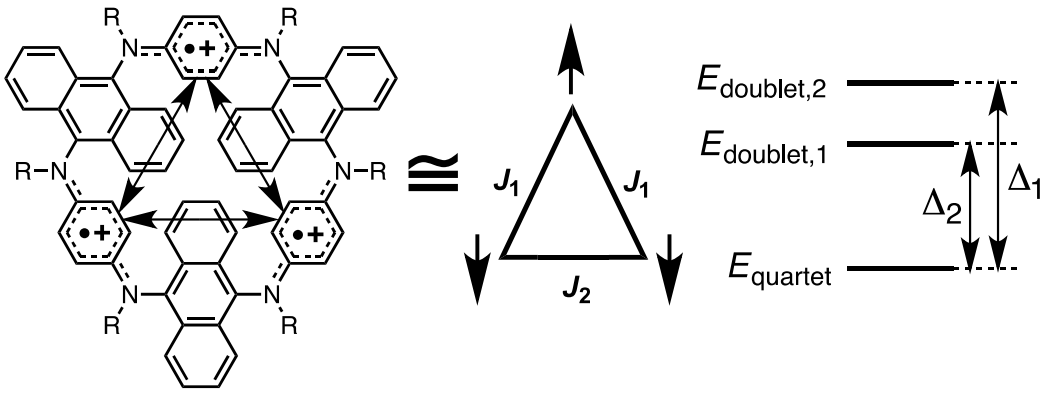

Figure 3.10. a) Plot of $\chi_M T$ versus T for **2a**$^{3+}$•**3[B(C$_6$F$_5$)$_4$]**$^-$ at 0.1 T. The solid curve represents the best theoretical fit; b) isosceles triangle 3-spin interacting model for **2a**$^{3+}$ and the energy level diagram for the two doublet states and the one quartet state.

3.4 Conclusion

In conclusion, the author has investigated the spin and charge distributions for radical cation and triradical trication of the highly-twisted anthrylene-embedded hexaaza[1_6]paracyclophane. The electrochemical, spectroelectrochemical, and ESR studies revealed the dynamically delocalized spin and charge distribution for the radical cation, despite somewhat segmentation due to the anthrylenes of π-conjugation through the macrocyclic molecular backbone. Furthermore, we have succeeded in isolation of the stable triradical trication salt of the macrocycle, in which three segmented PD-based radical spins were found to be mutually antiferromagnetically coupled with $J/k_B \simeq -74$ K, leading to a typical spin-frustrated 3-spin system. The present findings provide new insight into the design of troidal multispin molecular systems.

3.5 References

[1] a) T. A. Skotheim, J. Reynolds, Eds. *Handbook of Conducting Polymers, 2 Volume Set*. CRC press, Boca Raton, FL, **2007**; b) L. M. Tolbert, *Acc. Chem. Res*. **1992**, *25*, 561-568; P. F. Barbara, T. J. Meyer, M. A. Ratner, *J. Phys. Chem*. **1996**, *100*, 13148-13168.

[2] a) T. Nishinaga, A. Wakamiya, D. Yamazaki, K. Komatsu, *J. Am. Chem. Soc*. **2004**, *126*, 3163-; b) M. Tateno, M. Takase, M. Iyoda, K. Komatsu, T. Nishinaga, *Chem. Eur. J*. **2013**, *19*, 5457-5467.

[3] a) F. Zhang, G. Götz, H. D. F. Winkler, C. A. Schalley, P. Bäuerle, *Angew. Chem. Int. Ed*. **2009**, *48*, 6632-6635; b) F. Zhang, G. Götz, E. Mena-Osteritz, M. Weil, B. Sarkar, W. Kaim, P. Bäuerle, *Chem. Sci*. **2011**, *2*, 781-784; c) K. Asai, A. Fukazawa, S. Yamaguchi, *Chem. Commun*. **2015**, *51*, 6096-6099.

[4] a) M. Banerjee, S. V. Lindeman, R. Rathore, *J. Am. Chem. Soc*. **2007**, *129*, 8070-8071; b) M. Banerjee, R. Shukla, R. Rathore, *J. Am. Chem. Soc*. **2009**, *131*, 1780-1786.

[5] a) E. Kayahara, T. Kouyama, T. Kato, H. Takaya, N. Yasuda, S. Yamago, *Angew. Chem. Int. Ed*. **2013**, *52*, 13722-13726; b) M. R. Golder, B. M. Wong, R. Jasti, *Chem. Sci*. **2013**, *4*, 4285-4291.

[6] A. Ito, Y. Yokoyama, R. Aihara, K. Fukui, S. Eguchi, K. Shizu, T. Sato, K. Tanaka, *Angew. Chem. Int. Ed*. **2010**, *49*, 8205-8208.

[7] B. Grossmann, J. Heinze, T. Moll, C. Palivan, S. Ivan, G. Gescheidt, *J. Phys. Chem. B* **2004**, *108*, 4669-4672.

[8] a) A. Ito, K. Tanaka, *Pure Appl. Chem*. **2010**, *82*, 979-989; b) A. Ito, *J. Mater. Chem. C* **2016**, *4*, 4614-4625.

[9] a) S. Toyota, *Chem. Lett*. **2011**, *40*, 12-18; b) M. Yoshizawa, J. K. Klosterman, *Chem. Soc. Rev*. **2014**, *43*, 1885-1898.

[10] K. Ragavachari, *Theor. Chim. Acc*. **2000**, *103*, 361 and references cited therein.

[11] A. Dreuw, M. Head-Gordon, *Chem. Rev*. **2005**, *105*, 4009-4037.

[12] W. J. Hehre, L. Radom, P.v. R. Schleyer, J. A. Pople, *Ab Initio Molecular Orbital Theory*, Wiley, New York, **1986**.

[13] M. J. Frisch, *et al*., Gaussian 09 (Revision D.01), Gaussian, Inc., Wallingford CT, **2013**.

[14] Gupta, R. R. *Landolt-Börnstein, New Series II* (Eds.: Hellwege, K.-H.; Hellwege, A. M.); Springer Verlag: Berlin, 1986, vol.16 (Diamagnetic Susceptibility).

[15] P. Ruiz-Castillo, S. L. Buchwald, *Chem. Rev*. **2016**, *116*, 12564-12649.

[16] a) J. F. Hartwig, *Nature* **2008**, *455*, 314-322; b) J. F. Hartwig, *Acc. Chem. Res*. **2008**, *41*, 1534-1544.

[17] The same reaction between *N*,*N*'-dianisyl-*p*-phenylenediamine and 9,10-dibromo-anthracene resulted in a low yield (5%) of **2b**.

[18] CCDC 1545929 (**2a**), 1551588 (**2b**), and 1545930 (**2a**$^{3+}$•**3[B(C$_6$F$_5$)$_4$]**$^-$) contain the supplementary crystalic data for this paper. These data can be obtained free of charge from The Cambridge Crystallographic Data Centre via www.ccdc.cam.ac.uk/data_request/cif.

[19] The simulated DPV curve of **2a** was well fitted to the observed one by using the following oxidation potentials [$E_{oxidation}$ vs. Fc$^{0/+}$ (ne)]; E_1 = –0.10 V (1e), E_2 = +0.03 V (1e), E_3 = +0.07 V (1e), E_4 = +0.51 V (1e), E_5 = +0.57 V (1e), and E_6 = +0.61 V (1e).

[20] A. Ito, S. Inoue, Y. Hirao, K. Furukawa, T. Kato, K. Tanaka, *Chem. Commun*. **2008**, 3242-3244.

[21] M. Uebe, T. Kato, K. Tanaka, A. Ito, *Chem. Eur. J*. **2016**, *22*, 18923-18931.

[22] C. Lambert, G. Nöll, *J. Am. Chem. Soc*. **1999**, *121*, 8434-8442.

[23] a) A. V. Szeghalmi, M. Erdmann, V. Engel, M. Schmitt, S. Amthor, V. Kriegisch, G. Nöll, R. Stahl, C. Lambert, D. Leusser, D. Stalke, M. Zabel, J. Popp, *J. Am. Chem. Soc*. **2004**, *126*, 7834; b) Y. Hirao, A. Ito, K. Tanaka, *J. Phys. Chem. A* **2007**, *111*, 2951; c) A. Ito, D. Sakamaki, Y. Ichikawa, K. Tanaka, *Chem. Mater*. **2011**, *23*, 841.

[24] L. Catala, J. Le Moigne, N. Gruber, J. J. Novoa, P. Rabu, E. Belorizky, P. Turek, *Chem. Eur. J*. **2005**, *11*, 2440-2454.

[25] E. Sinn, *Coord. Chem. Rev*. **1970**, *5*, 313-347.

[26] The DFT-computed doublet-quartet energy difference ($\Delta E_{D-Q}/k_B$) of –209 K (B3LYP/6-31G*) was in good agreement with the experimental value of –223 K.

[27] a) K. Awaga, T. Okuno, A. Yamaguchi, M. Hasegawa, T. Inabe, Y. Maruyama, N. Wada, *Phys. Rev. B* **1994**, *49*, 3975-2981; b) J. Fujita, M. Tanaka, H. Suemune, N. Koga, K. Matsuda, H. Iwamura, *J. Am. Chem. Soc*. **1996**, *118*, 9347-9351; c) T. Itoh, K. Matsuda, H. Iwamura, K. Hori, *J. Am. Chem. Soc*. **2000**, *122*, 2567-2576; d) Y. Wu, M. D. Krzyaniak, J. F. Stoddart, M. R. Wasielewski, *J. Am. Chem. Soc*. **2017**, *139*, 2948-2951.

Chapter 4

Synthesis and Characterization of 5,12–Diamino-Substituted Tetracenes

4.1 Introduction

Recently, organic redox systems have been widely investigated because they have been used as functional materials in molecular electronics. Particularly, two-stage redox systems where their redox-active end groups are located outside a central arene π-system that has an aromatic character in the fully reduced state are classified into the Wurster-type, and one of the representative examples, *N*,*N*,*N'*,*N'*-tetramethyl-*p*-phenylenediamine (**TMPD**) is well-known for the precursor of the stable radical cation, Wurster's Blue (Figure 4.1a).[1] When the central arene π-system in **TMPD** is replaced by extended π-systems such as polycyclic aromatic hydrocarbons, oligoacene, the question of whether such a Wurster-type-like redox system retains the two-stage redox property is of great interest. In this sense, it has already been reported that bis(*N*,*N*-dialkylamino)- and

(*N*-*p*-anisyl-*N*-methylamino)-anthracene[2] and pentacene[3] (Figure 4.1b) showed only one two-electron oxidation process with a distinctive cyclic voltammogram. The observed electrochemical behavior was explained by the large structural change into a butterfly-like structure during the two-electron oxidation process, in which the central six-membered ring is folded along the C9–C10 (anthracene) or C6–C13 (pentacene) line (Figure 4.1b).

In contrast to *N*-dialkyl-substituted or N-alkyl-anisyl-substituted amino acene, the cyclic voltammogram of bis(*N*,*N*-dianisylamino)-anthracene and pentacene displayed reversible oxidation process, thus strongly suggesting no significant structural changes during the electrochemical oxidation. The radical cation of *N*-dianisyl-substituted diaminoanthracene is classified into the class Ⅲ or the borderline class Ⅲ/class Ⅱ mixed-valence compound. And The dication of bis(*N*,*N*-dianisylamino)anthracene is in a spin-singlet in the ground state with a small singlet-triplet energy gap, thus leading to its diradical character due to its thermally accessible excited spin-triplet state, and furthermore, the X-ray structural analysis revealed that the dication did not adopt the folding butterfly-like structure and the planarity of the anthrylene moiety was preserved. These results suggested that bis(*N*,*N*-dianisylamino)anthracene is classified as Wurster's type redox system. On the other hand, the radical cation of bis(*N*,*N*-dianisylamino)pentacene could not be found by chemical or electrochemical oxidation. And the dication of *N*-dianisyl-substituted pentacene showed the butterfly-like conformation of the pentacene moiety. These results suggested that bis(*N*,*N*-dianisylamino)pentacene is not classified as Wurster's type redox system.

These findings strongly suggest that the difference in the *N*-substituent patterns of oligoacenes and the oligoacene moiety causes the different redox behaviors. Herein the

author reports the synthesis of 5,12-diaminotetracenes, **1, 2** and **3** as a new class of redox-active tetracene and their electronic properties (Scheme 4.1). For a comparative study of the electronic structures of the oxidized states of **1**-**3**, the author has carried out cyclic voltammetry, spectroelectrochemistry, and ESR and fluorescence spectroscopy, as well as performed density functional theory (DFT) calculations.

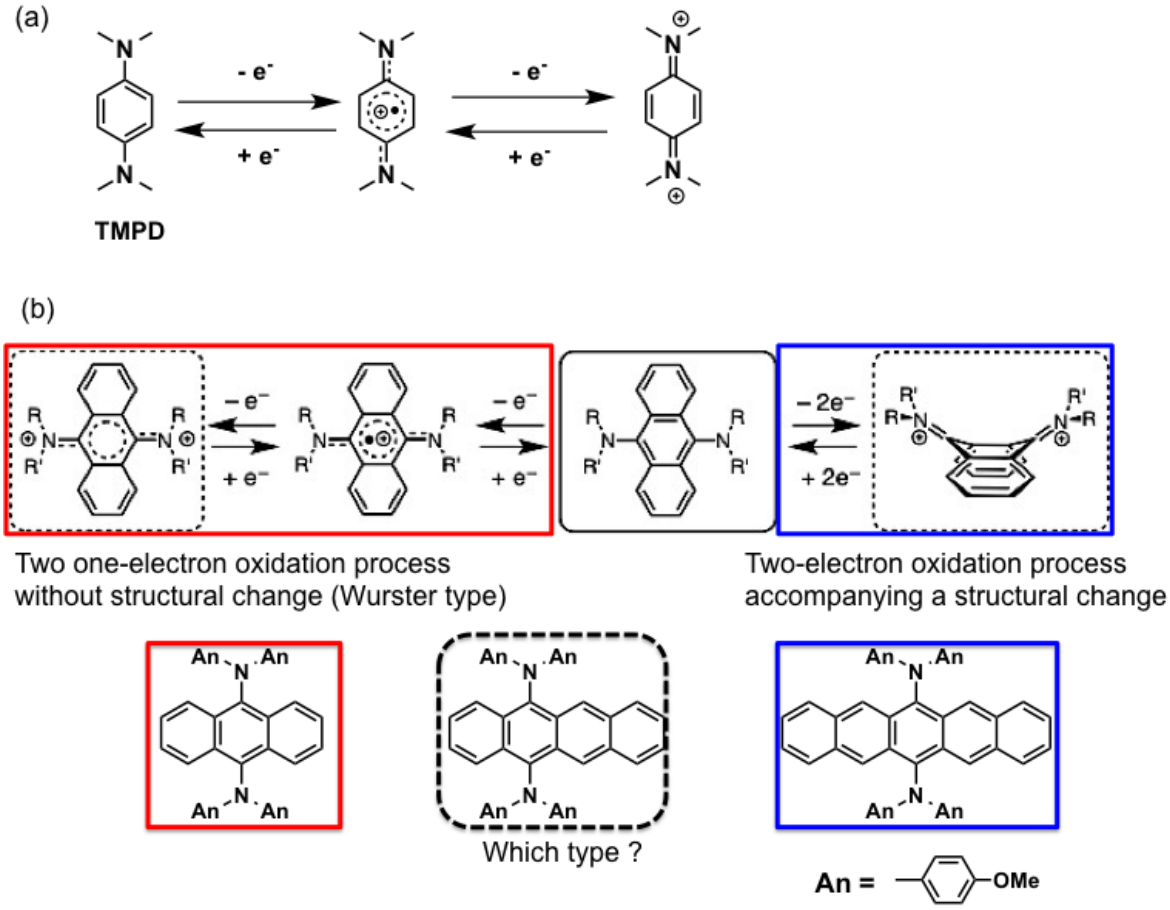

Figure 4.1. (a) TMPD as an exemplary two-stage Wurster-type redox system, (b) two directions of redox process for Bis(dianisylamino)acenes.

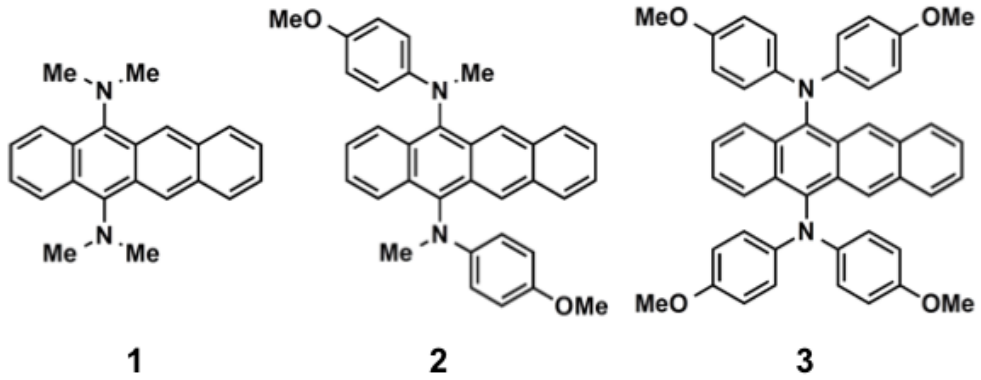

1 2 3

Scheme 4.1. Molecular Structures of **1**-**3**.

4.2 Experimental Section

4.2.1 Synthesis

All the purchased reagents were of standard quality, and used without further purification. All the purchased solvents were purified, dried, and degassed by standard procedures. Column chromatography was performed with silica gel (Kanto Chemical Co., Inc., silica gel 60N, spherical neutral). Elemental analyses were performed by Center for Organic Elemental Microanalysis, Kyoto University. ^{1}H and ^{13}C NMR spectra were measured by a JEOL JNM-AL400 FT-NMR spectrometer. Chemical shifts of NMR spectra are determined relative to internal tetramethylsilane (TMS) standard (δ), and are given in parts per million (ppm).

5, 12-Bis(*N*,*N*-dimethylamino)tetracene (**1**) : A toluene solution (1.0 M) of $TiCl_4$ (2.0 mL, 2.0 mmol) was added dropwise to a stirred suspension of 5, 12-tetracenequinone (0.26 g, 1.0 mmol) and a large excess of Fe powder (4.0 g) in toluene (20 mL) in an ice-cooled flask under Ar atmosphere, and then the resulting slurry was stirred at 0 °C. After 30 min, an excess of dimethylamine (6.0 mL, 12.0 mmol) was added to the stirred

slurry at 0 °C. The reaction mixture was shaded from bright light and stirring was continued for 70 hours. The resulting slurry was filtered by suction through amino silica gel (NH-DM1020, ca. 100 μm, Fuji Silysia Chemical Ltd., Japan) using Büchner funnel, and then the red layer was eluted with toluene. Evaporation of the filtrate afforded a red solid as a crude product. Chromatography on amino silica gel (toluene/*n*-hexane = 1:2) gave 0.14 g (44%) of **1** as a red solid; ^{1}H NMR (400 MHz, Acetone): δ 9.05(s, 2H), 8.32-8.35(m, 2H), 8.09-8.12(m, 2H), 7.40-7.44(m, 4H), 3.34(s, 12H); ^{13}C NMR (100 MHz, Acetone): δ144.3, 131.9, 131.2, 130.7, 129.3, 126.2, 125.9, 125.2, 124.8, 45.0; ESI HRMS: m/z calcd for $C_{22}H_{22}N_2$: 315.1856 $[M+H]^+$; found 315.1849; Elem. Anal. calcd (%) for C 84.04, H 7.05, N 8.91; found C 84.09, H 6.98, N 8.84.

5,12-Bis(*N*,*N*-anisylmethylamino)tetracene (**2**): Following the same procedure as described for the preparation of **1**, a dark red reaction mixture was obtained by using *N*-methyl-*p*-anisidine(1.3 g, 9.7 mmol). The resulting dark red slurry was filtered by suction through amino silica gel (NH-DM1020, ca. 100 μm, Fuji Silysia Chemical Ltd., Japan) using a Büchner funnel, and then the red layer was eluted with toluene. After evaporation of the filtrate, the crude product was chromatographed on silica gel (CH_2Cl_2/*n*-hexane = 3:2 as eluent) to afford **2** as a red solid (0.19 g, 38%); ^{1}H NMR (400 MHz, $CDCl_3$) δ 8.63(s, 2H), 7.92-7.95(m, 2H), 7.87-7.90(m, 2H), 7.30-7.35(m, 4H), 6.79, 6.76(d, *J* = 9.0 Hz, ca. 4H each), 6.55, 6.52(d, *J* = 9.0 Hz, ca. 4H each), 3.74, 3.73(s, ca. 6H each), 3.64, 3.61 (s, ca. 6H each); ^{13}C NMR (100 MHz, $CDCl_3$): δ 151.3, 151.2, 144.9, 144.8, 139.3, 139.3, 131.8, 130.6, 130.5, 129.5, 128.6, 125.9, 125.6, 125.0, 123.7, 114.9, 114.9, 112.8, 55.8, 40.0, 39.9; ESI HRMS: m/z calcd for $C_{34}H_{30}N_2O_2$: 498.2302 $[M]^+$; found 498.2293; Elem. Anal. calcd (%) for C 81.90, H 6.06, N 5.62;

found C 81.66, H 5.96, N 5.40.

5, 12-Bis(*N*,*N*-dianisylamino)tetracene (**3**): A toluene solution (1.0 M) of $TiCl_4$ (7.5 mL, 7.5 mmol) was diluted by 20 mL of toluene and added dropwise to a stirred and heated suspension of *p*-anisidine (1.9 g, 16 mmol) and 1,4-diazabicycro[2,2,2]octane (3.4 g, 30 mmol) in toluene (20 mL) under Argon atmosphere. After stirring 30 minutes, a suspension of 5, 12-tetracenquinone (1.3 g, 5.1 mmol) in toluene (30 mL) was added dropwise and stirred another 19 hours. The resulting slurry was filtered and evaporation of the filtrate afforded red liquid as a crude product. Crude product was chromatographed on amino silica gel (NH-DM1020, ca. 100 μm, Fuji Silysia Chemical Ltd., Japan), to afford **4** as orange solid (1.69 g). The suspension of **4** (0.46 g) and Pd/C (123 mg) in THF (20 mL) was heated and stirred for 1 hour. Hydrazine monohydrate (0.4 mL, 8.4 mmol) was added, shaded from bright light and stirred for another 3 hours. Evaporating at 50 °C, solvent was removed from the reaction mixture and the residue was washed with water to afford a purple solid, mixture of **5** and Pd/C. A mixture of **5** (0.57 g, mixture with Pd/C), 4-iodoanisole (0.94 g, 4.0 mmol), $Pd(dba)_2$ (28.8 mg, 0.05 mmol), Tri-*tert*-butylphosphoniumtetrafluoroborate (31.6 mg, 0.11 mmol) and NaO*t*Bu (486 mg, 5.1 mmol) in toluene (20 mL) was shaded from bright light and refluxed under Ar atmosphere for 17 hours. The resulting reaction mixture was cooled down to room temperature, extracted ethyl acetate, washed with brine and water and the organic layer was separated and dried over Na_2SO_4. After evaporation of the solvent, the crude product was chromatographed on silica gel (toluene) to afford **3** as a purple solid (376 mg, 55%); ^{1}H NMR (400MHz, CD_2Cl_2): δ 8.81(s, 2H), 8.15-8.18(m, 2H), 7.77-7.80(m, 2H), 7.28-7,31(m, 4H), 7.05(d, *J* = 9.0 Hz, 4H), 6.74(d, *J* = 9.0 Hz, 4H), 3.71(s, 12H);

^{13}C NMR (100 MHz, $CDCl_3$): δ 154.0, 142.2, 137.6, 131.8, 131.4, 130.3, 128.6, 126.2, 125.6, 125.2, 124.4, 121.3, 114.7, 55.5; ESI HRMS: m/z calcd for $C_{46}H_{38}N_2O_4$: 682.2826 $[M]^+$; found 682.2819; Elem. Anal. Calcd (%) for C 80.92, H 5.61, N 4.10; found C 80.97, H 5.83, N 4.10.

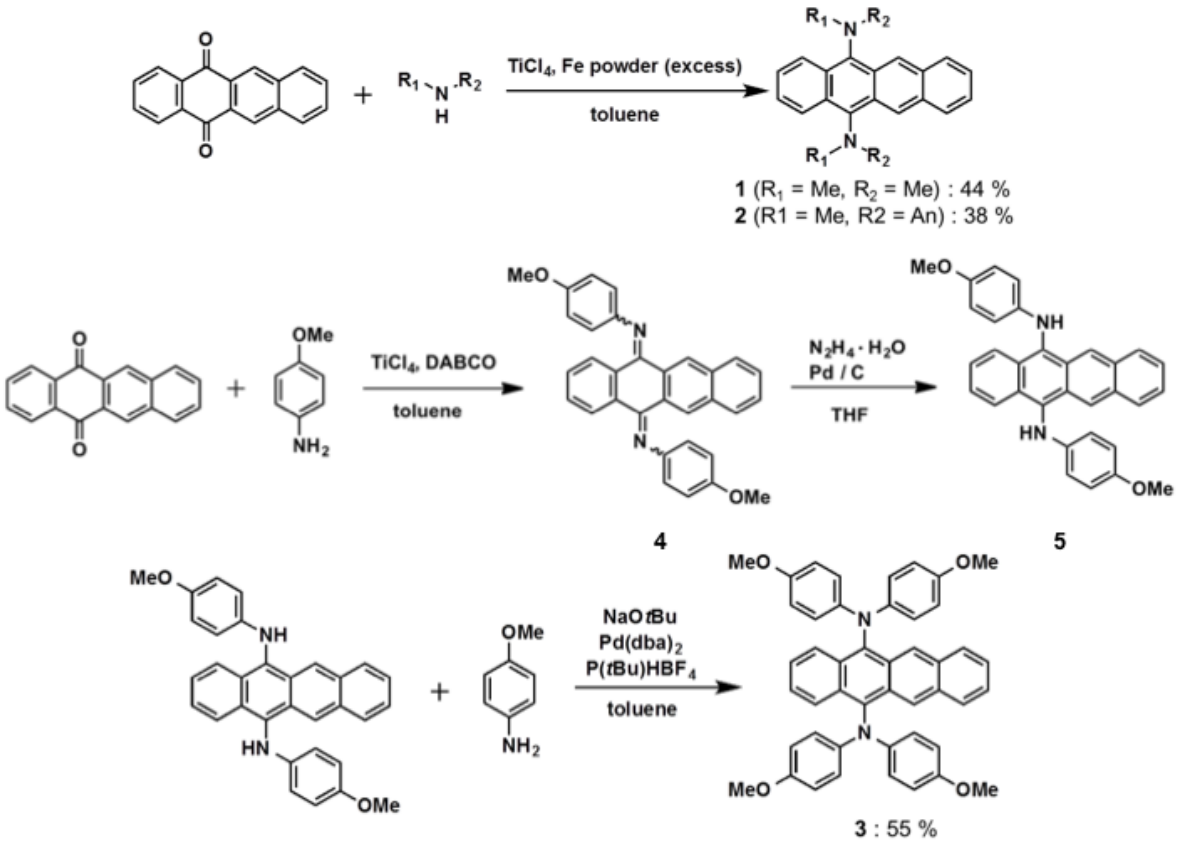

Scheme 4.2. Synthetic route of **1**-**3**.

4.2.2 DFT Calculations

Quantum chemical calculations were performed with using a hybrid Hartree–Fock/density functional theory (HF/DFT) method ((U)B3LYP).[4] Full geometrical optimization of **1** ,**2** , **3**, $\mathbf{1}^{\cdot+}$, $\mathbf{2}^{\cdot+}$, $\mathbf{3}^{\cdot+}$, $\mathbf{1}^{2+}$, $\mathbf{2}^{2+}$, and $\mathbf{3}^{2+}$ were carried out and furthermore, their local minimum structures were confirmed by performing subsequent frequency analyses. Excitation energies were examined by means of the time-dependent density functional method (TD-DFT) [5] based on the (U)B3LYP/6-31G*-optimized structures. All the computations employed the 6-31G* basis set.[6] All these computational approaches are implemented in Gaussian 09 package of ab initio MO calculation.[7]

4.2.3 Electrochemical Measurements

The redox properties were evaluated by cyclic voltammetry (CV) and differential pulse voltammetry (DPV) in CH_2Cl_2 solution at 298 K with 0.1 M tetra-*n*-butylammonium tetrafluoroborate ($TBABF_4$) as supporting electrolyte (scan rate 100 mV s^{-1}) using an ALS/chi Electrochemical Analyzer model 612A. A three-electrode assembly was used, which was equipped with a platinum disk (2 mm^2) and a platinum wire as the working and counter electrodes, respectively, and Ag/0.01 M $AgNO_3$ (acetonitrile) was used as the reference electrode. The redox potential were referenced against a ferrocene/ferrocenium ($Fc^{0/+}$) redox potential measured in the same electrolytic solution.

4.2.4 Spectroelectrochemical Measurements

Spectroelectrochemical measurements were carried out with a custom-made optically

transparent thin-layer electrochemical (OTTLE) cell (light pass length = 1 mm) equipped with a platinum mesh and a platinum coil as the working and counter electrodes, respectively, and Ag/0.01 M $AgNO_3$ (acetonitrile) was used as the reference electrode. The potential was applied with an ALS/chi Electrochemical Analyzer model 612A.

4.2.5 ESR Measurements

Cw-ESR Spectra were recorded on a JEOL JES-TE200 X-band ESR spectrometer, in which temperature was controlled by a JEOL ES-DVT3 variable-temperature unit in the range of 193-293 K. An Mn^{2+}/MnO solid solution was used as a reference.

4.2.6 Photophysical Measurements

Fluorescence spectra were recorded on an absolute photoluminescence quantum yield measurement system (HAMAMATSU Quantaurus-QY).

4.3 Results and Discussion

4.3.1 Synthesis

By following the same procedure as 6,13-bis(diethylamino)pentacene[3], Treatment of a solution of 5,12-tetracenequinone in the presence of an excess of Fe powder in toluene with 2 equivalents of $TiCl_4$ at 0 °C, and then addition of an excess of dimethylamine into the reaction mixture resulted in good yield of the corresponding 5,12-bis(dimethylamino)tetracene **1** (Scheme 4.2) Under the same condition, tetracenequinone reacted with *N*-methyl-*p*-anisidine to produce compound **2**. Unfortunately, attempt to prepare the bis(diarylamino)-substituted compounds from

tetracenequinone and dianisylamine under the same conditions was not successful.

The author then pursued different synthetic routes for the synthesis of 5,12-bis(dianisylamino)tetracene **3**. The author supposed that a treatment of a *p*-anisidine in the presence of DABCO with $TiCl_4$ in toluene, and then addition of tetracenequinone into the reaction mixture resulted in imine compound **4**. And then, the reduction of **4** with hydrazine resulted in amine compound **5**. Finally, compound **3** was prepared from **5** and 4-iodoanisole by the Buchward-Hartwig cross-coupling reaction[8,9].

4.3.2 Molecular and electronic structures in the neutral state

To gain insight into the electronic structures of compounds **1**–**3** in their neutral states, the quantum chemical calculations were conducted for **1**–**3** at the B3LYP/6-31G* level of density functional theory (DFT). The optimized geometrical parameters characterizing the molecular structures of **1**, **2**, and **3** are shown in Figure 4.2. Figure 4.2 shows the Kohn-Sham MO energy diagrams in the frontier orbital region for the optimized **1**, **2**, and **3**. As has been pointed out in the case of compound Bis(dianisylamino)anthracene,[2] the HOMO and the energetically neighboring occupied orbitals can be roughly classified into (i) amine-localized, (ii) anthrylene-localized, and (iii) delocalized molecular orbitals according to their relative distributions on the molecular structure, and there exist significant differences in energetic ordering of the above-mentioned three kinds of orbitals for **1**, **2** and **3**. As will be described later, the relative orderings of these occupied orbitals play a crucial role in the structural changes observed in the oxidized states of **1**–**3**.

In the fully *N*-methylated 5,12-diaminotetracene **1**, both the HOMO and LUMO are

localized on the tetracene moiety, thus corresponding to the HOMO and LUMO of tetracene itself, and a pair of nearly degenerate amine-localized molecular orbitals, HOMO-1 and HOMO-2, which are formed by in-phase and out-of-phase combinations of nitrogen-centered 2p AOs on two amino groups, are energetically lower than the tetracene-localized HOMO (Figure 4.2a). On the other hand, in the partially *N*-methylated tetracene **2**, in-phase and out-of-phase orbital interactions between the HOMO of tetracene itself and the two nitrogen-centered 2p AOs lead to the HOMO and HOMO-2 of delocalized type, while the LUMO is regarded as the tetracene-localized one (Figure 4.2b). Despite of the delocalized character, the HOMO of **2** markedly retains the shape of the tetracene HOMO. In contrast to compounds **1** and **2**, the HOMO and HOMO-1 of **3** are of amine-localized character, although the HOMO is still, to some extent, smeared out over the entire molecule (Figure 4.2c). The DFT calculations demonstrate that these differences arise from changes in both the shape and the ordering of the HOMO and the energetically neighboring occupied orbitals due to different orbital interactions between the tetracene moiety and the substituted amino groups with different *N*-substituents.

The observed lowest energy bands for **1**–**3** were confirmed by TD-DFT calculations for **1**, **2**, and **3**. Calculated vertical excitation energies and oscillator strengths are drawn in Figure 4.2. The first excitation corresponds to the excitation to the first singlet excited state ($S_0 \rightarrow S_1$), and the $S_0 \rightarrow S_1$ electronic transition is mainly described by the one-electron excitation from the HOMO to the tetracene-localized LUMO (Figure 4.2).

(a)

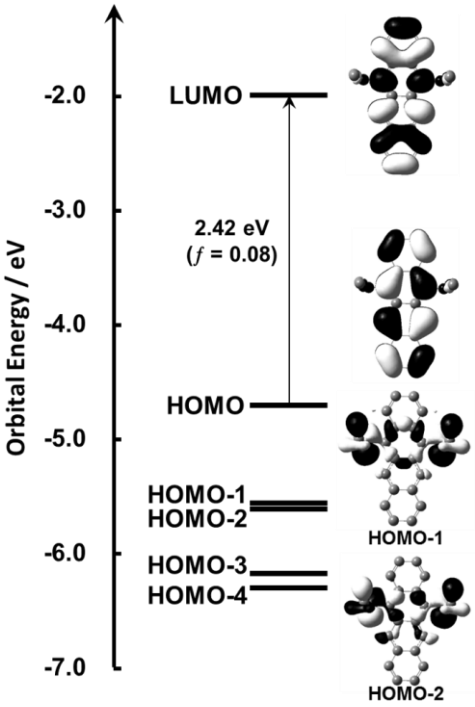
Orbital Energy / eV
-2.0
-3.0
-4.0
-5.0
-6.0
-7.0
LUMO
2.42 eV
(f = 0.08)
HOMO
HOMO-1
HOMO-2
HOMO-3
HOMO-4
HOMO-1
HOMO-2

(b)

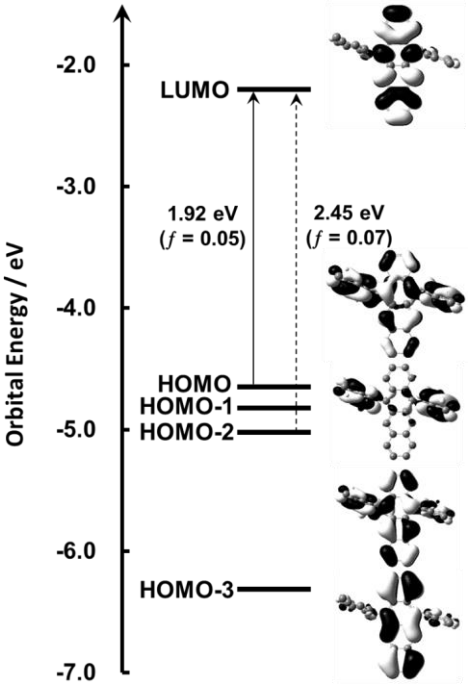
Orbital Energy / eV
-2.0
-3.0
-4.0
-5.0
-6.0
-7.0
LUMO
1.92 eV
(f = 0.05)
2.45 eV
(f = 0.07)
HOMO
HOMO-1
HOMO-2
HOMO-3

(c)

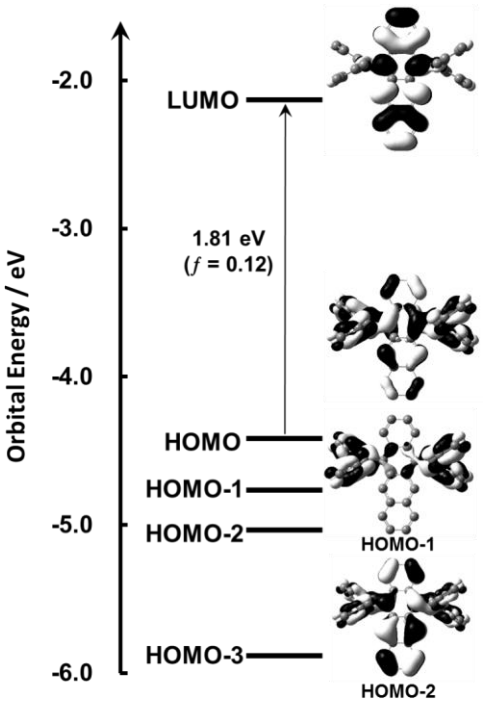

Figure 4.2. Schematic drawing the frontier Kohn-Sham orbitals for (a) **1**, (b) **2**, and (c) **3** at the B3LYP/6-31G* level theory.

4.3.3 Molecular and electronic structures in the oxidized state

Prior to discussion on the oxidized states of compounds **1**–**3**, their redox properties are organized on the basis of cyclic voltammetry measurements. The voltammograms obtained for **1**–**3** in CH_2Cl_2 are depicted in Figure 4.3. It should be noted here that the observed voltammogarms for **1** and **2** differ considerably from that for **3**. The fully and partially *N*-methylated 5,12-diaminotetracenes **1** and **2** exhibited a single oxidation peak [–0.37 and +0.04 V versus $Fc^{0/+}$ for **1** and **2**, respectively] and a single reduction peak [–0.72 and –0.38 V versus $Fc^{0/+}$ for **1** and **2**, respectively] on the return sweep with very large anodic/cathodic peak potential separation [ΔE = 0.35 and 0.34 V for **1** and **2**, respectively. These characteristic voltammograms are explainable by two-electron oxidation process which undergoes a considerable structural change between the neutral and dicationic states,[10,11] and thus, it is apparent that compounds **1** and **2** generate deformed dicationic species without an one-electron oxidation process. On the other hand, the fully *N*-anisyl-substituted 5,12-diaminotetracene **3** showed one quasi-reversible oxidation process. A closer inspection by the differential pulse voltammetry (DPV) and the simulation of the observed DPV clarified that the observed voltammogram consists of successive two reversible one-electron oxidations with a very small potential splitting [ΔE = 0.04 V] for the first and second oxidation processes [E_1 = +0.06 and E_2 = +0.10 V versus $Fc^{0/+}$]. The observed differences in the redox behaviors among **1**, **2**, and **3** were reminiscent of the *N*-substituent dependency on the redox properties for 9,10-diaminoanthracene and 6,13-diaminopentacenes.[2,3] What has to be noticed here is that the different redox behavior of **3** is no guarantee of suppression of the structural change of **3** upon oxidation, as has been demonstrated by the case of the fully-*N*-anisyl-substituted 9,10-diaminoanthracene and 6,13-diaminopentacene.[2,3]

Hence the author must check the absorption spectral change of compounds **1**–**3** during oxidation process.

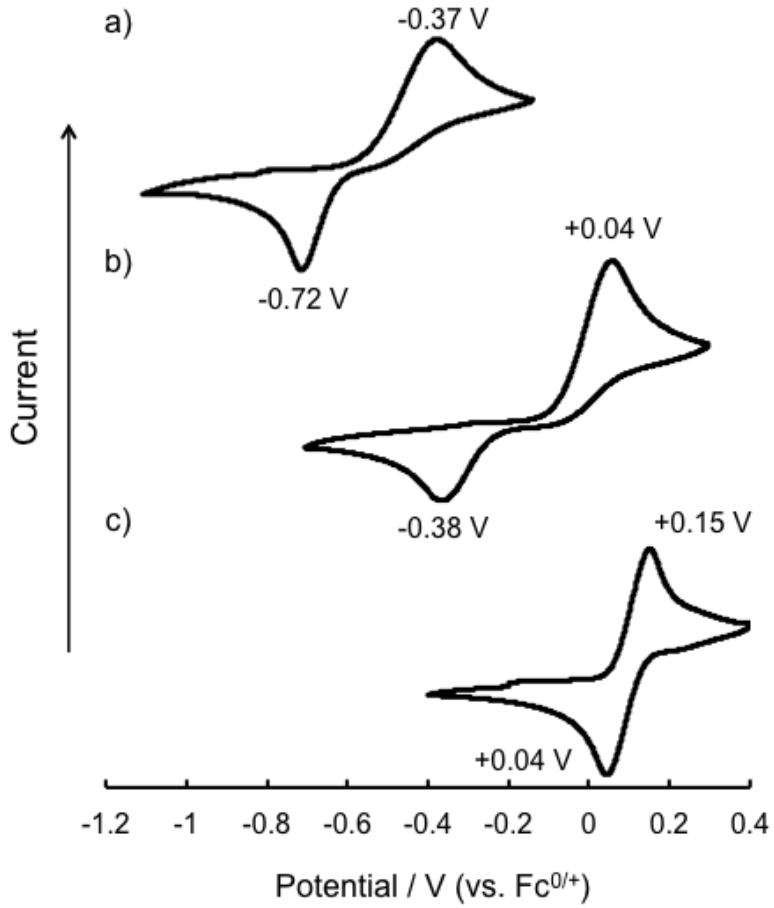

Figure 4.3. Cyclic voltammograms of a) **1**, b) **2**, and c) **3** in CH_2Cl_2 at 298 K, measured with 0.1 M *n*-Bu_4NBF_4 as the supporting electrolyte at a scan rate of 100 mV s^{-1}.

To ascertain the electronic states for the oxidized species of **1**–**3**, we recorded the change in the optical absorption spectra during electrochemical oxidation of **1** and **2**, and chemical oxidation of **3** by $AgSbF_6$ in CH_2Cl_2 (Figure 4.4). For the fully *N*-methylated 5,12-diaminotetracene **1**, the lowest energy band with a vibrational fine structure at 2.50 eV (496 nm), corresponding to the HOMO-LUMO transition localized on the tetracene moiety of **1**, was gradually changed into a new structure-less band at 3.30 eV (376 nm) with an isosbestic point at 2.95 eV (421 nm) during the oxidation process from **1** to $\mathbf{1}^{2+}$ (Figure 4.4a), thus indicating no generation of radical cationic species of **1**. A similar spectral change was also observed for the electrochemical oxidation of the partially *N*-methylated 5,12-diaminotetracene **2** (Figure 4.4b): the lowest energy bands with vibrational fine structure at 2.50 eV (497 nm), corresponding to the HOMO-LUMO transition localized on the tetracene moiety of **2**, were changed into a series of new bands originating from the generation of $\mathbf{2}^{2+}$ at 3.01 eV (412 nm), with an isosbestic points at 2.73 eV (455 nm), bypassing the generation of radical cation $\mathbf{2}^{\bullet+}$. In contrast, the spectral change of **3** upon the electrochemical oxidation clearly exhibited a two-step change, thus indicating the generation of radical cation $\mathbf{3}^{\bullet+}$. In the first oxidation process from **3** to $\mathbf{3}^{\bullet+}$, a lowest energy band newly appeared at 0.69 eV (1811 nm), together with the next lowest vibrational band at 1.15 eV (1075 nm) (Figure 4.4c). The lowest energy band was assigned to a charge-resonance (CR) band originating from the class III or the borderline class III/class II mixed-valence (MV) state[12] of $\mathbf{3}^{\bullet+}$. In fact, the observed CR transition energy was in good agreement with that calculated by TD-DFT for the UB3LYP/6-31G* optimized symmetrical structure of $\mathbf{3}^{\bullet+}$ (0.77 eV) corresponding to the transition from β–HOMO to β–LUMO (Figure 4.4c). The next lowest vibrational band at 1.15 eV was assigned to a tetracene radical cation

band.[13] This band was in good agreement with that calculated by TD-DFT for the UB3LYP/6-31G* optimized symmetrical structure of $\mathbf{3}^{\bullet+}$ (1.29 eV) corresponding to the transition from α–HOMO to α–LUMO. As mentioned below in ESR section, these bands suggest that the spin was delocalized from aminium radical cation into tetracecne moiety. In the second oxidation process from $\mathbf{3}^{\bullet+}$ to $\mathbf{3}^{2+}$, the lowest energy band at 0.69 eV gradually disappeared, whereas the next lowest energy band at 1.61 eV continued to grow up until the complete oxidation into $\mathbf{3}^{2+}$ (Figure 4.4d).

(a)

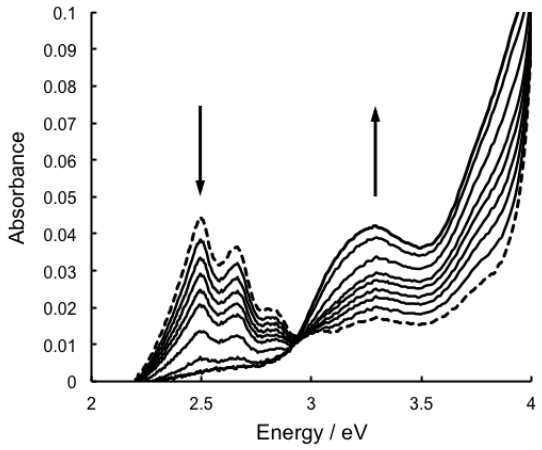

(b)

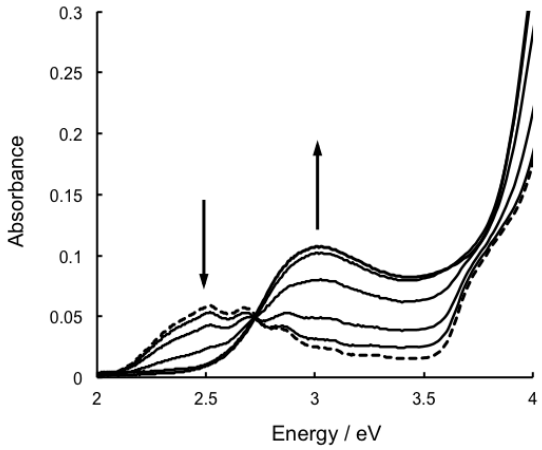

(c)

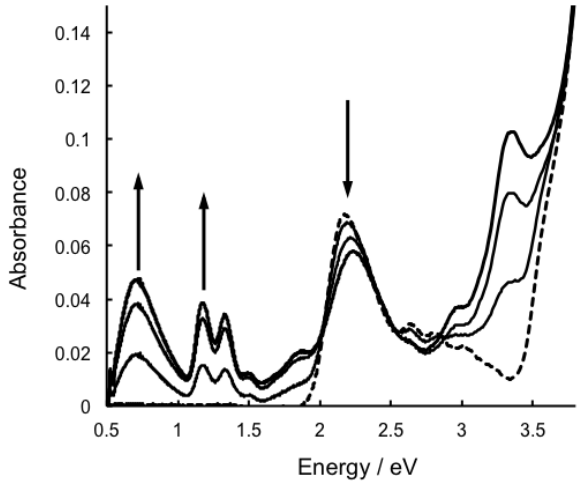

(d)

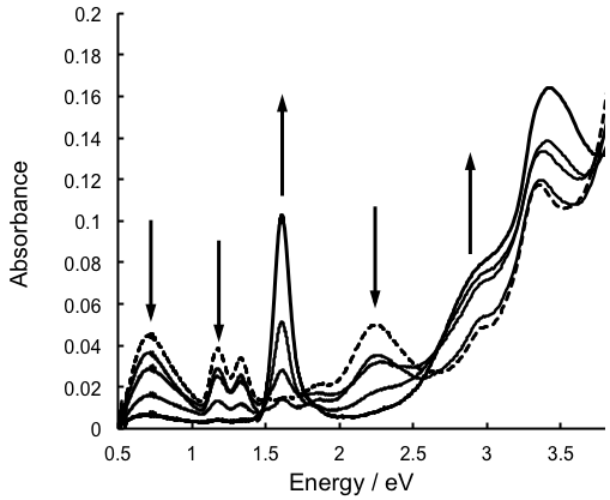

Figure 4.4. UV/Vis-NIR optical absorption spectra of the stepwise electrochemical oxidation (a) from **1** (broken line) to $\mathbf{1}^{2+}$ (bold line) and (b) from **2** (broken line) to $\mathbf{2}^{2+}$ (bold line) with 0.1 M *n*-Bu_4NBF_4, and chemical oxidation by $AgSbF_6$ (c) from **3** (broken line) to $\mathbf{3}^{\bullet+}$ (bold line), and (d) from $\mathbf{3}^{\bullet+}$ (broken line) to $\mathbf{3}^{2+}$ (bold line), in CH_2Cl_2 at 298 K.

To understand these spectroscopic observations for the oxidized states of **1**–**3**, the author carried out DFT calculations. The ground state structures for the oxidized species of **1**–**3** were first optimized. Although the radical cations of **1** and **2** were not observed experimentally, the author can determine theoretically the optimized structures of $\mathbf{1}^{\bullet+}$ and $\mathbf{2}^{\bullet+}$, including that of $\mathbf{3}^{\bullet+}$. As can be seen from Figure 4.5a, for all three compounds, the most energetically stable structure was found to adopt a planar structure with a fully aromatic tetracene moiety. In addition, it was predicted that, for $\mathbf{1}^{\bullet+}$, the butterfly-like structure, in which the central six-membered ring in the tetracene moiety is folded along C5–C12 line, lies 1.40 kcal mol^{-1} above the planar structure. Herein, note that the author was not able to find any local minima corresponding to the butterfly-like structures of both $\mathbf{2}^{\bullet+}$ and $\mathbf{3}^{\bullet+}$. On the other hand, the energetically most stable structure for $\mathbf{3}^{2+}$ takes the planar structure, while those for $\mathbf{1}^{2+}$ and $\mathbf{2}^{2+}$ the butterfly-like structure, in good accordance with the experimental observations (Figure 4.5b). In conjunction with the folding deformation of the tetracene moiety (the bend angles 132.2° and 133.6° for $\mathbf{1}^{2+}$ and $\mathbf{2}^{2+}$, respectively (Figure 4.6a)). On the other hand, the conspicuous geometrical changes are not seen throughout all the oxidized states of **3** (Figure 4.6b), thus indicating a clear difference from the diamagnetic quinoid dication of **TMPD**. More interestingly, the butterfly-like structure were not found for $\mathbf{3}^{2+}$, while the planar structure for $\mathbf{2}^{2+}$ lies 7.9 kcal mol^{-1} above the butterfly-like one. In addition, the author could not find any local minima corresponding to the planar structure of $\mathbf{1}^{2+}$.

The difference in the ground-state structures for $\mathbf{1}^{2+}$, $\mathbf{2}^{2+}$, and $\mathbf{3}^{2+}$ can be seen explicitly in the frontier molecular orbitals (Figure 4.7): in $\mathbf{1}^{2+}$ and $\mathbf{2}^{2+}$ with the butterfly-like structure, the MOs containing both in-phase and out-of-phase combinations of nitrogen-centered 2p AOs on two amino groups become unoccupied

(LUMO and LUMO+1 for $\mathbf{1}^{2+}$ and $\mathbf{2}^{2+}$), whereas the corresponding amine-localized MOs for $\mathbf{3}^{2+}$ with the planar structure are HOMO and LUMO. The structural change associated with the oxidation process of oligoacenes is in general qualitatively explainable by Clar's aromatic π-sextet rule, where the contribution of the Kekulé resonance structure with the largest number of disjoint aromatic π-sextets, that is, benzene-like moieties is decisive of characterization of properties of polycyclic aromatic hydrocarbons (PAHs).[14] Two-electron oxidation of 5,12-diaminotetracene with only one migrating π-sextet leads to loss of a π-bond. This situation can be compensated by the structural change, in which the central six-membered ring is folded along the C5–C12 line, so as to form an extra π-sextet (Figure 4.8).[15] As has already been described on the characteristics of the MOs for neutral species of **1**–**3**, the two-electron oxidation for **1** and **2** with the HOMO of tetracene-localized character inevitably leads to such a structural change according to the Clar's rule. On the other hand, the oxidation for **3** with the HOMO of amine-localized character does not significantly affect the π-conjugated structure of the tetracene moiety itself, so that the oxidized species of **3** retains the planar structure with radical centers localized mainly on the dianisylamino groups. The same can be said of the compounds **1**–**3**.

The observed lowest energy bands for $\mathbf{1}^{2+}$–$\mathbf{3}^{2+}$ were confirmed by TD-DFT calculations by using the optimized geometries for the butterfly-like structured $\mathbf{1}^{2+}$ and $\mathbf{2}^{2+}$, and for the planar structured $\mathbf{3}^{2+}$ (Figure 4.7). The lowest energy transitions for $\mathbf{2}^{2+}$ and $\mathbf{3}^{2+}$ are mainly described by the one-electron excitation from the HOMO to the LUMO [the *N*-phenyl-localized HOMO to the delocalized LUMO for $\mathbf{2}^{2+}$, and the amine-localized HOMO to the amine-localized LUMO for $\mathbf{3}^{2+}$], whereas that for $\mathbf{1}^{2+}$ corresponds to the contribution from tetracene-localized HOMO to the delocalized

LUMO (Figure 4.7).

(a)

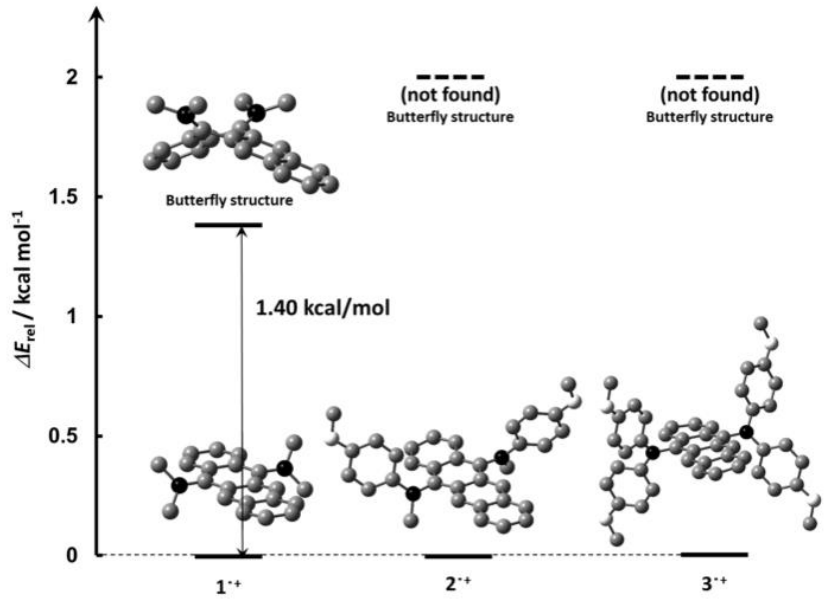

(b)

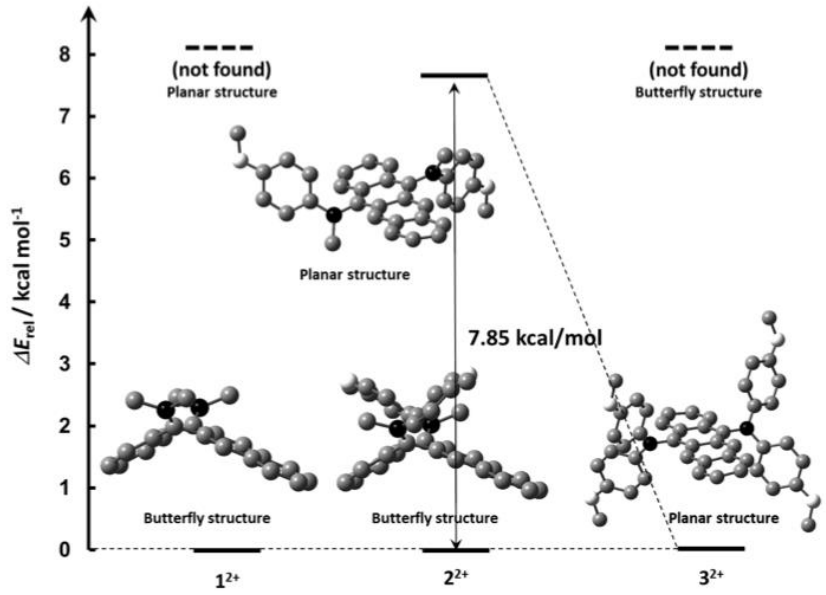

Figure 4.5. Relative energies (ΔE_{rel}) of a) $\mathbf{1}^{\bullet+}$, $\mathbf{2}^{\bullet+}$, and $\mathbf{3}^{\bullet+}$ in relation to planar structure and b) $\mathbf{1}^{2+}$, $\mathbf{2}^{2+}$, and $\mathbf{3}^{2+}$ in relation to butterfly structure.

(a)

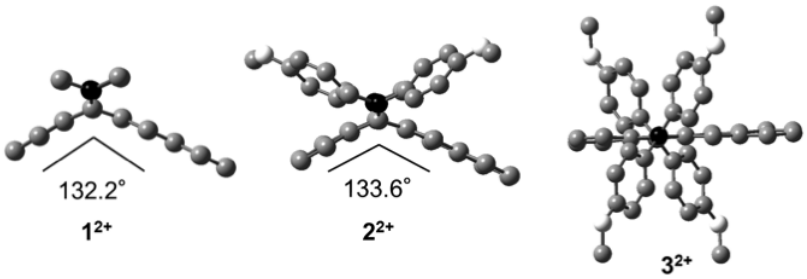

(b)

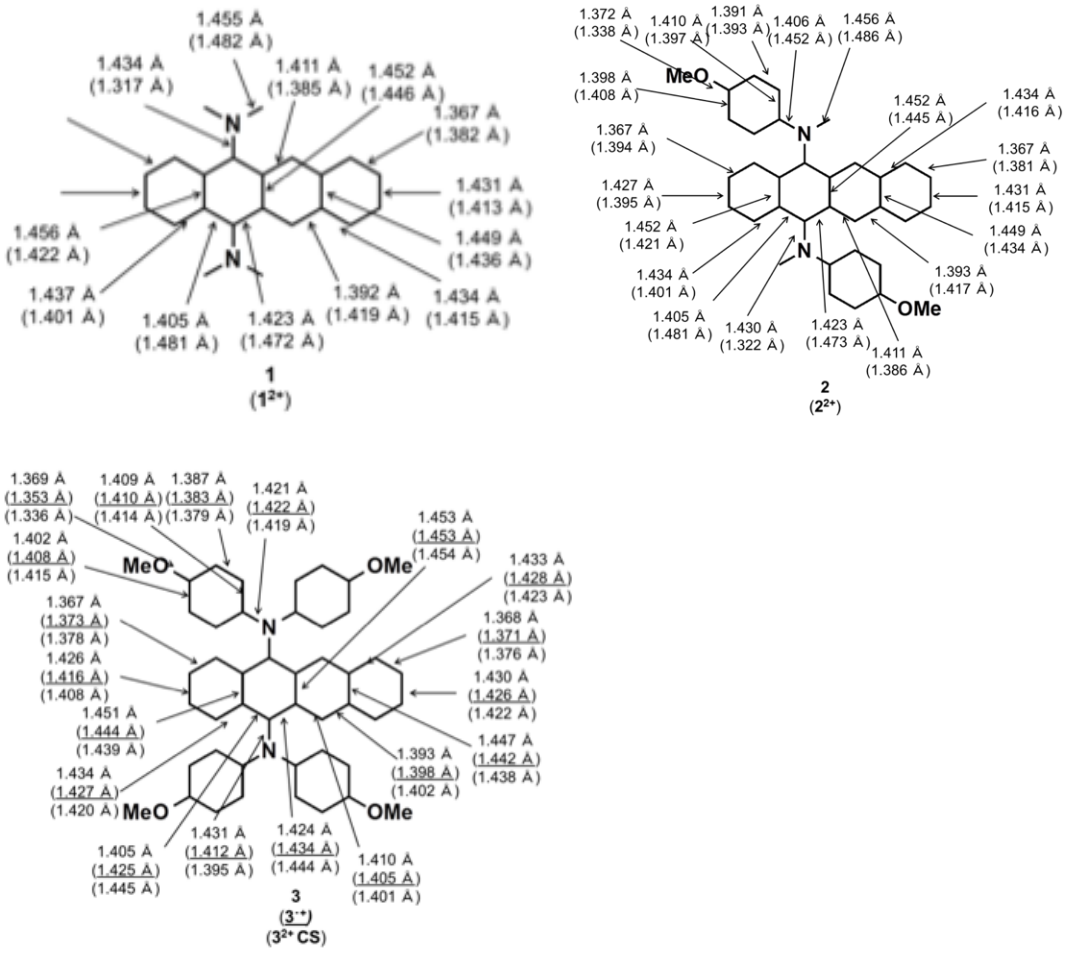

Figure 4.6. Selected geometrical parameters of the B3LYP/6-31G* optimized structures for neutral, radical cation and dication of **1**, **2**, and **3**: (a) the bend angles of the tetracene moiety; (b) the bond lengths.

(a)

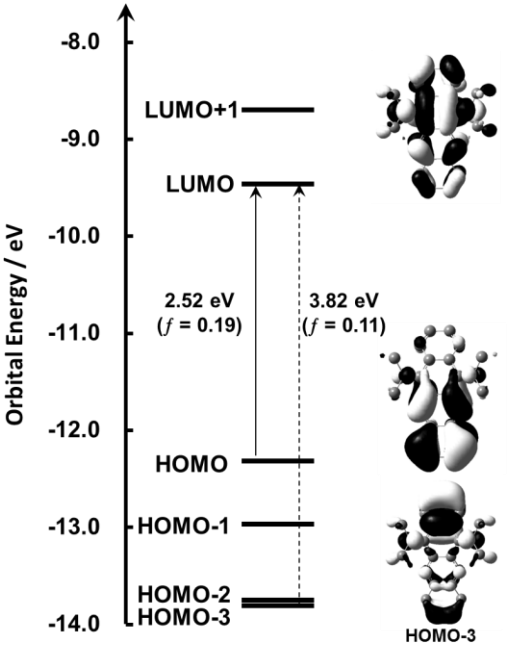
-8.0
-9.0
-10.0
-11.0
-12.0
-13.0
-14.0
Orbital Energy / eV
LUMO+1
LUMO
HOMO
HOMO-1
HOMO-2
HOMO-3
2.52 eV
(f = 0.19)
3.82 eV
(f = 0.11)
HOMO-3

(b)

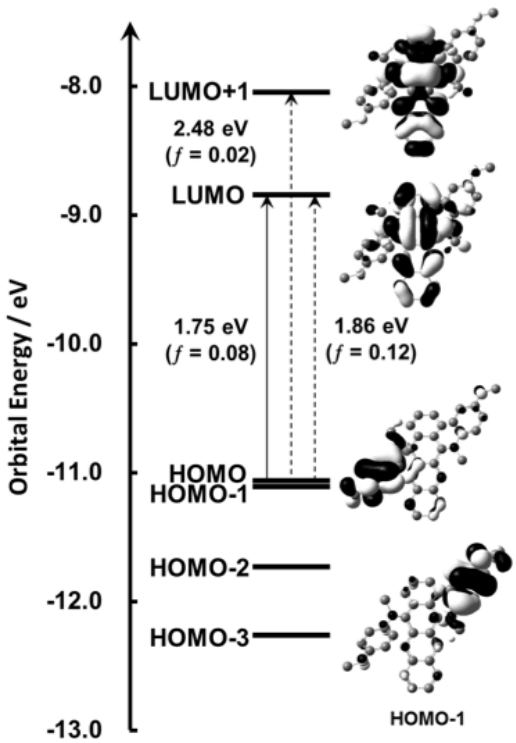
-8.0
-9.0
-10.0
-11.0
-12.0
-13.0
Orbital Energy / eV
LUMO+1
LUMO
HOMO
HOMO-1
HOMO-2
HOMO-3
2.48 eV
(f = 0.02)
1.75 eV
(f = 0.08)
1.86 eV
(f = 0.12)
HOMO-1

(c)

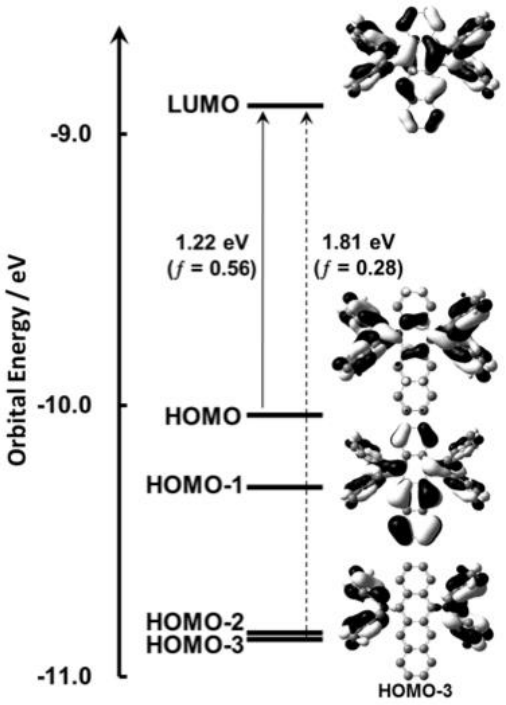

Figure 4.7. Frontier Kohn-Sham orbital energy levels for the ground state of (a) $\mathbf{1}^{2+}$, (b) $\mathbf{2}^{2+}$, and (c) $\mathbf{3}^{2+}$ at the B3LYP/6-31G* level of theory. The solid and broken arrows represent the major contributions related to the lowest and next lowest energy optical absorption bands observed experimentally for $\mathbf{1}^{2+}$–$\mathbf{3}^{2+}$.

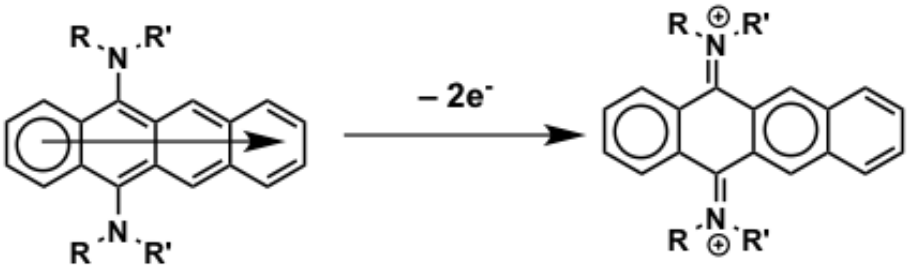

Figure 4.8. 5,12-diaminotetracene with only one migrating aromatic π-sextet. Two-electron oxidation leads to two aromatic π-sextets accompanying a butterfly-like deformation.

4.3.4 ESR Spectroscopy

In accordance with the electrochemical and spectroelectrochemical studies, we could not detect the existence of radical cation for **1** and **2**: when treated by less than one equiv of $AgSbF_6$ in CH_2Cl_2, the resulting oxidized species were found to be ESR-silent. On the other hand, the ESR spectrum of $\mathbf{3}^{\bullet+}$ was successfully observed by the chemical oxidation of **3** with 0.5 equiv of $AgSbF_6$ in CH_2Cl_2 at 293 K (Figure 4.9a). The optimum simulation of the observed five-line spectrum gave the following hyperfine coupling constants: $|a_N|$ = 0.35 mT (2N), $|a_{Ha}|$ = 0.11 mT (2H), $|a_{Hb}|$ = 0.05 mT (2H), $|a_{Hc}|$ = 0.04 mT (8H), $|a_{Hd}|$ = 0.02 mT (2H), $|a_{He}|$ = 0.01 mT (2H), and the contributions from the negligible hydrogen nuclei were incorporated in the line width of the spectral simulation (0.22 mT) (Figure 4.9b), with reference to the DFT-computed spin density distribution for the optimized planar structure of $\mathbf{3}^{\bullet+}$ (Figure 4.9c). This spectral feature provides evidence that the generated charge or spin distribution is extended into the tetracene core, in good accordance with the electrospectrochemistry results of $\mathbf{3}^{\bullet+}$, as described above. In addition, the spectral shape for $\mathbf{3}^{\bullet+}$ remained unchanged in the temperature range from 20 to –80˚C (Figure 4.10), again indicating the possibility of class III or the borderline class III/class II MV state of $\mathbf{3}^{\bullet+}$. Turning finally to the dication of **3**, the solution of $\mathbf{3}^{2+}$ turned out to be ESR-silent, as well as the dication of fully-*N*-anisyl-substituted 9,10-diaminoanthracene.[2]

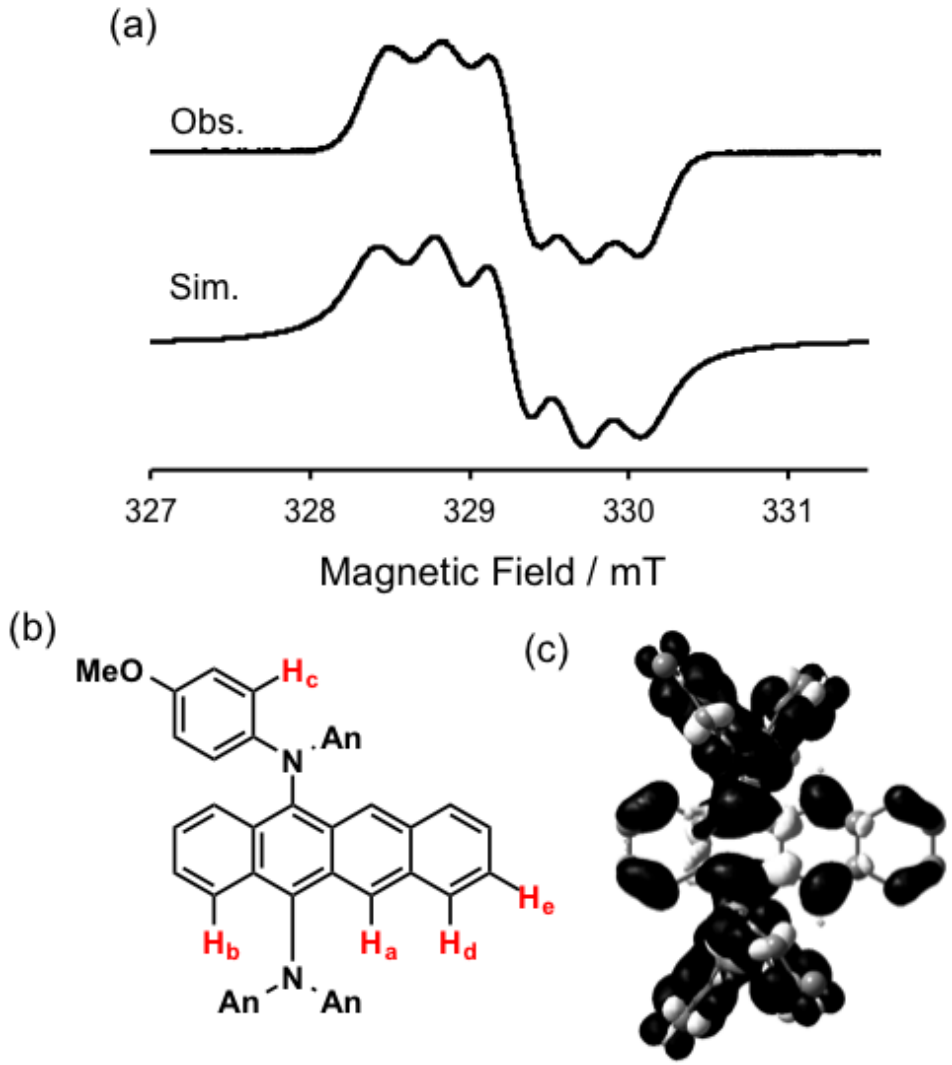

Figure 4.9. a) Observed and simulated X-band ESR spectrum of $\mathbf{3}^{\bullet+}$ recorded in CH_2Cl_2 at 293 K, (b) the designation of hydrogen nuclei by the simulated ESR spectrum, c) the DFT-computed spin density distribution of $\mathbf{3}^{\bullet+}$ (UB3LYP/6-31G*).

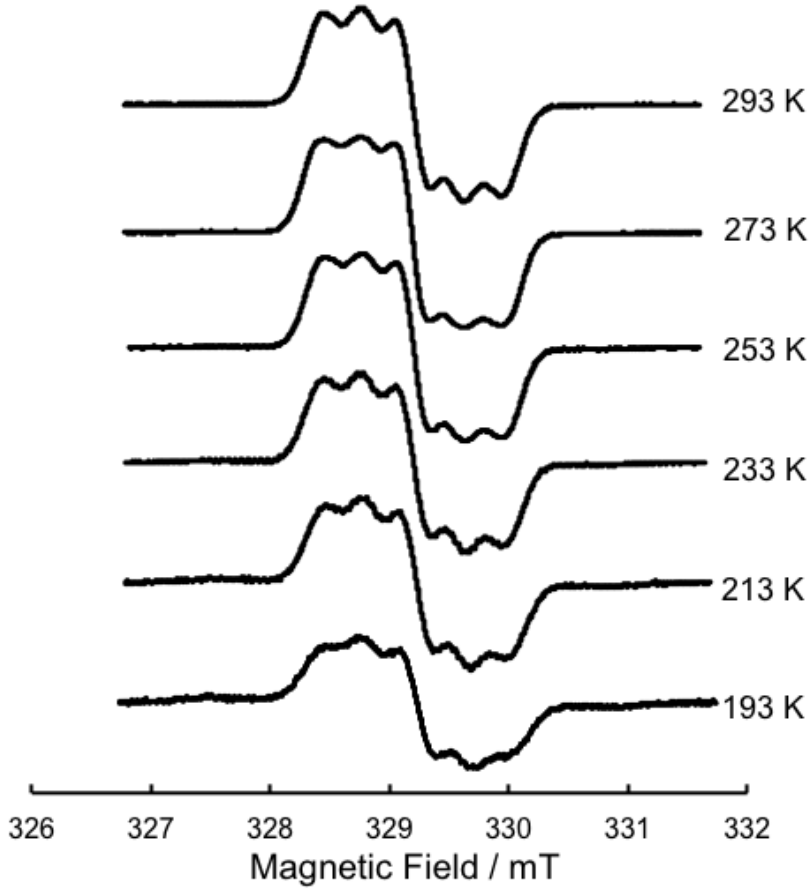

Figure 4.10. Temperature-dependent ESR spectra of $\mathbf{3}^{\bullet+}$ recorded in CH_2Cl_2.

4.3.5 Photophysical Properties

9,10-Bis(diphenylamino)anthracene exhibited bright fluorescence in solution from charge transfer state between diphenylamine and anthracene.[16,17,18] Furthermore, 9,10-bis(dimethylamino)anthracene did not exhibit fluorescence in solution, but it has the solid-state fluorescence behavior.[19] Compared to previous reported AIE luminogens, such as tetraphenylethenes, alkylamino-substituted anthracene exhibited several unique and beneficial features, such as simple structures, bright solid-state fluorescence, tunable fluorescence emission, and large Stokes shifts.[20] Amino substituted hydrocarbon materials are presumed to be promising fluorescence materials. Therefore, fluorescence spectra of 5,12-diaminotetracenes in solution and the solid state were recorded. bis(dimethylamino)tetracene **1** did not exhibit fluorescence in solution. But bis(methylanisylamino)tetarcene **2** exihibited fluorescence in hexane solution (quantum yield Φ_f = 0.24) and bis(dianisylamino)tetracene **3** exihibited fluorescence in hexane and toluene solution (quantum yield Φ_f = 0.91 in hexane and Φ_f = 0.36 in toluene). Moreover, **3** exhibited fluorescence in 2-MeTHF solution at 77 K (quantum yield Φ_f = 0.51). These results revealed that **2** and **3** has charge transfer transition between diphenylamine and tetracene in nonpolar solvents. Compound **1**-**3** have no solid-state fluorescence. Diaminotetracene derivatives were not AIE luminogens.

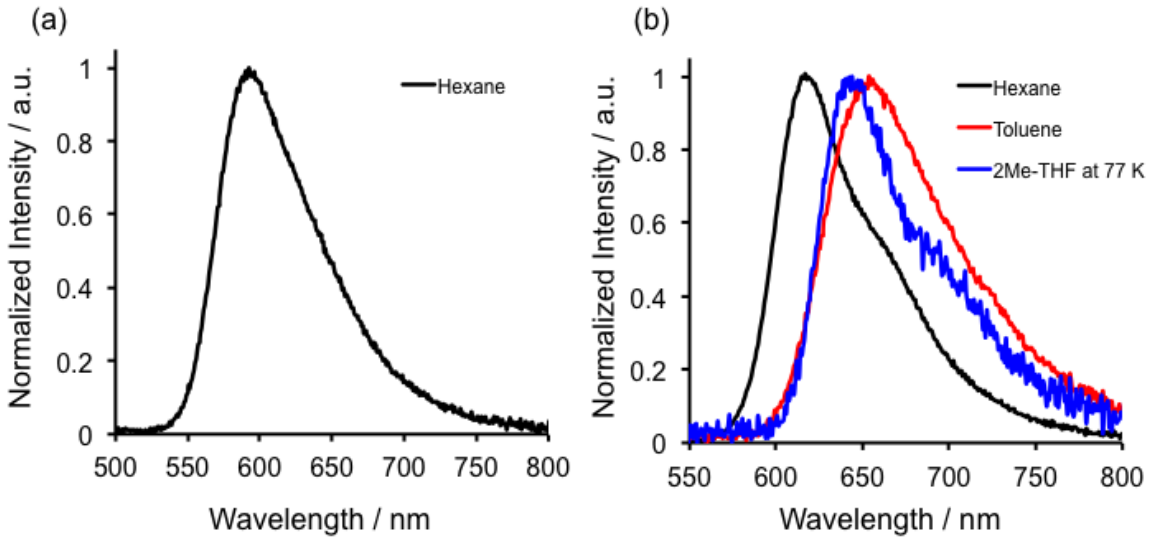

Figure 4.11. Emission spectra of (a) **2** and (b) **3** in various solvents.

(a) (b) (c) (d)

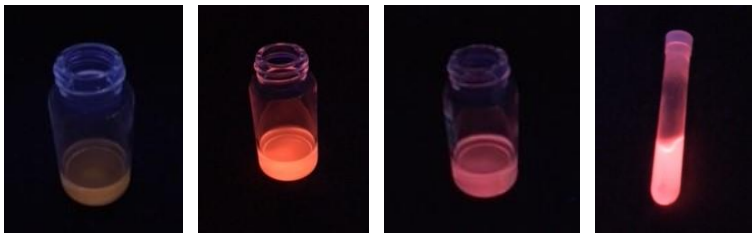

Figure 4.12. Photographs of (a) **2** in hexane, (b) **3** in hexane, (c) **3** in toluene, and (d) **3** in 2-MeTHF at 77 K with UV irradiation at 365 nm.

4.4 Conclusion

In conclusion, the author has shown that the influence of *N*-substituents on the electronic states for the neutral and oxidized species of 5,12-diaminotetracenes. In accordance with an increase in the number of *N*-anisyl-substituents, the frontier MOs of 5,12-diaminotetracenes changed from the tetracene-localized type to the amine-localized type. This tendency finally determines whether the significant structural change into the butterfly-like structure takes place in their oxidized species. The fully and partially *N*-alkylated 5,12-diaminotetracens **1** and **2** underwent the folding structural change along C5–C12 line in their dicationic state bypassing the generation of radical cation. In contrast, the fully *N*-anisyl-substituted 5,12-diaminotetracene **3** exhibited two-stage redox property with a very small oxidation potential splitting, indicating no significant structural changes throughout all the oxidation processes. The ESR measurements demonstrated that the radical cation of **3** is classified into the class III or the borderline class III/class II mixed-valence state, thus retaining planarity of the tetracene moiety. Moreover, **2** and **3** exhibited fluorescence in nonpolar solvents from charge transfer transition between diphenylamine and tetracene.

4.5 References

[1] K. Deuchert, S. Hünig, *Angew. Chem. Int. Ed.* **1978**, *17*, 875-886.

[2] M. Uebe, T. Kato, K. Tanaka, A. Ito, *Chem. Eur. J.* **2016**, *22*, 18923-18931.

[3] A. Ito, M. Uebe, K. Takahashi, H.Ishikawa, D. Sakamaki, H. Sato, T. Matsumoto, K. Tanaka, *Chem. Eur. J.* **2016**, *22*, 2165-2170.

[4] K. Ragavachari, *Theor. Chem. Acc*. **2000**, *103*, 361-363 and references cited therein.

[5] A. Dreuw, M. Head-Gordon, *Chem. Rev.* **2005**, *105*, 4009-4037.

[6] W. J. Hehre, L. Radom, P.v. R. Schleyer, J. A. Pople, *Ab Initio Molecular Orbital Theory*, Wiley, New York, **1986**.

[7] M. J. Frisch, *et al*., Gaussian 09 (Revision D.01), Gaussian, Inc., Wallingford CT, **2013**.

[8] D. S. Surry, S. L. Buchward, *Angew. Chem. Int. Ed.* **2008**, *47*, 6338-6361.

[9] a) J. F. Hartwig, *Nature* **2008**, *455*, 314-322; b) J. F. Hartwig, *Acc. Chem. Res.* **2008**, *41*, 1534-1544.

[10] K. Hu, D. H. Evans, *J. Electroanal. Chem.* **1997**, *423*, 29-35.

[11] a) N. E. Gruhn, N. A. Macias-Ruvalcaba, D. H. Evans, *J. Phys. Chem. A.* **2006**, *110*, 5650-5655; b) N. A. Macias-Ruvalcaba, D. H. Evans, *Chem. Eur. J.* **2007**, *13*, 4386-4395.

[12] a) J. Hankache. O. S. Wenger, *Chem. Rev.* **2011**, *111*, 5138-5178; b) A. Heckman, C. Lambert, *Angew. Chem. Int. Ed.* **2012**, *51*, 326-392.

[13] M. Uebe, K. Kawashima, K. Takahashi, A. Ito, *Chem Eur. J.* **2017**, *23*, 278-281.

[14] E. Clar, *The Aromatic Sextet*, Wiley, New York, **1972**.

[15] M. Solá, *Front. Chem.* **2013**, *1*, 22.

[16] Y. H. Yu, C. H. Hung, J. M. Yeh, P. T. Huang, *Org. Electron.* **2011**, *12*, 694-702.

[17] M. X. Yu, J. P. Duan, C. H. Lin, C. H. Cheng, Y. T. Tao, *Chem. Mater.* **2002**, *14*, 2958-3963.

[18] S. Sasaki, K. Hattori, K. Igawa, G. Konishi, *J. Phys. Chem. A* **2015**, *119*, 4898-4906.

[19] S. Sasaki, S. Suzuki, W. M. C. Sameera, K. Igawa, K. Morokuma, G. Konishi, *J. Am. Chem. Soc.* **2016**, *138*, 8194-8206.

[20] S. Sasaki, K. Igawa, G. Konishi, *J. Mater Chem. C* **2015**, *3*, 5940-5950.

Chapter 5

Synthesis and Characterization of 6,13-Diamino-Substituted Pentacenes

5.1 Introduction

Two-stage Wurster-type redox system is considered as one of the well-characterized multi-stage organic redox systems.[1] *Para*-phenylenediamines (**PD**), the typical examples of the two-stage Wurster-type, are electron-rich compounds, and thus can be readily converted into the stable semiquinone radical cation and the stable quinone dication by successive one-electron oxidations (Scheme 5.1a). As a "gedanken" experiment, it is interesting to speculate what would happen to the redox process if we assume that benzene ring as a cyclic π-system between two amino redox-active groups in **PD** is extended laterally by *cata*-fused benzene rings (Scheme 5.1b). In this line, 9,10-diaminoanthracenes have already been prepared, and their electronic properties including electrochemical properties have been partly examined.[2] When it comes to 6,13-diaminopentacenes, however, there are no noticeable reports not only on the

electronic properties but also on the synthesis.

From another point of view, pentacene has attracted growing interest as benchmark semiconductive materials for organic thin film transistors,[3] and to improve its poor solubility in common organic solvents and its chemical instability in solution when exposed to light and air, various kinds of functionalized pentacenes have been reported so far.[4] The author reports here on the synthesis of 6,13-diaminosubstituted pentacenes **1** as a new class of redox-active pentacene derivatives and their electronic properties (Scheme5.2).

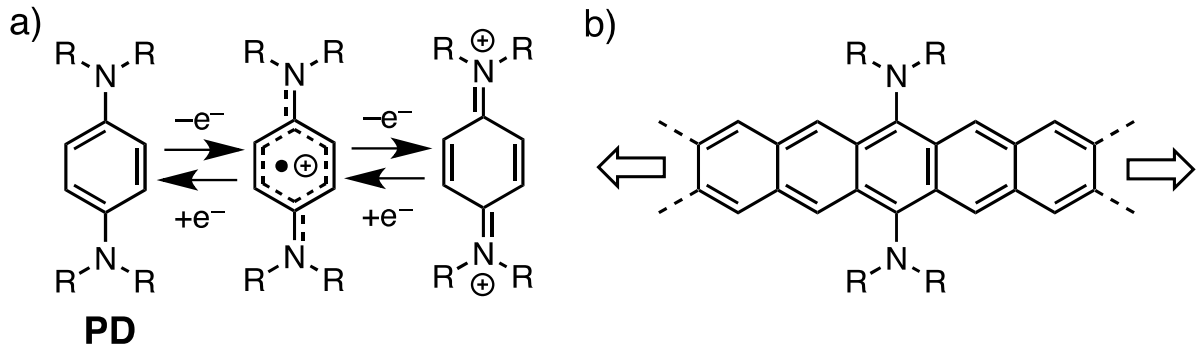

Scheme 5.1. a) *Para*-phenylenediamine (**PD**) as a typical example of the two-stage Wurster-type redox system, and b) hypothetical extension of the benzene moiety by *cata*-fused benzene rings.

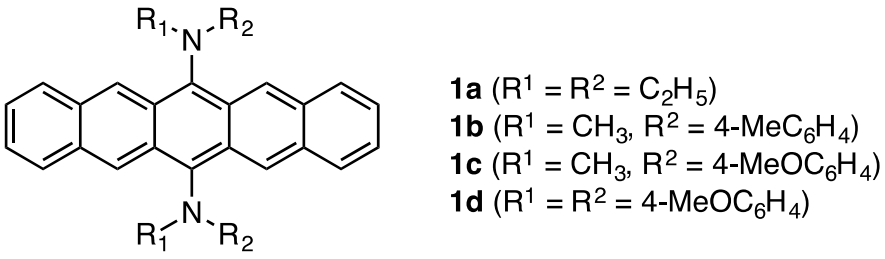

Scheme 5.2. 6,13-Diaminosubstituted pentacenes **1**.

5.2 Experimental Section

5.2.1 Synthesis

All the purchased reagents were of standard quality, and used without further purification. 6,13-dihydroxy-6,13-dihydropentacene was prepared by following the reported method.[4c] All the purchased solvents were purified, dried, and degassed by standard procedures. Column chromatography was usually carried out with silica gel (Kanto Chemical Co., Inc., silica gel 60N, spherical neutral). Elemental analyses were performed by Center for Organic Elemental Microanalysis, Kyoto University. ^{1}H and ^{13}C NMR spectra were measured by a JEOL JNM-AL400 FT-NMR spectrometer. Chemical shifts of NMR spectra are determined relative to internal tetramethylsilane (TMS) standard (δ), and are given in parts per million (ppm). Low resolution (LR) fast-atom-bombardment (FAB) mass spectra (MS) were recorded on a JEOL JMS-HX110A mass spectrometer with *m*-nitrobenzyl alcohol as a matrix. In addition, high resolution (HR) electrospray ionization (ESI) mass spectra were recorded using a mass spectrometer (Thermo Fischer EXACTIVE). UV-Vis-NIR absorption spectra were obtained with a Perkin-Elmer Lambda 950 spectrometer.

Synthesis of 6,13-Bis(*N*,*N*-diethylamino)pentacene (**1a**): A toluene solution (1.0 M) of $TiCl_4$ (2.0 mL, 2.0 mmol) was added dropwise to a stirred suspension of 6,13-pentacenequinone (308.3 mg, 1.0 mmol) and a large excess of Fe powder (4.0 g) in toluene (60 mL) in an ice-cooled flask under an Ar atmosphere, and then the resulting slurry was stirred at 0˚C. After 20 min, an excess of diethylamine (1.32 mL, 13.7 mmol) was added to the stirred slurry at 0˚C. After 10 min, the reaction mixture was shaded from bright light and stirring was continued for 27 to 48 h. Meanwhile, the reaction

mixture gradually turned dark blue. The resulting dark blue slurry was filtered by suction through amino silca gel (NH-DM1020, ~100 μm, Fuji Silysia Chemical Ltd., Japan) using a Büchner funnel, and then the blue layer was eluted with *n*-hexane. Evaporation of the filtrate afforded **1** as a dark blue solid (276.0 mg, 65.6%); m.p. 223˚C dec.; ^{1}H NMR (400 MHz, acetone-d_6) δ 1.16 (t, J = 7.07 Hz, 12H), 3.82 (q, J = 7.32 Hz, 8H), 7.36 (dd, J = 3.17, 6.59 Hz, 4H), 8.06 (dd, J = 3.17, 6.59 Hz, 4H), 9.17 (s, 4H); ^{13}C NMR (100 MHz, acetone-d_6) δ 15.80, 50.80, 125.42, 126.11, 129.70, 131.90, 131.99, 142.62; FAB LRMS (*m*-nitrobenzyl alcohol): *m*/*z* 419 (420 calcd for $C_{30}H_{32}N_2$, $[M]^+$); ESI HRMS: *m*/*z* calcd for $C_{30}H_{33}N_2$: 421.2638 $[M+H]^+$; found 421.2630; Anal calcd for $C_{30}H_{32}N_2$: C, 7.67; H, 85.67; N, 6.66. Found: C, 7.64; H, 85.67; N, 6.61.

Synthesis of 6,13-Bis(*N*,*N*-methyltolylamino)pentacene (**1b**): According to the same procedure as described for the preparation of **1a**, a dark blue reaction mixture was obtained by using *N*-methyl-*p*-toluidine (1.73 mL, 13.7 mmol). The resulting dark blue slurry was filtered by suction through amino silca gel (NH-DM1020, ~100 μm, Fuji Silysia Chemical Ltd., Japan) using a Büchner funnel, and then the blue layer was eluted with 1:1 *n*-hexane/toluene. Evaporation of the filtrate and washing of the residue with *n*-hexane afforded **2** as a dark blue solid (445.5 mg, 86.2%); m.p. > 300˚C; ^{1}H NMR (400 MHz, THF-d_8) δ 2.17, 2.19 (s, (~3 + ~3)H), 3.70, 3.74 (s, (~3 + ~3)H), 6.47-6.55 (m, 4H), 6.88-6.93 (m, 4H), 7.24 (dd, J = 3.17, 6.59 Hz, 4H), 7.84 (dd, J = 3.17, 6.59 Hz, 4H), 8.63 (s, 4H); ^{13}C NMR (100 MHz, THF-d_8) δ 20.44, 20.45, 40.04, 40.10, 113(br), 124.52, 126.08, 126.16, 126.38, 129.44, 130.10, 130.12, 130.37, 130.42, 133.07, 140.30, 149.38; FAB LRMS (*m*-nitrobenzyl alcohol): *m*/*z* 516 (516 calcd for

$C_{38}H_{32}N_2$, $[M]^+$); ESI HRMS: *m*/*z* calcd for $C_{38}H_{32}N_2$: 516.2560 $[M]^+$; found 516.2549.

Synthesis of 6,13-Bis(*N*,*N*-anisylmethylamino)pentacene (**1c**): According to the same procedure as described for the preparation of **1a**, a dark blue reaction mixture was obtained by using *N*-methyl-*p*-anisidine (1.88 g, 13.7 mmol). The resulting dark blue slurry was filtered by suction through amino silca gel (NH-DM1020, ~100 μm, Fuji Silysia Chemical Ltd., Japan) using a Büchner funnel, and then the blue layer was eluted with toluene. Evaporation of the filtrate and washing of the residue with ethanol afforded **3** as a dark blue solid (445.5 mg, 77.0%); m.p. 280-283˚C; ^{1}H NMR (400 MHz, acetone-d_6) δ 3.68 (s, 6H), 3.77, 3.80 (s, (~3 + ~3)H), 6.53-6.61 (m, 4H), 6.72-6.78 (m, 4H), 7.32 (dd, *J* = 3.34, 6.96 Hz, 4H), 7.91 (dd, *J* = 3.25, 6.47 Hz, 4H), 8.71 (s, 4H); ^{13}C NMR (100 MHz, $CDCl_3$) δ 40.08, 55.71, 55.82, 113.05, 114.96, 123.65, 123.79, 125.61, 128.82, 129.20, 129.24, 131.88, 139.36, 145.15, 145.19, 151.32, 151.36; FAB LRMS (*m*-nitrobenzyl alcohol): *m*/*z* 548 (548 calcd for $C_{38}H_{32}N_2O_2$, $[M]^+$); ESI HRMS: *m*/*z* calcd for $C_{38}H_{32}N_2O_2$: 548.2468 $[M]^+$; found 548.2447.

Synthesis of 6,13-dichloropentacene (**DCP**): Under an Ar atmosphere, 0.64 mL (8.7 mmol) of dimethylsulfide was added dropwise to a stirred solution of *N*-chlorosuccinimide (NCS) (0.85 g, 6.37 mmol) in CH_2Cl_2 (40 mL) in an ice-cooled flask equipped with a dropping funnel which was charged with a CH_2Cl_2 solution (30 mL) of 6,13-dihydroxy-6,13-dihydropentacene[4c] (228 mg, 0.73 mmol), and then the resulting solution was stirred at 0˚C. After 10 min, the charged solution in the dropping funnel was gradually added into the CH_2Cl_2 solution containing NCS, and then the reaction mixture was stirred for 19 h after removal of the ice bath. The reaction was

quenched by the addition of water, and then the reaction mixture was washed with brine. The purple-colored organic layer was separated and dried over Na_2SO_4. Evaporation of the solvent left **5** as a greenish purple powder (119 mg, 46.9%); m.p. > 300˚C; ^{1}H NMR (400 MHz, CD_2Cl_2) δ 7.74 (dd, *J* = 3.15, 6.23 Hz, 4H), 8.16 (dd, *J* = 3.17, 6.10 Hz, 4H), 8.94 (s, 4H); ^{13}C NMR (100 MHz, $CDCl_3$) δ 129.49, 129.82, 130.14, 130.63, 135.30, 183.03; ESI HRMS: *m*/*z* calcd for $C_{22}H_{12}Cl_2$: 346.0311 $[M]^+$; found 346.0301.

Synthesis of 6,13-Bis(*N*,*N*-dianisylamino)pentacene (**1d**): A mixture of dianisylamine (0.248 g, 1.08 mmol) and 6,13-dichloropentacene (94 mg, 0.27 mmol), Pd-PEPPSI-IPent[10] (10.2 mg, 0.013 mmol), and NaO*t*-Bu (0.104 g, 1.08 mmol) in toluene (5 mL) was refluxed under an Ar atmosphere for 24 h. The resulting reaction mixture was cooled down to room temperature, and then filtered through Celite. The filtrate was washed with brine, and then the organic layer was separated and dried over Na_2SO_4. After evaporation of the solvent, the crude product was chromatographed on silica gel (*n*-hexane/toluene = 1/1 as eluent) to afford **4** as a dark blue solid (16 mg, 8.1%); m.p. 298-300˚C; ^{1}H NMR (400 MHz, $CDCl_3$) δ 3.72 (s, 12H), 6.74 (d, *J* = 6.23 Hz, 8H), 7.12 (d, *J* = 6.23 Hz, 8H), 7.21 (dd, *J* = 3.26, 6.53 Hz, 4H), 7.72 (dd, *J* = 3.34, 6.71 Hz, 4H), 8.82 (s, 4H); ^{13}C NMR (100 MHz, $CDCl_3$) δ 55.52, 114.72, 121.41, 124.23, 125.59, 128.73, 130.00, 131.91, 137.62, 142.44, 154.02; ESI HRMS: *m*/*z* calcd for $C_{50}H_{40}N_2O_4$: 732.2983 $[M]^+$; found 732.2970.

5.2.2 DFT Calculations

Quantum chemical calculations were performed with using a hybrid Hartree–Fock/density functional theory (HF/DFT) method ((U)B3LYP).[5] Full

geometrical optimization of **1a**-**d** were carried out, and furthermore, their local minimum structures were confirmed by performing subsequent frequency analyses. Excitation energies were examined on the basis of the time-dependent density functional method (TD-DFT)[6] by using the (U)B3LYP/6-31G* optimized structures. All the computations employed the 6-31G* basis set.[7] All these computational approaches are implemented in Gaussian 09 package of ab initio MO calculation.[8]

5.2.3 Electrochemical Measurements

The redox properties were evaluated by cyclic voltammetry (CV) and differential pulse voltammetry (DPV) in CH_2Cl_2 solution at 298 K with 0.1 M tetra-*n*-butylammonium tetrafluoroborate ($TBABF_4$) as supporting electrolyte (scan rate 100 mV s^{-1}) using an ALS/chi Electrochemical Analyzer model 612A. A three-electrode assembly was used, which was equipped with a platinum disk (2 mm^2) and a platinum wire as the working and counter electrodes, respectively, and Ag/0.01 M $AgNO_3$ (acetonitrile) was used as the reference electrode. The redox potential were referenced against a ferrocene/ferrocenium ($Fc^{0/+}$) redox potential measured in the same electrolytic solution. The digital simulations for the observed CV curves were carried out by using the CV simulation software, DigiSim,[9] which was installed in the electrochemical analyzer. The simulations were based on the CV curves obtained with a single scan rate.

5.2.4 Spectroelectrochemical Measurements

Spectroelectrochemical measurements were carried out with a custom-made optically transparent thin-layer electrochemical (OTTLE) cell (light pass length = 1 mm)

equipped with a platinum mesh and a platinum coil as the working and counter electrodes, respectively, and Ag/0.01 M $AgNO_3$ (acetonitrile) was used as the reference electrode. The potential was applied with an ALS/chi Electrochemical Analyzer model 612A.

5.2.5 Crystallography for 1a, 1b and 1d

Data collections were performed on a Rigaku XtaLABmini CCD system with Mo-Kα radiation at 170 and 93 K for compounds **1a** and **1b**, respectively. Data for compound **1d** were corrected by using a Rigaku MM007 High brilliance RA generator/confocal optics and XtaLAB P200 system with Cu-Kα radiation at 100 K. The data were corrected for Lorentz and polarization effects. The structure was solved by using direct methods (SHELX-97[10] for **1a**, SIR-2004[11] for **1b**, and SIR-2011[12] for **1d**), expanded by using Fourier techniques, and refined by full-matrix least-squares of F^2 on the basis of 5475, 3172, and 3430 observed reflections and 289, 181, and 255 variable parameters for **1a**, **1b**, and **1d**, respectively. The non-hydrogen atoms were refined anisotropically and hydrogen atoms were refined by using the riding model. All the calculations were performed by using CrystalStructure crystallographic software package,[13] except for refinement, which was performed by using SHELX-97. CCDC-1420390, -14203991, and -1420392 contain the supplementary crystallographic data for **1a**, **1b**, and **1d**, respectively, for this paper. These data can be obtained free of charge from the Cambridge Crystallographic Data Centre via www.ccdc.cam.ac.uk/data_request/cif.

5.3 Results and Discussion

It is already known that aromatic ketones and aldehydes undergo condensation with amines in the presence of titanium(IV) chloride ($TiCl_4$) to give the corresponding imines.[14] As a related reaction, Koketsu and co-workers have reported a $TiCl_4$-mediated reaction of anthraquinone with diethylamine (Scheme 5.3a).[15] In this reaction, although diethylamine easily reacts with anthraquinone in which the carbonyl groups are strongly activated by $TiCl_4$, the final process to afford 9,10-diaminoanthracene (**2**) must proceed in a reductive manner without any reducing agents. In a first experiment to obtain the 6,13-diaminopentacene, we tried the reaction between 6,13-pentacenequinone (**PQ**) and diethylamine in the presence of $TiCl_4$ by following the same procedure in Scheme 5.2a. The reaction mixture immediately turned deep blue, which was a sign of success, but finally we could only get traces of desired product after hydrolytic work-up. This result strongly suggests that the generated deep-blue intermediate with the pentacene backbone probably decomposes with hydrolysis, and moreover, that the reducing agent is also needed for completion of this reaction. Treatment of a solution of **PQ** in the presence of an excess of Fe powder in toluene with 2 equivalents of $TiCl_4$ at 0˚C and addition of an excess of diethylamine into a reaction mixture resulted in a good yield of the corresponding 6,13-diaminopentacene **1a** (Scheme 5.3b). Under the same conditions, **PQ** reacts with *N*-methyl-*p*-toluidine (or *N*-methyl-*p*-anisidine) to produce the corresponding disubstituted product **1b** (or **1c**). However, unfortunately, attempts to prepare the bis(diarylamino)-substituted compounds from **PQ** and several kinds of diarylamines under the same conditions were not successful.

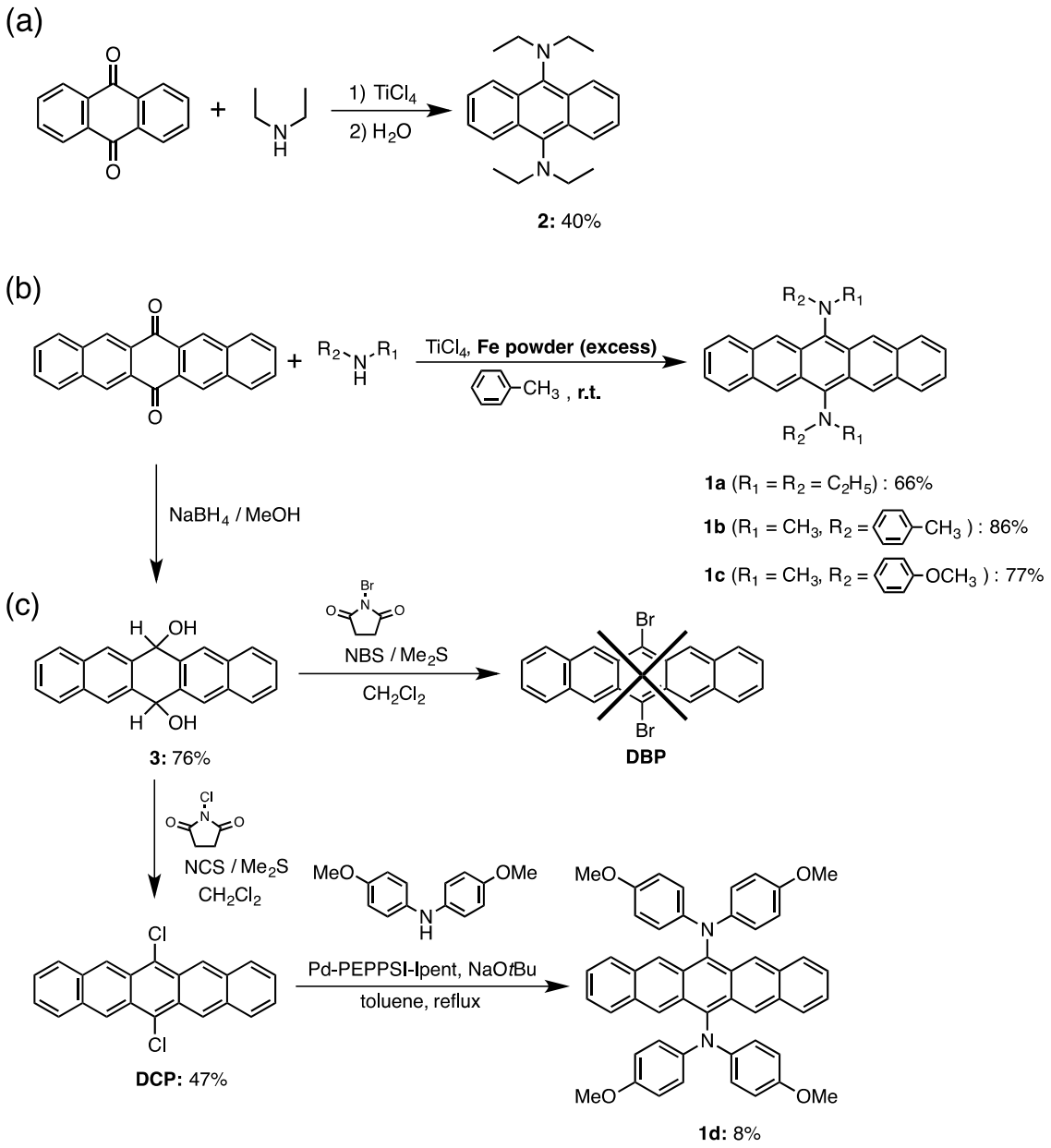

Scheme 5.3. Synthetic routes for (a) **2**, (b) **1a**–**c**, and (c) **1d**.

The author then pursued different synthetic routes for 6,13-bis(diarylamino)-substituted pentacenes. The most promising route was to utilize the Pd-catalyzed amination of 6,13-dihalopentacene with corresponding diarylamines. First of all, the author has started to prepare 6,13-dihalopentacene from **PQ**: **PQ** was

converted into 6,13-dihydroxy-6,13-dihydropentacene (**3**) by reduction with $NaBH_4$ in MeOH at room temperature by following a reported method,[4c] and then, the author supposed that treatment of **3** with NCS or NBS/dimethylsufide in CH_2Cl_2 can lead to the corresponding 6,13-dihalopentacene. As a consequence, this reaction gave 6,13-dichloropentacene[16] (**DCP**) in 47% yield, whereas 6,13-dibromopentacene was not obtained. Finally, 6,13-bis(dianisylamino)substituted pentacene (**1d**) was prepared in 2.4, 4.5, and 8.0 % yield by the cross-coupling reaction with use of $Pd(dba)_2$/Xphos,[17] $Pd(dba)_2$/Qphos,[18] and Pd-PEPPSI-IPent[19] as the catalyst, respectively (Scheme 5.3c).

The X-ray molecular structures of **1a**, **1b**, and **1d** are shown in Figure 5.1.[20] The amino-substituents of **1a** and **1b** were nearly orthogonal to the π-face of pentacene moiety, whereas the dihedral angle between the dianisylamino-substituents and the pentacene plane for **1c** ranged from 69˚ to 75˚. The pyramidal character of the amino groups decreased in the order **1a** > **1b** > **1d**. Noticeable π-interactions between adjacent molecules were not observed for **1a** and **1b**, while the sign of π-π-stacking was seen along the *a*-axis in the crystal of **1d** (Figure 5.2).

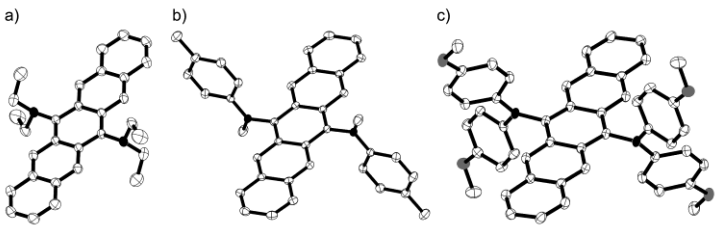

Figure 5.1. ORTEP representation of a) **1a** (one of two crystallographically independent molecules is depicted here.), b) **1b**, and c) **1d** with thermal ellipsoids set at 50% probability level. Hydrogen atoms are omitted for clarity.

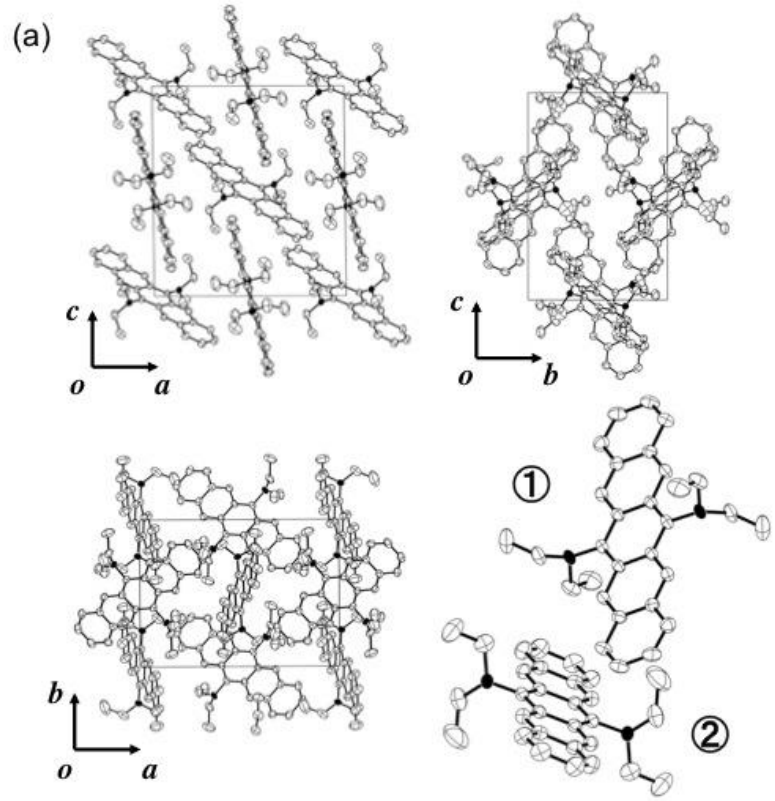
(a)
c
o
a
c
o
b
b
o
a
①
②

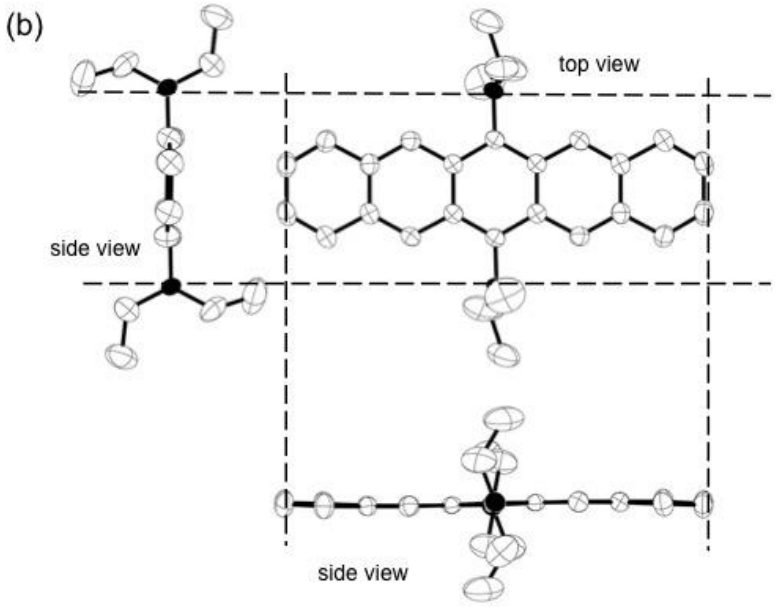
(b)
top view
side view
side view

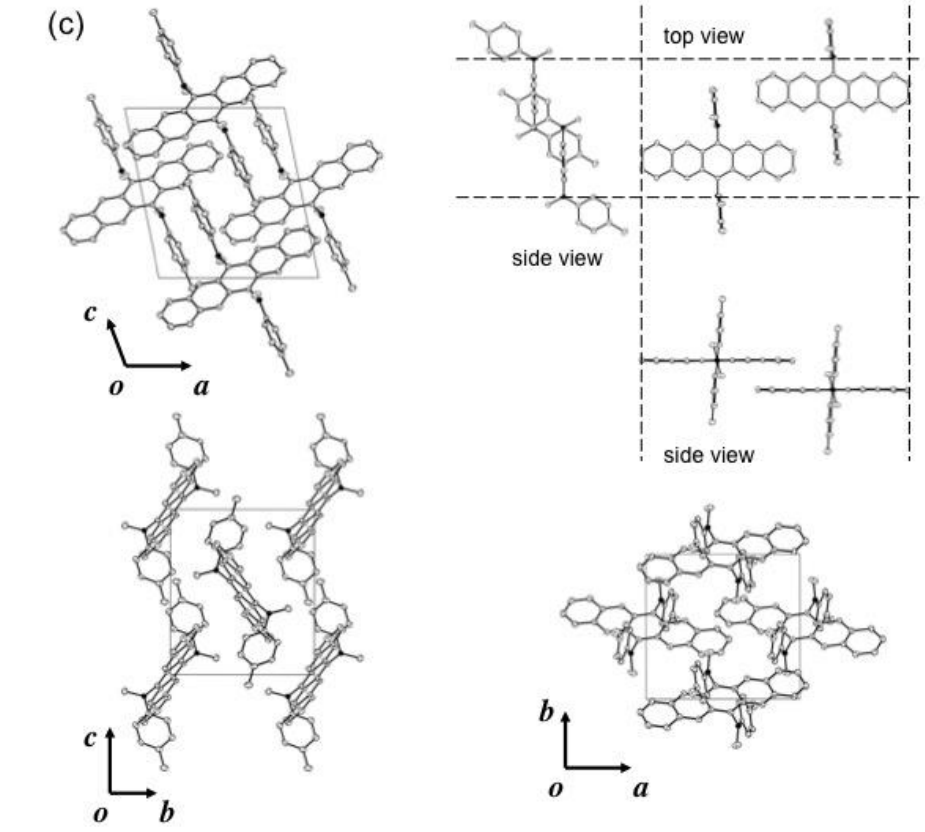
(c)
top view
side view
side view
c
o
a
c
o
b
b
o
a

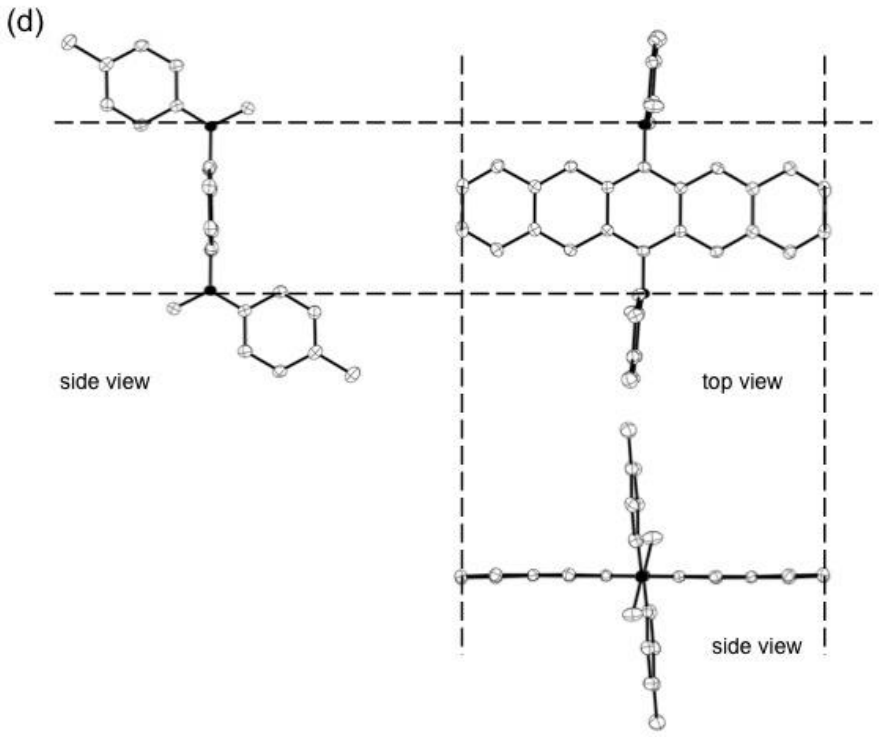
(d)
side view
top view
side view

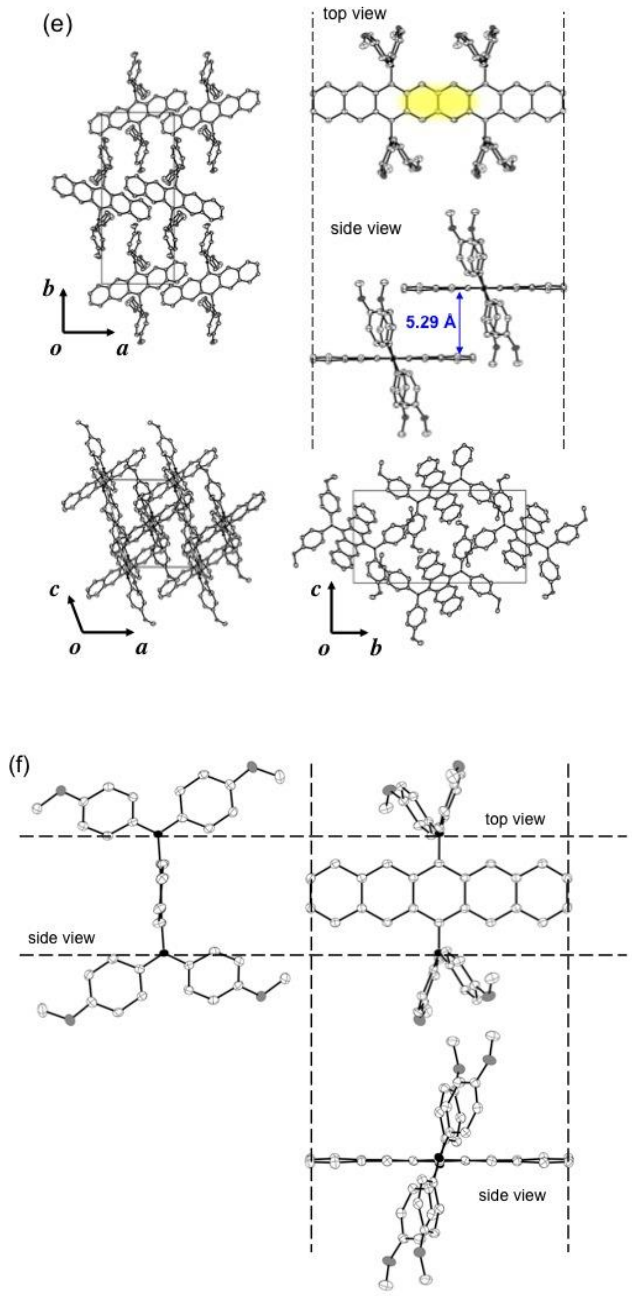

Figure 5.2. (a) Views of the crystal packing for **1a**, and two crystallographically independent molecules ① and ②, (b) moleular structure of **1a**, (c) views of the crystal packing for **1b**, and views of two adjacent molecules, (d) moleular structure of **1b**, (e) views of the crystal packing for **1d**, and views of two adjacent molecules, and (f) moleular structure of **1d**.

The compounds **1a**–**d** were easily dissolved not only in polar organic solvents such as THF and CH_2Cl_2, and $CHCl_3$, but also in nonpolar organic solvents such as *n*-hexane and toluene. In particular, **1a** was freely soluble in almost all the common organic solvents. As shown in Figure 5.3, the absorption spectra of **1a**–**d** in $CHCl_3$ exhibited the so-called p band with the vibrational progression (at λ_{max} larger than 600 nm) and the α band at around 400 nm, which appears typically for pentacene and its derivatives.[21] The bathochromic shift of the structureless p band for **1d** (84 nm as compared with pentacene in *o*-dichlorobenzene) is probably due to the strong donor ability of dianisylamino substituents. The stability of **1a**–**d** in solution was maintained in the air under dark conditions, but **1a** showed a slight degradation as compared to **1b**-**d**. The intensity of absorption spectra of **1a**-**d** in solution, however, displayed a rapid decrease in the air under the UV irradiation at 250 nm (Figure 5.4). As for the hydrolytic resistance of **1a**-**d**, the addition of 1 mM aq. HCl caused a rapid hydrolysis of **1a** into **PQ**, whereas the hydrolytic degradation of **1b**-**d** into **PQ** was not observed. When the stronger acid like trifluoroacetic acid was added, however, **1b**-**d** also decomposed rapidly into **PQ** (Figure 5.5).

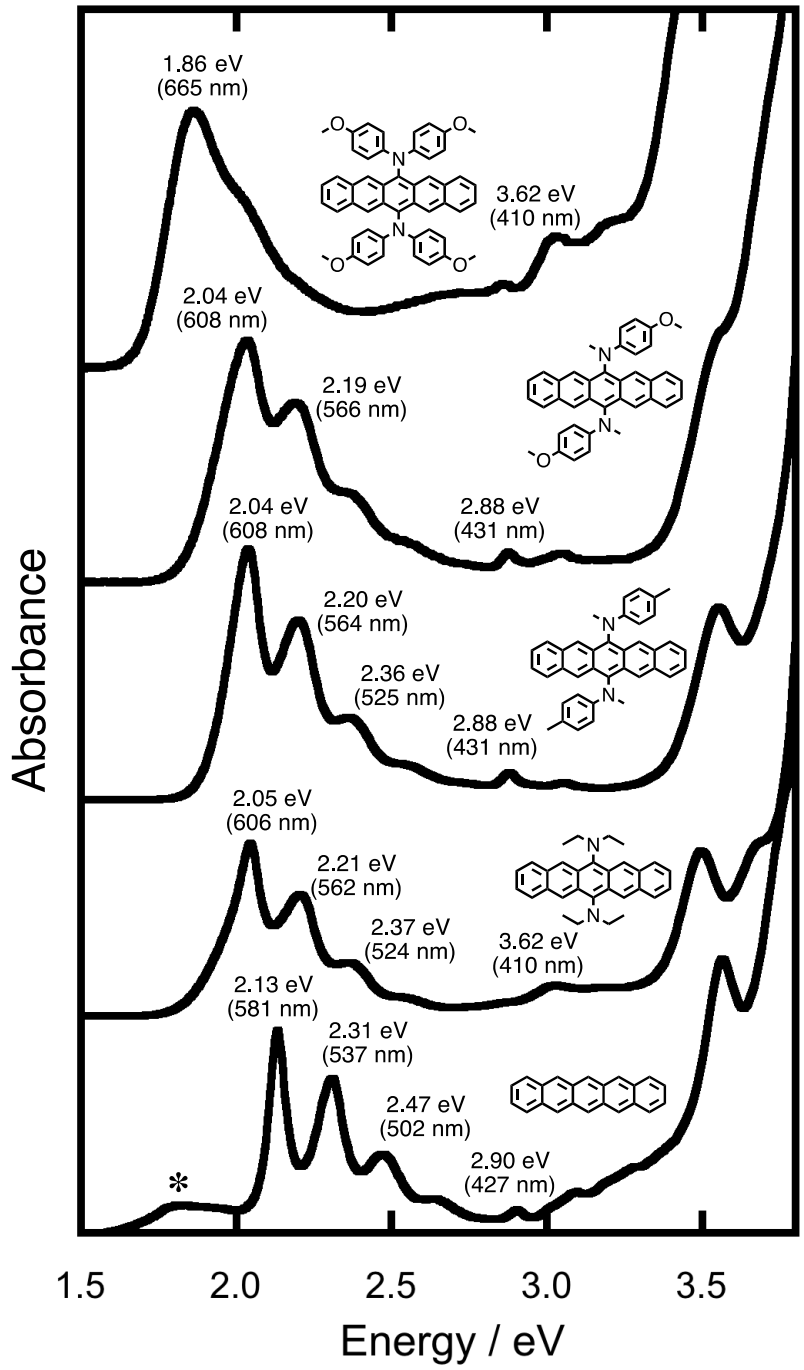

Figure 5.3. Absorption spectra of **1a**–**d** in CH_2Cl_2 at 298 K together with that of pentacene in *o*-dichlorobenzene at 298 K; the observed band marked with an asterisk is due to dispersion of pentacene crystals precipitated in solution.

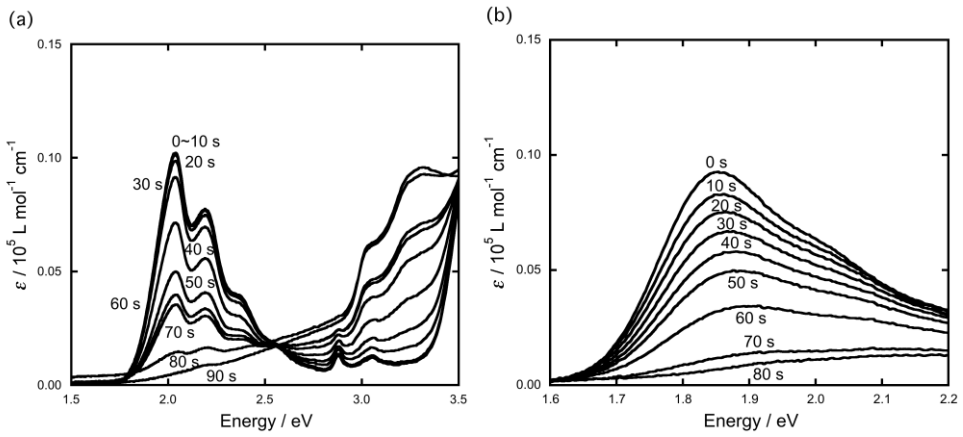

Figure 5.4. Absorption spectral change associated with the photodegradation of a) **1c** and b) **1d** at room temperature under UV irradiation at 250 nm in the saturated air conditions in $CHCl_3$.

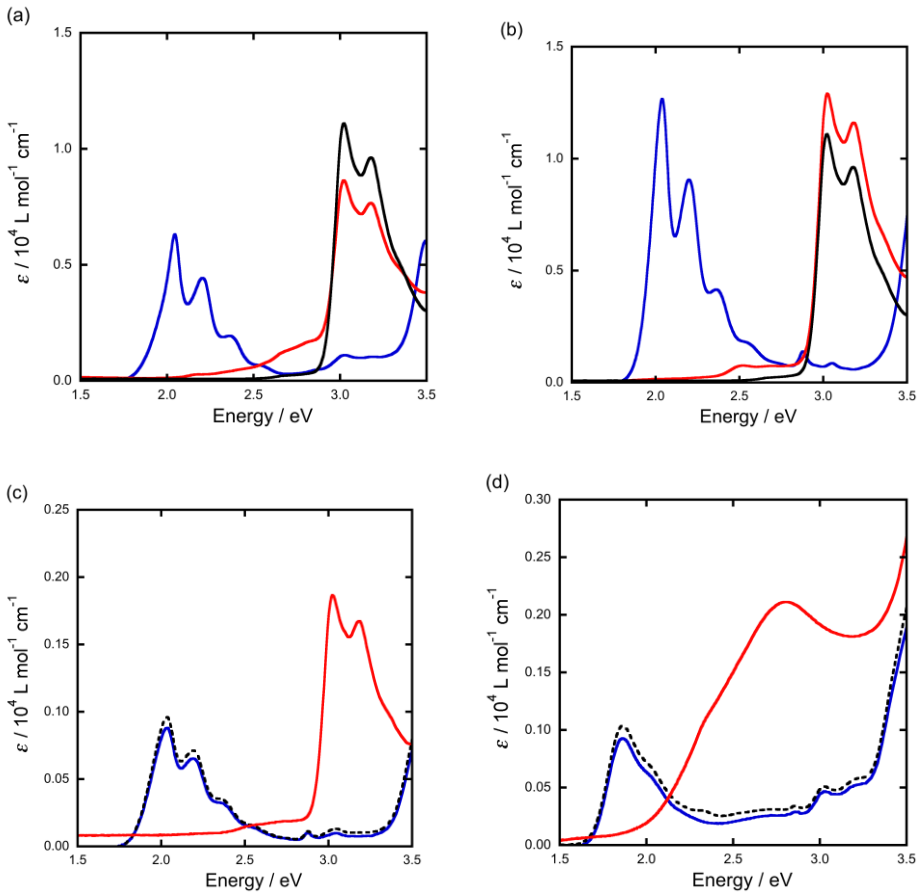

Figure 5.5. Absorption spectra of (a) **1a** and (b) **1b** in $CHCl_3$ before (blue line) and after (red line) addition of trifluoroacetic acid (TFA) together with the spectrum of 6,13-pentacenequinone (**PQ**) in $CHCl_3$, and absorption spectra of (c) **1c** and (d) **1d** in in $CHCl_3$ before (blue line) and after addition of 0.1 M aq. HCl (broken line) and trifluoroacetic acid (TFA) (red line).

To gain insight into the electronic influence on the pentacene moiety by substitution of amino groups, the redox properties of **1a-d** were studied by cyclic voltammetry (Figure 5.6). The voltammograms of **1a-c** exhibited a single oxidation peak (–0.34, +0.02, and –0.11 V vs. $Fc^{0/+}$ for **1a**, **1b**, and **1c**, respectively) and one reduction peak (–0.71, –0.51, and –0.52 V vs. $Fc^{0/+}$ for **1a**, **1b**, and **1c**, respectively) on the return sweep

with a very large anodic/cathodic peak separation (ΔE = 0.37, 0.53, and 0.41 V for **1a**, **1b**, and **1c**, respectively). Such a voltammogram is often encountered for a successive one-electron oxidation processes with inverted oxidation potentials: the first oxidation potential (E_1) being more positive than the second one (E_2), thus leading to a seemingly two-electron oxidation at the same potential, as has been previously observed for 9,10-bis(dimethylamino)anthracene and so on,[2a,22] which undergo a considerable structural change between neutral and dicationic states, leading to a significant inner reorganization energy.[23] From the curve fitting of the observed voltammograms (Figure 5.7),[2a,24] the first and second oxidation potentials (vs $Fc^{0/+}$) were evaluated to be E_1 = –0.38 and E_2 = –0.52 V for **1a**; E_1 = +0.01 and E_2 = –0.32 V for **1b**; E_1 = –0.11 and E_2 = –0.34 V for **1c**, thus indicating an increase the donor ability of pentacene moiety (E_1 = +0.26 V[3a] in hot *o*-dichlorobenzene (150˚C)). The simulated much slower heterogeneous electron transfer rates k_1 and k_2 (8.0×10^{-3} and 2.0×10^{-4} cm s^{-1}, respectively, at the scan rate of 0.1 V s^{-1}) for the first and second oxidation processes of **1a**–**c** strongly suggest the sluggishness of the two-electron transfer. In contrast, for **1d**, a single quasi-reversible two-electron redox wave was observed at an oxidation potential of E_{ox} = –0.05 V (vs $Fc^{0/+}$). In addition, the heterogeneous two-electron transfer rate was estimated to be 1.3×10^{-1} cm s^{-1} at the scan rate of 0.1 V s^{-1}, indicating a relatively fast oxidation process as compared to those of **1a**–**c**. This observation suggested no significant structural change between neutral and dicationic states for **1d**. In conjunction with the electrochemical studies, the author could not find the existence of radical cation for **1a**–**d** when treated with less than one equivalent of the Magic Blue in CH_2Cl_2, by the ESR spectroscopy, and moreover, chemically oxidized dications for **1a**–**d** were found to be ESR-silent in CH_2Cl_2.

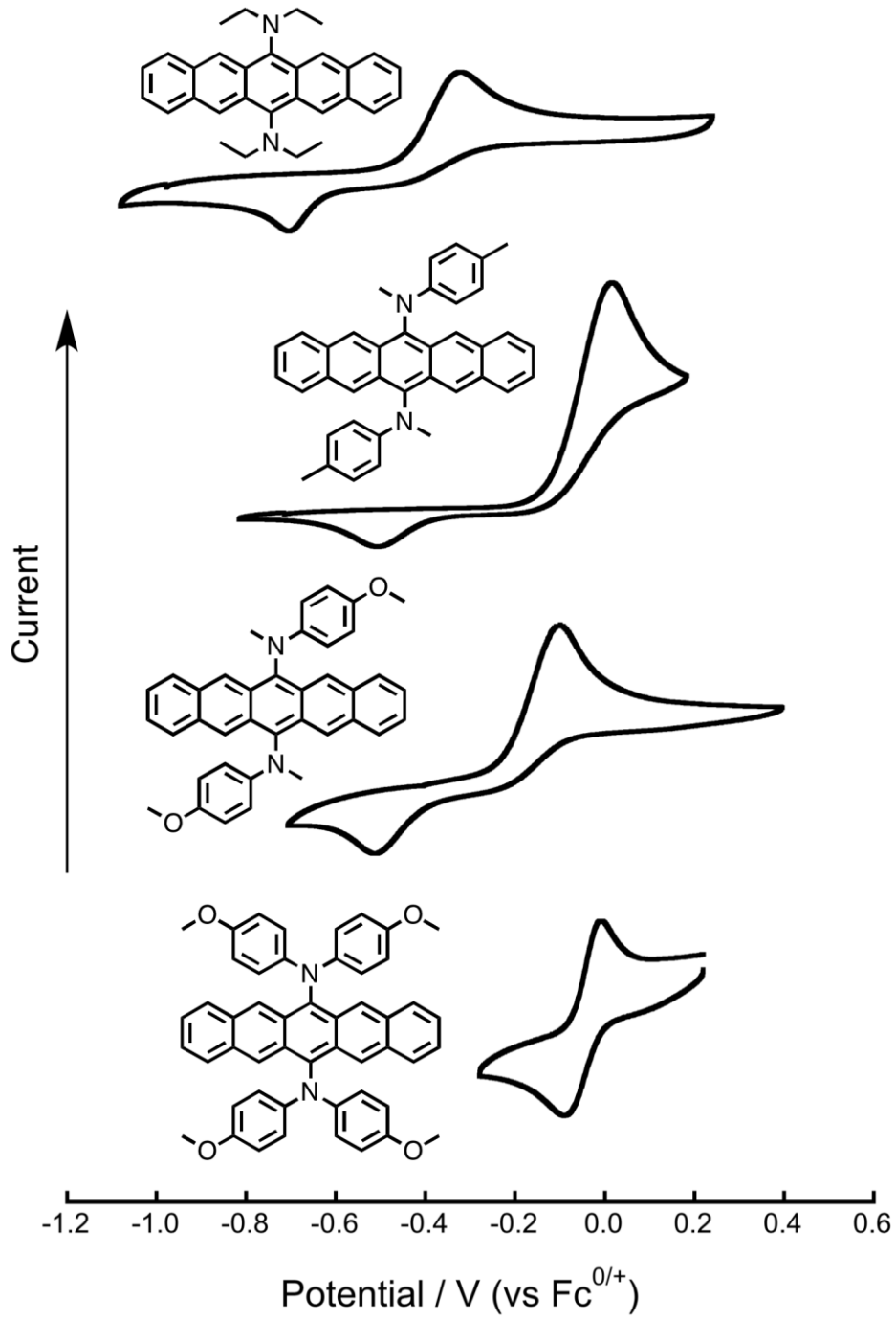

Figure 5.6. Cyclic voltammograms of **1a** in MeCN and **1b**–**d** in CH_2Cl_2 at 298 K, measured with 0.1 M nBu$_4$NBF$_4$ as supporting electrolyte at the scan rate 100 mVs^{-1}.

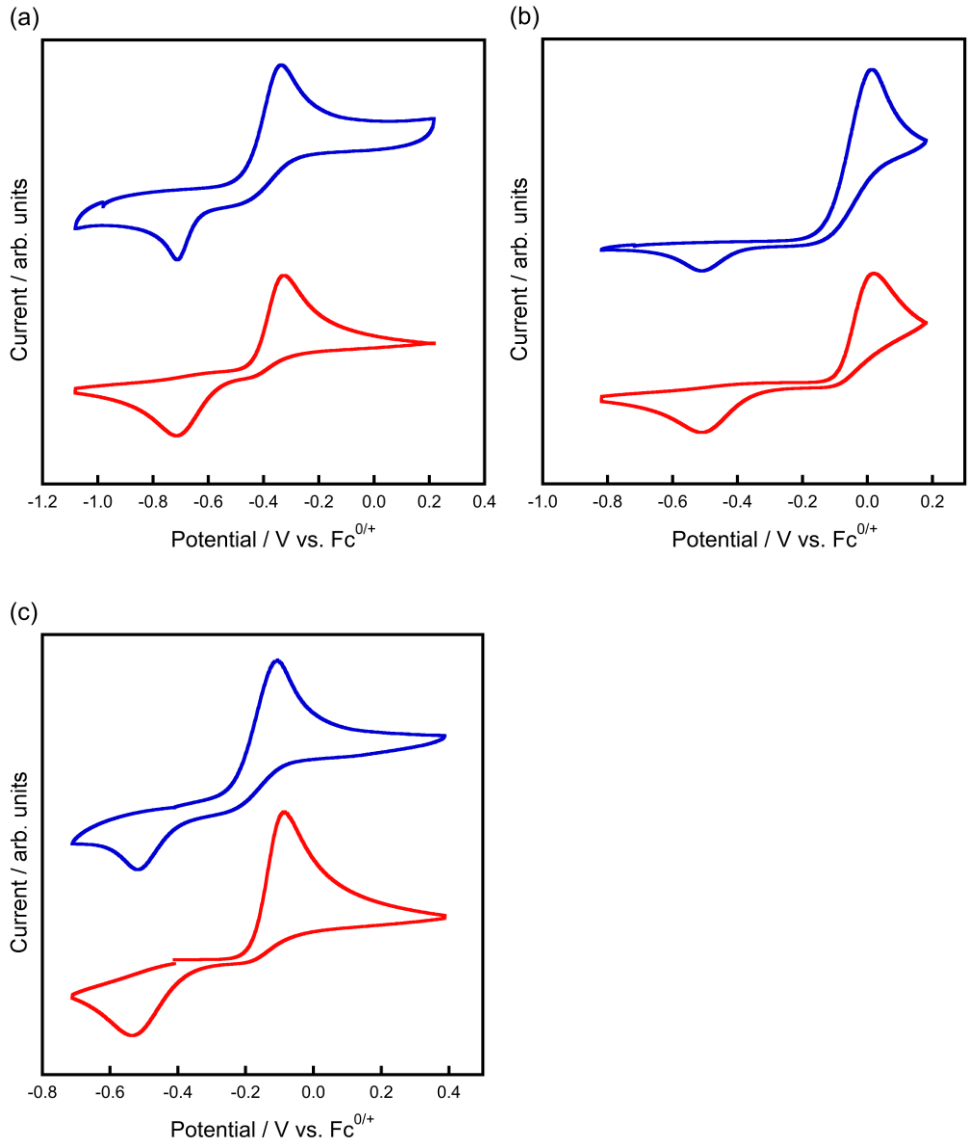

Figure 5.7. Observed (blue) and simulated (red) cyclic voltammograms in CH_2Cl_2 (in MeCN for **1a**) at 298 K (scan rate 0.1 V s^{-1}) for (a) **1a**, (b) **1b**, and (c) **1c**; Simulated parameters (standard formal potential, standard rate constant, transfer coefficient): E_1 = –0.38 V, k_1 = 8.0×10–3 cm s^{-1}, α_1 = 0.5, E_2 = –0.52 V, k_2 = 2.0×10^{-4} cm s^{-1}, α_2 = 0.5, for **1a**; E_1 = +0.01 V, k_1 = 8.0×10^{-3} cm s^{-1}, α_1 = 0.5, E_2 = –0.32 V, k_2 = 2.0×10^{-4} cm s^{-1}, α_2 = 0.5, for **1b**; E_1 = –0.11 V, k_1 = 8.0×10^{-3} cm s^{-1}, α_1 = 0.5, E_2 = –0.34 V, k_2 = 2.0×10^{-4} cm s^{-1}, α_2 = 0.5, for **1c**. All diffusion coefficients set equal to 1.0×10^{-5} cm^2 s^{-1}.

In addition, the author monitored the absorption spectrum change during electrochemical oxidation of neutral to dicationic states for **1a**–**d** (Figure 5.8). As a consequence, the p- and α-band in the lower energy region observed for **1a**–**d** gradually disappeared, and new bands emerged in the higher energy region (> 2.5 eV), thus indicating the loss of planarity for the pentacene moiety in the dicationic states of **1a**–**d**. Moreover, the author also observed the reversibility from the generated dication to the original neutral species for **1a**–**d** spectroelectrochemically, when the reverse bias applied. Irrespectively, the author could not obtain single crystals suitable for X-ray structural analysis of dications of **1a**–**d**.

To get a more specific picture of the geometrical and electronic features of dications of **1a**–**d**, the author carried out DFT calculations at B3LYP/6-31G* level of theory. In each case, we found that the most favorable conformation is a "butterfly-like" conformation in which the central benzene ring in the pentacene moiety is bended along the C6–C13 line (Scheme 5.4). For the dication of **1a**, the optimized planar conformation with fully aromatic pentacene moiety could not be found. On the other hand, the optimized planar conformations were predicted to be 9.63 and 7.58 kcal mol^{-1} higher in energy than the butterfly-like conformations for the dications of **1b** and **1c**, respectively. More noteworthy, the butterfly-like conformation was also revealed to be more stable than the planar one for the dication of **1d**, but only slightly (0.16 kcal mol^{-1}). This trend in the relative energy between the planar and butterfly-like conformations is consistent with the observed electrochemical behaviors for the dications of **1a**–**d**. As seen in the characteristic geometrical parameters such as the bend angle in the pentacene moiety (Figure 5.9), it was found that the dication of **1d** diminished deformation from the planar conformation, thus leading to the observed quasi-reversible

redox behavior with the smallest inner reorganization energy. Although the present *N*-substituent effect seems to be closely related to the extent of delocalized character of occupied frontier MOs over entire molecule of **1a**–**d** (Figure 5.10), the more elaborate theoretical consideration is probably needed to clarify the origin of the deformation from the planar conformation of the pentacene moiety in conjunction with the pseudo-Jahn-Teller effect.[25]

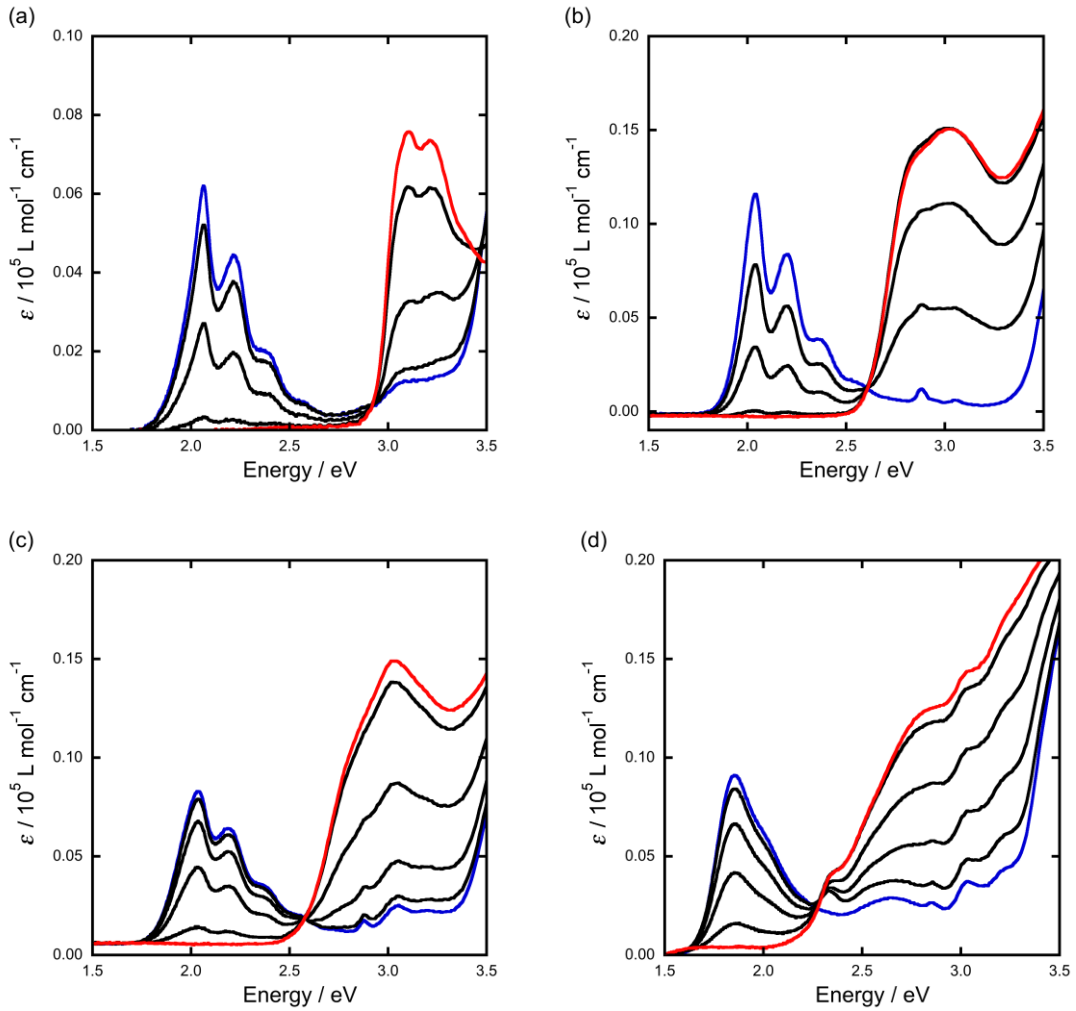

Figure 5.8. UV-vis-NIR absorption spectra of the stepwise electrochemical oxidation of (a) **1a**, (b) **1b**, (c) **1c**, and (d) **1d** from neutral (in blue) to dication (in red) in CH_2Cl_2 (at 1×10^{-4} M) containing 0.1 M *n*-Bu_4NBF_4 at 298 K.

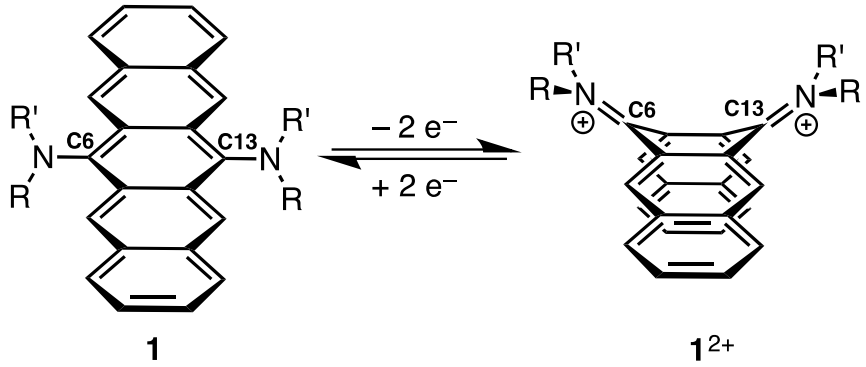

Scheme 5.4. Two-electron oxidation of **1** and the "butterfly-like" conformation of $\mathbf{1}^{2+}$.

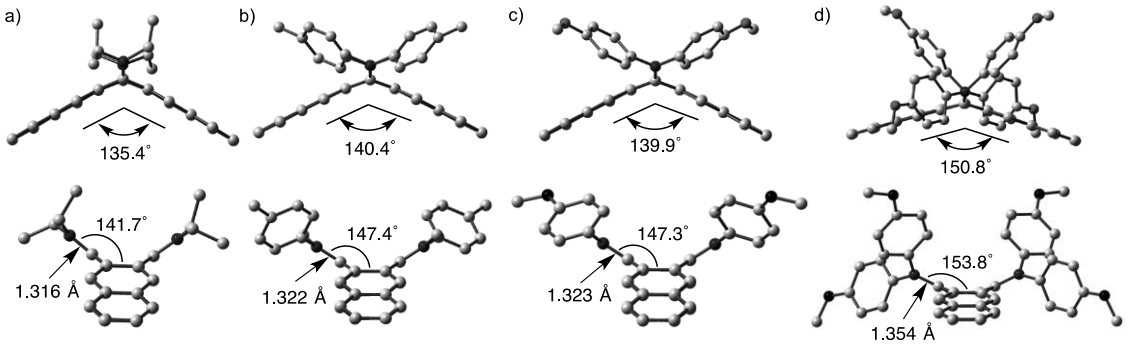

Figure 5.9. B3LYP/6-31G* ground state minima and important geometrical parameters for the dication of a) **1a**, b) **1b**, c) **1c**, and d) **1d**; each view is shown along the short axis (top) and the long axis (bottom) of the pentacene backbone.

(a)

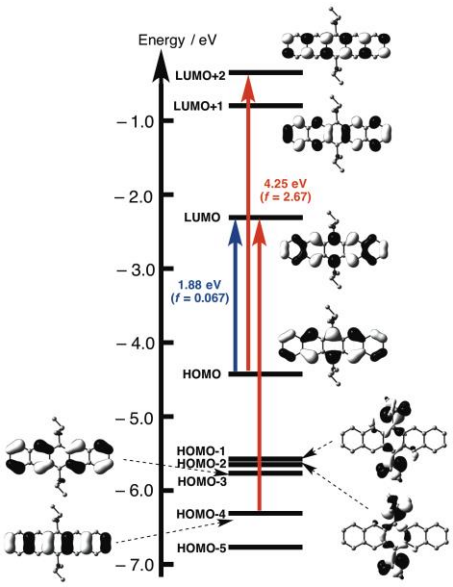

(b)

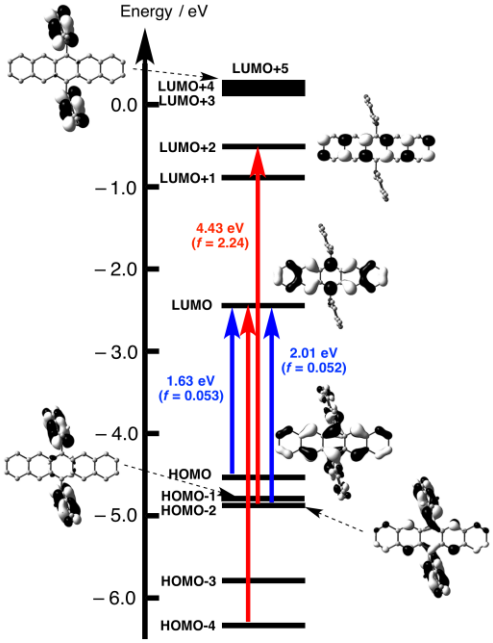

Figure 5.10. Frontier Kohn-Sham orbital energy levels for (a) **1a** and (b) **1c** at the B3LYP/6-31G* level of theory. The blue and red arrows represent the major contribution to the lowest and next lowest energy transitions, respectively, on the basis of TD-DFT calculations.

(c)

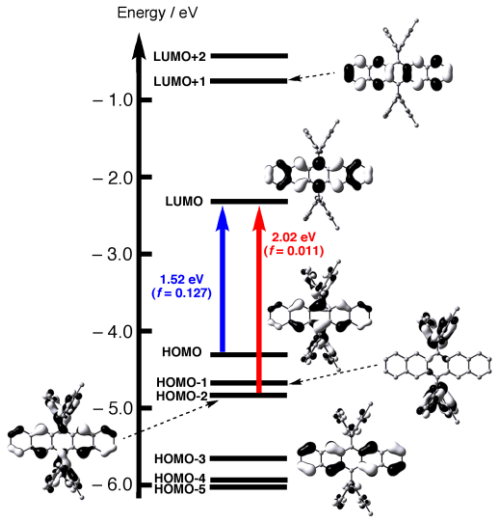

(d)

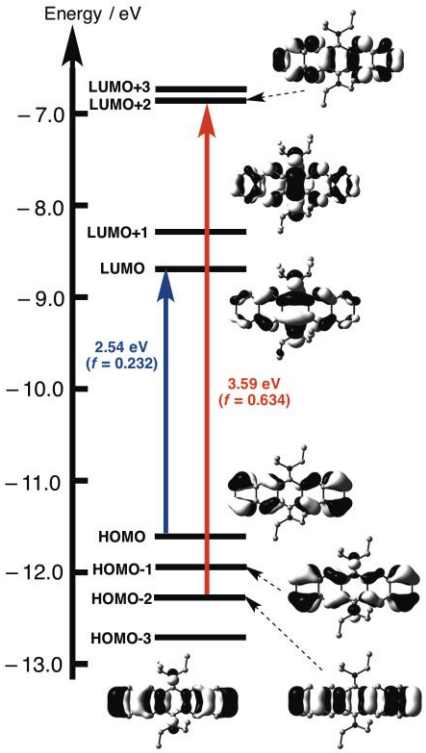

Figure 5.10. (continued) Frontier Kohn-Sham orbital energy levels for (c) **1d** and (d) **1a**$^{2+}$ at the B3LYP/6-31G* level of theory. The blue and red arrows represent the major contribution to the lowest and next lowest energy transitions, respectively, on the basis of TD-DFT calculations.

(e)

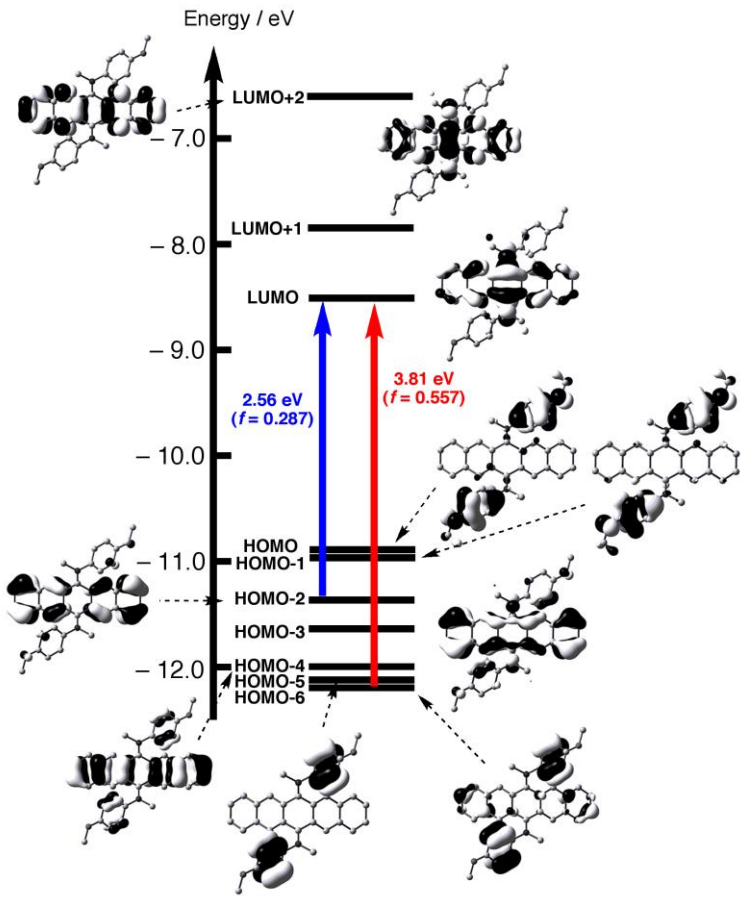

Figure 5.10. (continued). Frontier Kohn-Sham orbital energy levels for (e) **1c**$^{2+}$ at the B3LYP/6-31G* level of theory. The blue and red arrows represent the major contribution to the lowest and next lowest energy transitions, respectively, on the basis of TD-DFT calculations.

(f)

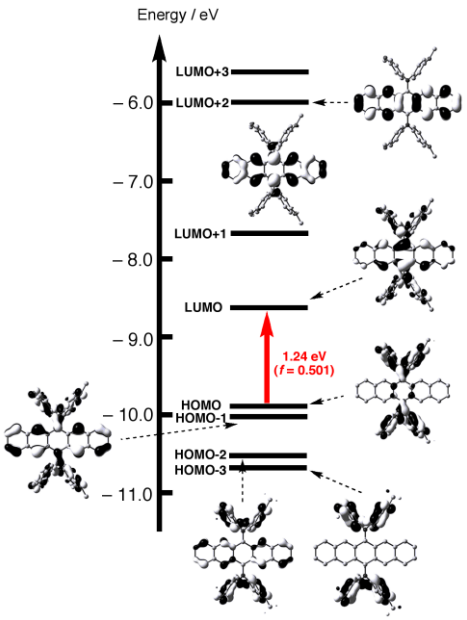

(g)

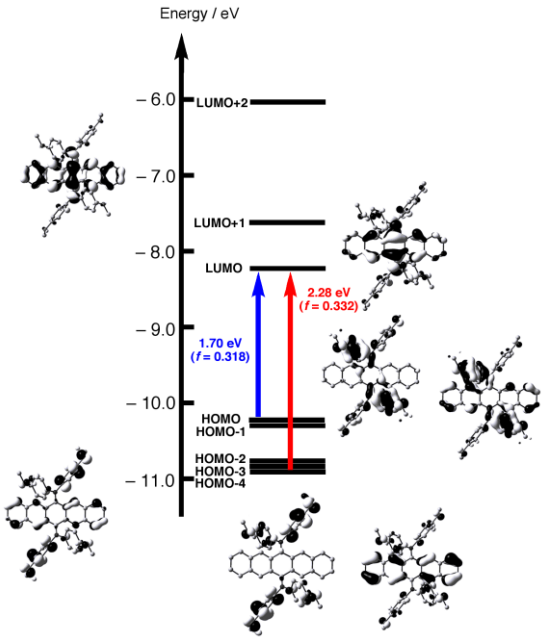

Figure 5.10. (continued). Frontier Kohn-Sham orbital energy levels for (f) planar and (g) butterfly-like conformations of **1d**$^{2+}$ at the B3LYP/6-31G* level of theory. The blue and red arrows represent the major contribution to the lowest and next lowest energy transitions, respectively, on the basis of TD-DFT calculations.

5.4 Conclusion

The results presented herein demonstrate that the newly prepared π-extended congeners of **PD**, **1a**–**d**, can be regarded as a new class of pentacene derivatives with both stronger donor ability and enhanced solubility for common organic solvents, and moreover, the two-electron oxidation process of **1a**–**d** was found to be accompanied by the substantial structural change into the "butterfly-like" conformation of the pentacene moiety, which causes a considerable inner reorganization energy for **1a**–**c**. It was confirmed that the extent of deformation from the planar pentacene moiety in the dication of 6,13-diaminopentacene can be fine-tuned by varying the kind of *N*-substituents.

5.5 References

[1] K. Deuchert, S. Hünig, *Angew. Chem. Int. Ed. Engl*. **1978**, *17*, 875-886.

[2] a) K. Hu, D. H. Evans, *J. Electroanal. Chem*. **1997**, *423*, 29-35; b) C. Lambert, C. Risko, V. Coropceanu, J. Schelter, S. Amthor, N. E. Gruhn, J. C. Durivage, J.-L. Brédas, *J. Am. Chem. Soc*. **2005**, *127*, 8508-8516.

[3] a) M. Bendikov, F. Wudl, *Chem. Rev*. **2004**, *104*, 4891-4945; b) J. E. Anthony, *Angew. Chem. Int. Ed*. **2008**, *47*, 452-483.

[4] a) J. E. Anthony, J. S. Brooks, D. L. Eaton, S. R. Parkin, *J. Am. Chem. Soc*. **2001**, *123*, 9482-9483; b) Y. Sakamoto, T. Suzuki, M. Kobayashi, Y. Gao, Y. Fukai, Y. Inoue, F. Sato, S. Tokito, *J. Am. Chem. Soc*. **2004**, *126*, 8138-8140; c) K. Kobayashi, R. Shimaoka, M. Kawahata, M. Yamanaka, K. Yamaguchi, *Org. Lett*. **2006**, *8*, 2385-2388; d) D. Lehnherr, R. McDonald, R. R. Tykwinski, *Org. Lett*. **2008**, *10*, 4163-4166; e) S. Katsuta, D. Miyagi, H. Yamada, T. Okujima, S. Mori, K. Nakayama, H. Uno, *Org. Lett*. **2011**, *13*, 1454-1457; f) J. Li, M. Wang, S. Ren, X. Gao, W. Hong, H. Li, D. Zhu, *J. Mater. Chem*. **2012**, *22*, 10496; g) C. Pramanik, Y. Li, A. Singh, W. Lin, J. L. Hodgson, J. B. Briggs, S. Ellis, P. Müller, N. E. McGruer, G. P. Miller, *J. Mater. Chem. C* **2013**, *1*, 2193-2201; h) Y. Kawabata, A. Shimizu, T. Shinada, R. Tanaka, Y. Teki, *Angew. Chem. Int. Ed*. **2013**, *52*, 6643-6647.

[5] K. Raghavachari, *Theor. Chem. Acc*. **2000**, *103*, 361-363 and references cited therein.

[6] a) R. Bauernschmitt, R. Ahlrichs, *Chem. Phys. Lett*. **1996**, *256*, 454-464; b) M. E. Casida, C. Jamorski, K. C. Casida, D. R. Salahub, *J. Chem. Phys*. **1998**, *108*, 4439-4449; c) R. E. Stratmann, G. E. Scuseria, M. J. Frisch, *J. Chem. Phys*. **1998**, *109*, 8218-8224.

[7] W. J. Hehre, L. Radom, P. v. R. Schleyer, J. A. Pople, *Ab Initio Molecular Orbital Theory*, Wiley, New York, **1986**.

[8] M. J. Frisch, G. W. Trucks, H. B. Schlegel, G. E. Scuseria, M. A. Robb, J. R. Cheeseman, G. Scalmani, V. Barone, B. Mennucci, G. A. Petersson, H. Nakatsuji, M. Caricato, X. Li, H. P. Hratchian, A. F. Izmaylov, J. Bloino, G. Zheng, J. L. Sonnenberg, M. Hada, M. Ehara, K. Toyota, R. Fukuda, J. Hasegawa, M. Ishida, T. Nakajima, Y. Honda, O. Kitao, H. Nakai, T. Vreven, J. A. Montgomery, Jr., J. E. Peralta, F. Ogliaro, M. Bearpark, J. J. Heyd, E. Brothers, K. N. Kudin, V. N. Staroverov, T. Keith, R. Kobayashi, J. Normand, K. Raghavachari, A. Rendell, J. C. Burant, S. S. Iyengar, J. Tomasi, M. Cossi, N. Rega, J. M. Millam, M. Klene, J. E. Knox, J. B. Cross, V. Bakken, C. Adamo, J. Jaramillo, R. Gomperts, R. E. Stratmann, O. Yazyev, A. J. Austin, R. Cammi, C. Pomelli, J. W. Ochterski, R. L. Martin, K. Morokuma, V. G. Zakrzewski, G. A. Voth, P. Salvador, J. J. Dannenberg, S. Dapprich, A. D. Daniels, O. Farkas, J. B. Foresman, J. V. Ortiz, J. Cioslowski, and D. J. Fox, Gaussian 09, Revision C.01, Gaussian, Inc., Wallingford CT, **2010**.

[9] M. Rudolph, D. P. Reddy, S. W. Feldberg, *Anal. Chem*. **1994**, *66*, 589.

[10] G. M. Sheldrick, *Acta Cryst*. *A* **2008**, *64*, 112.

[11] M. C. Burla, R. Caliandro, M. Camalli, B. Carrozzini, G. L. Cascarano, L. De Caro, C. Giacovazzo, G. Polidori, R. Spagna, *J. Appl. Cryst*. **2005**, *38*, 381.

[12] M. C. Burla, R. Caliandro, M. Camalli, B. Carrozzini, G. L. Cascarano, C. Giacovazzo, M. Mallamo, A. Mazzone, G. Polidori, R. Spagna, *J. Appl. Cryst*. **2012**, *45*, 357.

[13] CrystalStructure 4.0 and 4.1, Crystal Structure Analysis Package: Rigaku Corporation, Tokyo 196-8666, Japan, **2000-2014**.

[14] a) I. Moretti, G. Torre, *Synthesis* **1970**, 141; b) W. B. Jennings, C. J. Lovely, *Tetrahedron* **1991**, *47*, 5561-5568.

[15] M. Tamano, Y. Nagai, J. Koketsu, *Nippon Kagaku Kaishi* **1988**, 1977-1983.

[16] The author could measure the ^{1}H- and ^{13}C-NMR spectra of **DCP**, although **DCP** was reported in ref.[4f] not to be soluble enough for NMR analysis.

[17] X. Huang, K. W. Anderson, D. Zim, L. Jiang, A. Klapars, S. L. Buchwald, *J. Am. Chem. Soc*. **2003**, *125*, 6653-6655.

[18] Q. Shelby, N. Kataoka, G. Mann, J. Hartwig, *J. Am. Chem. Soc*. **2000**, *122*, 10718-10719

[19] M. G. Organ, S. Calimsiz, M. Sayah, K. H. Hoi, A. J. Lough, *Angew. Chem. Int. Ed*. **2009**, *48*, 2383-2387

[20] CCDC 1420390 (**1a**), 1420391 (**1b**), and 1420392 (**1d**) contain the supplementary crystallographic data. These data can be obtained free of charge from the Cambridge Crystallographic Data Centre via www.ccdc.cam.ac.uk/data_request/cif.

[21] W. Schmidt, *J. Chem. Phys*. **1977**, *66*, 828-845.

[22] D. H. Evans, K. Hu, *J. Chem. Soc. Faraday Trans*. **1996**, *92*, 3983-3990.

[23] B. Brielbeck, J. C. Rühl, D. H. Evans, *J. Am. Chem. Soc*. **1993**, *115*, 11898-11905.

[24] Although an ECE mechanism cannot be ruled out, the present EE mechanism with inversion of potentials gave better simulations: for the case where the redox process was characterized as an ECE-type mechanism, see for instance: M. Horner, S. Hünig, *J. Am. Chem. Soc*. **1977**, *99*, 6122-6124.

[25] I. B. Bersuker, *Chem. Rev*. **2013**, *113*, 1351-1390.

Part 2

Optical Properties of Triphenylamine-Based Functional Materials

Introduction

To date, fluorescent molecules continue to attract great interest in conjunction with their device application such as organic light-emitting diodes (OLEDs),[1,2] and thus, various kinds of fluorescent molecules have already been so far prepared.[3] To fabricate efficient and reliable devices, it is important to design fluorescent molecules with thermal and chemical stability[4], as well as high fluorescence quantum yield.[5,6] In light-emitting process, when a molecule in the ground state S_0 state absorbs a photon, it makes a vertical transition to a Frank-Condon (FC) excited state. Then, the excited molecule in the FC state undergoes structural deformation, also called vibrational relaxation. After vibrational relaxation, the excited state reaches an adiabatic state, called reorganization. The reorganization energy is the origin of the Stokes shift. The fluorescence is so rapid that the radiative transition comes from the adiabatic state. The

fluorescence quantum yield is increased by a large transition dipole moment.[7] Non-radiative transitions such as internal conversion and intersystem crossing also occur. The fluorescence quantum yield is determined from the competition between radiative and non-radiative transitions. The vibronic couplings play an important role in vibrational relaxation and internal conversion.[8-11]

Triphenylamine is typical non-fluorescent molecules, and its excited states undergo non-radiative decay with internal conversion and vibrational relaxation. As exemplified in Figure 1a, a weak absorption band in the shoulder of an intense absorption band at about 300 nm corresponds to the HOMO-LUMO transition of trianisylamine (TAA),[12] and TAA can be substantially regarded as non-fluorescent molecule.[13] Time-dependent DFT calculations (TD-DFT) illustrates that the weak shoulder band at about 365 nm can be assigned to the transition mainly from the HOMO (31*a*) with distribution over the nitrogen p orbital and three phenyl rings to the LUMO (32*a*) without contribution of the nitrogen p orbital, thus indicating these two orbitals are related to the fluorescent process in TAA (Figure 1b).

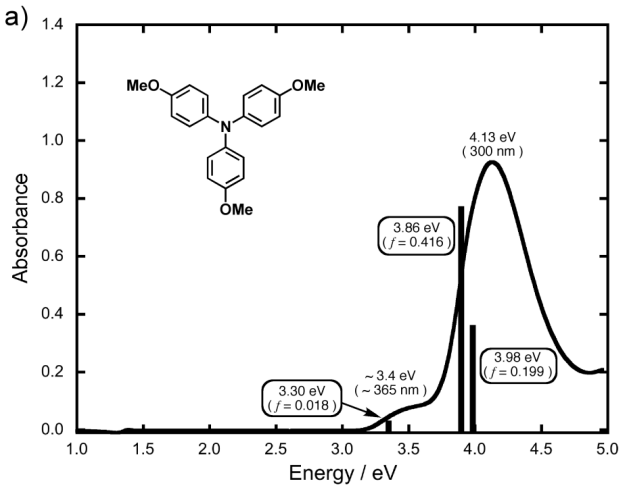

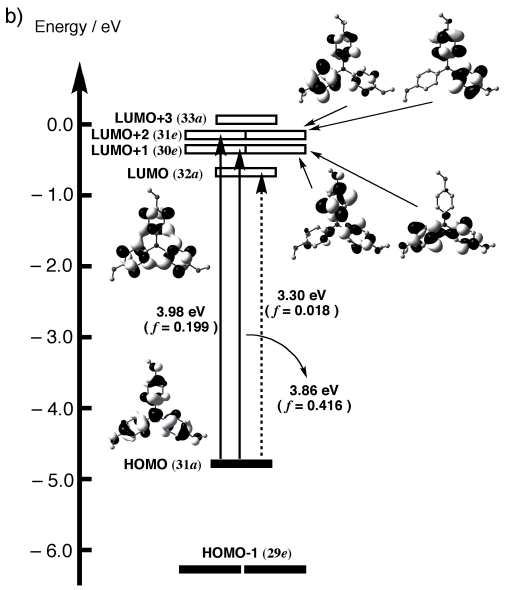

Figure 1. a) Absorption spectrum of trianisylamine (TAA) in CH_2Cl_2 at room temperature. The black sticks designate the TD-DFT-calculated lower energy transition energies and their relative oscillator strengths at B3LYP/6-31+G*. b) Frontier Kohn-Sham orbital energy levels for trianisylamine (TAA) at the B3LYP/6-31+G* level of theory (in C_3 symmetry). The broken and solid arrows represent the major contribution to the lowest and next-lowest energy transitions, respectively, on the basis of TD-DFT calculations.

Recently, it has been reported that aryl amines that are introduced with organoboron have donor-acceptor unique electrochemical and photophysical properties. These compounds have dipolar organic chromophores with donor-π-acceptor (D-π-A) motifs, where the electron donor and acceptor moieties are suitably substituted at the periphery of the π-conjugated system for efficient excited-state intramolecular charge transfer (ICT).[14-24] These molecules have large transition dipole moment and exhibit characteristic emission spectra because of excited ICT.

In Chapter 1, for the fluorescence enhancement of non-fluorescent triphenylamine, the author newly prepared singly, doubly, and triply carborane-substituted triphenylamines and investigated these molecules by means of electrochemical and spectrochemical measurements, and DFT calculations.

In Chapter 2 and 3, the author synthesized new donor-acceptor compounds that have electron-donating amino groups and electron-accepting boryl groups. These compounds were characterized by analysis of crystal structure and cyclic voltammetry, ESR and UV/vis absorption, fluorescence spectroscopy.

References

[1] U. Mitschke, P. Bäuerle, *J. Mater. Chem.* **2000**, *10*, 1471-1507.

[2] H. Sasabe, J. Kido, *J. Mater. Chem. C.* **2013**, *1*, 1699-1707.

[3] M. Zhu, C. Yang, *Chem. Rev. Soc.* **2013**, *42*, 4963-4976.

[4] J. R. Sheats, H. Antoniadis, M. Hueschen, W. Leonard, J. Miller, R. Moon, D. Roitman, A. Stocking, *Science* **1996**, *273*, 884-888.

[5] C. -H. Zhao, A. Wakamiya, Y. Inukai, S. Yamaguchi, *J. Am. Chem Soc.* **2006**, *128*, 15934-15935.

[6] M. Shimizu, Y. Takeda, M. Higashi, T. Hiyama, *Angew. Chem. Int. Ed.* **2009**, *48*, 3653-3656.

[7] T. Sato, M. Uejima, N. Iwahara, N. Haruta, K. Shizu, K. Tanaka, *J. Phys Conf. Ser.* **2013**, *428*, 012010.

[8] M. Uejima, T. Sato, D. Yokoyama, K. Tanaka, J. -W. Park, *Phys. Chem. Chem. Phys.* **2014**, *16*, 14244-14256.

[9] T. Sato, K. Tokunaga, K. Tanaka, *J. Phys. Chem. A* **2008**, *112*, 758-767.

[10] M. Uejima, T. Sato, K. Tanaka, H. Kaji, *Chem. Phys.* **2014**, *430*, 47-55.

[11] M. Uejima, T. Sato, M. Detani, A. Wakamiya, F. Suzuki, H. Suzuki, T. Fukushima, K. Tanaka, Y. Murata, C. Adachi, H. Kaji, *Chem. Phys. Lett.* **2014**, *602*, 80-83.

[12] S. J. Strickler, R. A. Berg, *J. Chem. Phys.* **1962**, 37, 814-822.

[13] C. Quinton, V. Alain-Rizzo, C. Dumas-Verdes, F. Miomandre, G. Clavier, P. Audebert, *RSC Adv*. **2014**, *4*, 34332-34342.

[14] J. C. Doty, B. Babb, P. J. Grisdale, M. Glogowski, J. L. R. Williams, *J. Organomet. Chem*. **1972**, *38*, 229-236.

[15] N. S. Makarov, S. Mukhopadhyay, K. Yesudas, J. -L. Brédas, J. W. Perry, *J. Phys.*

Chem. A **2012**, *116*, 3781-3793.

[16] M. Mao, M. -G. Ren, Q. -H. Song, *Chem. Eur. J.* **2012**, *18*, 15512-15522.

[17] A. G. Bonn, O. S. Wenger, *J. Org. Chem.* **2015**, *80*, 4097-4107.

[18] a) Z. Zhang, R. M. Edkins, J. Nitsch, K. Fucke, A. Steffen, L. E. Longobardi, D. W. Stephan, C. Lambert, T. B. Marder, *Chem. Sci.* **2015**, *6*, 308-321; (b) Z. Zhang, R. M. Edkins, J. Nitsch, K. Fucke, A. Eichhorn, A. Steffen, Y. Wang, T. B. Marder, *Chem. Eur. J.* **2015**, *21*, 177-190.

[19] R. Stahl, C. Lambert, C. Kaiser, R. Wortmann, R. Jakober, *Chem. Eur. J.* **2006**, *12*, 2358-2370.

[20] Z. Yuan, C. D. Entwistle, J. C. Collings, D. Albesa-Jové, A. S. Batsanov, J. A. K. Howard, N. J. Taylor, H. M. Kaiser, D. E. Kaufmann, S. -Y. Poon, W. -Y Wong, C. Jardin, S. Fathallah, A. Boucekkine, J. -F. Halet, T. B. Marder, *Chem. Eur. J.* **2006**, *12*, 2758-2771.

[21] a) G. Zhou, M. Baumgarten, K. Müllen, *J. Am. Chem. Soc.* **2008**, *130*, 12477-12484; b) A. Proń, G. Zhou, H. Norouzi-Arasi, M. Baumgarten, K. Müllen, *Org. Lett.* **2009**, *11*, 3550-3553. c) A. Proń, M. Baumgarten, K. Müllen, *Org. Lett.* **2010**, *12*, 4236-4239.

[22] a) P. Chen, R. A. Lalancette, F. Jäkle, *Angew. Chem. Int. Ed.* **2012**, *51*, 7994-7998; b) P. Chen, A. S. Marshall, S. -H. Chi, X. Yin, J. W. Perry, F. Jäkle, *Chem. Eur. J.* **2015**, *21*, 18237-18247.

[23] a) R. Kurata, K. Kaneda, A. Ito, *Org. Lett.* **2017**, *19*, 392-395; b) R. Kurata, A. Ito, M. Gon, K. Tanaka, Y. Chujo, *J. Org. Chem.* **2017**, *82*. 5111-5121.

[24] C. Wang, Q. -W Xu, W. -N. Zhang, Q. Peng, C. -H. Zhao, *J. Org. Chem.* **2015**, *80*, 10914-10924.

Chapter 1

Fluorescence Enhancement of Non-Fluorescent Triphenylamine: A Recipe to Utilize Carborane Cluster Substituents

1.1 Introduction

To date, light-emitting molecules continue to attract great interest in conjunction with their device application such as organic light-emitting diodes (OLEDs),[1] and thus, various kinds of fluorescent molecules have already been so far prepared.[2] However, given that light-emitting efficiency of non-fluorescent molecules can be enhanced by general guiding principles, many more options become available for exploitation of new fluorescent molecules. As an example of typical non-fluoescent molecules, oligoarylamines are designated, and their excited states undergo nonradiative decay with internal conversion and vibrational relaxation. As exemplified in Figure 1.1a, a weak absorption band in the shoulder of an intense absorption band at about 300 nm corresponds to the HOMO-LUMO transition of trianisylamine (TAA),[3] and TAA can be substantially regarded as non-fluorescent molecule.[4] Time-dependent DFT

calculations (TD-DFT) illustrates that the weak shoulder band at about 365 nm can be assigned to the transition mainly from the HOMO (31*a*) with distribution over the nitrogen p orbital and three phenyl rings to the LUMO (32*a*) without contribution of the nitrogen p orbital, thus indicating these two orbitals are related to the fluorescent process in TAA (Figure 1.1b).

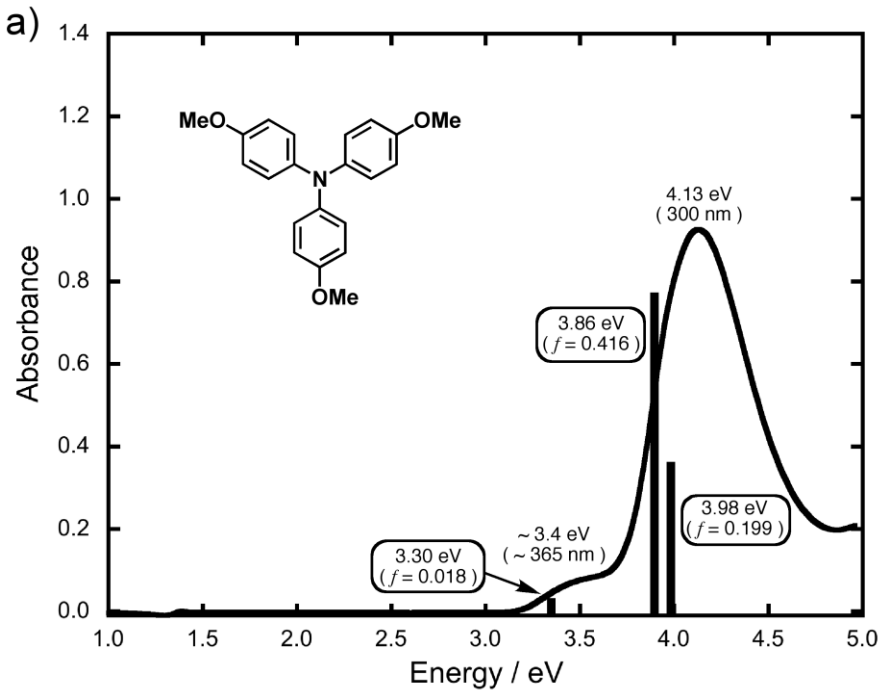

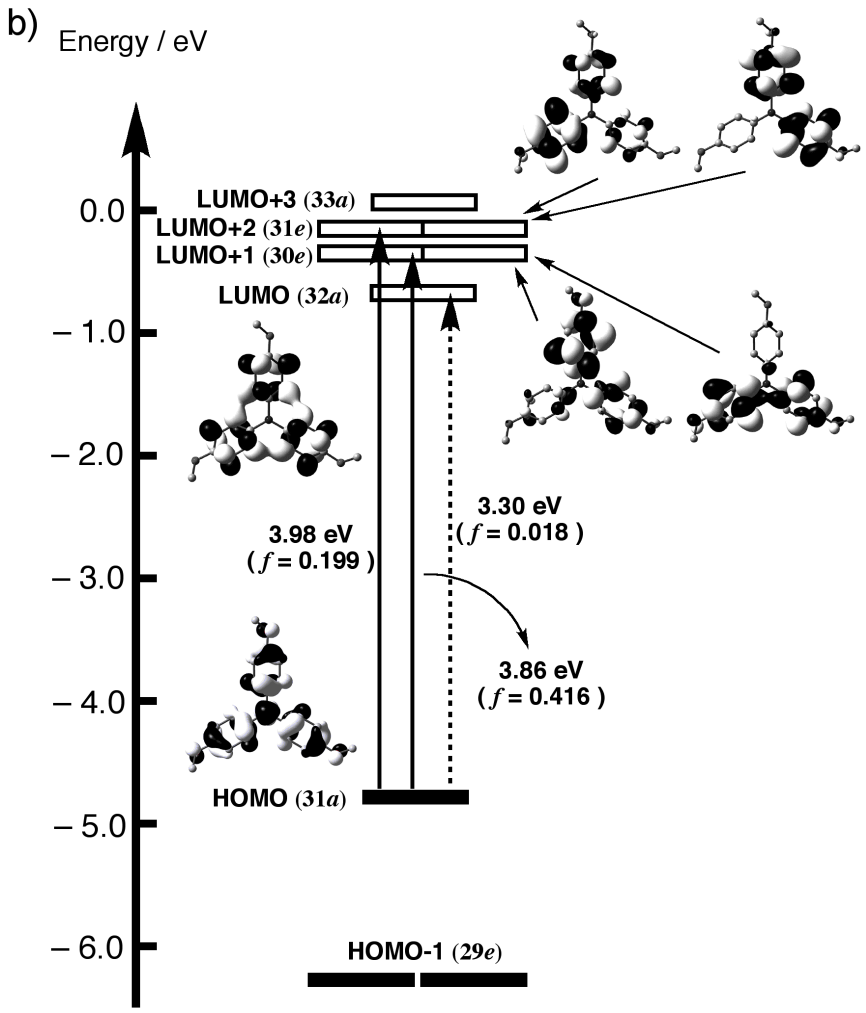

Figure 1.1. a) Absorption spectrum of trianisylamine (TAA) in CH_2Cl_2 at room temperature. The black sticks designate the TD-DFT-calculated lower energy transition energies and their relative oscillator strengths at B3LYP/6-31+G*. b) Frontier Kohn-Sham orbital energy levels for trianisylamine (TAA) at the B3LYP/6-31+G* level of theory (in C_3 symmetry). The broken and solid arrows represent the major contribution to the lowest and next-lowest energy transitions, respectively, on the basis of TD-DFT calculations.

Non-radiative decay mainly originates from both vibrational relaxation process and internal conversion process ($S_1 \rightarrow S_0$). Internal conversion process is, in general, caused by vibronic interaction (electron-phonon interaction). It has been demonstrated that the off-diagonal vibronic coupling constants (VCCs) between S_1 and S_0 states directly related to the rate constant of internal conversion; in fact, on the basis of the theoretical molecular design reducing off-diagonal VCCs, a newly prepared anthracene derivative exhibited suppressing effect on internal conversion process, that is, an increase in fluorescence quantum yield.[5] The off-diagonal VCC can be represented by the integral of the vibronic coupling density (VCD) between S_1 and S_0 states, and furthermore, the VCD equals the multiplication of the overlap density between S_1 and S_0 states and the potential derivative with respect to the normal coordinate of the vibrational mode.[6] According to the VCD analysis, a guiding principle to suppress non-radiative decay by the introduction of substituents is deduced: *if an excited state, which is expected to be the emitting state, originates from the excitation between a pair of molecular orbitals (HOMO and LUMO for the most cases), one of the MOs should be delocalized over the entire molecule, whereas the other should be localized on the non-fluorescent core molecular unit, presuming that the potential derivative does almost unchanged before and after the introduction of substituents*.[7] According to this guiding principle, the author reports here on the fluorescence enhancement of non-fluorescent triphenylamine by substitution of suitable substituents.

The author has been searching for suitable one for triarylamines in the arsenal of non-fluorescent substituents, and finally, monocarba-*closo*-dodecaborate[12] ($CB_{11}H_{12}^-$; hereinafter referred to as ‘carborane’) has been chosen as the best one. For instance, when one of the methoxy groups in TAA is substituted by carborane, the electronic

structure of the substituted TAA (**1**) was estimated by DFT and TD-DFT calculations (Figure 1.2). Importantly, the specific characteristics of the HOMO with the nitrogen p orbital and the LUMO without the nitrogen p orbital for TAA remained unchanged by the carborane substitution, thereby ensuring the same emission process as TAA is anticipated for **1**; in other words, the fluorophore of **1** is still the triphenylamine core. In addition, the HOMO of **1** extends over the carborane substituent, while the LUMO is mostly localized on the triarylamine moiety. More importantly, it was confirmed that the vibrational modes originating from carborane substituents do not participate in the maximum-coupling modes, on the basis of VCC analysis.[7] Overall, these remarkable features of **1** meet the requirements for the above-mentioned guiding principle: the overlap density between HOMO and LUMO in **1** is reduced effectively by the extension of the distribution of HOMO into the carborane substituent, as compared to that in TAA.[7] The DFT calculations for doubly and triply carborane-substituted triphenylamines (**2** and **3**) have also the same trend as **1** (Figures 1.3 and 1.4).

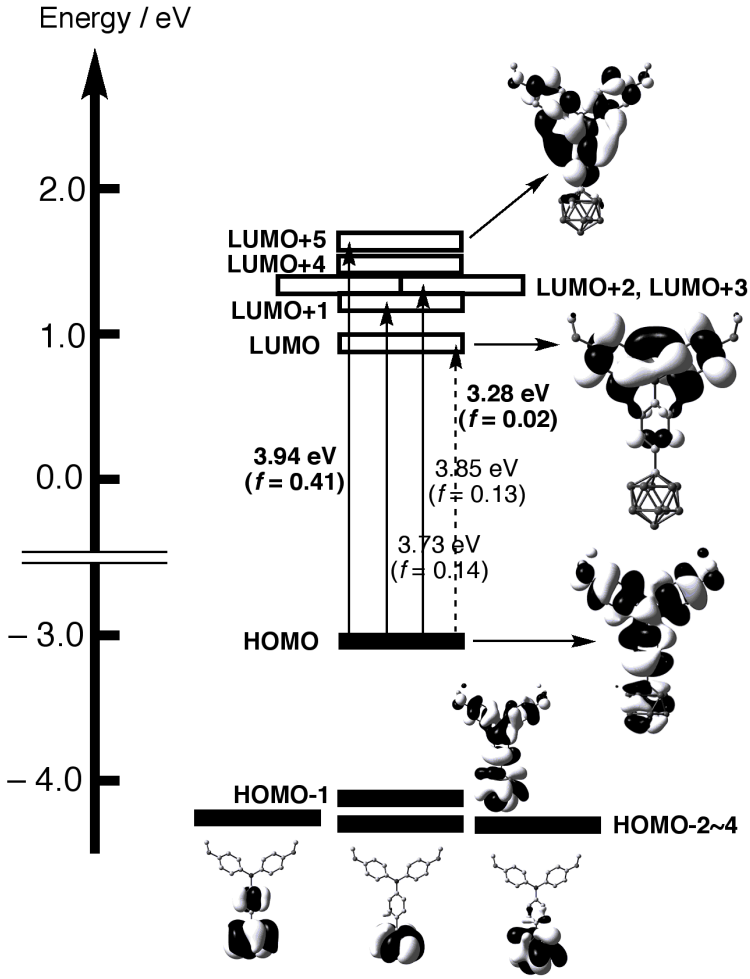

Figure 1.2. Frontier Kohn-Sham orbital energy levels for carborane-substituted triarylamine **1** at the B3LYP/6-31+G* level of theory (in C_1 symmetry). The broken and solid arrows represent the major contribution to the lowest and next-lowest energy transitions, respectively, on the basis of TD-DFT calculations.

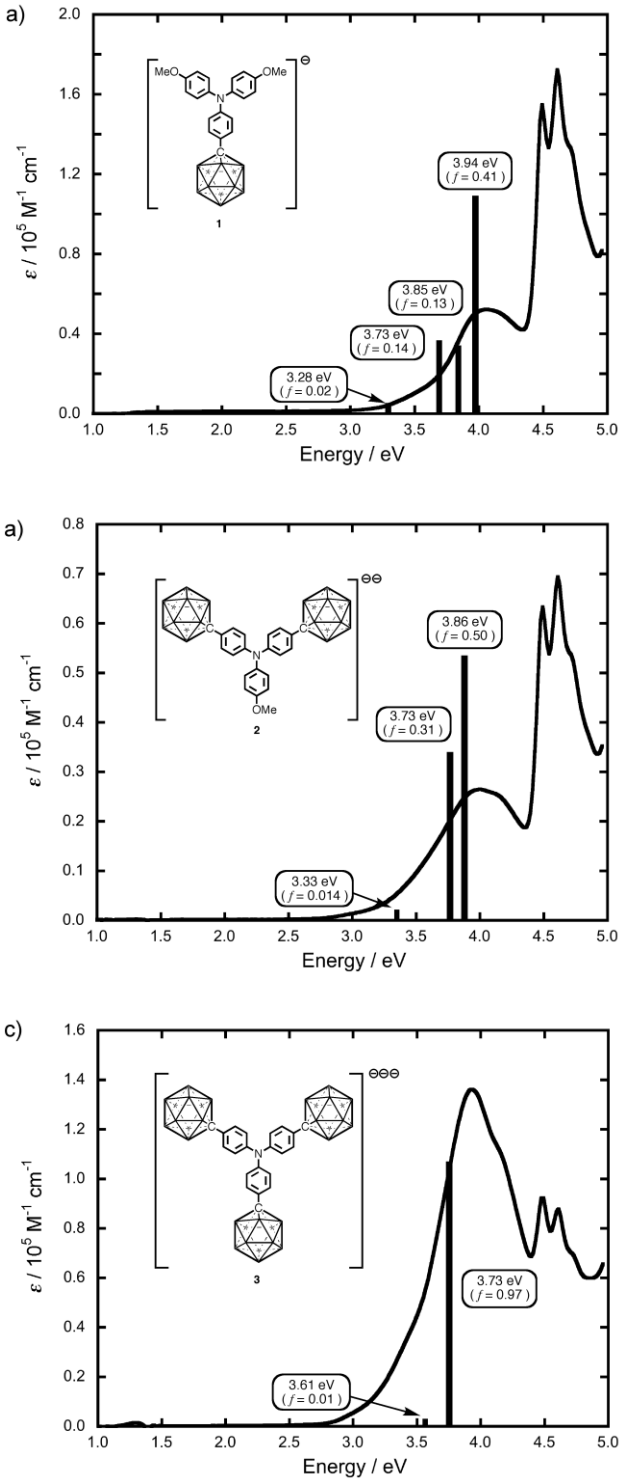

Figure 1.3. Absorption spectra of a) **1**, b) **2**, and c) **3** in CH_2Cl_2 at room temperature. The black sticks designate the TD-DFT-calculated lower energy transition energies and their relative oscillator strengths at B3LYP/6-31+G* (see Figure 1.4).

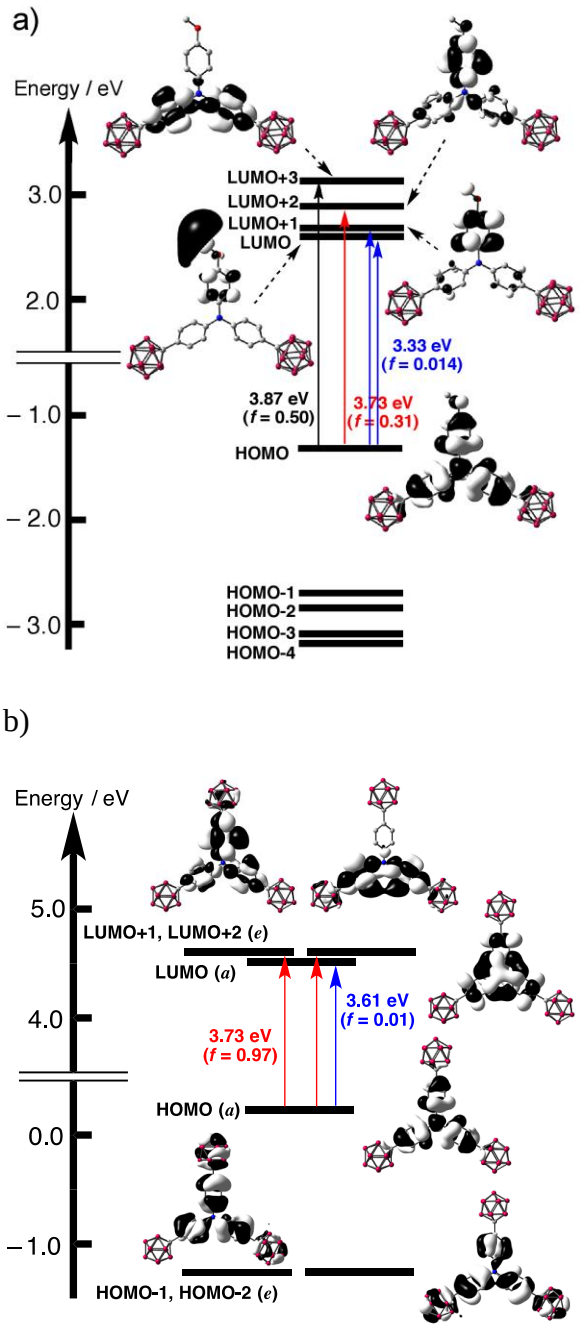

Figure 1.4. Frontier Kohn-Sham orbital energy levels for caroborane-substituted triarylamines a) **2** and b) **3** at the B3LYP/6-31+G* level of theory (in C_1 symmetry for **2** and in C_3 symmetry for **3**). The red and blue (and black for **2**) arrows represent the major contribution to the lowest and next-lowest energy transitions, respectively, on the basis of TD-DFT calculations.

1.2 Experimental Section

1.2.1 Synthesis

All the purchased reagents were of standard quality, and used without further purification. All the purchased solvents were purified, dried, and degassed by standard procedures. Column chromatography was performed with silica gel (Kanto Chemical Co., Inc., silica gel 60N, spherical neutral). Elemental analyses were performed by Center for Organic Elemental Microanalysis, Kyoto University. ^{1}H and ^{13}C NMR spectra were measured by a JEOL JNM-AL400 FT-NMR spectrometer. Chemical shifts of NMR spectra are determined relative to internal tetramethylsilane (TMS) standard (δ), and are given in parts per million (ppm). UV-Vis-NIR absorption spectra were obtained with a Perkin-Elmer Lambda 950 spectrometer. High resolution electrospray ionization (ESI) mass spectra were acquired using a Thermo Fischer EXACTIVE mass spectrometer. Fluorescence spectra were recorded on an absolute PL quantum yield measurement system (HAMAMATSU Quantaurus-QY).

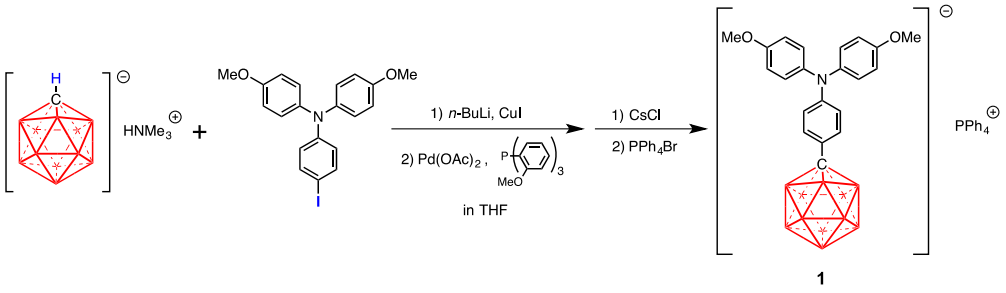

Scheme 1.1. Synthesis of compound **1**.

4-(Carba-*closo*-dodecaborate-1-yl)-4',4"-dimethoxytriphenylamine (1):

$[Me_3NH]^+[1\text{-}CHB_{11}H_{11}]^-$ (0.10 g, 0.5 mmol) was charged in a flask and dried under

reduced pressure at 120˚C for 1 h. The flask charged with argon, and 4 mL of anhydrous THF was added at room temperature. The solution was cooled to -78˚C and a *n*-hexane solution (1.6 M) of *n*-BuLi (0.7 mL, 1.1 mmol) was added. The mixture was stirred at 0˚C for 1 h, and then it was added to CuI (0.10 g, 0.55 mmol) in flask. The reaction mixture was warmed to room temperature and stirred for 30 min. To the reaction mixture was added a solution of palladium(II) acetate (6.2 mg 0.026 mmol), tris(*o*-methoxyphenyl)phosphine (29 mg, 0.16mmol), and 4,4'-dimethoxy-4"-iodotriphenylamine (0.24 g, 0.55 mmol) in 6 mL of anhydrous THF at 0 ˚C. After stirring at room temperature for 24 h, the reaction mixture was poured into distilled water at 0˚C and extracted with AcOEt. Organic layer was separated and dried over Na_2SO_4. The solvent was evaporated, and the obtained material was purified by silica gel column chromatography (AcOEt : hexane = 1:1 and then MeCN). For the counter cation exchange, the AcOEt solution (20 mL) of **1** was washed with 20% aqueous CsCl solution (3 × 10 mL), and then the combined organic phases were evaporated and the resulting material was again dissolved in a small amount of AcOEt and filtered to remove residual CsCl. After the evaporation, the white solid was washed with water and *n*-hexane, and dried under vacuum to afford pure Cs • **1**. Further counter cation exchange with tetraphenylphosphonium ion (PPh_4^+) was carried out with MeOH solution of PPh_4Br. Cs • **1** was dissolved in 1.0 mL of MeOH, and the resulting solution was added to a 10 mL of 20% MeOH solution of PPh_4Br. The resulting solution was stirred for 30 min to give a white solid. The white solid was filtered off, and washed with MeOH and hexane, and finally, dried under vacuum to obtain pale yellow solid PPh_4 • **1** (348 mg, 43.2%); ^{1}H NMR (400MHz, acetonitrile-d_3) δ 7.88-7.93 (m, 4H for PPh_4^+), 7.67-7.75 (m, 16H for PPh_4^+), 7.22-7.26 (m, 2H), 6.95-6.98 (m, 4H), 6.83-6.86

(m, 4H), 6.55-6.59 (m, 2H), 3.74 (s, 6H); ESI HRMS: *m*/*z* calcd for $C_{21}H_{29}O_2NB_{11}$: 446.3289 $[M–PPh_4]^–$; found 446.3302.

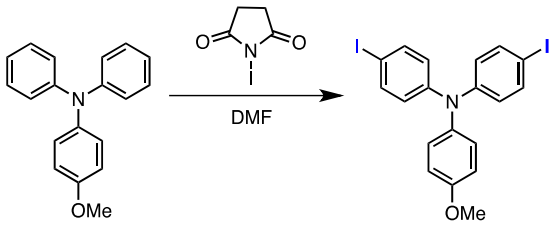

Scheme 1.2. Synthesis of 4,4'-diiodo-4"-methoxytriphenylamine.

4,4'-diiodo-4"-methoxytriphenylamine: To a 50 mL of chloroform solution of 4-methoxytriphenylamine (0.55 g, 2 mmol), *N*-iodosuccinimide (NIS) (1.12 g, 5mmol) in DMF was added in small portions at 0˚C. After stirring at room temperature for 24 h, the reaction mixture was washed with aqueous solution of Na_2SO_3, aqueous solution of $NaHCO_3$, and water. And then the organic layer was dried over Na_2SO_4. After evaporation of the solvent, silica gel column chromatography (CH_2Cl_2 : *n*-hexane = 1:1) afforded 4,4'-diiodo-4"-methoxytriphenylamine (0.972 g 92.2%) as pale yellow solid. ^{1}H NMR (400 MHz, $CDCl_3$) δ 7.46-7.50 (m, 4H), 7.00-7.04 (m, 2H), 6.81-6.86 (m, 2H), 6.75-6.79 (m, 4H), 3.75 (s, 3H); ^{13}C NMR (100 MHz, $CDCl_3$): δ 156.7, 147.4, 139.5, 138.1, 127.6, 124.7, 115.0, 84.7, 55.5 ; ESI HRMS: *m*/*z* calcd for $C_{19}H_{15}ONI_2$: 526.9234 $[M]^+$; found 526.9234.

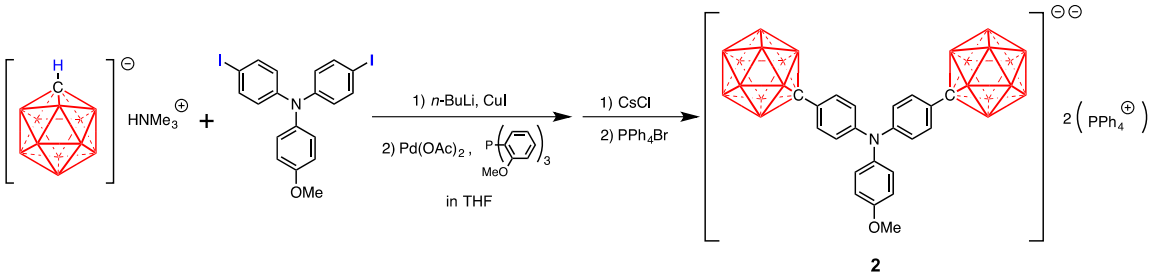

2

Scheme 1.3. Synthesis of compound **2**.

4,4'-Bis(carba-*closo*-dodecaborate-1-yl)-4"-methoxytriphenylamine (2):

According to the same procedure as described for the preparation of **1**, pale yellow solid $(PPh_4)_2$ • **2** (102 mg, 22.3%) was obtained by using 4,4'-diiodo-4"-methoxytriphenylamine (0.11 g, 0.2 mmol); ^{1}H NMR (400MHz, acetone-d_6) δ 7.95-8.01 (m, 8H for PPh_4^+), 7.77-7.91(m, 32H for PPh_4^+), 6.62-7.52 (m, 12H), 3.55 (s, 3H); ESI HRMS: *m*/*z* calcd for $C_{21}H_{37}ONB_{22}$: 278.7528 (= 557.5026/2) $[M–2(PPh_4)]^{2–}$; found 278.7535.

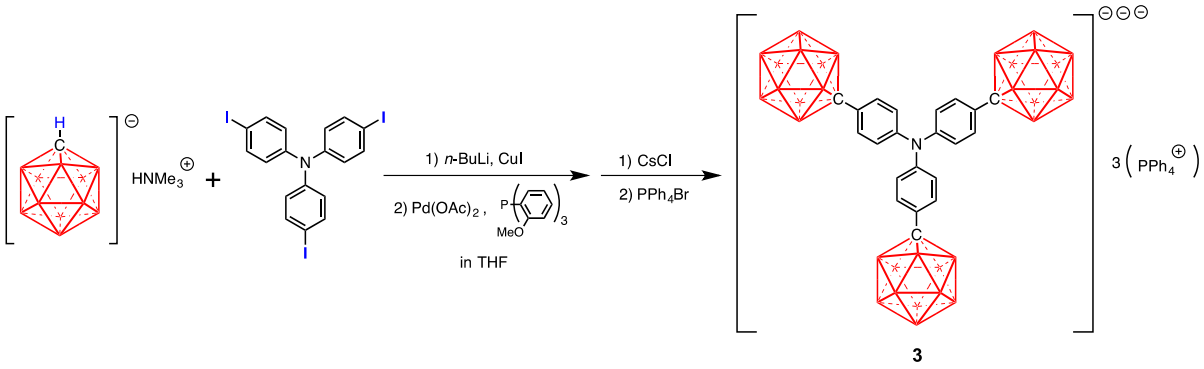

3

Scheme 1.4. Synthesis of compound **3**.

4,4'4"-tris(carba-*closo*-dodecaborate-1-yl)triphenylamine (3):

According to the same procedure as described for the preparation of **1**, pale yellow solid

$(PPh_4)_3$ • **3** (93 mg, 61.0 %) was obtained by using 4,4',4''-triiodotriphenylamine (0.15 g, 0.15 mmol); ^{1}H NMR (400MHz, tetrahydrofuran-d_8) δ 7.87-7.91 (m, 12H for PPh_4^+), 7.72-7.76 (m, 48H for PPh_4^+), 7.13 (d, J=8.8 Hz, 6H) 6.40 (d, J=8.5 Hz, 6H) ; ESI HRMS: *m*/*z* calcd for $C_{21}H_{45}NB_{33}$: 222.8941 (= 668.6823/3) $[M–3(PPh_4)]^{3–}$; found 222.8952.

1.2.2 DFT Calculations

Quantum chemical calculations were performed with using a hybrid Hartree–Fock/density functional theory (HF/DFT) method (B3LYP).[8] Full geometrical optimization for the ground S_0 state of **1**–**3** was carried out and furthermore, their local minimum structures were confirmed by performing subsequent frequency analyses. Full geometrical optimization for the excited S_1 state of **1**–**3** was carried out on the basis of time-dependent density functional theory (TD-DFT)[9] with the same functional. All the computations employed the 6-31+G* basis set.[10] All these computational approaches are implemented in Gaussian 09 package of ab initio MO calculation.[11]

1.2.3 Electrochemical Measurements

The redox properties were evaluated by cyclic voltammetry (CV) and differential pulse voltammetry (DPV) in CH_2Cl_2 solution at 298 K with 0.1 M tetra-*n*-butylammonium tetrafluoroborate ($TBABF_4$) as supporting electrolyte (scan rate 100 mV s^{-1}) using an ALS/chi Electrochemical Analyzer model 612A. A three-electrode assembly was used, which was equipped with a platinum disk (2 mm^2) and a platinum wire as the working and counter electrodes, respectively, and Ag/0.01 M $AgNO_3$ (acetonitrile) was used as the reference electrode. The redox potential were referenced

against a ferrocene/ferrocenium ($Fc^{0/+}$) redox potential measured in the same electrolytic solution.

1.2.4 Spectroelectrochemical Measurements

Spectroelectrochemical measurements were carried out with a custom-made optically transparent thin-layer electrochemical (OTTLE) cell (light pass length = 1 mm) equipped with a platinum mesh and a platinum coil as the working and counter electrodes, respectively, and Ag/0.01 M $AgNO_3$ (acetonitrile) was used as the reference electrode. The potential was applied with an ALS/chi Electrochemical Analyzer model 612A.

1.2.5 Photophysical Measurements

UV/Vis-NIR absorption spectra were obtained with a Perkin-Elmer Lambda 950 spectrometer. Fluorescence spectra were recorded on an absolute photoluminescence quantum yield measurement system (HAMAMATSU Quantaurus-QY).

1.3 Results and Discussion

With these points in mind, the author decided to investigate singly, doubly, and triply carborane-substituted triphenylamines **1**–**3** (Scheme 1.5). The target molecules **1**–**3** were successfully prepared from $[Me_3NH]^+[closo\text{-}CHB_{11}H_{11}]^-$ and the corresponding iodo-substituted triarylamine [*N*,*N*-bis(4-methoxyphenyl)-*N*-(4-iodophenyl)amine for **1**, *N*,*N*-bis(4-iodophenyl)-*N*-(4-methoxyphenyl)amine for **2**, and tris(4-iodophenyl)amine for **3**] by using palladium-catalyzed copper-mediated C–C cross-coupling reaction which has been recently developed by Uchiyama and co-workers.[13] The author has

finally obtained **1**–**3** as PPh_4^+ salts in 42, 22, and 61% yield, respectively, after successive counter ion exchange. These compounds were insoluble in nonpolar solvents due to their ionic character.

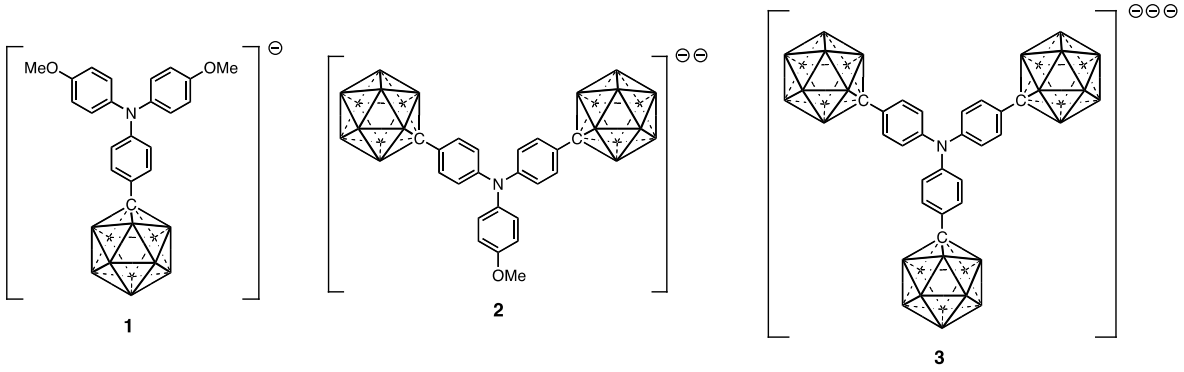

Scheme 1.5. Monocarba-closo-dodecaborate-substituted triphenylamines **1**–**3**. B atomic symbols in the carborane moieties are omitted for clarity.

For the carborane-substituted triphenylamines **1**–**3**, single reversible oxidation waves were observed at $E_{1/2}$ = +0.19 V (**1**), +0.30 V (**2**), and +0.35 V (**3**) vs $Fc^{0/+}$ by cyclic voltammetry in CH_2Cl_2 (Figure 1.5), indicating that the electron removal basically takes place from the triphenylamine core, although the oxidation potential increases with the number of carborane-substituents [$E_{1/2}$ = +0.13 V vs $Fc^{0/+}$ for TAA in CH_2Cl_2]. In addition, the absorption spectrum of **1**–**3** in CH_2Cl_2 (Figure 1.6) displayed a weak shoulder band similar to that of TAA (Figure 1.1a). Moreover, the absorption spectrum of oxidized species for **1**–**3** was also similar to that for the radical cation of TAA (Figure 1.6). These data provide evidence that the carborane-substitution does not influence on the electronic structure of triphenylamine core, in accordance with the aforementioned DFT results.

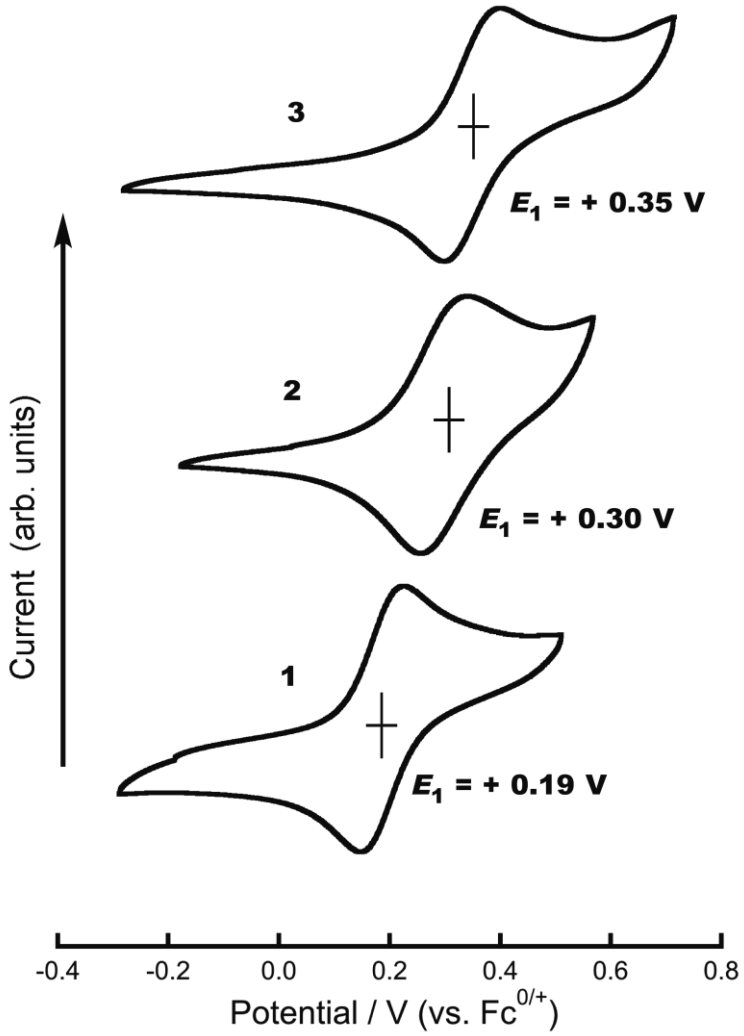

Figure 1.5. Cyclic voltammograms (CV) of **1**–**3**, measured in CH_2Cl_2 (at 1×10^{-3} M) containing 0.1 M *n*-Bu_4NBF_4 at 298 K (scan rate 100 mV s^{-1}).

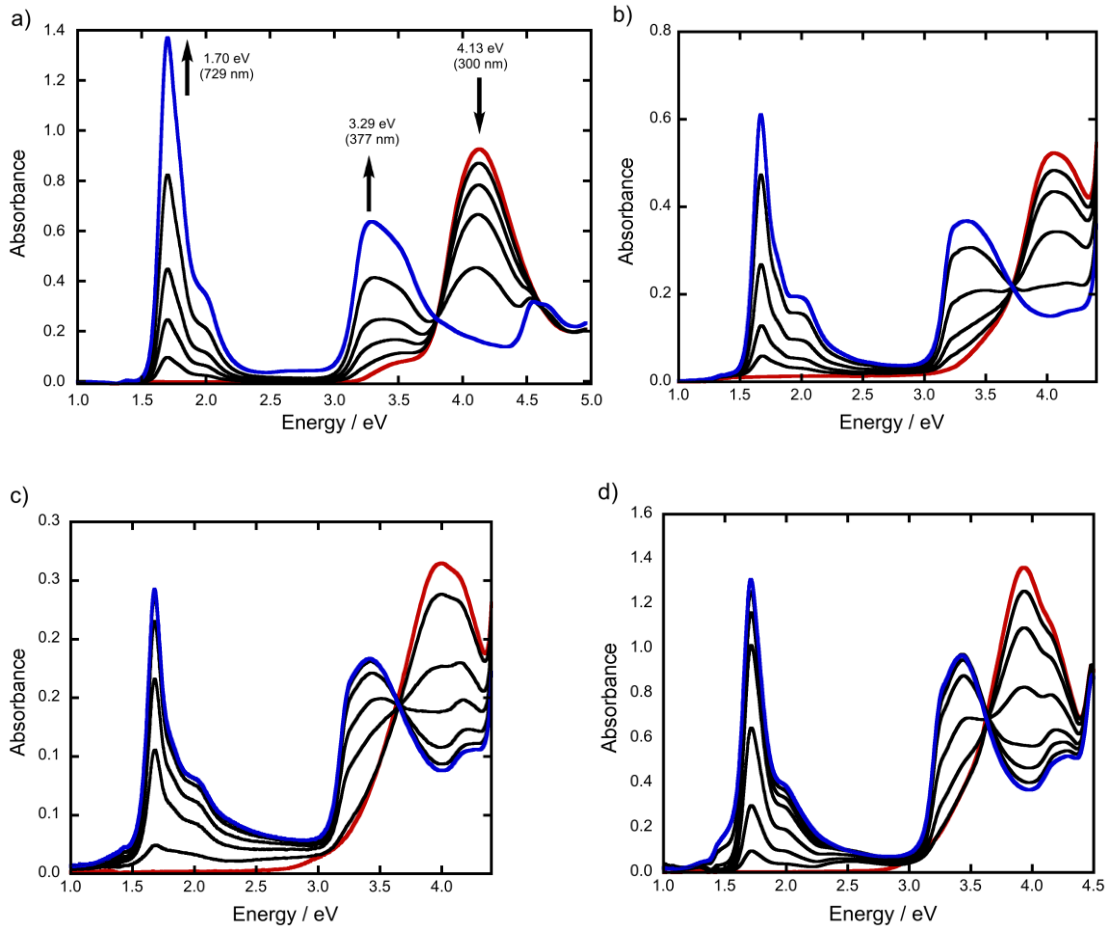

Figure 1.6. UV-vis-NIR absorption spectra of the stepwise electrochemical oxidation of a) TAA [from neutral (in red) to radical cation (in blue)], b) **1** [from anion (in red) to neutral radical (in blue)], c) **2** [from dianion (in red) to radical anion (in blue)], and d) **3** [from trianion (in red) to radical dianion(in blue)] in CH_2Cl_2 (at 1×10^{-4} M) containing 0.1 M *n*-Bu_4NBF_4 at 298 K.

In contrast with TAA, compounds **1**–**3** exhibited fluorescence in the blue to green visible region with good efficiency in CH_2Cl_2 solution (Figure 1.7a). The fluorescence data are summarized in Table 1.1 and the spectra of **1**–**3** are shown in Figure 1.7b. The emission maxima were blue-shifted with increasing number of carborane-substituents.

To elucidate the origin of the blue-shift in the emission spectra in connection with the number of carborane-substituents, the geometries for the adiabatic S_1 excited states of **1**–**3** were optimized with the TD-DFT methodology at the B3LYP/6-31+G* level of theory. The S_1-optimized structures of **1**–**3** are shown in Figure 1.8, in comparison with the corresponding S_0-optimized ones. For **1**, one of the two anisyl rings is considerably twisted along the C–N bond, and moreover, adopts an anti-quinoid structure with lengthened central benzene bonds and C-N bond in the S_1 excited state, whereas the phenyl ring which is directly linked with the carborane cluster takes an quinoid structure. Similar to **1**, the S_1 excited state of **2** has a twisted anti-quinoid anisyl ring. On the other hand, any salient structural deformations are not seen in the S_1 excited state of **3**, predicting the smallest geometry relaxation among three derivatives **1**–**3**.[14] The difference in these relaxed structures in the S_1 excited state is closely related to the vibrational relaxation, thus leading to the difference in emission maxima. The computed Stokes shifts (83 nm for **1**, 111 nm for **2**, 23 nm for **3**) qualitatively reproduce the observed trend of emission maxima for **1**–**3** (Table 1.1).

Table 1.1. Observed and TD-DFT calculated photophysical data for **1**–**3**.

Com	λ_{em} [nm] ([eV])[a,b]	Φ_f [c]	Transition (f [d])	λ_{calc} [nm] ([eV]) [e]	HOMO-LUMO [%] [f]
1	524 (2.37)	0.11	$S_1 \rightarrow S_0$ (0.009)	461 (2.69)	99
			[$S_1 \leftarrow S_0$ (0.016)	378 (3.28)	98]
2	500 (2.48)	0.14	$S_1 \rightarrow S_0$ (0.008)	483 (2.57)	99
			[$S_1 \leftarrow S_0$ (0.014)	372 (3.33)	33 [g]]
3	471 (2.63)	0.16	$S_1 \rightarrow S_0$ (0.009)	366 (3.39)	98
			[$S_1 \leftarrow S_0$ (0.010)	343 (3.61)	97]

[a] 1×10^{-5} M in CH_2Cl_2. [b] Emission maximum upon photoexcitation at 350 nm (3.54 eV). [c] Absolute quantum yield determined with a calibrated integrating sphere system. [d] Calculated oscillator strength. [e] Emission energies were evaluated as the reverse of excitation to S_1 from S_0 at the optimized S_1 geometries. [f] Contribution of HOMO–LUMO transition. [g] Dominant contribution was LUMO+1 ← HOMO (65%).

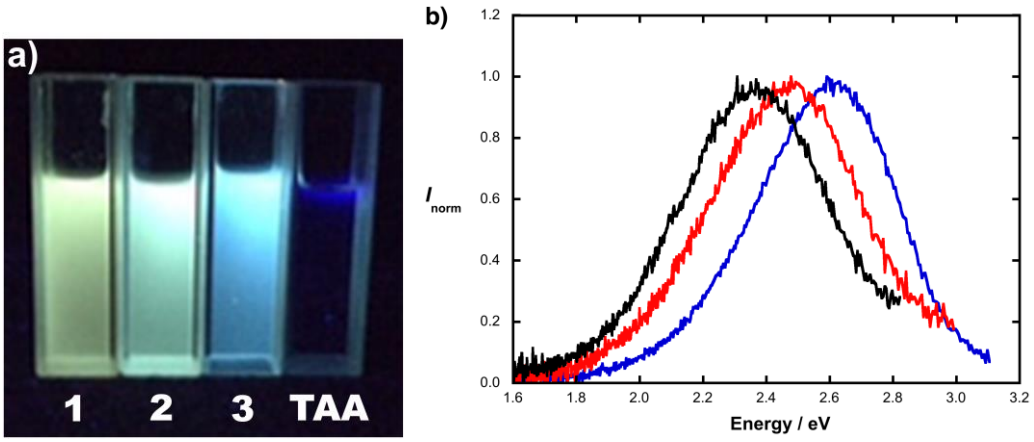

Figure 1.7. a) Photograph of the CH_2Cl_2 solution of compounds **1**–**3**, and TAA with UV irradiation at 365 nm. b) Fluorescence spectra of **1** (black), **2** (red), and **3** (blue) in CH_2Cl_2 at 1×10^{-5} M.

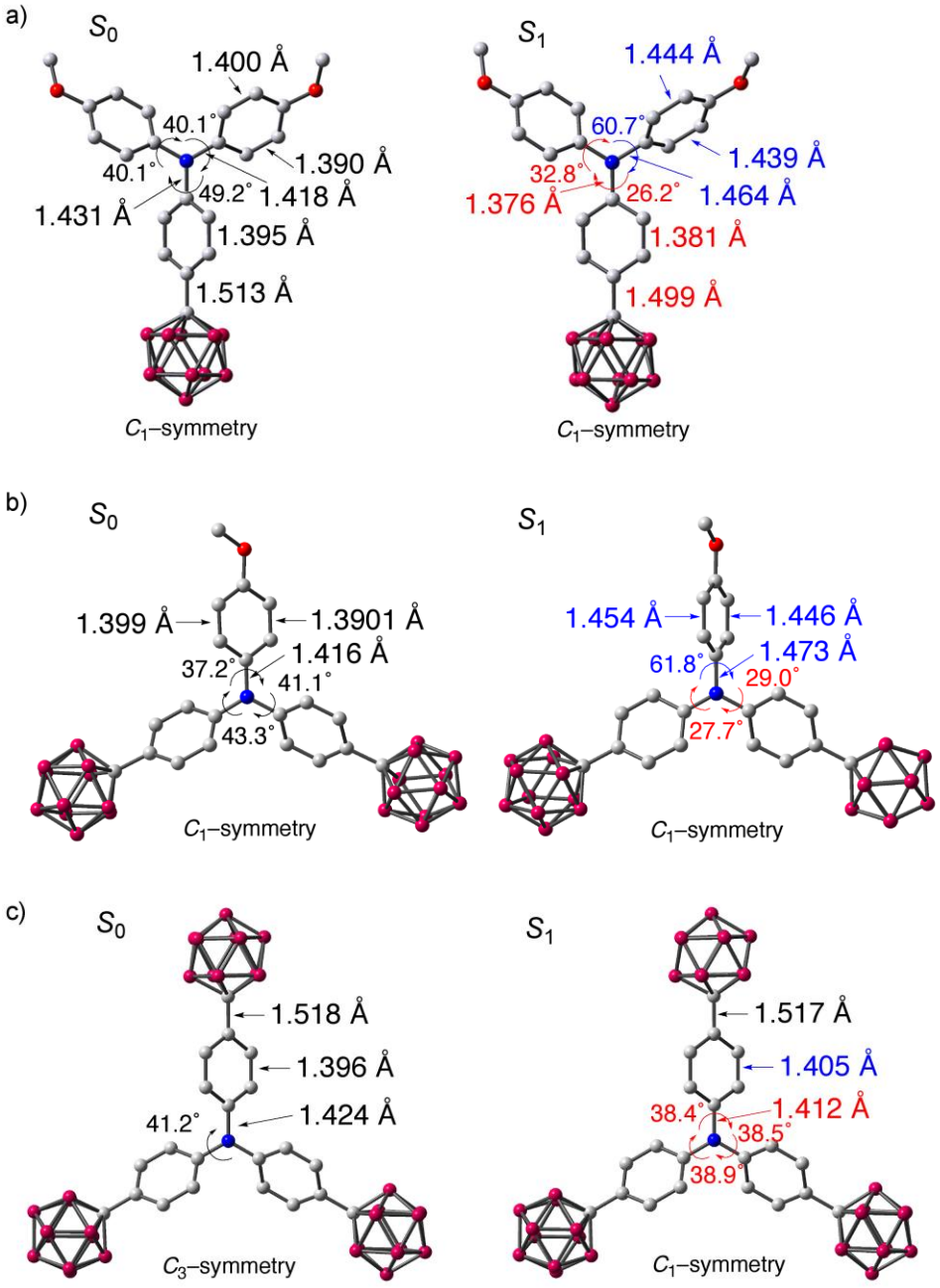

Figure 1.8. Comparison between the geometries of the DFT-optimized S_0 state (left) and the TD-DFT-optimized S_1 state (right) of a) **1**, b) **2**, and c) **3** at the B3LYP/6-31+G* level of theory. The selected geometrical parameters showing noticeable changes are shown, and the blue and red figures represent the enlarged and reduced geometrical parameters, respectively, in the S_1 excited state. Hydrogen atoms are omitted for clarity.

1.4 Conclusion

In conclusion, the molecular design based on reduced vibronic coupling analysis[7] succeeded in achieving the desired emission efficiency for triphenylamine as a typical non-fluorescent parent compound by substituting carborane clusters, as has been clarfied by newly prepared singly, doubly, and triply carborane-substituted triphenylamine derivatives **1**–**3**. Carborane substituents take an active role in reducing distribution of the HOMO in parent unsubstituted π-conjugated molecular moieties, without any influence on the LUMO, by partial delocalization of the HOMO to the carborane substituents, thus leading to the suppression of non-radiative decay in light-emitting compounds. This molecular design principle is also expected to be applicable to various non-fluorescent π-conjugated molecular systems and further work on this line is currently under investigation.

1.5 References

[1] a) U. Mitschke, P. Bäuerle, *J. Mater. Chem*. **2000**, *10*, 1471-1507; b) H. Sasabe, J. Kido, *J. Mater. Chem. C*. **2013**, *1*, 1699-1707.

[2] M. Zhu, C. Yang, *Chem. Soc. Rev*. **2013**, *42*, 4963-4976.

[3] According to the Strickler-Berg equation [S. J. Strickler, R. A. Berg, *J. Chem. Phys.* **1962**, *37*, 814-822.], a weak absorption band relating to the $S_1 \leftarrow S_0$ transition results in a small value of the corresponding fluorescence rate constant, leading to the low fluorescence efficiency.

[4] The author has evaluated the light-emitting property of trianisylamine (TAA) by fluorescence spectroscopy, and a CH_2Cl_2 solution of TAA showed a considerably weak fluorescence band (Φ_F = 0.01) at 400 nm. Non-fluorescent property of triarylamines has also been recently reported in MeCN solution: C. Quinton, V. Alain-Rizzo, C. Dumas-Verdes, F. Miomandre, G. Clavier, P. Audebert, *RSC Adv*. **2014**, *4*, 34332-34342.

[5] a) M. Uejima, T. Sato, K. Tanaka, H. Kaji, *Chem. Phys*. **2014**, *430*, 47-55; b) M. Uejima, T. Sato, M. Detani, A. Wakamiya, F. Suzuki, H. Suzuki, T. Fukushima, K. Tanaka, Y. Murata, C. Adachi, H. Kaji, *Chem. Phys. Lett*. **2014**, *602*, 80-83.

[6] a) T. Sato, K. Tokunaga, K. Tanaka, *J. Phys. Chem. A*. **2008**, *112*, 758-767.; b) T. Sato, M. Uejima, N. Iwahara, N. Haruta, K. Shizu, K. Tanaka, *J. Phys.: Conf. Ser*. **2013**, *428*, 0120101-19.

[7] Y. Kameoka, M. Uebe, A. Ito, T. Sato, K. Tanaka, *Chem. Phys. Lett*. **2014**, *615*, 44-49.

[8] K. Ragavachari, *Theor. Chem. Acc*. **2000**, *103*, 361-363 and references cited therein.

[9] A. Dreuw, M. Head-Gordon, *Chem. Rev.* **2005**, *105*, 4009-4037.

[10] W. J. Hehre, L. Radom, P.v. R. Schleyer, J. A. Pople, *Ab Initio Molecular Orbital*

Theory, Wiley, New York, **1986**.

[11] M. J. Frisch, *et al*., Gaussian 09 (Revision D.01), Gaussian, Inc., Wallingford CT, **2013**.

[12] C. Douvris, J. Michl, *Chem. Rev*. **2013**, *113*, 179-233.

[13] J. Kanazawa, R. Takita, A. Jankowiak, S. Fujii, H. Kagechika, D. Hashizume, K. Shudo, P. Kaszyński, M. Uchiyama, *Angew. Chem. Int. Ed*. **2013**, *52*, 8017-8021.

[14] The origin of the smallest vibrational relaxation for **3** can be ascribed to the fact that the higher symmetric structure of **3** as compared to the other derivatives **1** and **2** leads to the smallest diagonal vibronic coupling constants at the Franck-Condon state: see ref. [5].

Chapter 2

Electronic and Photophysical Properties of Anthraceneamines Substituted by Organoboron

2.1 Introduction

Today, light-emitting molecules continue to attract great interest in conjunction with their device application such as organic light-emitting diodes (OLEDs),[1] and thus, various kinds of fluorescent molecules have already been so far prepared.[2] Oligoarylamines are highly important substances as hole-transporting materials in OLED device and solar cell.[3] However, they are non-fluorescent molecules.[4] Recently, it has been reported that aryl amines that are introduced with organoboron have donor-acceptor unique electrochemical and photophysical properties. These compounds have dipolar organic chromophores with donor-π-acceptor (D-π-A) motifs, where the electron donor and acceptor moieties are suitably substituted at the periphery of the π-conjugated system for efficient excited-state intramolecular charge transfer (ICT).[5-15] The photophysical properties of such “push-pull” molecular systems depend on a choice

of π-bridging units and a suitable combination of electron-donor (D) and electron-acceptor (A) substituents.

In this work, we synthesized new donor-acceptor compounds **1** and **2** that have anthracene as π-bridging unit (Scheme 2.1). We predicted that these compounds have solid-state fluorescence because they have perpendicular structure due to steric effect of anthracene. These compounds were characterized by analysis of crystal structure and cyclic voltammetry, ESR and UV/vis absorption, fluorescence spectroscopy.

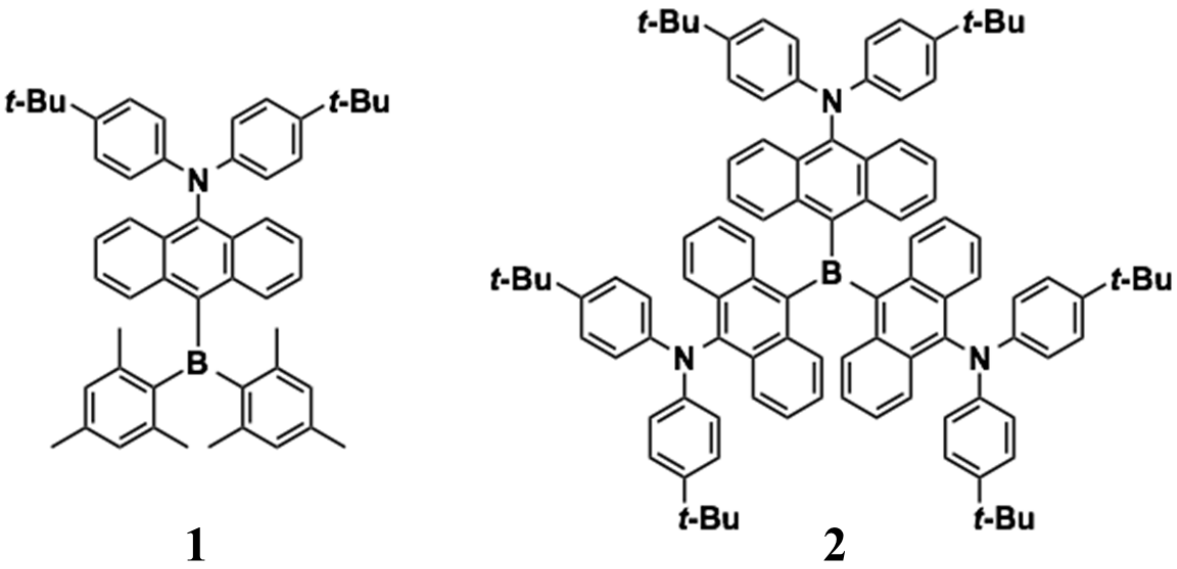

Scheme 2.1. Molecular Structure of **1** and **2**.

2.2 Experimental Section

2.2.1 Synthesis

All the purchased reagents were of standard quality, and used without further purification. All the purchased solvents were purified, dried, and degassed by standard procedures. Column chromatography was performed with silica gel (Kanto Chemical

Co., Inc., silica gel 60N, spherical neutral). Elemental analyses were performed by Center for Organic Elemental Microanalysis, Kyoto University. ^{1}H and ^{13}C NMR spectra were measured by a JEOL JNM-AL400 FT-NMR spectrometer. Chemical shifts of NMR spectra are determined relative to internal tetramethylsilane (TMS) standard (δ), and are given in parts per million (ppm).

N,N-Bis(4-tert-butylphenyl)-9-anthraceneamine (3): Under a Argon atmosphere, N,N-Bis(4-tert-butylphenyl)amine (5.15 g, 20 mmol), 9-bromoanthracene (5.63 g 20 mmol), $P(t\text{-}Bu)_3HBF_4$ (0.35 g, 1.2 mmol), $Pd(dba)_2$ (0.35 g, 0.6 mmol), and NaOt-Bu (2.9 g, 30 mmol) were suspended in toluene (75 mL) and stirred at Reflux for 24 h. The reaction mixture was washed with Brine and dried over Na_2SO_4. After evaporation of the solvent, silica gel column chromatography with toluene afforded **3** (7.40 g, 77.4%) as yellow solid. ; ^{1}H NMR (400MHz, $CDCl_3$) δ 8.50 (s, 1H), 8.15 (d, 4H, *J*=7.81), 8.06 (d, 4H, *J*=7.81), 7.43-7.47 (m, 4H), 7.37-7.41 (m, 4H), 7.13-7.17 (m, 4H), 6.97-7.01 (m, 4H), 1.26 (s, 18H); ^{13}C NMR (100MHz, $CDCl_3$) 145.23, 143.37, 137.59, 132.79, 130.88, 128.76, 126.52, 126.44, 125.81, 125.40, 124.70, 119.50, 34.50, 31.39 ; ESI HRMS: m/z calcd for $C_{34}H_{35}N$: 457.2764 $[M]^+$; found 457.2758; Elem. Anal. Calcd (%) for C 89.28, H 7.66, N 3.06; found C 89.25, H 7.85, N 3.07.

10-Bromo-N,N-Bis(4-tert-butylphenyl)-9-anthraceneamine (4): Under a Argon atmosphere, to a 200 mL of chloroform solution of N,N-Bis(4-tert-butylphenyl)-9-anthraceneamine (6.87 g, 15 mmol), N-bromosuccinimide (NBS) (2.76 g, 15.5 mmol) in DMF was added in small portions at 0˚C. After stirring at room temperature for 24 h, the reaction mixture was washed

with aqueous solution of Na_2SO_3, aqueous solution of $NaHCO_3$, and water. And then the organic layer was dried over Na_2SO_4. After evaporation of the solvent, silica gel column chromatography with toluene afforded **4** (6.80 g, 84.4%) as yellow solid. ^{1}H NMR (400 MHz, $CDCl_3$) δ 7.46-7.50 (m, 4H), 7.00-7.04 (m, 2H), 6.81-6.86 (m, 2H), 6.75-6.79 (m, 4H), 3.75 (s, 3H); ^{13}C NMR (100 MHz, $CDCl_3$): δ 156.7, 147.4, 139.5, 138.1, 127.6, 124.7, 115.0, 84.7, 55.5 ; ESI HRMS: m/z calcd for $C_{34}H_{34}NBr$: 583.1869 $[M]^+$; found 583.1867; Elem. Anal. Calcd (%) for C 76.12, H 6.34, N 2.61, Br 14.93; found C 75.13, H 6.40, N 2.60, Br 14.37.

10-(Dimesitylboryl)-N,N-Bis(4-tert-butylphenyl)-9-aminoanthracene (1): Under a Argon atmosphere, butyllithium (2 mL, 3.2 mmol, 1.6 M in hexane)was added to a stirred solution of **4** (1.60 g, 3 mmol) in 20 mL Et_2O at -78 ℃. The reaction mixture was stirred for 15 min at -78 ℃ and then a solution of dimesitylboranefluoride (0.80 g, 3 mmol) in 10 mL Et_2O was added. After stirring for 24 h at room temperature, the reaction mixture was suspended in CH_2Cl_2 and washed with Brine and dried over Na_2SO_4. After evaporation of the solvent, silica gel column chromatography with CH_2Cl_2:hexane = 1:1 afforded 1 (0.84 g, 39.5%) as yellow solid. ; ^{1}H NMR (400MHz, CD_2Cl_2) δ 7.99-8.60 (m, 4H), 7.24-7.18 (m, 2H), 7.13-7.09 (m, 2H), 7.09 (d, 4H, *J*=8.54), 6.89 (d, 4H, *J*=8.54), 6.83+6.60 (s+s, 2H+2H), 2.20 (s, 6H), 2.10+1.60 (s+s, 6H+6H), 1.17 (s, 18H) ; ^{13}C NMR (100 MHz, CD_2Cl_2): δ 147.5, 145.9, 145.5, 144.1, 141.4, 141.0, 140.5, 140.2, 135.5, 130.7, 129.6, 129.4, 126.5, 126.3, 125.4, 119.7, 34.4, 31.5, 23.6, 21.4 ; ESI HRMS: m/z calcd for $C_{52}H_{56}NB$: 705.4500 $[M]^+$; found 705.4492; Elem. Anal. Calcd (%) for C 88.51 H 7.94, N 1.99; found C 87.20, H 7.99, N 1.99.

Tris{N,N-Bis(4-tert-butylphenyl)-9-aminoanthryl}borane (2): Under a Argon atmosphere, butyllithium (4.4 mL, 7 mmol, 1.6 M in hexane)was added to a stirred solution of **4** (3.49 g, 6.5 mmol) in 50 mL Et_2O at -78 ℃. The reaction mixture was stirred for 15 min at -78 ℃ and then a solution of $BF_3 \cdot OEt_2$ (0.28 g, 2 mmol) was added. After stirring for 24 h at room temperature, the reaction mixture was suspended in CH_2Cl_2 and washed with Brine and dried over Na_2SO_4. After evaporation of the solvent, silica gel column chromatography with CH_2Cl_2:hexane=1:3 afforded 2 (1.57 g, 56.8%) as red solid. ; ^{1}H NMR (400MHz, $CDCl_2$) δ 8.15-8.20 (m, 12H), 7.25-7.30(m, 6H), 7.18-7.22 (m, 12H), 6.98-7.02 (m, 12H), 6.94-6.99 (m, 6H), 1.26 (s, 54H); ^{13}C NMR (100 MHz, $CDCl_2$) δ 149.1, 145.6, 144.4, 142.4, 136.6, 131.3, 129.7, 126.9, 126.7, 126.5, 125.9, 120.1, 34.6, 31.7 ; ESI HRMS: m/z calcd for $C_{102}H_{102}N_3B$: 1380.8178 $[M]^+$; found 1380.8178 ; Elem. Anal. Calcd (%) for C 88.51 H 7.94, N 1.99; found C 88.76, H 7.40, N 3.04.

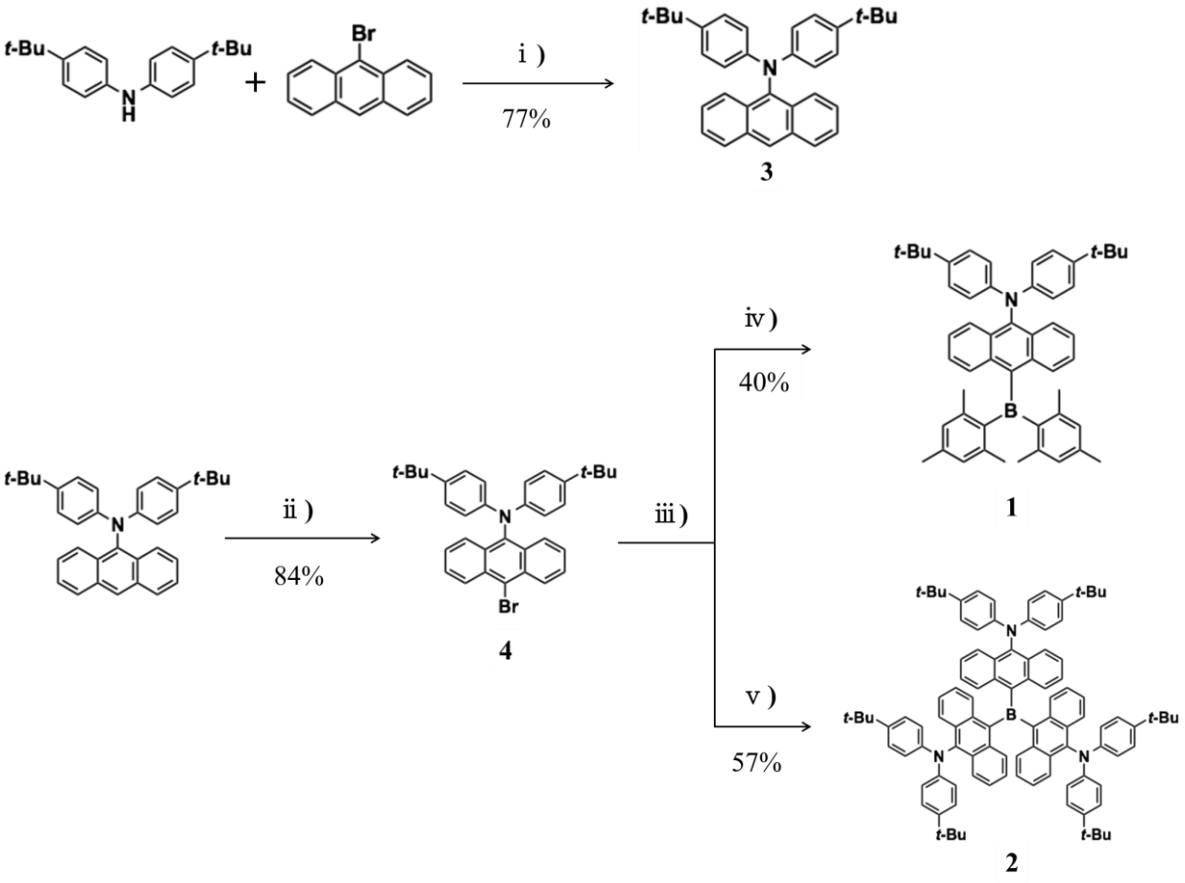

Scheme 2.2. Synthesis of **1** and **2**. i) P(*t*-Bu)$_3$HBF$_4$, Pd(dba)$_2$, NaO*t*-Bu, toluene ; ii) NBS in DMF, CHCl$_3$, iii) BuLi, Et$_2$O ; iv Mes$_2$BF, Et$_2$O ; v) BF$_3$·Et$_2$O, Et$_2$O.

2.2.2 DFT Calculations

Quantum chemical calculations were performed with using a hybrid Hartree–Fock/density functional theory (HF/DFT) method (B3LYP).[16] Full geometrical optimization for the ground S_0 state of **1** and **2** was carried out and furthermore, their local minimum structures were confirmed by performing subsequent frequency analyses. Excitation energies were examined by means of the time-dependent density functional theory (TD-DFT)[17] based on the (U)B3LYP/6-31G*-optimized structures. All the computations employed the 6-31G* basis set.[18] All these

computational approaches are implemented in Gaussian 09 package of ab initio MO calculation.[19]

2.2.3 X-ray crystal structure analysis

Crystallographic data for **1** were collected on a Rigaku XtaLAB mini diffractometer at 93±1 K using graphite-monochromated Mo Kα radiation (λ = 0.71075 Å) from a rotating anode operating at 50 kV and 12 mA. The structures were solved by direct method (SIR2008[20]) and refined by full-matrix least-squares procedures on F^2 (SHELXL-97[21]). The non-hydrogen atoms were refined anisotropically. All the hydrogen atoms were located on the calculated positions, and refined as a riding model. All calculations were performed using the CrystalStructure crystallographic software package (versions 4.0; Rigaku Corporation), except for the refinement, which was performed using SHELXL-97.

2.2.4 Electrochemical Measurements

The redox properties were evaluated by cyclic voltammetry (CV) and differential pulse voltammetry (DPV) in CH_2Cl_2 (oxidation) and THF(reduction) solution at 298 K with 0.1 M tetra-*n*-butylammonium tetrafluoroborate ($TBABF_4$) as supporting electrolyte (scan rate 100 mV s^{-1}) using an ALS/chi Electrochemical Analyzer model 612A. A three-electrode assembly was used, which was equipped with a platinum disk (2 mm^2) and a platinum wire as the working and counter electrodes, respectively, and Ag/0.01 M $AgNO_3$ (acetonitrile) was used as the reference electrode. The redox potential were referenced against a ferrocene/ferrocenium ($Fc^{0/+}$) redox potential measured in the same electrolytic solution.

2.2.5 Spectroelectrochemical Measurements

Spectroelectrochemical measurements were carried out with a custom-made optically transparent thin-layer electrochemical (OTTLE) cell (light pass length = 1 mm) equipped with a platinum mesh and a platinum coil as the working and counter electrodes, respectively, and Ag/0.01 M $AgNO_3$ (acetonitrile) was used as the reference electrode. The potential was applied with an ALS/chi Electrochemical Analyzer model 612A.

2.2.6 ESR Measurements

Cw-ESR Spectra were recorded on a JEOL JES-TE200 X-band ESR spectrometer, in which temperature was controlled by a JEOL ES-DVT3 variable-temperature unit in the range of 193-293 K.

2.2.7 Photophysical Measurements

UV/Vis-NIR absorption spectra were obtained with a Perkin-Elmer Lambda 950 spectrometer. Fluorescence spectra were recorded on an absolute photoluminescence quantum yield measurement system (HAMAMATSU Quantaurus-QY).

2.3 Results and Discussion

2.3.1 Synthesis

The synthesis of **1** and **2** is outlined in Scheme 2.2 The diphenylamino-anthracene **3** was synthesized by Buchward-Hartwig coupling.[22,23] And then, Compound **4** was synthesized by boromination of **3**. After lithiation of **4**, reaction of aryllithium with dimesitylfluoroborane or trifuluoroborane yielded **1** and **2**, respectively. As shown in

Figure 2.1, the room temperature ^{1}H NMR spectra of **1** in toluene-d_8 showed two broad singlet signal at 6.57 ppm and 6.80 ppm, which can be assigned to the mesityl proton at the positions *meta* to the boron atom (*m*-Mes). The author carried out the variable temperature ^{1}H NMR measurement in the temperature range from 293 K to 353 K. From 313 K, these two signals gradually broadened with increasing temperature, and finally coalesced into one sharp signal at 353 K. This result was caused by anthracene steric effect. As mentioned below, crystal structure of **1** showed that rotary motion of methyl at the position of mesityl was inhibited by anthracene proton. On the basis, the activation energy for rotational barriers ($\Delta G^{\ddagger}$) was estimated as 15.8 kcal mol^{-1}.[24]

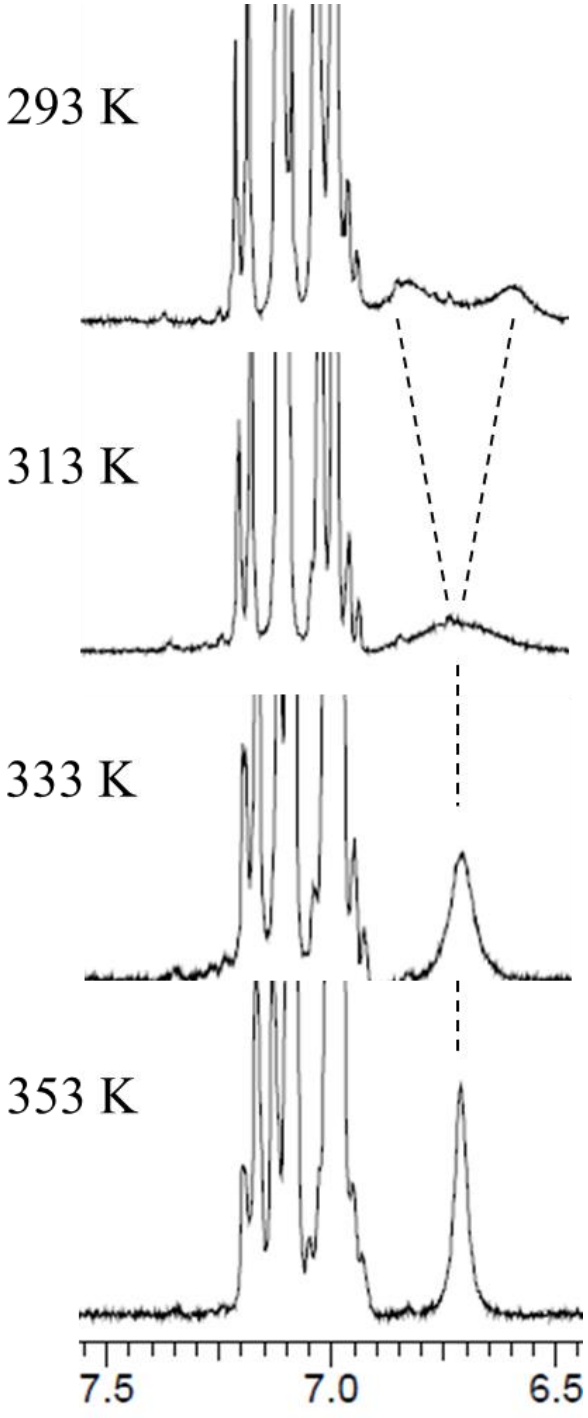

Figure 2.1. VT ^{1}H NMR spectra of **1** in toluene-d_8.

2.3.2 Molecular and electronic structures in the neutral state

To understand the electronic states of these compounds further, and to examine the orbitals involved in the electronic transitions, the author carried out DFT calculations. The ground-state structures of **1** and **2** were optimized at the B3LYP/6-31G* level of theory using the molecular structure of **1** from X-ray diffraction measurement and C_3-symmetry **2** from a part of **1** as starting geometries. The frontier Kohn-Sham orbitals of **1** and **2** are shown in Figure 2.2. The HOMO of **1** is localized on anthrylamine moiety and LUMO of **1** is localized on anthrylborane moiety. Compound **2** has two degeneracy anthrylamine-localized HOMOs due to C_3-symmetry. LUMO is three-anthrylborane moiety. The interaction between boron p-orbiral and three-anthryl π-orbirals lower the LUMO energy level. And the first excited singlet state (S_1) **1** and **2** are expected to be described by a transition from the amine-localized HOMO to the boron-localized LUMO, that is, a transition of ICT.

Slow evaporation of a dilute mixed solution (*n*-Hexane/CH_2Cl_2) of a yellow product **1** gave yellow single crystals suitable for X-ray structure analysis. However, we could not obtain single crystals suitable for X-ray structure analysis of compound **2**. Compound **1** crystalized in the triclinic space group $P\bar{1}$ (Table 2.1). As shown in Figure 2.3, the molecular structure of **1** in the crystal showed a planar conformation at the nitrogen and boron centers, respectively, as is apparent from the sum of the C–N–C and C–B–C angles (359.6˚ for the nitrogen center and 360˚ for the boron center). The intramolecular separation between the nitrogen and boron centers was 5.841(6) Å. As is expected from the steric congestion between the 9,10-anthrylene and the bulky diarylamino and diarylboryl groups, the NC_3 and BC_3 planes were considerably twisted against the anthrylene π-face (torsion angles of 81.2˚ and 59.2˚, respectively). Because

of the overcrowded structure of **1**, the adjacent anthracene cores are fully separated from each other (Figure 2.4). The packing arrangement of **1** revealed a slipped stacked motif along the *a*-axis with the interplanar separation of 7.04 Å between parallel anthrylene π-faces of two molecules (Figure 2.4b), thus indicating no clear evidence of π-π interactions between the stacked anthracene cores. Such a crystal structure can contribute to an effective suppression of fluorescence quenching of **1** in the solid state (vide infra).

(a)

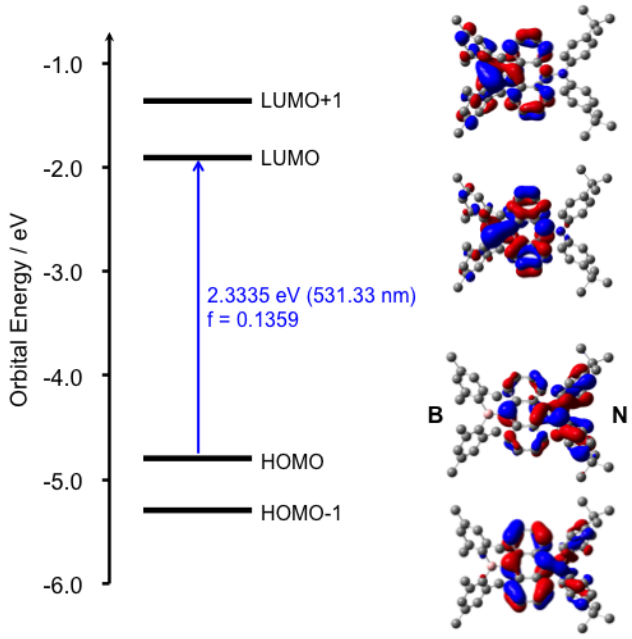

(b)

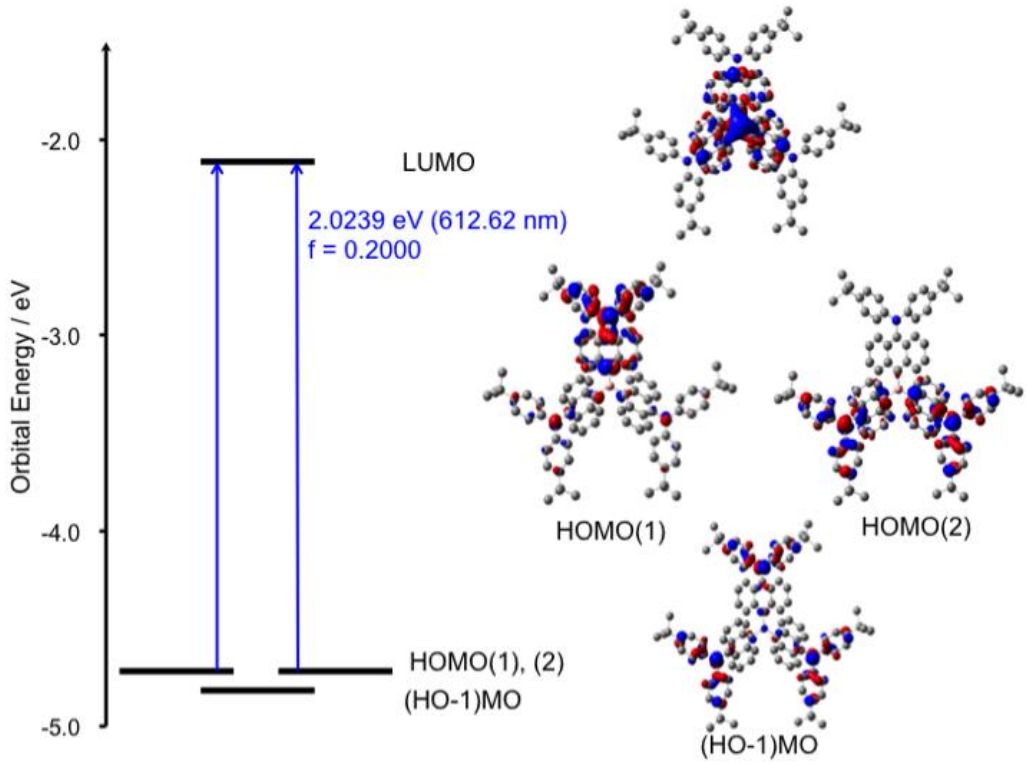

Figure 2.2. Schematic drawing the frontier Kohn-Sham orbitals for **1** and **2** at the B3LYP/6-31G* level theory.

Table 2.1: Selected crystallographic data for compound **1**.

Empirical formula	$C_{52}H_{56}BN$
Formula weight	705.83
Crystal color, habit	yellow, block
Crystal size [mm^3]	0.350×0.250×0.100
T [K]	93±1
Crystal system	triclinic
Space group	$P\bar{1}$ (#2)
a [Å]	8.070(9)
b [Å]	14.129(14)
c [Å]	19.29(2)
α [∨]	74.76(3)
β [∨]	78.97(3)
γ [∨]	81.27(4)
V [$Å^3$]	2071(4)
Z	2
ρ_{calcd} [g cm^{-3}]	1.132
Φ(000)	760.00
λ [⊕]	MoKα / 0.71075
$2\theta_{\mu\alpha\xi}$ [∨]	50.4
Collected data	19071
Unique data / R_{int}	7389/0.0471
No. of parameters	499
Reflection/Parameter Ratio	14.81
Goodness-of-fit on F^2	1.093
R_1 [$I > 2\sigma$], wR_2 (all reflections)	0.0682, 0.1791
Residual density [e $Å^{-3}$]	0.28/-0.29

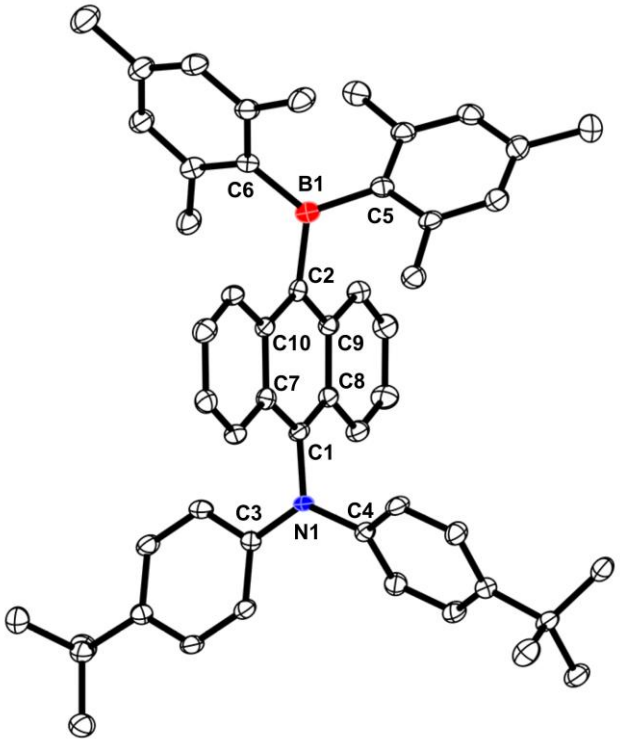

Figure 2.3. ORTEP diagram of **1** (determined from the X-ray structural analysis at 93 K). Hydrogen atoms are omitted for clarity; the thermal ellipsoids are shown at the 50% probability level. Selected bond lengths (Å): N1–C1 1.427(3); N1–C3 1.409(4); N1–C4 1.424(4); B1–C2 1.585(4); B1–C5 1.582(5); B1–C6 1.562(4). Dihedral angles: C3–N1–C1–C7 85.0(3)˚; C4–N1–C1–C8 78.6(3)˚; C10–C2–B1–C6 –61.5(3)˚; C9–C2–B1–C5 –55.1(3)˚.

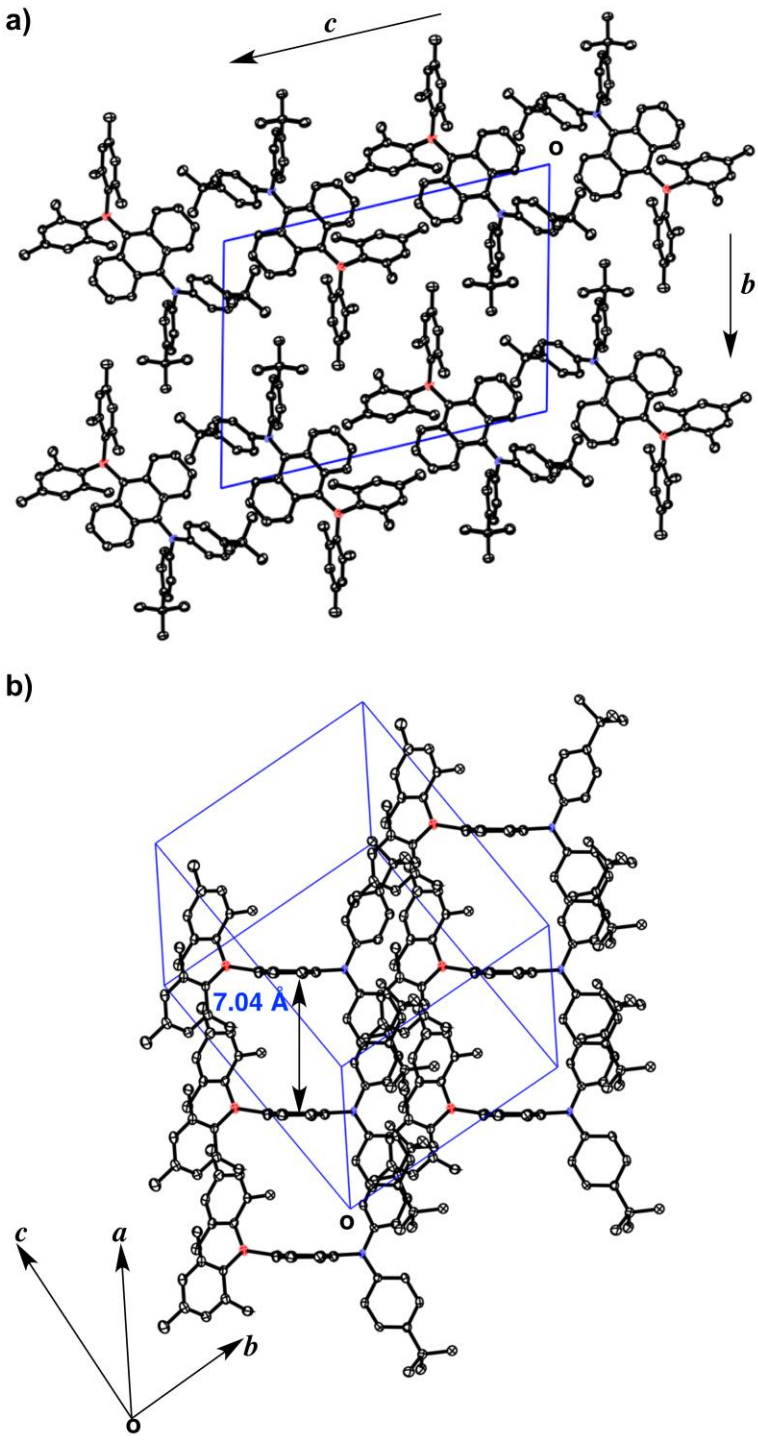

Figure 2.4. Molecular packing of **1** in the crystal viewed down a) the *a*-axis and b) the slipped stacked motif along the *a*-axis. Hydrogen atoms are omitted for clarity; boron and nitrogen atoms are colored in red and blue, respectively.

2.3.3 Electrochemistry and electrospectrochemistry

Information about the frontier orbital energies and the stability of radical ions in solution of **1** and **2** was obtained by cyclic voltammetry (CV) and differential pulse voltammetry (DPV) in CH_2Cl_2 (for oxidation) and in THF (for reduction) using *n*-Bu_4NBF_4 as electrolyte. The corresponding oxidation and reduction potentials are summarized in Table 2.2. For **1**, single reversible oxidation waves were observed at $E_{1/2}$ = +0.43 V vs $Fc^{0/+}$ in CH_2Cl_2, indicating that the electron removal basically takes place from the triarylamine core. On the other hand, single irreversible oxidation peak potential for **2** were observed at E_{ox} = +0.64 V vs $Fc^{0/+}$ in CH_2Cl_2. **2** was found to be decomposed after three electron oxidation. From the simulation of the observed differential pulse voltammogram (DPV), the oxidation process of **2** correspond to the generation of trication (quasi-three-electron transfer: 0.45 V (1e), 0.52 V (1e), and 0.58 V (1e)) can be judged. The reduction waves ($E_{1/2}$(red)) observed for **1** and **2** are ascribed to those of the triarylborane cores; $E_{1/2}$(red) at -2.20 and -1.88 V, respectively. The reduction potential of **2** showed a negative shift of 0.32 V compared to that of **1**, indicating that **2** has a stronger electron-accepting property than **1**, owing to the effective orbital interaction between three anthracene and boron atom. This observation is in good correlation with the DFT-calculated HOMO and LUMO levels (Table 2.2). The electrochemical band gaps of **1** and **2** were thus determined to be 2.63 and 2.33 eV, respectively, in good accordance with the optical band gaps, as described below.

Table 2.2. Electrochemical potentials[a] by CV (scan rate: 0.1 V s^{-1}) and DPV at room temperature, and electrochemically estimated and DFT-computed (B3LYP/6-31G*) HOMO and LUMO energies.

					Electrochemical [f]		DFT	
Comp	E_{1ox} [b] / V	E_{2ox} [b] / V	E_{3ox} [b] / V	E_{1red} [c] / V	HOMO / eV	LUMO / eV	HOMO / eV	LUMO / eV
1	+0.43 [d]	—	—	-2.20 [d]	-5.23	-2.60	-4.77	-1.91
2	+0.45 [e]	+0.53 [e]	+0.60 [e]	-1.88 [d]	-5.25	-2.92	-4.78	-2.28

[a] Potentials are given vs. ferrocene/ferrocenium redox couple ($Fc^{0/+}$).

[b] Measured in CH_2Cl_2.

[c] Measured in THF.

[d] Half-wave potential by CV measurement.

[e] Determined by DPV simulation.

[f] Estimated assuming that the HOMO energy of ferrocene lies 4.80 eV below the vacuum level (see ref 25)

In order to clarify the electronic properties of the cationic states of **1** and **2**, the absorption spectral changes upon electrochemical oxidation were measured by the spectral electronic method. Figure 2.5a shows the spectral changes during the oxidation processes from neutral **1** to $\mathbf{1}^{+}$. In this oxidation process, a new absorption band at 0.88 eV, 1.78 eV, and 3.44 eV appeared. By the result of the TD-DFT calculation, the lowest band (0.88 eV) was assignable to the charge transfer transition from the anthracene core and amino radical cationic moiety. The next lowest band (1.78 eV) was assignable to the anthracene radical cation band possessing vibrational structure[26] and the aminium radical cation band[27]. Figure 2.5b showed the spectral changes during the oxidation processes from neutral **2** to $\mathbf{2}^{+}$. In this oxidation process, a new absorption band at 0.91 eV, 1.73 eV, and 3.54 eV appeared. By the result of the TD-DFT calculation, the lowest band (0.91 eV) was assignable to the charge transfer band from anthracene core and aminoradical moiety. The second lowest band (1.78 eV) is assignable to the anthracene radical cation band possessing vibrational structure and the aminium radical cation band. These absorption bands were similar to $\mathbf{1}^{+}$. However, as the oxidation potential was increased, the spectrum of **2** decayed. And low intensity of the absorption bands suggested the decomposition of the oxidized species of **2**. This result accorded with cyclic voltammogram of **2** which was irreversible oxidation peak potential for **2**.

(a)

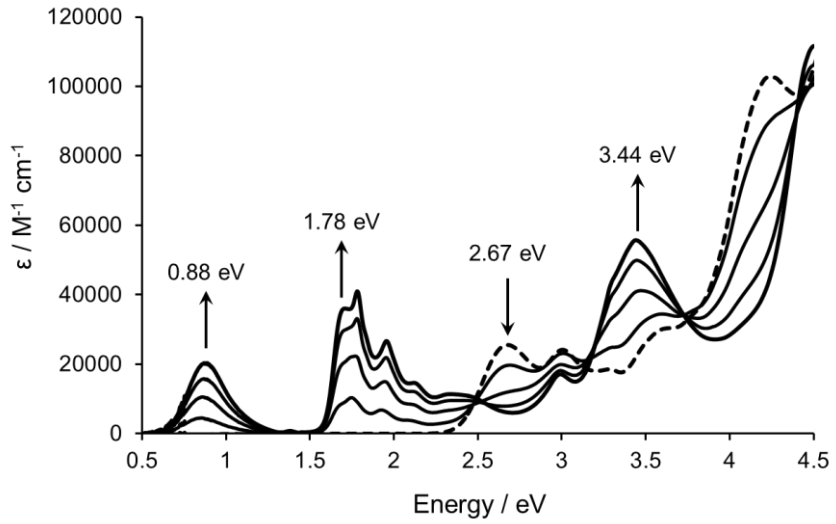

(b)

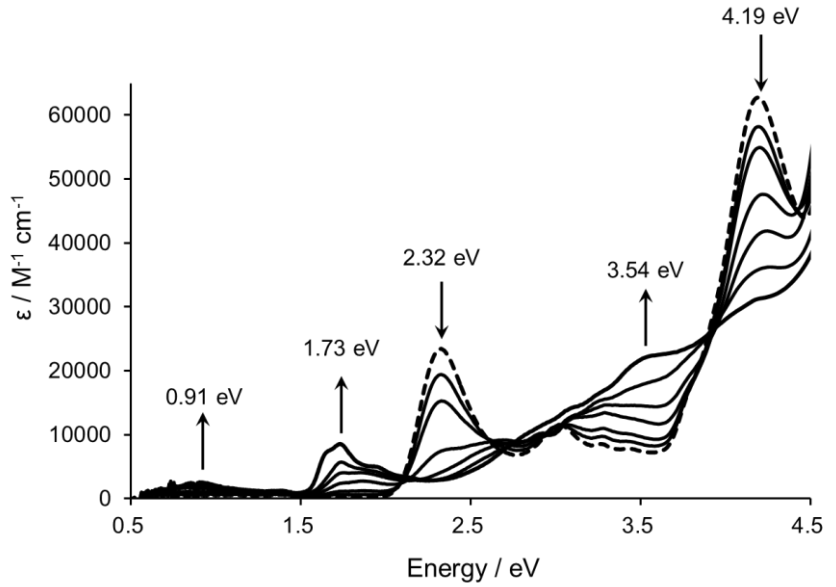

Figure 2.5. UV-vis-NIR absorption spectra of the stepwise electrochemical oxidation of **1** (a) and **2** (b) measured in CH_2Cl_2 (at 1×10^{-3} M) containing 0.1 M n-Bu_4NBF_4 at 298 K.

2.3.4 ESR Spectroscopy

The ESR spectrum of $\mathbf{1}^+$ generated by chemical oxidation of **1** by 0.5 equivalent of antimony pentachloride in dichloromethane was measured. As shown in Figure 2.6, the spectrum with three lines was observed at 293 K. On the basis of the spectrum simulation, the hyperfine coupling constants were determined: $|a_N|$ = 0.78 mT (1N), $|a_{Ha}|$ = 0.20 mT (4H), $|a_{Hb}|$ = 0.10 mT (4H), $|a_{Hc}|$ = 0.18 mT (2H), $|a_{Hd}|$ = 0.13 mT (2H), $|a_{He}|$ = 0.08 mT (2H), and the contributions from the negligible hydrogen nuclei were incorporated in the line width of the spectral simulation (0.16 mT). The DFT calculations resulted in the spin distribution on both nitrogen and anthracene moiety. However, the spin density of $\mathbf{1}^+$ is almost localized on nitrogen atom. This spectral feature provides evidence that the generated charge or spin distribution is extended into the anthracene core, in good accordance with the electrospectrochemistry results of $\mathbf{1}^+$, as described above. Solution ESR spectrum of $\mathbf{1}^+$ did not depend on temperature. The ESR spectrum of **2** was silent. This result suggests the instability of the oxidized species of **2**.

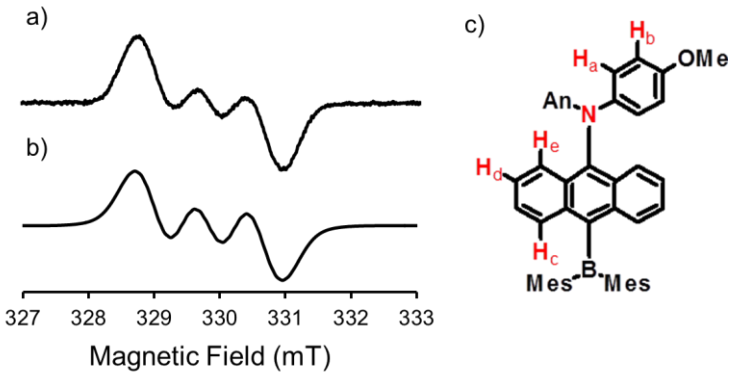

Figure 2.6. ESR spectrum of $\mathbf{1}^+$: a) in CH_2Cl_2 at 293 K b) simulated, and c) the designation of hydrogen nuclei.

2.3.5 Photophysical Properties

The optical absorption spectra of **1** and **2** were measured in various solvents (Figure 2.7). Compound **1** showed a structureless lowest-energy absorption band with absorption maxima at 470 nm in *n*-hexane corresponding to the $S_1 \leftarrow S_0$ excitation (Figure 2.7 and Table 2.3). Similarly, a structureless absorption band corresponding to the $S_1 \leftarrow S_0$ excitation of **2** was also observed at 530 nm in *n*-hexane. These spectra are more red-shifted than triarylborane core ((9-anthryl)dimesitylborane : 420 nm and trianthrylborane : 470nm)[28]. Therefore, these absorption bands are attributed by an intramolecular charge transfer (ICT) transition between the donor amino and accepter boron moieties. The red-shifted absorption of **2** compared to **1** shows the increasing the number of the donor moiety and LUMO of **2** has lower energy than that of **1** due to having three anthracenyl moieties. From the lowest-energy absorption onsets in *n*-hexane, the optical band gaps of **1** and **2** were estimated to be 2.64 eV (470 nm) and 2.34 eV (530 nm), respectively. These values are in good agreement with the electrochemically estimated HOMO-LUMO energy gap (2.63 eV for **1** and 2.33 eV for **2**). And the orbital mixing between the frontier MOs of anthracene core, diarylamino, and diarylboryl groups is explicit in the next-lowest energy bands with a complicated spectral shape below 400 nm. As is apparent from Table 2.3, it should be noted that both **1** and **2** exhibit virtually no solvatochromism in the absorption spectra irrespective of increasing solvent polarity. This strongly suggests small dipole moments of both **1** and **2** in the ground states (Figure 2.8). TD-DFT calculations (B3LYP/6-31G*) of **1** and **2** gave 531 nm and 612 nm for the excitation wavelength corresponding to the $S_1 \leftarrow S_0$ excitation. This lowest-energy excitation is described mainly by the HOMO-LUMO

transition. Considering the amino-localized HOMO and the borano-localized LUMO (Figure 2.2), this transition is of the ICT character. To elucidate the nature of the broad lowest-energy bands of **1** and **2**, we studied the effects of a fluoride ion from TBAF on the absorption spectra. A fluoride ion is known to act as a Lewis base for p-orbital of boron atom and coordinates with the boron atom in a triarylborane derivative.[29,30] As seen in Figure 2.9, the lowest energy absorption bands of **1** and **2** in THF attenuated upon addition of TBAF and the absorption spectra in the presence of sufficient amounts of TBAF have similar spectra. The results demonstrate that the lowest energy absorption bands of these triarylboranes are strongly influenced by boron atom.

In contrast with no solvatohromism in absorption spectra, both **1** and **2** displayed a pronounced bathochromism in emission spectra [excitation wavelength: 460 nm (**1**) and 500 nm (**2**)] with increasing solvent polarity from *n*-hexane to CH_2Cl_2, resulting in a bathochromic shift of 98 nm (**1**) and 67 nm (**2**), respectively, as has been reported for some B-π-N molecular system[5-15] (Figure 2.10 and Table 2.3). Such a positive bathochromic shift in emission spectra, as opposed to no solvatochromism in absorption spectra, is indicative of an efficient ICT from the N center to the B center through anthracene π-bridging unit, that is, a large excited-state dipole moment as compared with the ground-state one, which is also supported by the DFT-calculated dipole moment: 12.38 D (**1**) and 8.70 D (**2**), respectively, for the S_1 excited-states at the Frank-Condon (FC) geometries of **1** and **2** (Figure 2.8).

Turning now to the evaluation of the observed fluorescence quantum yields (Φ_F) for **1** and **2** and their dependence on the solvent polarity (Table 2.3), compound **1** showed the highest quantum yield of 0.63 in *n*-hexane with lowest polarity. With increasing solvent polarity, however, the quantum yield gradually decreased. Such a solvent polarity

dependency of Φ_F is typically found in the lower-energy emission from the ICT excited state, and can be explained by the so-called energy-gap law[31], in which non-radiative decay becomes favorable due to a small energy separation between the ground and excited states.

To estimate experimental dipole moment changes between the ground and excited states, the Strokes shifts ($\Delta\nu$) for **1** and **2** were plotted as a function of solvent polarity parameters (Δf), according to the Lippert-Mataga method (Equation (2.1))[32], where h is Planck constant, c the speed of light, a the radius of the solvent cavity formed around the molecule considered (Onsager radii),[33] μ_{ex} and μ_g (and $\mu_{ex} - \mu_g = \Delta\mu$) the excited- and ground-stated dipole moments, and $\Delta\nu^{vac}$ the extrapolation of $\Delta\nu$ to the gas phase, respectively. In addition, Δf is defined by the dielectric constant ε_s and the refractive index n for each solvent (Equation 2.2)

$$\Delta\nu = \frac{2\Delta f}{hca^3}(\mu_{ex} - \mu_g)^2 + \Delta\nu^{vac} \qquad (2.1)$$

$$\Delta f = \frac{\varepsilon_s - 1}{2\varepsilon_s - 1} - \frac{n^2 - 1}{2n^2 + 1} \qquad (2.2)$$

The Lippert-Mataga plot showed a linear relationship with the solvent polarity, and the slope, which is proportional to $(\Delta\mu)^2$, was estimated as 9497 cm^{-1} for **1** and 4861 cm^{-1} for **2** (Figure 2.11). Estimation of the Onsager radius is usually associated with significant uncertainty, and even small errors in a_0 will have a large impact on the estimated value for $\Delta\mu_{eg}$ when attempting to extract dipole moment changes from the slope of the Lippert-Mataga plot. The DFT-calculated dipole moments have close

values: 12.38 D (**1**) and 8.70 D (**2**), respectively. However, the slope of **1** and **2** is very different value. The reason is that **2** has a larger Onsager radii than **1** due to molecular size.

In the solid state, compound **1** and **2** exhibited yellow color emission (λ_{em} = 560 nm, Φ_F = 0.14) and red color emission (λ_{em} = 643 nm, Φ_F = 0.16), respectively (Figure 2.11). As is the apparent from the molecular packing in the crystal of **1** (Figure 2.4), the bulky D/A substituents hinder the effective π-π interactions between the anthracene cores, resulting in the solid-state photoluminescence for both compounds.

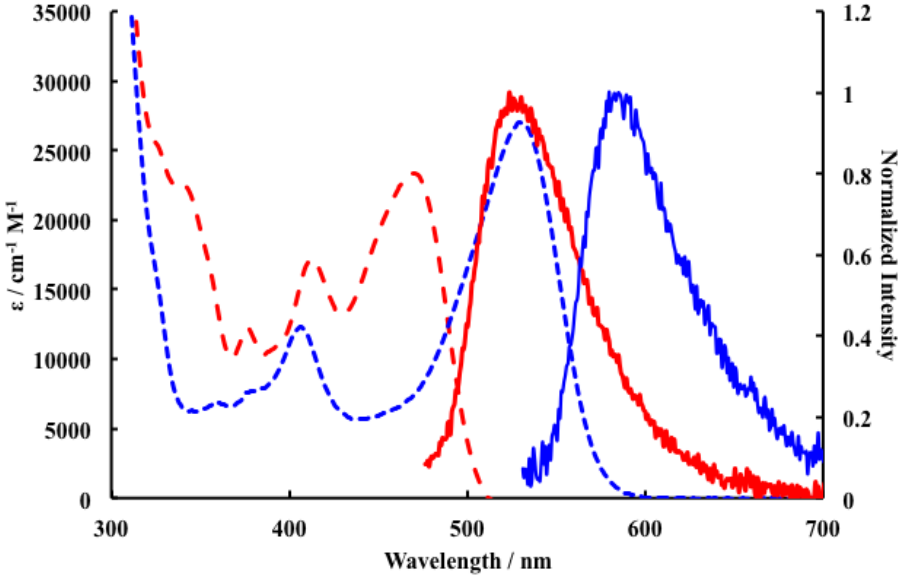

Figure 2.7. UV-visible absorption (dashed line) and emission (solid line) spectra of **1** (red) and **2** (blue) in hexane.

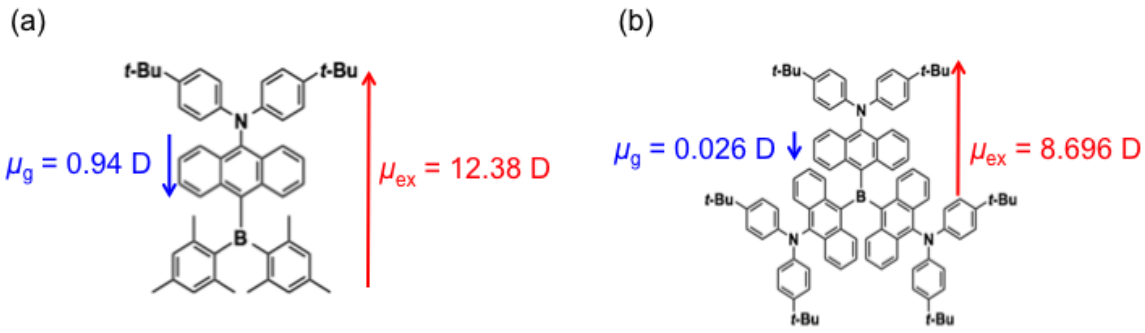

Figure 2.8. Molecular structures of (a) **1** and (b) **2**, together with schematic representation of (TD-)DFT-computed (B3LYP/6-31G*) ground (μ_g) and excited (μ_{ex} at the Frank-Condon (FC) geometry) dipole moments.

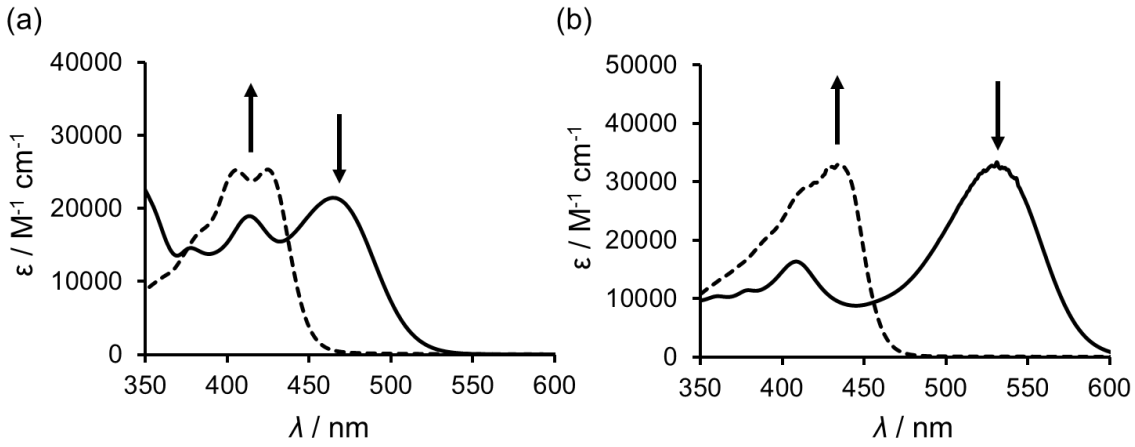

Figure 2.9. Absorption spectra of (a) **1** and (b) **2** in the absence (solid line) and presence (broken line) of TBAF in THF.

Table 2.3: Photophysical data for **1** and **2** in solution and in the solid state at room temperature.

	1				**2**			
	λ_{abs} [a] / nm	λ_{em} [b] / nm	Φ_F [c]	Stokes Shift / eV	λ_{abs} / nm	λ_{em} / nm	Φ_F	Stokes Shift / eV
n-Hexane	470	524	0.63	0.272	530	585	0.37	0.220
Toluene	471	560	0.61	0.418	536	610	0.32	0.281
$CHCl_3$	465	583	0.54	0.540	533	624	0.16	0.339
CH_2Cl_2	463	601	0.43	0.615	533	637	0.08	0.380
n-BuCN	462	612	0.26	0.658	533	650	0.09	0.419
AcCN	461	621	0.15	0.693	533	652	0.05	0.425
Solid	-	560	0.14		-	643	0.16	

[a] 1×10^{-5} M in CH_2Cl_2. [b] Emission maximum upon photoexcitation at 460 nm (**1**) and 500 nm (**2**). [c] Absolute quantum yield determined with a calibrated integrating sphere system.

(a)

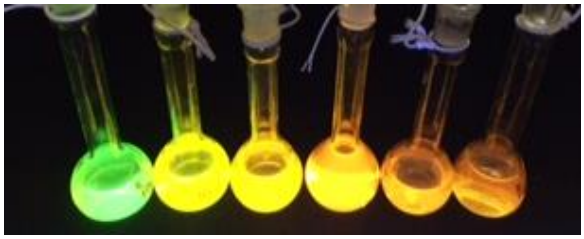

(b)

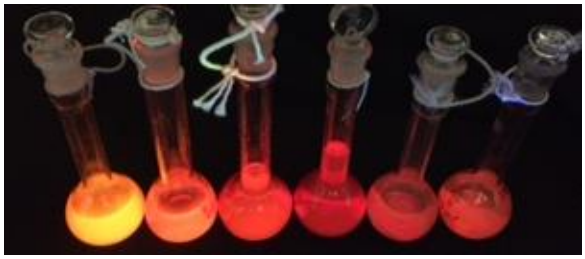

(c)

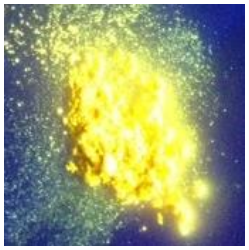

(d)

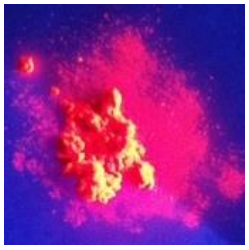

Figure 2.10. Photograph of the hexane (left), toluene, $CHCl_3$, CH_2Cl_2, *n*-BuCN and AcCN (right) solution of compounds (a) **1** (b) **2**, (c) solid state of **1**, and (d) solid state of **2** with UV irradiation at 365 nm.

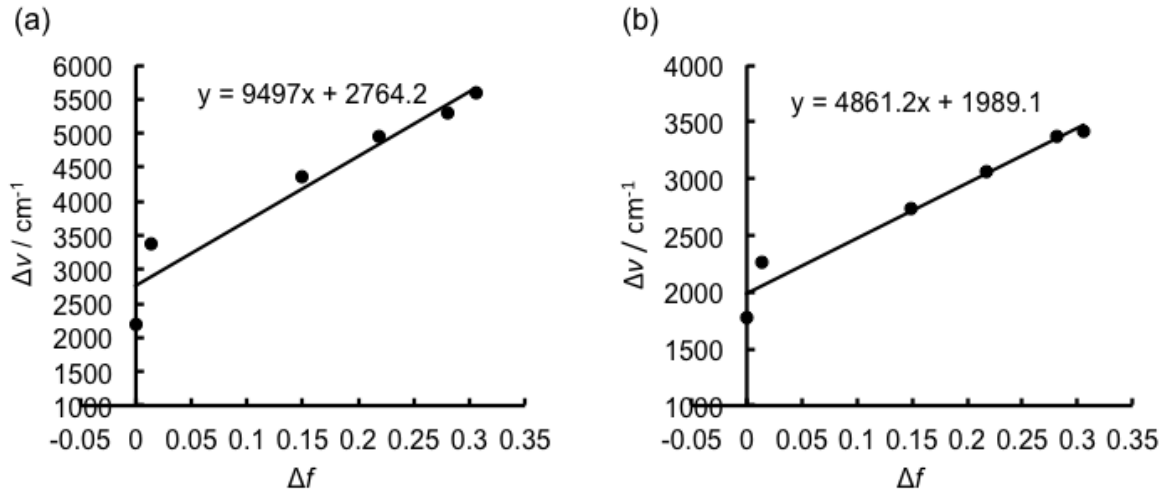

Figure 2.11. Lippert-Mataga plots for (a) **1** and (b) **2**.

2.4 Conclusion

Nitrogen-boron donor-accepter anthrancene derivatives **1** and **2** have been synthesized. From the DFT consideration, the HOMO is localized on arylamino moiety and the LUMO localized on arylborane moiety. HOMO-LUMO gap were confirmed by the electrochemical and optical absorption spectroscopic studies. By the spectroelectrochemistry and ESR measurements, **1** was a relatively stable radical cation species and the spin distribution of **1** was mainly localized on nitrogen atom and slightly delocalized on anthracene moiety. However, the oxidized species of **2** has instability by the spectroelectrochemistry and ESR measurements.

Both **1** and **2** exhibited virtually no solvatochromism in the absorption spectra irrespective of increasing solvent polarity due to the small dipole moment in the ground state. In contrast with no solvatohromism in absorption spectra, both **1** and **2** displayed a pronounced bathochromism in emission spectra with increasing solvent polarity due to the large dipole moment in the S_1 excited-state at the FC geometries. These results are characteristic of donor-π-accepter ICT molecules.

Finally, as has been disclosed by the X-ray structural analysis of the crystals of **1** and **2**, it is noteworthy that **1** exhibited solid-state fluorescence, owing to the fact that steric hindrance of the bulky dianisylamino- and dimesitylboryl-substituents hinders the concentration quenching in the solid-state. In particular, **1** and **2** showed yellow-colored emission at 560 nm with the quantum yield of 0.14 and red-colored emission at 643 nm with the quantum yield of 0.16. These findings show the potential ability of anthracene derivatives to optoelectric applications.

2.5 References

[1] a) U. Mitschke, P. Bäuerle, *J. Mater. Chem.* **2000**, *10*, 1471-1507; b) H. Sasabe, J. Kido, *J. Mater. Chem. C.* **2013**, *1*, 1699-1707.

[2] M. Zhu, C. Yang, *Chem. Rev. Soc.* **2013**, *42*, 4963-4976.

[3] a) Y. Shirota, *J. Mater. Chem.* **2000**, *10*, 1-25; b) M. Thelakkat, *Macromol. Mater. Eng*. **2002**, *287*, 442-461; c) Y. Shirota, H. Kageyama, *Chem. Rev.* **2007**, *107*, 953-1010.

[4] M. Uebe, A. Ito, Y. Kameoka, T. Sato, K. Tanaka, *Chem. Phys. Lett.* **2015**, *633*, 190-194.

[5] J. C. Doty, B. Babb, P. J. Grisdale, M. Glogowski, J. L. R. Williams, *J. Organomet. Chem*. **1972**, *38*, 229-236.

[6] N. S. Makarov, S. Mukhopadhyay, K. Yesudas, J. -L. Brédas, J. W. Perry, *J. Phys. Chem. A* **2012**, *116*, 3781-3793.

[7] M. Mao, M. -G. Ren, Q. -H. Song, *Chem. Eur. J.* **2012**, *18*, 15512-15552.

[8] A. G. Bonn, O. S. Wenger, *J. Org. Chem.* **2015**, *80*, 4097-4107.

[9] a) Z. Zhang, R. M. Edkins, J. Nitsch, K. Fucke, A. Steffen, L. E. Longobardi, D. W. Stephan, C. Lambert, T. B. Marder, *Chem. Sci.* **2015**, *6*, 308-321; (b) Z. Zhang, R. M. Edkins, J. Nitsch, K. Fucke, A. Eichhorn, A. Steffen, Y. Wang, T. B. Marder, *Chem. Eur. J.* **2015**, *21*, 177-190.

[10] R. Stahl, C. Lambert, C. Kaiser, R. Wortmann, R. Jakober, *Chem. Eur. J.* **2006**, *12*, 2358-2370.

[11] Z. Yuan, C. D. Entwistle, J. C. Collings, D. Albesa-Jové, A. S. Batsanov, J. A. K. Howard, N. J. Taylor, H. M. Kaiser, D. E. Kaufmann, S. -Y. Poon, W. -Y Wong, C. Jardin, S. Fathallah, A. Boucekkine, J. -F. Halet, T. B. Marder, *Chem. Eur. J.* **2006**, *12*, 2758-2771.

[12] a) G. Zhou, M. Baumgarten, K. Müllen, *J. Am. Chem. Soc.* **2008**, *130*, 12477-12484; b) A. Proń, G. Zhou, H. Norouzi-Arasi, M. Baumgarten, K. Müllen, *Org. Lett.* **2009**, *11*, 3550-3553. c) A. Proń, M. Baumgarten, K. Müllen, *Org. Lett.* **2010**, *12*, 4236-4239.

[13] a) P. Chen, R. A. Lalancette, F. Jäkle, *Angew. Chem. Int. Ed.* **2012**, *51*, 7994-7998; b) P. Chen, A. S. Marshall, S. -H. Chi, X. Yin, J. W. Perry, F. Jäkle, *Chem. Eur. J.* **2015**, *21*, 18237-18247.

[14] a) R. Kurata, K. Kaneda, A. Ito, *Org. Lett.* **2017**, *19*, 392-395; b) R. Kurata, A. Ito, M. Gon, K. Tanaka, Y. Chujo, *J. Org. Chem.* **2017**. *82*. 5111-5121.

[15] C. Wang, Q. -W Xu, W. -N. Zhang, Q. Peng, C. -H. Zhao, *J. Org. Chem.* **2015**, *80*, 10914-10924.

[16] K. Ragavachari, *Theor. Chem. Acc*. **2000**, *103*, 361-363 and references cited therein.

[17] A. Dreuw, M. Head-Gordon, *Chem. Rev.* **2005**, *105*, 4009-4037.

[18] W. J. Hehre, L. Radom, P.v. R. Schleyer, J. A. Pople, *Ab Initio Molecular Orbital Theory*, Wiley, New York, **1986**.

[19] M. J. Frisch, *et al*., Gaussian 09 (Revision D.01), Gaussian, Inc., Wallingford CT, **2013**.

[20] M. C. Burla, R. Caliandro, M. Camalli, B. Carrozzini, G. L. Cascarano, L. De Caro, C. Giacovazzo, G. Polidori, D. Siliqi, R. Spagna, *J. Appl. Crystallogr*. **2007**, *40*, 609-613.

[21] G. M. Sheldrick, *Acta Crystallogr., Sect. A: Found. Crystallogr*. **2008**, *64*, 112-122.

[22] D. S. Surry, S. L. Buchward, *Angew. Chem. Int. Ed.* **2008**, *47*, 6338-6361.

[23] a) J. F. Hartwig, *Nature* **2008**, *455*, 314-322; b) J. F. Hartwig, *Acc. Chem. Res.*

2008, *41*, 1534-1544.

[24] J. Sandstrçm, *Dynamic NMR Spectroscopy*, Academic Press, New York, **1982**.

[25] J. Pommerehne, H. Vestweber, W. Guss, R. F. Mahrt, H. Bässler, M. Porsch, J. Daub, *Adv. Mater.* **1995**, *7*, 551-554.

[26] M. Uebe, K. Kawashima, K. Takahashi, A. Ito, *Chem. Eur. J.* **2017**, *23*, 278-281.

[27] M. Uebe, T. Kato, K. Tanaka, A. Ito, *Chem. Eur. J.* **2016**, *22*, 18923-18931.

[28] S. Yamaguchi, S. Akiyama, K. Tamao, *J. Am. Chem. Soc.* **2000**, *122*, 6335-6336.

[29] S. Yamaguchi, S. Akiyama, K. Tamao, *J. Am. Chem. Soc.* **2001**, *123*, 11372-11375.

[30] A. Ito, K. Kawanishi, E. Sakuda, N. Kitamura, *Chem. Eur. J.* **2014**, *20*, 3940-3953.

[31] a) R. Englman, J. Jortner, *J. Mol. Phys.* **1970**, *18*, 145-164; b) W. Siebrand, *J. Chem. Phys.* **1971**, *55*, 5843.

[32] a) E. Z. Lippert, *Naturforsch. A* **1955**, *10*, 541;-545 b) N. Mataga, Y. Kaifu, M. Koizumi, *Bull. Chem. Soc. Jpn.* **1955**, *28*, 690-691.

[33] L. Onsagar, *J. Am. Chem. Soc.* **1936**, *58*, 1486-1493.

Chapter 3

Diazadibora[1.1.1.1]*m,p,m,p*-cyclophanes:Ambipolar Conjugated Macrocycles with Different B–π–N Embedded Patterns

3.1 Introduction

Owing to their potential application in organic (opto)electronics based on the isoelectronic and isosteric relationship between C=C and B=N units, the chemistry of BN-embedded organic π-systems has been paid much attention as a rapidly progressing field.[1] In parallel, ambipolar π-conjugated molecular systems incorporating borane electron-acceptor (the B center) and amine electron-donor (the N center) groups as B-π-N units have also been actively investigated in conjunction with the development of fluorescent sensors for small anions, nonlinear optical materials for bioimaging, and emitting and/or charge-transporting materials for organic light-emitting diodes (OLEDs).[2] Among these B-π-N embedded aromatics, the "π-extended borazine" (**MC-B3N3**)[3] was reported by Jäkle and co-workers as the first example of

π-conjugated B-π-N macrocycles where three B-π-N units are embedded into shape-persistent macrocyclic molecular backbone, and exhibited its unique electronic properties of having a smaller HOMO-LUMO gap despite the relatively higher LUMO than the corresponding hexaboracyclophane[4] and the relatively lower HOMO than the corresponding hexaazacyclophane,[5] thereby resulting in strong blue fluorescence [λ_{em} = 460 nm (Φ_F = 0.76) in CH_2Cl_2], solvatochromic emission, and the cyanide ion sensing. However, examples of B-π-N type macrocycles are still scarce.[6]

Recently, dibenzo[*a*,*e*]pentalene analogues containing two B=N units with different orientation patterns have been prepared to examine the effect of the B=N orientation patterns on their physicochemical properties, and it has been clarified that the different orientation patterns can lead to a big difference in their antiaromaticity and resulting optoelectronic properties.[7] Inspired by this work, the author envisioned that two *para*-phenylene-bridged B-π-N embedded diazadibora[1_4]*m*,*p*,*m*,*p*-cyclophanes **1** and **2** would have been intriguing to elucidate how the *para*-phenylene-bridged B-π-N orientation patterns affect their (opto)electronic properties (Scheme 3.1). The macrocycle **1** has the two B-π-N units in anti-parallel fashion, thus leading to a potential quadrupolar molecule, whereas the macrocycle **2** in parallel fashion. In addition, the author also prepared the remaining isomer **3**, which contains two *meta*-phenylene-bridged B-π-N units, to characterize the effect of *meta*-phenylene-bridging in the B-π-N unit. Herein the author reports the (opto)electronic and structural characteristics of these ambipolar π-conjugated B-π-N macrocycles.

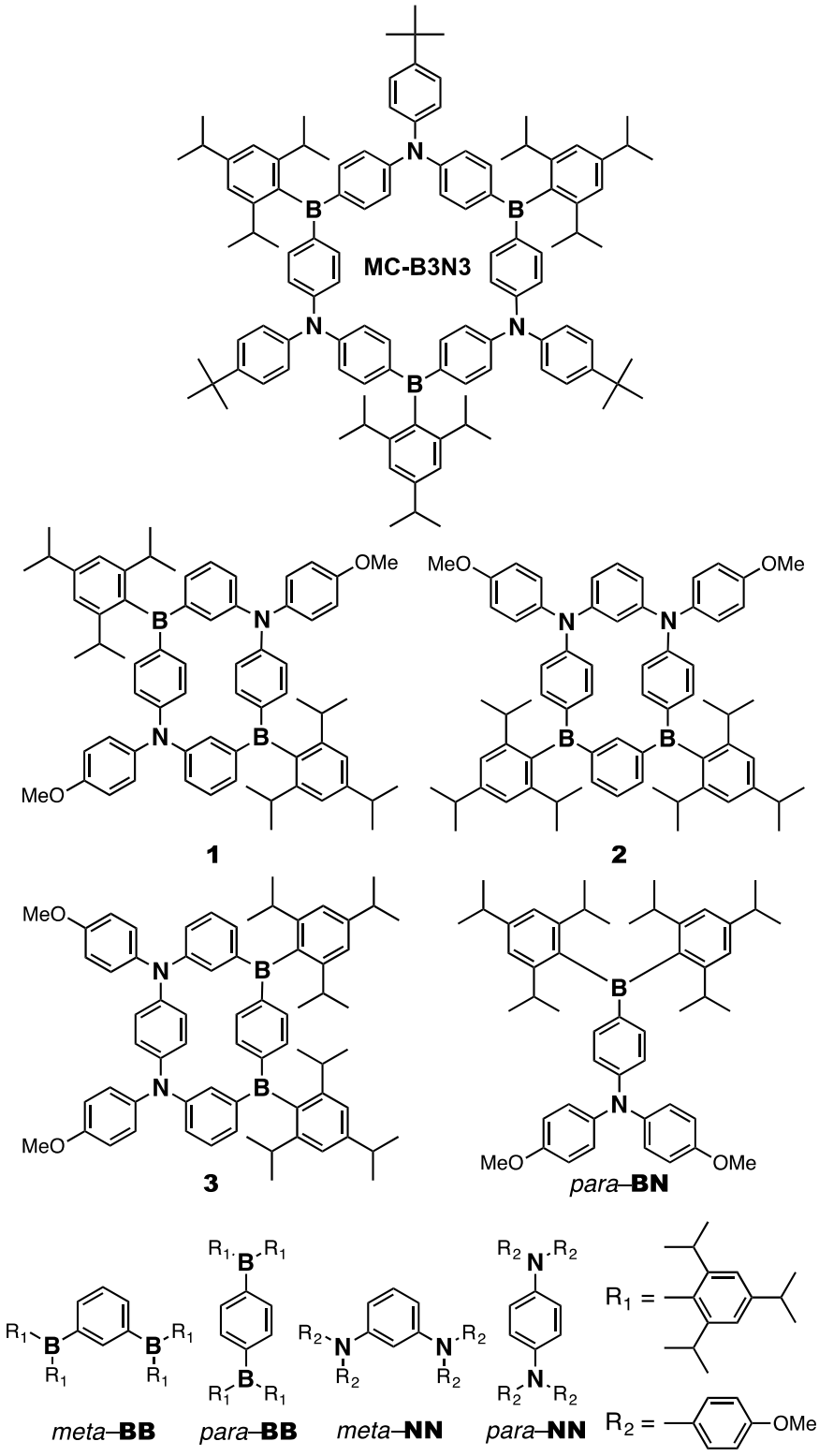

Scheme 3.1. Ambipolar π-conjugated B-π-N macrocycles **MC-B3N3**, **1**–**3**, and their reference compounds.

3.2 Experimental Section

3.2.1 Synthesis

All the purchased reagents were of standard quality, and used without further purification. Dimethyl 2,4,6-triisopropylphenylboronate (TripB$(OMe)_2$) was prepared by following the reported method.[8] All the purchased solvents were purified, dried, and degassed by standard procedures. Column chromatography was usually carried out with silica gel (Kanto Chemical Co., Inc., silica gel 60N, spherical neutral). Preparative recycling gel permeation chromatography (GPC) was performed with a Model LC-9201 recycling preparative HPLC (Japan Analytical Industry Co., Ltd.) equipped with JAIGEL-1H/JAIGEL-2H columns using toluene as an eluent. ^{1}H and ^{13}C NMR spectra were measured by a JEOL JNM-AL400 FT-NMR spectrometer. Chemical shifts of NMR spectra are determined relative to internal tetramethylsilane (TMS) standard (δ), and are given in parts per million (ppm). In addition, high resolution (HR) electrospray ionization (ESI) mass spectra were recorded using a mass spectrometer (Thermo Fischer EXACTIVE). UV-Vis-NIR absorption spectra were obtained with a Perkin-Elmer Lambda 950 spectrometer.

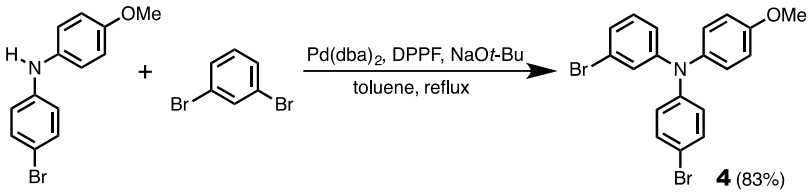

3-Bromo-4'-bromo-4"-methoxytriphenylamine (4): A mixture of *m*-dibromobenzene (16.0 g, 68.0 mmol), 4-bromo-4'-methoxydiphenylamine (2.36 g, 8.50 mmol), Pd$(dba)_2$

(0.264 g, 0.46 mmol), DPPF (0.534 g, 0.96 mmol), and NaO*t*Bu (1.27 g, 13.2 mmol) in toluene (70 ml) was refluxed with stirring under an argon atmosphere for 24 h. The resulting mixture was washed with brine. The organic layer was separated and dried over Na_2SO_4. After evaporation of the solvent, the crude product was chromatographed on silica gel (*n*-hexane/dichloromethane = 4/1 as eluent), to give **4** as colorless oil (3.06 g, 83%): ^{1}H NMR (400 MHz, acetone-d_6): δ = 7.43 (d, J = 9.0 Hz, 2H), 7.19 (t, J = 15 Hz, 1H), 7.12-7.07 (m, 4H), 6.98-6.94 (m, 5H), 3.82 (s, 3H); ^{13}C NMR (100 MHz, acetone-d_6): δ = 158.2, 150.2, 147.6, 140.0, 133.1, 131.6, 128.9, 125.6, 125.3, 125.1, 123.2, 121.4, 116.0, 115.4, 55.7; ESI HRMS: *m/z* calcd for $C_{19}H_{15}BrNO$: 432.9494 $[M]^+$; found 432.9490.

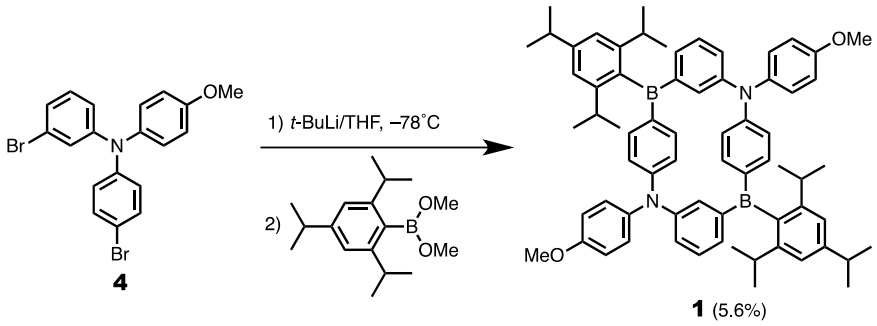

1: To a solution of **4** (1.70 g, 3.93 mmol) in 400 ml of anhydrous THF was added slowly 1.9 M *t*-BuLi in pentane (8.4 ml, 16 mmol) at –78˚C under argon atmosphere, and the mixture was stirred at this temperature for 10 min. Then TripB(OMe)$_2$ (1.21 ml, 4.0 mmol) was added at –78˚C, and the mixture was stirred at this temperature for 1 h. Finally, the reaction mixture was stirred at room temperature overnight. After evaporation of the solvent, the residue was dissolved in chloroform, and filtered through Celite. The crude product obtained after evaporation of the solvent was roughly purified

by chromatography on silica gel (toluene/*n*-hexane = 1/1 as eluent). The resulting product was dissolved in a small portion of toluene, and reprecipitated by adding excess of acetone to obtain **1** as a pale yellow powder (0.109 g, 5.6%): mp 278–279˚C; ^{1}H NMR (400 MHz, $CDCl_3$): δ = 7.61 (d, J = 2.0 Hz, 2H), 7.49 (d, J = 8.6 Hz, 4H), 7.15-7.22 (m, 8H), 7.09 (d, J = 9.0 Hz, 4H), 6.93-7.00 (m, 6H), 6.86 (d, J = 9.0 Hz, 4H), 3.79 (s, 6H), 2.80 (m, 2H), 2.56 (m, 4H), 1.28 (d, J = 6.8 Hz, 12H), 1.03 (m, 24H); ^{13}C NMR (100 MHz, $CDCl_3$): δ = 156.8, 150.2, 148.7, 148.1, 146.3, 145.0, 139.6, 139.0, 138.2, 136.8, 130.6, 130.5, 128.3, 128.2, 125.3, 119.8, 119.7, 114.8, 55.4, 35.4, 34.2, 24.3, 24.1; ESI HRMS: *m/z* calcd for $C_{68}H_{76}B_2N_2O_2$: 975.6166 $[M+H]^+$; found 975.6167.

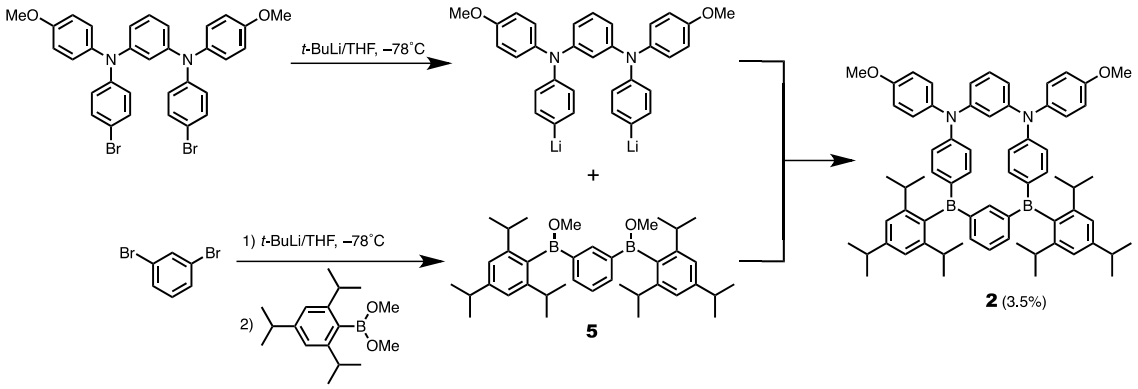

2: To a solution of 1,3-dibromobenzene (0.121 g, 0.512 mmol) in 10 ml of anhydrous THF was added slowly 1.9 M *t*-BuLi in pentane (1.05 ml, 2.0 mmol) at –78˚C under argon atmosphere, and the mixture was stirred at this temperature for 20 min. Then TripB(OMe)$_2$ (0.3 ml, 1.0 mmol) was added at –78˚C, and the mixture was stirred at this temperature for 15 min. Finally, the reaction mixture was stirred at room temperature overnight to obtain bisborinate ester **5**. As-prepared **5** was used in the subsequent

reaction without further purification. To a solution of *N*,*N'*-dianisyl-*N*,*N'*-bis(4-bromophenyl)-1,3-benzenediamine **6**[9] (0.317 g, 0.503 mmol) in 50 ml of anhydrous THF was added slowly 1.9 M *t*-BuLi in pentane (1.05 ml, 2.0 mmol) at –78˚C under argon atmosphere, and the mixture was stirred at this temperature for 20 min. The prepared THF solution of **5** was added dropwise to the stirred solution of the dilithiated **6** at –78˚C under argon atmosphere, and the reaction mixture was stirred at this temperature for 1 h. Finally, the reaction mixture was stirred at room temperature overnight. After evaporation of the solvent, the residue was chromatographed on amino silica gel (NHDM1020, ca. 100 μm, Fuji Silysia Chemical Ltd. Japan) (toluene/*n*-hexane = 2/5 as eluent) and further purified by preparative recycling HPLC to give **2** as a pale yellow powder (17.2 mg, 3.5%): mp 260–261˚C; ^{1}H NMR (400 MHz, $CDCl_3$): δ = 7.89 (m, 1H), 7.71 (m, 2H), 7.64 (d, *J* = 8.1 Hz, 4H), 7.41 (m, 1H), 7.36 (t, *J* = 12 Hz, 1H), 7.19 (d, *J* = 8.8 Hz, 4H), 7.01–7.12 (m, 4H+1H), 6.95 (s, 4H), 6.87 (d, *J* = 8.8 Hz, 4H), 6.51 (m, 2H), 3.81 (s, 6H), 2.89 (m, 2H), 2.46 (m, 4H), 1.27 (d, *J* = 7.1 Hz, 12H), 0.90–1.03 (m, 24H); ^{13}C NMR (100 MHz, $CDCl_3$): δ = 156.7, 150.5, 148.6, 148.0, 147.9, 142.4, 140.8, 139.9, 138.7, 138.4, 136.1, 129.9, 128.1, 126.9, 119.7, 119.5, 118.3, 117.9, 114.7 (Probably two signals in the aromatic region are accidentally overlapped.), 55.4, 35.3, 34.2, 24.2, 24.1; ESI HRMS: *m/z* calcd for $C_{68}H_{76}B_2N_2O_2$: 975.6166 $[M+H]^+$; found 975.6145.

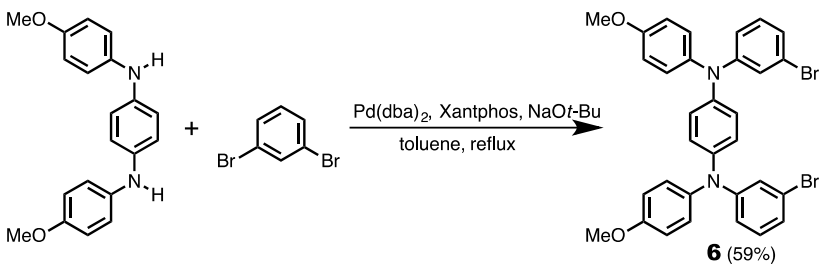

***N,N'*-dianisyl-*N,N'*-bis(3-bromophenyl)-1,4-benzenediamine (6)**: A mixture of *N,N'*-dianisyl-1,4-phenylenediamine (1.83 g, 5.71 mmol), 1,3-dibromobenzene (4.04 g, 17.1 mmol), $Pd(dba)_2$ (58 mg, 0.1 mmol), Xantphos[10] (116 mg, 0.2 mmol), and NaO*t*Bu (1.64 g, 17.1 mmol) in toluene (30 ml) was refluxed with stirring under an argon atmosphere for 19 h. The reaction mixture was washed with brine, and the organic layer was dried over Na2SO4. After evaporation of the solvent, the crude product was chromatographed on silica gel (toluene/*n*-hexane = 3/1 as eluent) to give **6** as a white powder (2.13 g, 59%): ^{1}H NMR (400 MHz, acetone-d_6): δ = 7.08–7.16 (m, 6H), 6.99–7.06 (m, 8H), 6.93–6.99 (m, 4H), 6.87–6.91 (m, 2H), 3.81 (s, 6H); ^{13}C NMR (100 MHz, acetone-d_6): δ = 157.9, 150.9, 143.4, 140.2, 131.4, 128.7, 126.1, 124.0, 123.5, 123.0, 119.8, 115.9, 55.7.

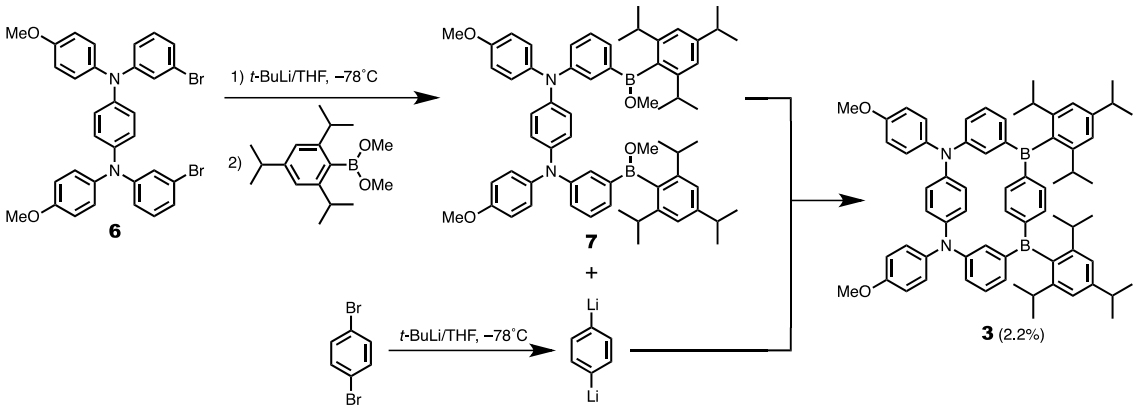

3: To a solution of **6** (2.79 g, 4.42 mmol) in 80 ml of anhydrous THF was added slowly 1.9 M *t*-BuLi in pentane (9.3 ml, 17.7 mmol) at –78˚C under argon atmosphere, and the mixture was stirred at this temperature for 20 min. Then $TripB(OMe)_2$ (2.65 ml, 8.84 mmol) was added at –78˚C, and the mixture was stirred at this temperature for 15 min. Finally, the reaction mixture was stirred at room temperature overnight to obtain

bisborinate ester **7**. As-prepared **7** was used in the subsequent reaction without further purification. To a solution of *p*-dibromobenzene (1.04 g, 4.42 mmol) in 300 ml of anhydrous THF was added slowly 1.9 M *t*-BuLi in pentane (9.3 ml, 17.7 mmol) at –78˚C under argon atmosphere, and the mixture was stirred at this temperature for 25 min. The prepared THF solution of **7** was added dropwise to the stirred solution of the dilithiated benzene at –78˚C under argon atmosphere, and the reaction mixture was stirred at this temperature for 20 min. Finally, the reaction mixture was stirred at room temperature for 6 hrs. After evaporation of the solvent, the residue was chromatographed on amino silica gel (NHDM1020, ca. 100 μm, Fuji Silysia Chemical Ltd. Japan) (toluene/*n*-hexane = 1/1 as eluent) and further purified by preparative recycling HPLC to give **3** as a orange-colored solid (95 mg, 2.2%): mp 261–262˚C; ^{1}H NMR (400 MHz, $CDCl_3$): δ = 7.52 (s, 4H), 7.05–7.23 (m, 16H), 7.00 (s, 4H), 6.86 (d, *J* = 9.0 Hz, 4H), 3.78 (s, 6H), 2.91 (m, 2H), 2.48 (m, 4H), 1.28 (d, *J* = 7.1 Hz, 12H), 1.02 (d, *J* = 6.6 Hz, 12H), 0.95 (d, *J* = 6.8 Hz, 12H); ^{13}C NMR (100 MHz, CD_2Cl_2): δ = 156.7, 149.6, 149.2, 148.1, 147.1, 144.1, 143.0, 140.7, 139.5, 135.2, 130.1, 129.9, 128.4, 127.9, 125.8, 124.0, 120.3, 115.0, 55.8, 36.0, 34.7, 24.3, 24.2; ESI HRMS: *m/z* calcd for $C_{68}H_{76}B_2N_2O_2$: 974.6098 $[M]^+$; found 974.6087.

3.2.2 DFT Calculations

Quantum chemical calculations were performed with using a hybrid Hartree–Fock/density functional theory (HF/DFT) method (B3LYP).[11] Full geometrical optimization for the ground S_0 state was carried out and furthermore, their local minimum structures were confirmed by performing subsequent frequency analyses. Excitation energies were examined by means of the time-dependent density functional

theory (TD-DFT)[12] based on the (U)B3LYP/6-31G*-optimized structures. All the computations employed the 6-31G* basis set.[13] All these computational approaches are implemented in Gaussian 09 package of ab initio MO calculation.[14]

3.2.3 X-ray crystal structure analysis

Data collections were performed on a Rigaku XtaLABmini CCD system with Mo-Kα radiation at 93±1 K for compounds **1**, **2**, and **3**. The data were corrected for Lorentz and polarization effects. The structure was solved by using direct methods (SHELXD version 2013/2[15] for **1**, SHELXS version 2013/1[15] for **2**, and SIR92[16] for **3**), expanded by using Fourier techniques, and refined by full-matrix least-squares of F^2 on the basis of 7317, 14211, and 13912 observed reflections and 588, 820, and 923 variable parameters for **1**, **2**, and **3**, respectively, by using SHELXL version 2014/7.[15] The non-hydrogen atoms were refined anisotropically and hydrogen atoms were refined by using the riding model. All the calculations were performed by using CrystalStructure crystallographic software package,[16] except for refinement, which was performed by using SHELX-97. CCDC-1420390, -14203991, and -1420392 contain the supplementary crystallographic data for **1**, **2**, and **3**, respectively, for this paper. These data can be obtained free of charge from the Cambridge Crystallographic Data Centre via www.ccdc.cam.ac.uk/data_request/cif.

Table 3.1. Selected crystallographic data for **1**, **2**, and **3**

	1	**2**	**3**
CCDC	1588312	1588315	1588316
Empirical formula	$C_{69}H_{77}B_2Cl_3N_2O_2$	$C_{70}H_{76}B_2Cl_4N_2O_2$	$C_{69}H_{78}B_2Cl_2N_2O_3$
Formula weight	1094.36	1140.81	1075.91
T [K]	93±1	93±1	93±1
Crystal system	monoclinic	triclinic	monoclinic
Space group	$C2/c$ (#15)	$P\bar{1}$ (#2)	$P2_1/n$ (#14)
a [Å]	27.6206(19)	12.9836(9)	12.4296(6)
b [Å]	9.0523(6)	15.4560(10)	32.066(2)
c [Å]	26.8182(18)	16.7961(11)	16.1020(12)
α [°]	90	76.300(6)	90
β [°]	106.842(12)	88.524(7)	105.358(14)
γ [°]	90	73.293(6)	90
V [Å^3]	6417.7(9)	3133.2(4)	6188.6(9)
Z	4	2	4
ρ_{calcd} [g cm^{-3}]	1.133	1.209	1.155
μ [cm^{-1}]	1.863 (MoKα)	2.347 (MoKα)	6.458 (CuKα)
F(000)	2328	1208	2296
Crystal size [mm^3]	0.45×0.15×0.09	0.42×0.22×0.20	0.38×0.18×0.09
Crystal color, habit	colorless, block	colorless, block	colorless, block
λ [Å]	MoKα / 0.71075	MoKα / 0.71075	MoKα / 0.71075
$2\theta_{max}$ [°]	54.9	55.0	55.1
Collected data	32675	32367	49936
Unique data / R_{int}	7317/0.0455	14211/0.0398	13920/0.0888
No. of parameters	588	820	923
Reflection/Parameter Ratio	12.44	17.33	15.07
Goodness-of-fit on F^2	1.605	1.044	1.030
R_1 [$I > 2\sigma$], wR_2 (all reflections)	0.1269, 0.4219	0.0636, 0.1875	0.0762, 0.1540
Residual density [e Å^{-3}]	1.07/-0.70	0.99/–1.08	0.56/–0.73

3.2.4 Electrochemical Measurements

The redox properties were evaluated by cyclic voltammetry (CV) and differential pulse voltammetry (DPV) in CH_2Cl_2 (oxidation) and THF(reduction) solution at 298 K with 0.1 M tetra-*n*-butylammonium tetrafluoroborate ($TBABF_4$) as supporting electrolyte (scan rate 100 mV s^{-1}) using an ALS/chi Electrochemical Analyzer model 612A. A three-electrode assembly was used, which was equipped with a platinum disk (2 mm^2) and a platinum wire as the working and counter electrodes, respectively, and Ag/0.01 M $AgNO_3$ (acetonitrile) was used as the reference electrode. The redox potential were referenced against a ferrocene/ferrocenium ($Fc^{0/+}$) redox potential measured in the same electrolytic solution.

3.2.5 Spectroelectrochemical Measurements

Spectroelectrochemical measurements were carried out with a custom-made optically transparent thin-layer electrochemical (OTTLE) cell (light pass length = 1 mm) equipped with a platinum mesh and a platinum coil as the working and counter electrodes, respectively, and Ag/0.01 M $AgNO_3$ (acetonitrile) was used as the reference electrode. The potential was applied with an ALS/chi Electrochemical Analyzer model 612A.

3.2.6 ESR Measurements

Cw-ESR Spectra were recorded on a JEOL JES-TE200 X-band ESR spectrometer, in which temperature was controlled by a JEOL ES-DVT3 variable-temperature unit in the range of 193-293 K.

3.2.7 Photophysical Measurements

UV/Vis-NIR absorption spectra were obtained with a Perkin-Elmer Lambda 950 spectrometer. Fluorescence spectra were recorded on an absolute photoluminescence quantum yield measurement system (HAMAMATSU Quantaurus-QY).

3.3 Results and Discussion

Newly synthesized macrocycles **1**–**3**[7] crystallized as colorless blocks, which were grown by slow evapolation of a dilute mixed solution ($CHCl_3$/EtOH for **1**; CH_2Cl_2/MeOH for **2** and **3**), and their molecular structures were confirmed by X-ray crystallography (Figure 3.1; Table 3.1). All the molecules have an alternate *meta-para*-linked macrocyclic structure with an approximate rectangular plane formed by the two boron and two nitrogen atoms, and **1** has a crystallographic C_2 symmetry, while **2** and **3** have an approximate C_s symmetry. Compounds **1** and **2** exhibited fluorescent in the solid state (Φ_F = 0.05 and 0.15, respectively), whereas compound **3** was essentially non-emissive both in the solid state and in solution (Φ_F < 0.01 in CH_2Cl_2) (Table 3.3).

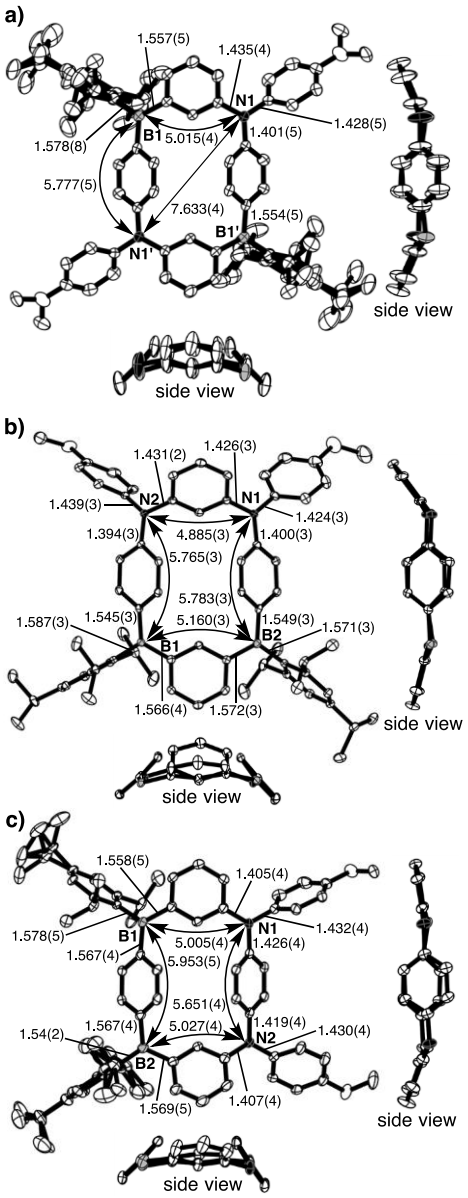

Figure 3.1. ORTEP diagrams and selected bond lengths (Å) of a) **1**, b) **2**, and b) **3**, as determined from X-ray structural analysis at 93±1 K. Hydrogen atoms are omitted for clarity; boron, nitrogen, and oxygen atoms are depicted in grey octants, black octants, and white hollows, respectively; the thermal ellipsoids are shown at the 50% probability level.

To characterize the electronic structures of **1**–**3**, the author has performed the DFT and TD-DFT calculations for **1**–**3** (B3LYP/6-31G*) [the optimized structures for **1**, **2**, and **3** had C_2, C_s, and C_s symmetries, respectively], and the relative energy levels of frontier Kohn-Sham orbitals are summarized in Figure 3.2. Commonly for all the compounds, the HOMO and HOMO-1 are distributed mainly over the two nitrogen centers, while the LUMO and LUMO+1 mostly over the two boron centers, and moreover, the HOMO (LUMO) and HOMO-1 (LUMO+1) for **1** and **3** comprise in-phase and out-of-phase combination of two N (B) p-orbitals, while the HOMO-1 to LUMO+1 of **2** are of non-bonding character, originating from the *meta*-phenylenediamine and *meta*-phenylenediborane moieties. The spatially non-overlapping MOs (**1**), the non-bonding MOs (**2**), and the spatially overlapping MOs (**3**) open the energy gap between the HOMO and HOMO-1 (and also the LUMO and LUMO+1) in this order. Consequently, compound **3** has the smallest HOMO-LUMO gap. However, the optical absorption spectrum for **3** exhibited a very weak $S_1 \leftarrow S_0$ band, as was also supported by the TD-DFT results (Figure 3.3): the small spatial overlap between the HOMO and LUMO resulted in the small $S_1 \leftarrow S_0$ transition dipole moment (oscillator strength: f = 0.015), thus leading to a considerable decrease in the fluorescence quantum yield for **3**.

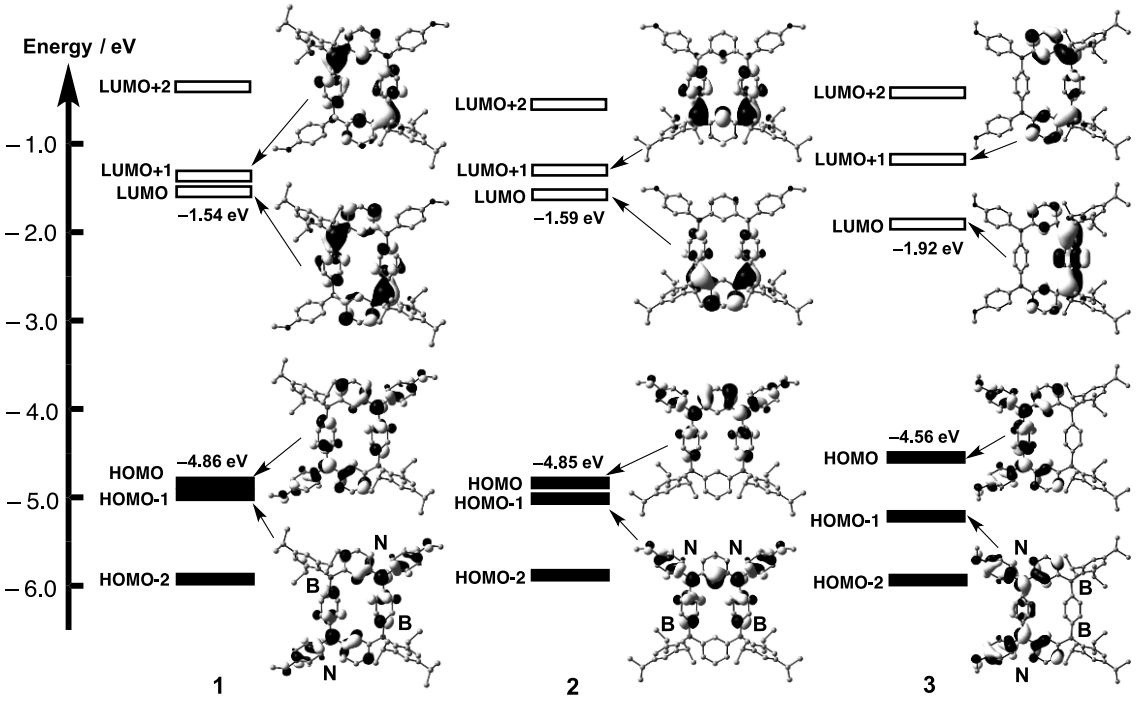

Figure 3.2. Electronic effects of the embedded patterns of the B-π-N units (**1**–**3**), calculated at the B3LYP/6-31G* level of theory.

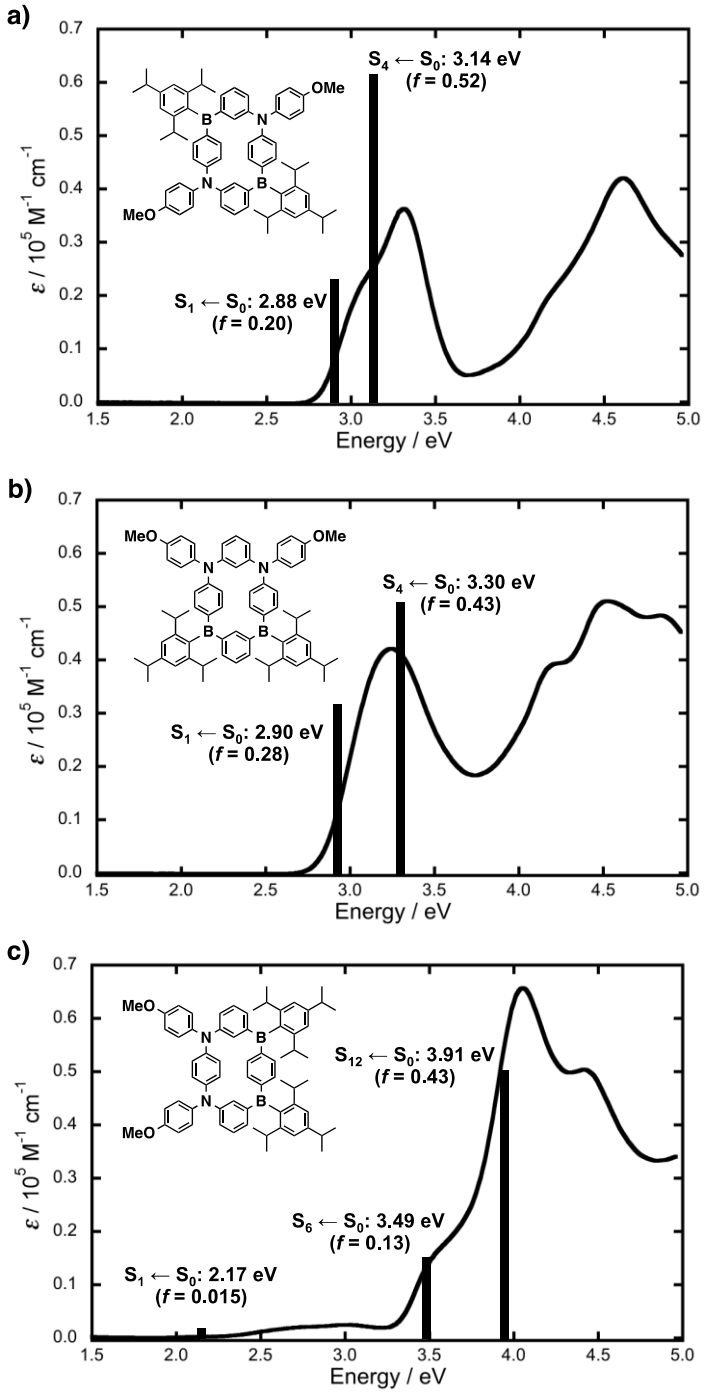

Figure 3.3. Absorption spectrum of a) **1**, b) **2**, and c) **3** in CH_2Cl_2 at 298 K. The black sticks designate the TD-DFT-calculated main transition energies in lower energy region and their relative oscillator strengths at B3LYP/6-31G* level of theory.

To ascertain the electronic communication between the two B and two N centers, we measured the cyclic and differential pulse voltammograms of **1**–**3**. The oxidation and reduction potentials of **1**–**3** were summarized in Table 3.2, together with those of their related compounds. All the compounds displayed two one-electron and two one-reduction steps according to redox-active two B and two N centers. Judging from the potential separations ΔE^{ox} (and ΔE^{red}), it has been demonstrated that the electronic communication between the two N centers (and the B centers) increases in the order of **1**, **2**, and **3**, in close relation to the difference in conjugation pathway (weak *meta*-phenylene and strong *para*-phenylene linkages) as well as the spatial separation between the redox-active centers. In addition, as already unveiled by **MC-B3N3**, **1** and **2** possess both more positive oxidation and negative reduction potentials owing to the existence of adjacent electron-accepting B and electron-donating N centers through the *para*-phenylene linker, while **3** has relatively lower oxidation and reduction potentials because of the weak conjugation via the *meta*-phenylene linker. As a consequence, the electrochemical HOMO-LUMO gaps of **1** and **2** [2.91 and 2.86 eV, which are consistent with the optical HOMO-LUMO gaps (2.84 and 2.87 eV)] are similar to that of **MC-B3N3** (2.99 eV), whereas the HOMO-LUMO gap of **3** (2.23 eV) has the smallest value among the reported ambipolar π-conjugated B-π-N macrocycles, though the $S_1 \leftarrow S_0$ transition of **3** is very weak (Figure 3.3).

Table 3.2. Comparison of electrochemical potentials[a] [V vs $Fc^{0/+}$, scan rate: 0.1 Vs^{-1}].

	E_3^{red}	E_2^{red}	E_1^{red}	ΔE^{red} [b]	E_1^{ox}	E_2^{ox}	E_3^{ox}	ΔE^{ox} [c]
1	—	–2.82[d]	–2.52[d]	0.30	+0.39	+0.53	—	0.14
2	—	–3.05[d]	–2.50[d]	0.55	+0.36	+0.60	—	0.24
3	—	–2.95[d]	–2.21[d]	0.74	+0.02	+0.34	—	0.32
MC-B3N3[e]	–2.84	–2.72	–2.53	0.19	+0.46	+0.65	+0.94	0.19
meta-**BB**	—	–2.90[d]	–2.49[d]	0.41	—	—	—	—
para-**BB**	—	–2.77[d]	–2.08[d]	0.69	—	—	—	—
meta-**NN**	—	—	—	—	+0.17	+0.46	—	0.29
para-**NN**	—	—	—	—	–0.14	+0.34	—	0.48

[a] Measured in 1 mM CH_2Cl_2 solution (in the anodic region) and 1 mM THF solution (in the cathodic region) with 0.1 M [$n$$Bu_4N$][$BF_4$] at 298 K. [b] $\Delta E^{red} = E_1^{red} - E_2^{red}$. [c] $\Delta E^{ox} = E_2^{ox} - E_1^{ox}$. [d] Determined by differential pulse voltammetry. [e] From Ref. [3].

The relatively low oxidation potentials of **1**–**3** suggest the possibility of generating the stable monocation and dication of these compounds. Thus, we tried to monitor the optical absorption spectral change during stepwise chemical oxidation of **1**–**3** with $AgSbF_6$ in CH_2Cl_2 (Figure 3.4). However, for **2**, we encountered an unexpected rapid decomposition of the oxidized species, when chemically oxidized. Alternatively, UV/vis-NIR spectroelectrochemistry was conducted for **2** (Figures 3.4b and 3.4c). Upon chemical oxidation of **1** from neutral through radical cation to dication, only one absorption band at 1.68 eV due to the localized aminium radical cationic moiety was

observed, and interestingly, no intervalence charge-transfer (IVCT) band was detected in the NIR region. In contrast, the radical cation of **2** exhibited three new bands at 0.55, 1.71, and around 2.5 eV (sh), and further oxidation of $\mathbf{2}^{\bullet+}$, into dication $\mathbf{2}^{2+}$ led to a disappearance of the lowest-energy band. This spectral change at 0.55 eV is indicative of the IVCT band for $\mathbf{2}^{\bullet+}$. Turning to the oxidation process of **3** to the dication (Figure 3.5), the observed spectral change was in good accordance with that for the oxidation process of *para*-NN,[18] as expected from the *para*-phenylenediamine-embedded structure of **3**.

To gain more insight into the nature of oxidized species, the author measured the variable-temperature ESR (VT-ESR) spectra for $\mathbf{1}^{\bullet+}$ (Figure 3.6a), though the same measurements are not possible for $\mathbf{2}^{\bullet+}$ because of the aforementioned rapid decomposition of the chemically oxidized species. Quite interestingly, the observed spectrum showed a five-line pattern at 293 K, indicating the hyperfine coupling with two equivalent nitrogen nuclei. Another interesting aspect was a gradual decrease of the central three lines with decreasing temperature, and therefore, the intramolecular charge/spin transfer (ICT/IST) in $\mathbf{1}^{\bullet+}$ is thermally activated, which is characteristic of class-II mixed-valence MV compounds.[19] Spectral simulation of the observed VT-ESR spectra of $\mathbf{1}^{\bullet+}$ by using the ESR-EXN program[20] gave the first-order rate constant (k_{th}) for the ICT/IST process at each temperature (Figure 3.6a), and finally, from the Arrhenius plot, we estimated the activation barrier (ΔG^*) for the thermally activated ICT/IST at 1.83 kcal mol^{-1} for $\mathbf{1}^{\bullet+}$. In the class-II MV states, the ΔG^* value can be related to the electronic coupling (V) and the reorganization energy (λ) by Eq. (3.1).[21]

$$\Delta G^{*} = \frac{(\lambda - 2V)^2}{4\lambda} \qquad (3.1)$$

Hence, the electronic coupling for $\mathbf{1}^{\bullet+}$ can be deduced from Eq. (3.1) by using the VT-ESR barrier, ΔG^{*}, and the optically determined λ, which corresponds to the energy of the IV-CT band maximum. The MV state of $\mathbf{1}^{\bullet+}$ was also examined by DFT calculations (BLYP35/SVP + CPCM(CH_2Cl_2))[22], which predict the activation barrier (ΔG^{*}) in the double well potential is 3.68 kcal mol^{-1} for $\mathbf{1}^{\bullet+}$ and the computed transition energy for optically induced ICT/IST process was 6723 cm^{-1}, and furthermore, the computed small oscillator strength (f = 0.015) supports the difficulty of the observation of IVCT band for $\mathbf{1}^{\bullet+}$. Judging from the DFT-computed transition energy, even though the IV-CT band was not observed for $\mathbf{1}^{\cdot+}$, the electronic coupling can be estimated to be 3.68 kcal mol^{-1} (= 1287 cm^{-1}) for $\mathbf{1}^{\cdot+}$. The estimated energy diagram for the ICT/IST of $\mathbf{1}^{\cdot+}$ is summarized in Figure 3.6b. Turning to the VT-ESR spectra for $\mathbf{3}^{\bullet+}$, the observed spectrum with five-line hyperfine structure at 293 K corresponds to the equally charge/spin distribution on the two equivalent nitrogen nuclei within the ESR timescale, and the spectral line shape remained unchanged in the measured temperature range (193–293 K), strongly suggesting the class-III MV state for $\mathbf{3}^{\bullet+}$. For macrocycle **1**, we could observe a fine-structured ESR for $\mathbf{1}^{2+}$, when 2 equiv of $AgSbF_6$ were added in CH_2Cl_2 solution of **1** (Figure 3.7), thus indicating the formation of a biradical with probably largely independent unpaired spins.[23] The average spin-spin distance between the diagonally positioned two N atoms was roughly estimated to be 8 Å within the point-dipole approximation,[24] which is in good agreement with the separation of 7.63 Å by the X-ray analysis of **1**, suggesting the spin distribution is highly localized on the two nitrogen centers.

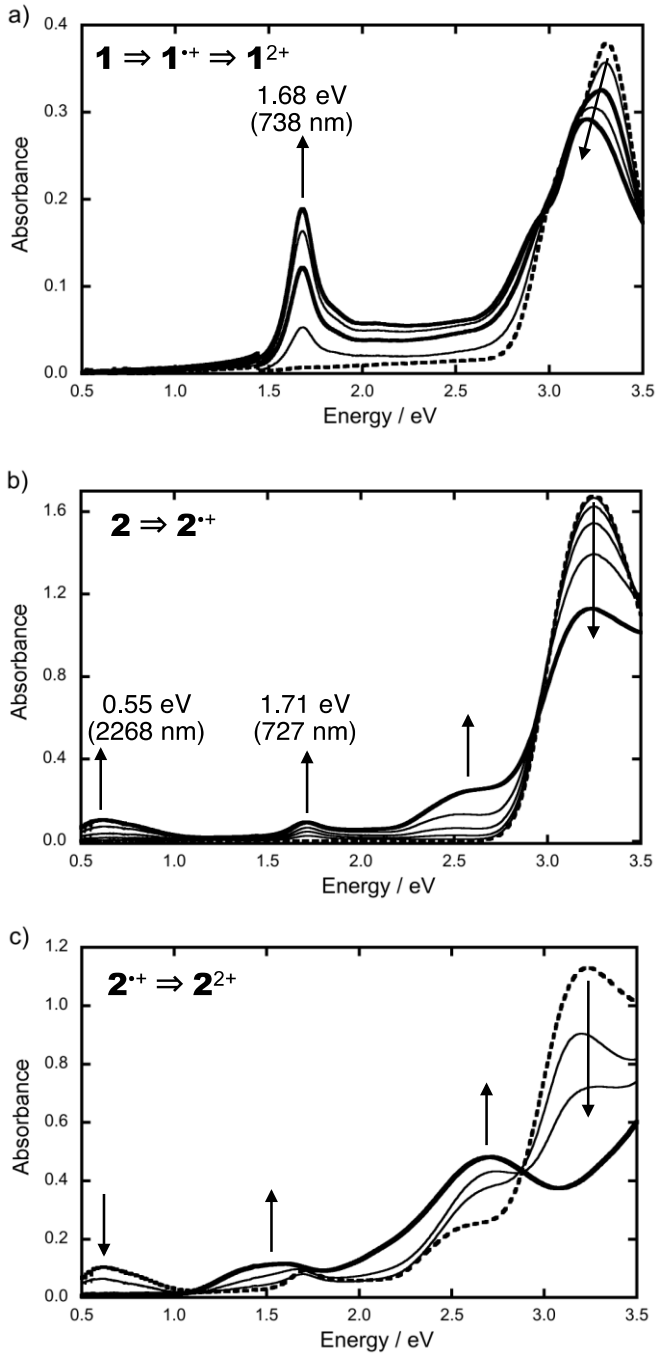

Figure 3.4. UV/Vis-NIR optical absorption spectra of a) the stepwise chemical oxidation with $AgSbF_6$ from **1** (broken line) to $\mathbf{1}^{2+}$ (solid line), and the stepwise electrochemical oxidation b) from **2** (broken line) to $\mathbf{2}^{\bullet+}$ (solid line) and c) from $\mathbf{2}^{\bullet+}$ (broken line) to $\mathbf{2}^{2+}$ (solid line), in CH_2Cl_2 (at 1×10^{-4} M) at 298 K.

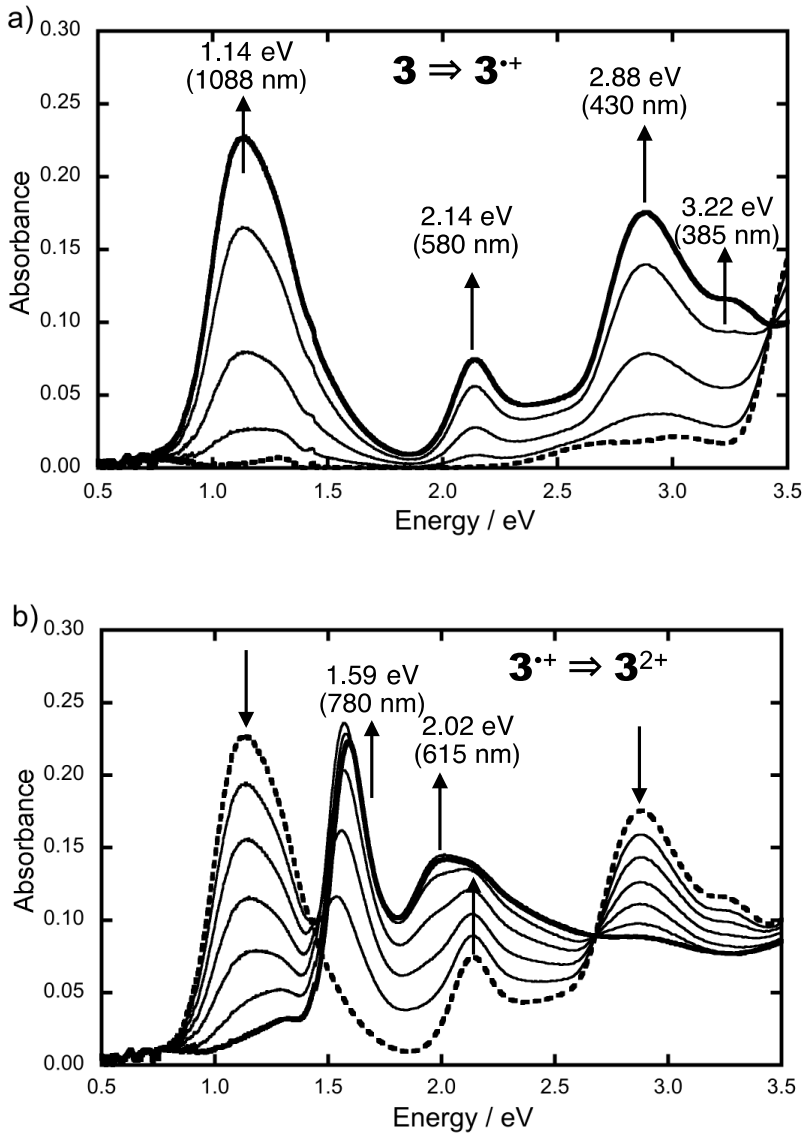

Figure 3.5. UV/Vis-NIR optical absorption spectra of the stepwise electrochemical oxidation a) from **3** (broken line) to $\mathbf{3}^{\bullet+}$ (solid line) and b) from $\mathbf{3}^{\bullet+}$ (broken line) to $\mathbf{3}^{2+}$ (solid line) in CH_2Cl_2 (at 1×10^{-4} M) at 298 K.

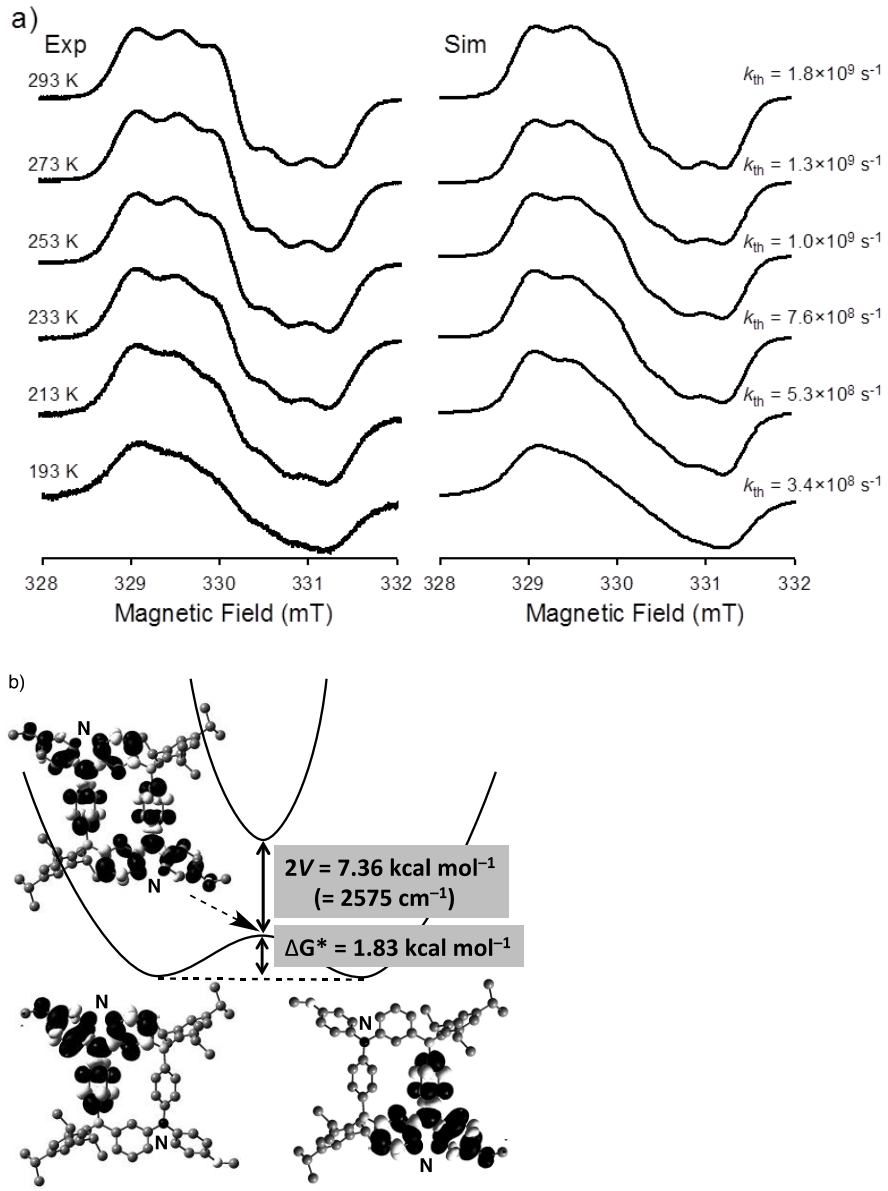

Figure 3.6. a) Observed X-band VT-ESR spectra (left) and simulated spectra with determined intramolecular ICT/IST rates (k_{th}) (right) of $\mathbf{1}^{\bullet+}$ in CH_2Cl_2 (at 1×10^{-3} M) by oxidation with 0.5 equiv of $AgSbF_6$, and b) the schematic energy diagrams for the ICT/IST of $\mathbf{1}^{\bullet+}$ in CH_2Cl_2; the depicted molecular structures with spin density distribution are the optimized structures at the local minima and the saddle point in double-well potential [BLYP35/SVP + CPCM(CH_2Cl_2) level of theory].

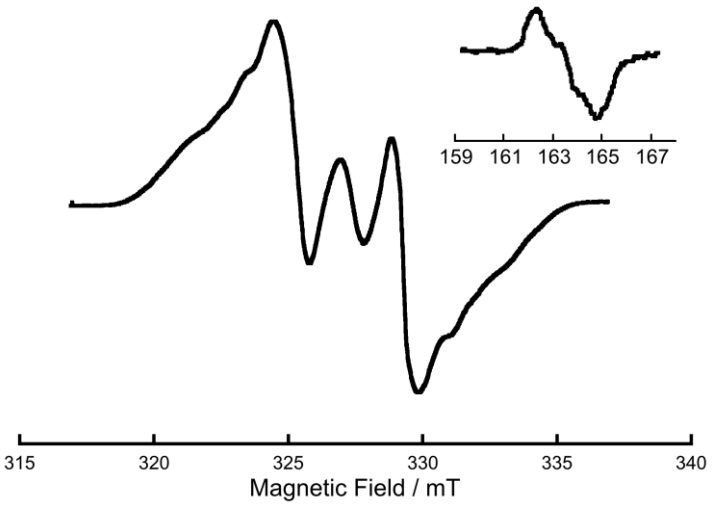

Figure 3.7. X-band ESR spectra of $\mathbf{1}^{2+}$ in CH_2Cl_2 at 123 K. Inset: The forbidden ΔM_S = ±2 resonance at 123 K.

The optical absorption and emission spectroscopic data of compounds **1**, **2**, and their related compounds in common organic solvents with different polarity are summarized in Table 3.3. Judging from the TD-DFT results (Figure 3.3), the absorption maxima for **1** and **2** are assigned to the ICT from the lone pairs of N atoms to the vacant p orbitals of B atoms ($S_1 \leftarrow S_0$ and $S_2 \leftarrow S_0$ transitions), and more importantly, their ICT band shapes and maxima almost remained unchanged, as is often in the case with these B-π-N type aromatics.[2,25] In contrast, both **1** and **2** exhibited a pronounced bathochromic shift in emission spectra with increasing solvent polarity, demonstrating a large excited-state dipole moment based on the efficient ICT from N center to B center through π-bridging macrocyclic backbone (Figure 3.8 and 3.9). The quantum yield of **1** was moderate (Φ_F = 0.16 to 0.40), while that of **2** was comparable to **MC-B3N3**. More interestingly, **1** showed a inverse energy-gap law in degassed organic solvents, whereas **2** obeyed the energy-gap law characteristic for ICT-based emitters,[26] as is apparent from the sharp

decrease of quantum yield in degassed CH_3CN (Φ_F = 0.22). Additionally, the Stokes shifts for both **1** and **2** were remarkably large as compared with that for **MC-B3N3**. In relation to this observation, the phenomena of the symmetry-breaking in the excited state driven by structural and/or solvent fluctuations have been discussed and observed actually in multi-polar molecules.[27] Therefore, we carried out the TD-DFT optimization of the S_1 states of both **1** and **2** at the B3LYP/6-31G* level of theory in order to investigate the structural relaxation from the Franck-Condon geometries. As shown in Figure 3.10, it was confirmed that the rectangular macrocyclic structures could be easily distorted in the relaxed S_1 states, thereby resulting in the localization of the highest and lowest singly occupied MO (H-SOMO and L-SOMO). The TD-DFT results predict that this symmetry-breaking causes the large excited dipole moments for **1** (16.7 D) and **2** (22.5 D).

Table 3.3. Photophysical properties of **1**, **2**, and their related compounds.

	Solvent	λ_{abs} [a]	λ_{em} [b]	Δν	Φ_F [c]
		[nm]	[nm]	[cm^{-1}]	
1	*n*-hexane	373	436	3874	0.12 (0.16)
	toluene	377	458	4691	0.16 (0.20)
	THF	374	480	5905	0.24 (0.28)
	CH_2Cl_2	375	493	6383	0.30 (0.36)
	CH_3CN	372	516	7502	0.28 (0.40)
	solid		470		0.05
2	*n*-hexane	383	433	3015	0.43 (0.71)
	toluene	387	461	4148	0.58 (0.81)
	THF	383	500	6110	0.63 (0.80)
	CH_2Cl_2	382	518	6873	0.61 (0.79)
	CH_3CN	378	564	8725	0.17 (0.22)
	solid		465		0.15
MC-B3N3[d]	CH_2Cl_2	420, 390[d]	460	~2300	0.76
para-**BN**[e]	CH_2Cl_2	386	554	7856	0.56 (0.67)

[a] Absorption maximum at the lowest energy band measured at 1×10^{-4} M. [b] Emission maximum upon photoexcitation at λ = 380 nm measured at 1×10^{-5} M (at λ = 340 nm for solid state measurements). [c] Absolute fluorescence quantum yield determined with a calibrated integrating sphere system; the value in parentheses was measured in degassed solvent. [d] From Ref. [3]; the values of λ_{abs} for two energy bands were reported for toluene solution. [e] Emission maximum upon photoexcitation at λ = 320 nm measured at 1×10^{-5} M.

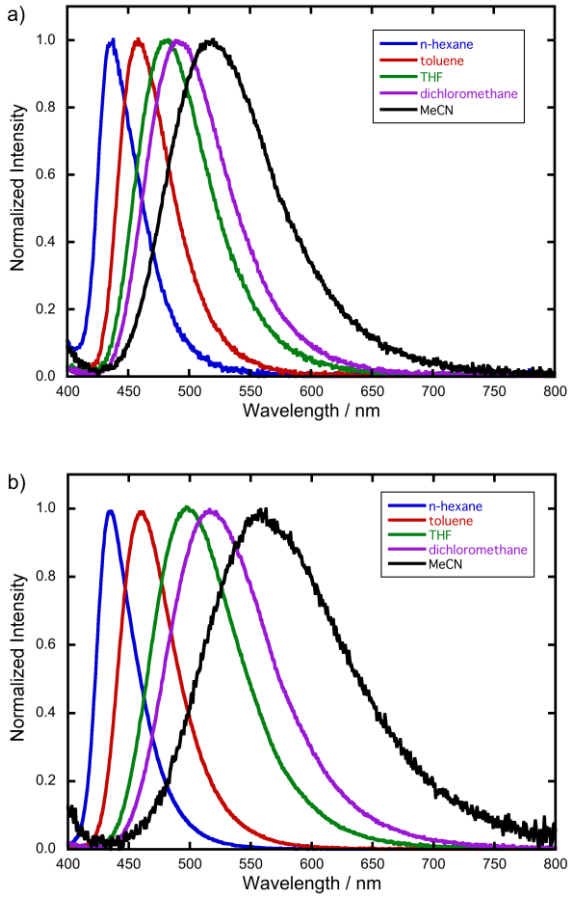

Figure 3.8. Emission spectra of a) **1** and b) **2** in various solvents with different polarity (at 1×10^{-5} M).

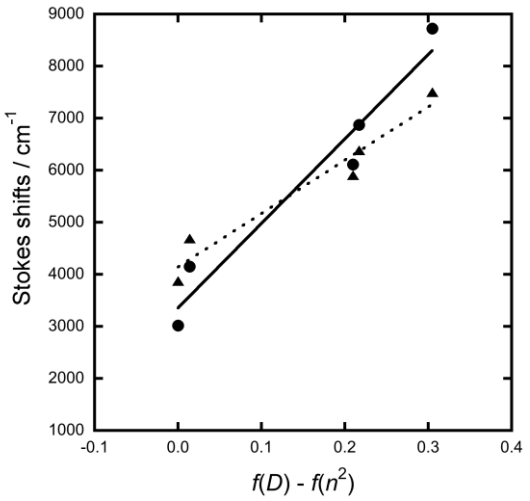

Figure 3.9. Lippert-Mataga plots for **1** (triangle) and **2** (circle).

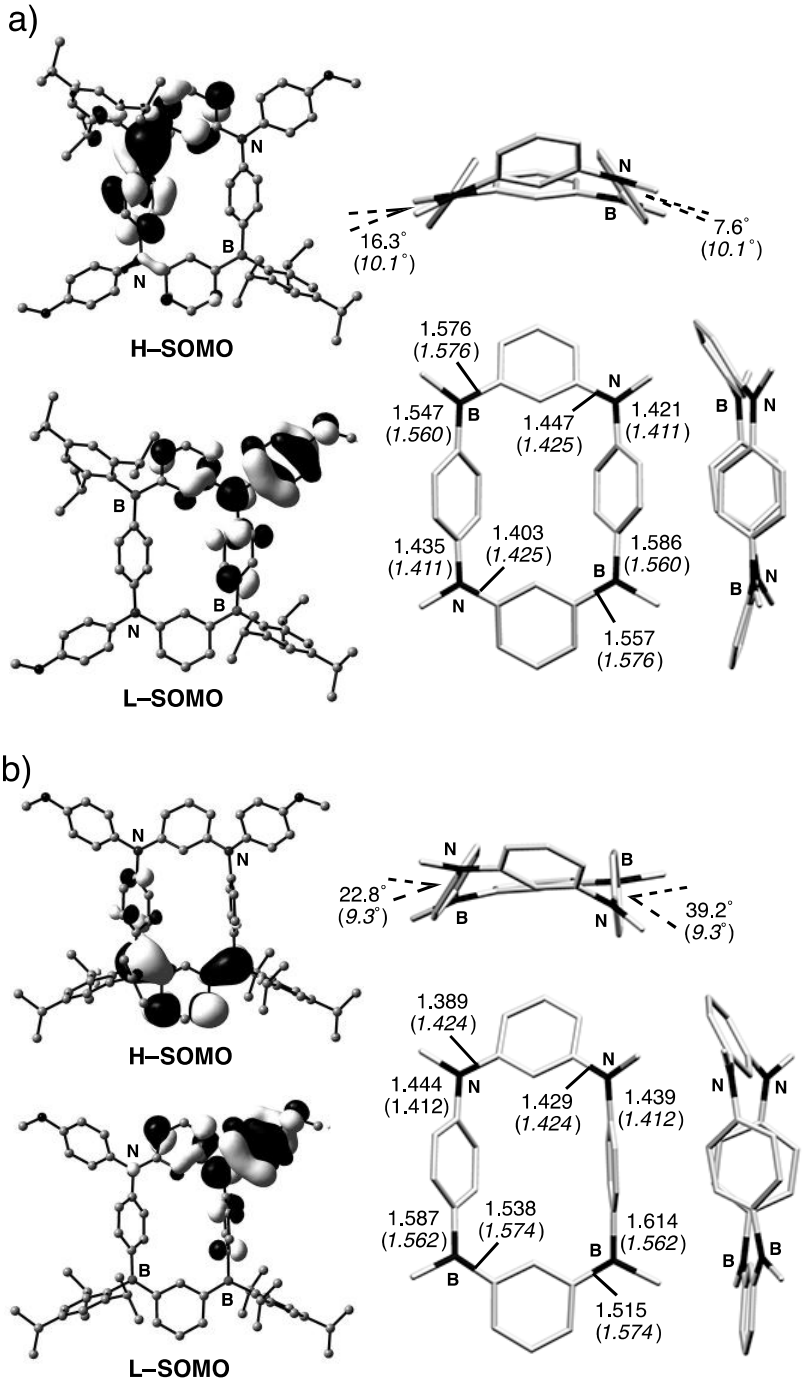

Figure 3.10. Molecular structures with selected bond lengths (Å) and dihedral angles between the adjacent BC_3 and NC_3 planes, and the frontier orbitals of the TD-DFT-optimized S_1 state of a) **1** and b) **2** at the B3LYP/6-31G* level of theory. The values in parentheses correspond to those for the DFT-optimized S_0 states.

3.4 Conclusion

In this chapter, new ambipolar π-conjugated B-π-N macrocycles **1**–**3** revealed that significantly different electronic and optical properties were attributed to the different B-π-N embedded patterns. Oxidized species $\mathbf{1}^{\bullet+}$ and $\mathbf{1}^{2+}$ exhibited an interesting IVCT phenomenon and a biradical character, respectively. *Meta*-phenylene-linked B-π-N moieties resulted in non-emissive macrocycle **3**. The anti-parallelly B-π-N embedded **1** disclosed the ICT-based fluorescence obeying an unusual inverse energy-gap law, while the parallelly embedded **2** strongly emitted following the energy-gap law for the usual ICT-based emitters. The extension to multiply B-π-N embedded macrocycles is also expected to show intriguing (opto)electronic properties.

3.5 References

[1] a) M. M. Morgan, W. E. Piers, *Dalton Trans*. **2016**, *45*, 5920-5924; b) H. Helten, *Chem. Eur. J*. **2016**, *22*, 12972-12982.

[2] L. Ji, S. Griesbeck, T. B. Marder, *Chem. Sci*. **2017**, *8*, 846-863, and references therein.

[3] P. Chen, R. A. Lalancette, F. Jäkle, *Angew. Chem. Int. Ed*. **2012**, *51*, 7994-7998.

[4] P. Chen, F. Jäkle, *J. Am. Chem. Soc*. **2011**, *133*, 20142-20145.

[5] A. Ito, Y. Yokoyama, R. Aihara, K. Fukui, S. Eguchi, K. Shizu, T. Sato, K. Tanaka, *Angew. Chem. Int. Ed*. **2010**, *49*, 8205-8208.

[6] P. Chen, X. Yin, N. Baser-Kirazli, F. Jäkle, *Angew. Chem. Int. Ed*. **2015**, *54*, 10768-10772.

[7] X.-Y. Wang, A. Narita, X. Feng, K. Müllen, *J. Am. Chem. Soc*. **2015**, *137*, 7668-7671.

[8] A. Pelter, K. Smith, D. Buss, Z. Jin, *Heteroatom Chem.* **1992**, *3*, 275-277.

[9] S. I. Hauck, K. V. Lakshmi, J. F. Hartwig, *Org. Lett*. **1999**, *1*, 2057-2060.

[10] M. Kranenburg, Y. E. M. van der Burgt, P. C. J. Kamer, P. W. N. M. van Leeuwen, *Organometallics* **1995**, *14*, 3081-3089.

[11] K. Ragavachari, *Theor. Chem. Acc*. **2000**, *103*, 361-363 and references cited therein.

[12] A. Dreuw, M. Head-Gordon, Chem. Rev. **2005**, *105*, 4009-4037.

[13] W. J. Hehre, L. Radom, P.v. R. Schleyer, J. A. Pople, *Ab Initio Molecular Orbital Theory*, Wiley, New York, **1986**.

[14] M. J. Frisch, *et al*., Gaussian 09 (Revision D.01), Gaussian, Inc., Wallingford CT, **2013**.

[15] G. M. Sheldrick, *Acta Cryst*. *A* **2008**, *64*, 112-122.

[16] A. Altomare, G. Cascarano, C. Giacovazzo, A. Guagliardi, A, *J. Appl. Cryst*. **1993**, *26*, 343-350.

[17] CrystalStructure 4.2, Crystal Structure Analysis Package: Rigaku Corporation, Tokyo 196-8666, Japan, **2000-2015**

[18] C. Lambert, G. Nöll, *J. Am. Chem. Soc*. **1999**, *121*, 8434-8442.

[19] a) J. Hankache, O. S. Wenger, *Chem. Rev*. **2011**, *111*, 5138-5178; b) A. Heckmann, C. Lambert, *Angew. Chem. Int. Ed.* **2012**, *51*, 326-392.

[20] J. Heinzer, *Mol. Phys.* **1971**, *22*, 167-177.

[21] B. S. Brunschwig, C. Creutz, N. Sutin, *Chem. Soc. Rev*. **2002**, *31*, 168-184.

[22] M. Parthey, M. Kaupp, *Chem. Soc. Rev*. **2014**, *43*, 5067-5088.

[23] The DFT-computed singlet–triplet energy difference was estimated to be 0.04 kcal mol^{-1}, suggesting the degeneracy between the two spin states for $\mathbf{1}^{2+}$.

[24] N. Hirota, *J. Am. Chem. Soc*. **1967**, *89*, 32-41

[25] a) R. Kurata, K. Kaneda, A. Ito, *Org. Lett*. **2017**, *19*, 392-395; b) R. Kurata, A. Ito, M. Gon, K. Tanaka, Y. Chujo, *J. Org. Chem*. **2017**, *82*, 5111-5121.

[26] a) R. Engleman, J. Jortner, *Mol. Phys*. **1970**, *18*, 145-164; b) W. Siebrand, *J. Chem. Phys.* **1971**, *55*, 5843.

[27] a) F. Terenziani, A. Painelli, C. Katan, M. Charlot, M. Blanchard-Desce, *J. Am. Chem. Soc*. **2006**, *128*, 15742-15755; b) F. Terenziani, O. V. Przhonska, S. Webster, L. A. Padilha, Y. L. Slominsky, I. G. Davydenko, A. O. Gerasov, Y. P. Hovtun, M. P. Shandura, A. D. Kachkovski, D. J. Hagan, E. W. Van Stryland, A. Painelli, *J. Phys. Chem. Lett.* **2010**, *1*, 1800-1804; c) E. Vauthey, *ChemPhysChem* **2012**, *13*, 2001-2011; d) B. Dereka, A. Rosspeintner, Z. Li, R. Liska, E. Vauthey, *J. Am. Chem. Soc*. **2016**, *138*, 4643-4649.

Part 3

Charge/Spin Transfer Mechanisms of Triphenylamine-Based Functional Materials

Introduction

Mixed-valence(MV) systems provide a excellent model in investigating the electron or charge transfer phenomena.[1,2] Organic MV compounds are effective hole-transport materias in OLEDs, solar cells. However, the importance of organic MV chemistry should not be seen in terms of the direct applicability of these species but the wealth of knowledge about electron or charge transfer phenomena that has been gained through their study. Mixed valence system has two redox sites with linker and two redox centers with differential oxidation states. Marcus introduced the model for the potential energy surfaces constructed from the two degenerate parabolic energy surfaces.[3] Each surface represents the valence state with the spin or charge localized on one redox active site. If the electronic coupling appeared between these valence states, their two parabolic energy surfaces avoid crossing in their intersection region, and results in two adiabatic

energy surfaces of which splitting is twice the electronic coupling energy V. As a result, the shape of the lower adiabatic energy surface is determined by the relative size of the electronic coupling energy V and the vertical energy gap λ at the energy minimum for the diabatic surface. Robin and Day classified mixed valence compounds into three classes according to the delocalization or localization charge or spin (Figure 1). [4]

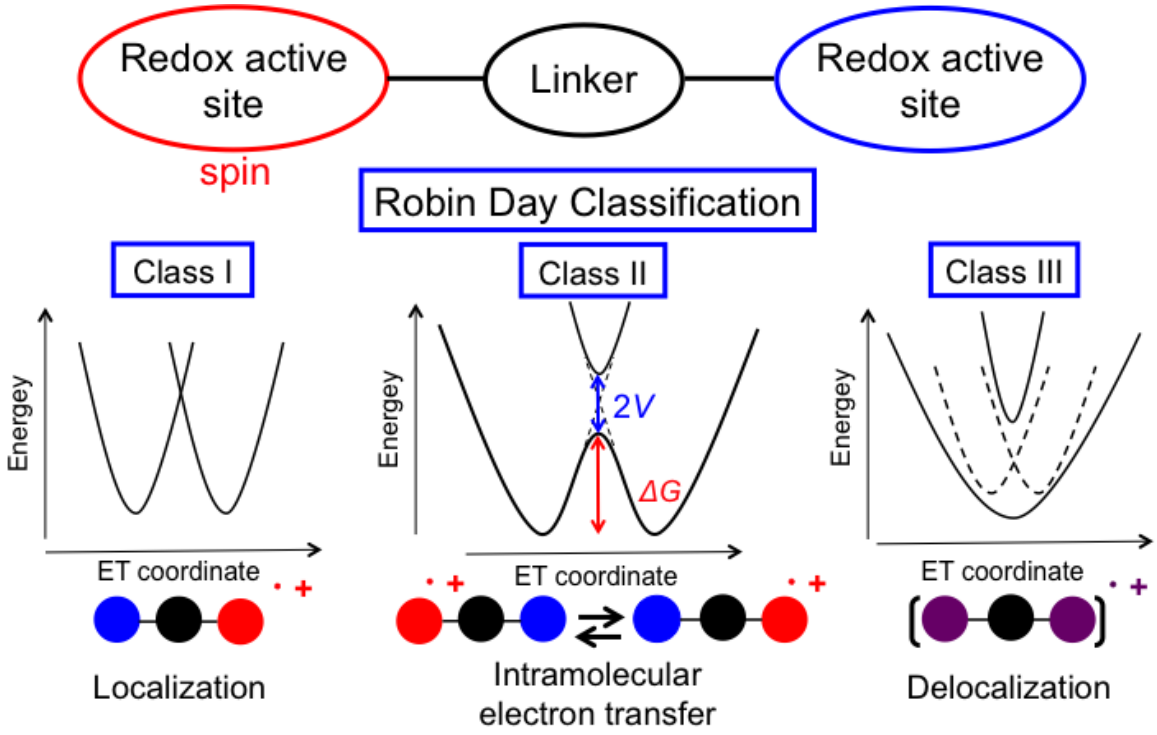

Figure 1. Potential energy surface for mixed-valence systems.

In class I, the charge or spin is completely localized on one redox center, because the redox active sites do not interact with each other owing to $V = 0$. When the electronic coupling V is smaller than $\lambda/2$, class II refers to weakly interacting redox centers and with the extra charge localized at one of the redox centers. Class II mixed-valence compounds have double well potential and intramolecular electron transfer with the

barrier ΔG. Optical excitation from one minimum to Frank-Condon state of the upper surface is observed as a broad and nearly Gaussian-shaped absorption band which is often observed in the near-IR (NIR) region, and commonly referred to as the intervelence charge transfer (IVCT) band. This excitation is associated with photo-induced electron transfer between the two redox sites. Recently, Kaupp and co-workers pointed out the fact that the frequently used B3LYP hybrid functional may often lead to erroneous results in organic class-II MV compounds. when the lowest-energy transition IVCT band was examined by the time-dependent DFT (TD-DFT) calculations. [5] In fact, the B3LYP/6-31G* geometrical optimization for triphenylamine based class-II MV compounds gave the symmetrical structure, and the lowest-energy transition energy was computed to be much lower energy than observed band. Hence, we have also performed the DFT calculations for triphenylamine based class-II MV compounds by using the BLYP-based hybrid functional with 35% exact exchange and the SVP basis sets[6] (BLYP35/SVP),[5] including the solvation effect by the CPCM version[7] of polarizable continuum solvent model. As a result, the asymmetric optimized structure with the spin-density being localized on one of the redox active site was obtained, and the computed transition energy assignable to the observed IV-CT band. From the observed IVCT band, the electronic coupling (V) were evaluated by the Mulliken-Hush theory [Eq. (1)]:[2]

$$V = \frac{\mu_{ab}\tilde{\nu}_{\max}}{\Delta\mu_{12}} \qquad (1)$$

where μ_{ab} is the transition moment, which is determined by integration of the IV-CT

band, $\tilde{\nu}_{max}$ the energy of the IV-CT band maximum, $\Delta\mu_{12}$ the difference in the diabatic dipole moments between the ground and excited states, which is calculated by Eq. (2),

$$\Delta\mu_{12} = \sqrt{(\Delta\mu_{ab})^2 + 4(\mu_{ab})^2} \qquad (2)$$

from the difference in the adiabatic dipole moments between the ground and excited states $\Delta\mu_{ab}$. Besides the above-mentioned optical ICT/IST, thermally activated ICT/IST event can be observable by the variable-temperature electron spin resonance (VT-ESR) spectroscopy. On the class-II MV compounds bearing two nitrogen atoms, the ESR spectral intensities of the central three lines decreased gradually with the decreasing temperature. Such a temperature dependency clearly indicates that the five-line pattern at room temperature is induced by thermally activated ICT/IST between the two triarylamine redox centers on the ESR time scale.[8-10] The observed VT-ESR spectra at various temperatures can be simulated using the ESR-EXN program when there exists the intramolecular dynamic spin exchange among the multi-redox-active centers.[11] From the simulation, the first-order rate constants (k_{th}) for the thermally activated ICT/IST process between the two triarylamine redox centers can be obtained [Eq. (3)]:

$$k_{th} = A\exp\left(-\frac{\Delta G^*}{k_B T}\right) \qquad (3)$$

From the clear linear relationship between ln(k_{th}) and 1/T which the Arrhenius plot gave, the activation barrier (ΔG^*) for the thermally activated ICT/IST was estimated. In the

case of degenerate MV states, the ΔG^* value can be related to the electronic coupling (V) and the reorganization energy (λ) by Eq. (4).[12]

$$\Delta G^* = \frac{(\lambda - 2V)^2}{4\lambda} \qquad (4)$$

Hence, the electronic couplings can be deduced from Eq. (4) by using the VT-ESR barrier, ΔG^*, and the optically determined λ, which corresponds to the energy of the IV-CT band maximum. The energy barrier for the thermal electron transfer vanishes for class III compounds at $V \geq \lambda/2$. In class III MV compounds, the electronic coupling is so strong that the lower adiabatic energy surface has only a single minimum. In this case, the charge or spin can be fully delocalized over the two redox active sites, and then the formal charge on each redox active site is 1/2 charges. The absorption band maximum λ occurs at $2V$. However, Nelsen et al. demonstrated that such a simple model should not be used to analyze delocalized MV compounds and, moreover, pointed out that the estimated value of V ($V = \lambda/2$) is substantially underestimated.[13] Delocalized MV compounds have a symmetrical charge or spin distribution, and therefore, on the linker. This means that a usual quantum chemical calculation permits the assignment of the lowest energy absorption bands of delocalized MV compounds to specific electronic transitions.

The radical cation species of triphenylamine-based materials are one of the most comprehensively MV compounds.[1,2] The reason is because the most of the triphenylamine-based radical cations show characteristic absorption in visible and/or NIR region owing to intramolecular electron transfer, and these radical species often

show the ESR spectra with well-resolved hyperfine splitting from the nuclear spins of the nitrogen atom. As mentioned in General Introduction, triphenylamine-based materials are widely used in organic electronic devices. Thus, it is important to clarify the intramolecular electron transfer of triphenylamine-based materials from the view point of material science.

In Chapter 1 and 2, radical cations of bis(triarylamine) bridged by *ortho-, meta-, and para*-phenylene and *ortho*-carborane cluster have been prepared to elucidate the difference in intramolecular charge/spin transfer (ICT/IST) pathway due to the different bridging units. Electrochemistry, absorption spectroscopy, VT-ESR spectroscopy, and DFT calculations reveal which classes in MV states these radical cations are.

References

[1] J. Hankache, O. S. Wenger, *Chem. Rev*. **2011**, *111*, 5138-5178.

[2] A. Heckmann, C. Lambert, *Angew. Chem. Int. Ed.* **2012**, *51*, 326-392.

[3] R. A. Marcus, N. Sutin, *Biochim. Biophys. Acta* **1985**, *811*, 265-322.

[4] M. Robin, P. Day, *Adv. Inorg. Chem. Radiochem.* **1976**, *10*, 247-422.

[5] a) M. Renz, K. Theilacker, C. Lambert, M. Kaupp, *J. Am. Chem. Soc*. **2009**, *131*, 16292-16302; b) M. Renz, M. Kess, M. Diedenhofen, A. Klamt, M. Kaupp, *J. Chem. Theory Comput*. **2012**, *8*, 4189-4203; c) M. Parthey, M. Kaupp, *Chem. Soc. Rev*. **2014**, *43*, 5067-5088.

[6] A. Schöfer, H. Horn, R. Ahlrichs, *J. Chem. Phys*. **1992**, *97*, 2571-2577.

[7] M. Cossi, N. Rega, G. Scalmani, V. Barone, *J. Comput. Chem*. **2003**, *24*, 669-681.

[8] Y. Hirao, M. Urabe, A. Ito, K. Tanaka, *Angew. Chem. Int. Ed.* **2007**, *46*, 3300-3303.

[9] K. Lancaster, S. A. Odom, S. C. Jones, S. Thayumanavan, S. R. Marder, J.-L. Brédas, V. Coropceanu, S. Barlow, *J. Am. Chem. Soc*. **2009**, *131*, 1717-1723.

[10] D. R. Kattnig, B. Mladenova, G. Grampp, C. Kaiser, A. Heckmann, C. Lambert, *J. Phys. Chem. C* **2009**, *113*, 2983-2995.

[11] J. Heinzer, *Mol. Phys.* **1971**, *22*, 167-177.

[12] B. S. Brunschwig, C. Creutz, N. Sutin, *Chem. Soc. Rev*. **2002**, *31*, 168-184.

[13] a) S. F. Nelsen, M. N. Weaver, J. I. Zink, J. P. Telo, *J. Am. Chem. Soc.* **2005**, *127*, 10611-10622; b) S. F. Nelsen, M. N. Weaver, J. P. Telo, B. L. Lucht, S. Balow, *J. Org. Chem.* **2005**, *70*, 9326-9333.

Chapter 1

Recognizing Through-Bond and Through-Space Self-Exchange Charge/Spin Transfer Pathways in Bis(triarylamine) Radical Cations with Similar Geometrical Arrangements

1.1 Introduction

Since the first report of the spectroscopic analysis of the so-called intervalence charge-transfer (IV-CT) band for *meta*-phenylene-bridged bis(triarylamine) (BTA) radical cation $\mathbf{1}^{\bullet+}$,[1] the understanding of mixed-valence (MV) compounds containing triarylamine units as purely organic redox centers has been at the forefront of research in fundamental intramolecular CT (ICT) phenomena.[2] Among three kinds of phenylene-bridged BTAs, both *meta*- and *para*-phenylene-bridged BTA radical cations $\mathbf{1}^{\bullet+}$ and $\mathbf{2}^{\bullet+}$ have been investigated by optical methods, and the electronic couplings (V) between the two triarylamine redox centers were estimated to be 181 and 1000 cm^{-1}, respectively.[1,3] In these two BTA-based MV compounds, it should be basically

sufficient to consider only the through-bond electronic communication of two different ICT pathways: the through-bond and through-space ones. When it comes to the *ortho*-phenylene-bridged BTA radical cation $\mathbf{3}^{\bullet+}$, the situation might be completely changed, though no reports to date on the mixed-valency of $\mathbf{3}^{\bullet+}$. In fact, sterically overcrowded *ortho*-phenylene-bridged oligoarylamine radical cations, $\mathbf{6}^{\bullet+}$ and $\mathbf{7}^{\bullet+}$, rejected the apparent dichotomy, thus exhibiting significant contribution of both through-bond and through-space interaction to the IV-CT event.[4] Probably, more importantly, in conjunction with the so-called toroidal delocalization/conjugation of charge/spin in radical cations of redox-active hexaarylbenzene derivatives like **5**,[5] where the through-space charge delocalization is supposed to be realized through six arene units attached to the central benzene ring in a paddlewheel-like fashion, the compound $\mathbf{3}^{\bullet+}$ also serves as an optimal dyad model compound of $\mathbf{5}^{\bullet+}$ to estimate the contribution of the through-bond and through-space interaction.

In addition, as an antipode of the π-conjugated through-bond interaction via ortho-phenylene in $\mathbf{3}^{\bullet+}$, the σ-conjugated through-bond interaction via *ortho*-carborane[6] cluster in $\mathbf{4}^{\bullet+}$, if it does exist, is intriguing. As shown in Figure 1.1, the BTAs **3** and **4** have similar geometrical arrangements on the two nitrogen redox centers,[7] although the orientation of the two NC_3 planes differs between the two compounds.[8] As such, radical cations of these compounds are attractive analogs for exemplifying a segregation of covalent and noncovalent pathways in the IV-CT process.

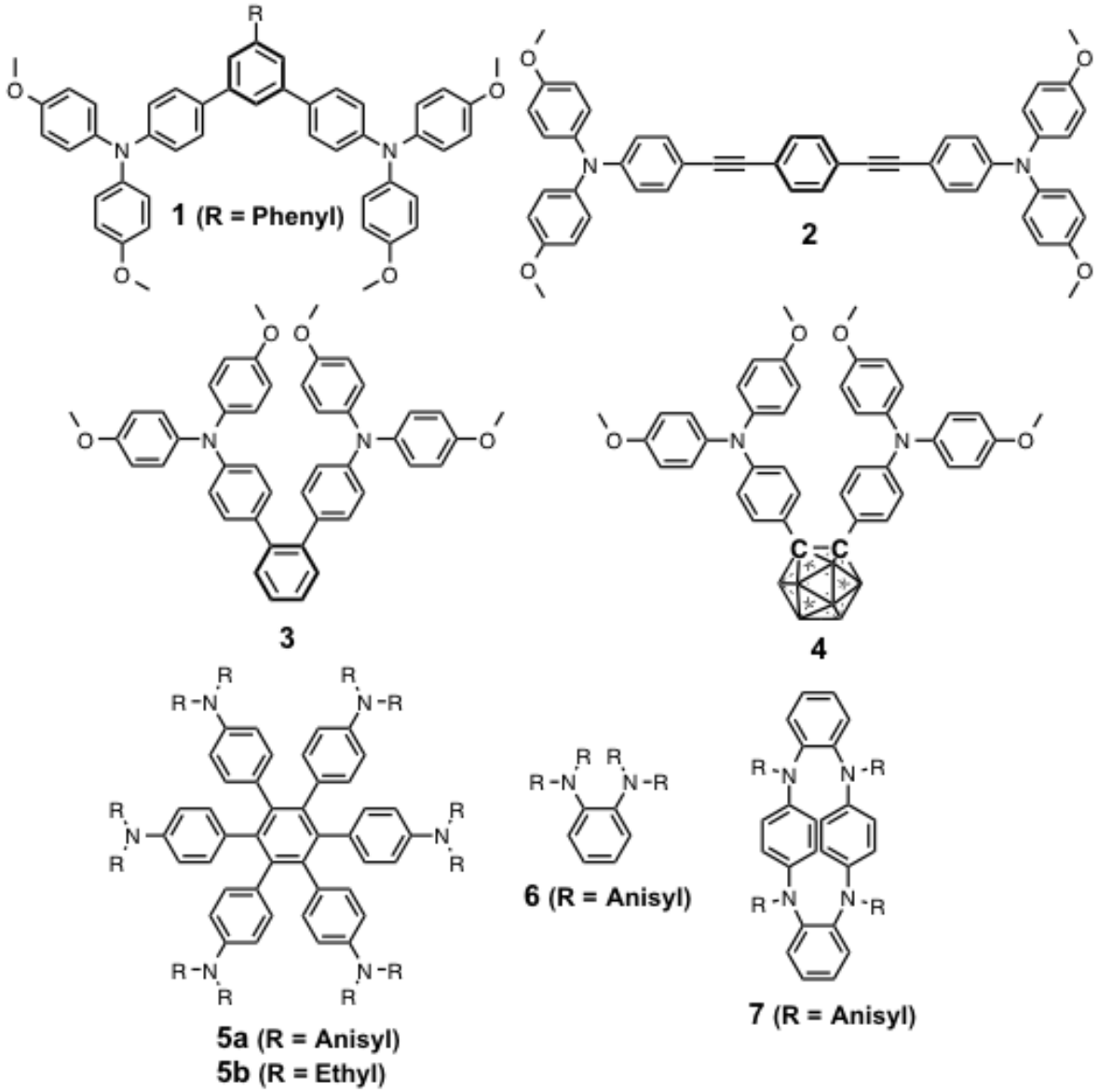

Scheme 1.1. Bis(triarylamine)s **1**–**4** and the related compounds **5**–**7**.

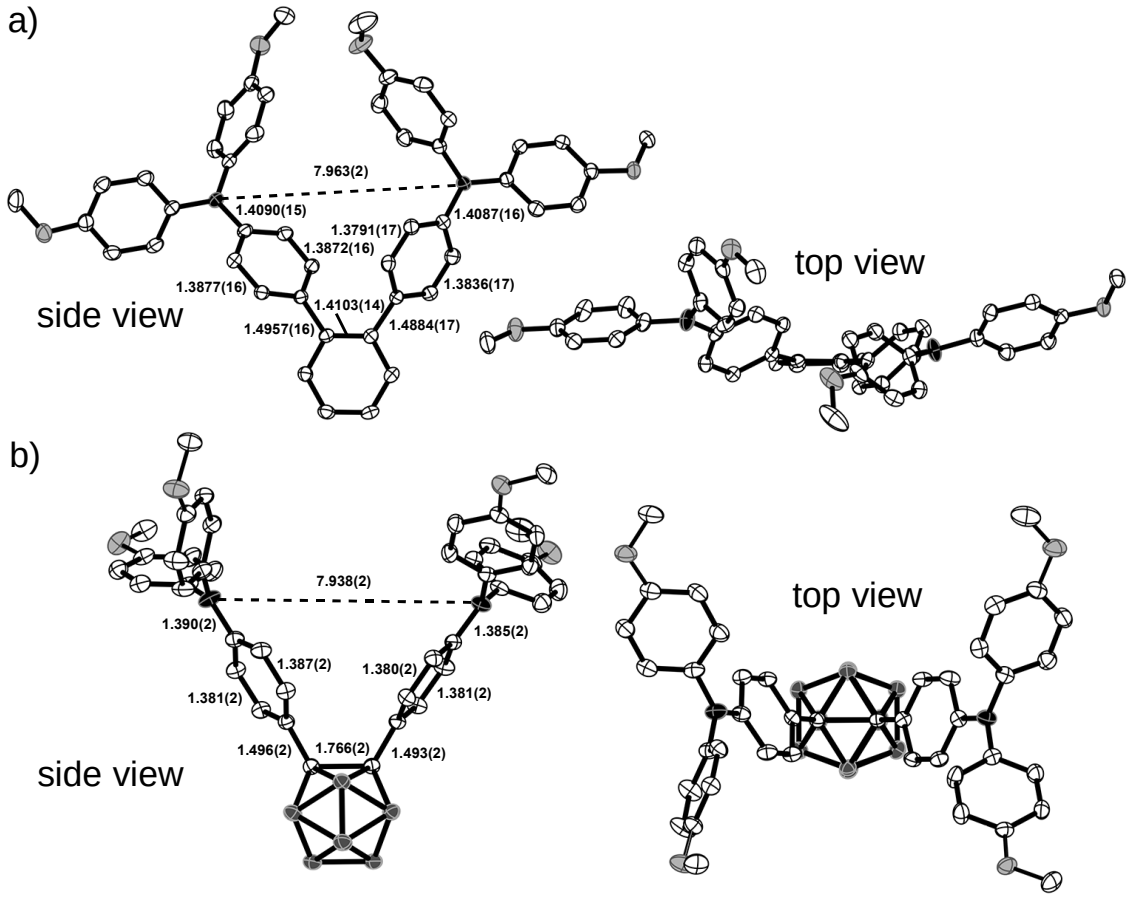

Figure 1.1. Molecular structures and selected bond lengths of a) **3** and b) **4** (one of the two crystallographically independent molecules) in the solid state at 144(1) K. Ellipsoids are set at 50% probability; hydrogen atoms are omitted for clarity; nitrogen atoms are colored in black.

1.2 Experimental Section

1.2.1 Synthesis

All the purchased reagents were of standard quality, and used without further purification. All the purchased solvents were purified, dried, and degassed by standard procedures. Column chromatography was performed with silica gel (Kanto Chemical Co., Inc., silica gel 60N, spherical neutral). Elemental analyses were performed by

Center for Organic Elemental Microanalysis, Kyoto University. ^{1}H and ^{13}C NMR spectra were measured by a JEOL JNM-AL400 FT-NMR spectrometer. Chemical shifts of NMR spectra are determined relative to internal tetramethylsilane (TMS) standard (δ), and are given in parts per million (ppm). UV/Vis-NIR absorption spectra were obtained with a Perkin-Elmer Lambda 950 spectrometer. High resolution (HR) electrospray ionization (ESI) mass spectra were acquired using a Thermo Fischer EXACTIVE mass spectrometer.

Synthesis of (**3**)[9]: A mixture of 4,4"-Dibromo-*o*-terphenyl (388 mg, 1 mmol), 4,4'-Dimethoxydiphenylamine (229 mg, 2.5 mmol), NaO*t*Bu (384 mg, 4 mmol), $Pd(dba)_2$ (50 mg, 0.05 mmol), $P(tBu)_3HBF_4$ (50 mg, 0.1 mmol) in toluene (15 mL) was refluxed under Ar atmosphere for 24 h. The resulting mixture was cooled down to room temperature and washed with brine. The organic layer was separated and dried over Na_2SO_4. After evaporation of the solvent, the crude product was chromatographed on silica gel (toluene : dichloromethane = 3:1 as eluent) and recrystallized from toluene/ *n*-hexane to afford **3** as a white solid (242 mg, 35.4%); m.p. 143-144 ˚C ; ^{1}H NMR (400 MHz, CDCl3) δ 7.37-7.40 (m, 2H), 7.32-7.35 (m, 2H), 7.04 (d, *J* = 9.0 Hz, 8H), 6.95 (d, *J* = 8.5 Hz, 4H), 6.82 (d, *J* = 9.0 Hz, 8H), 6.80 (d, *J* = 8.5 Hz, 4H), 3.78 (s, 12H); ^{13}C NMR (100 MHz, $CDCl_3$): δ 155.5, 146.9, 141.0, 140.3, 133.9, 130.3, 130.1, 126.9, 126.3, 120.0, 114.5, 55.5; APCI HRMS: m/z calcd for $C_{46}H_{40}N_2O_4$: 684.2983 $[M]^+$; found 684.2972 ; elemental analysis (%) calcd for $C_{46}H_{40}N_2O_4$: C, 80.68; H, 5.89; N, 4.09; found: C, 80.75; H, 5.97; N, 3.93.

Synthesis of (**4**): A mixture of 4,4'-dibromodiphenyl-*o*-carborane[10] (908 mg, 2 mmol),

4,4'-Dimethoxydiphenylamine (962 mg, 4.2 mmol), NaO*t*Bu (576 mg, 6 mmol), $Pd(dba)_2$ (100 mg, 0.1 mmol), $P(tBu)_3HBF_4$ (100 mg, 0.05 mmol) in toluene (30 mL) was refluxed under Ar atmosphere for 24 h. The resulting mixture was cooled down to room temperature and washed with brine. The organic layer was separated and dried over Na_2SO_4. After evaporation of the solvent, the crude product was chromatographed on silica gel (*n*-hexane : dichloromethane = 1:2 as eluent) and recrystallized from toluene/n-hexane to afford **4** as a yellow solid (1.13 g, 75.5%); m.p. 111 ˚C ; ^{1}H NMR (400 MHz, $CDCl_3$) δ 7.13 (d, *J* = 8.5 Hz ,4H), 6.98 (d, *J* = 8.5 Hz, 8H), 6.81 (d, *J* = 8.5 Hz, 8H), 6.60 (d, *J* = 8.5 Hz, 4H), 3.78(s, 12H); ^{13}C NMR (100 MHz, $CDCl_3$): δ 156.4, 149.9, 139.6, 131.4, 127.1, 121.6, 117.7, 114.8, 86.8, 55.5; ESI HRMS: m/z calcd for $C_{42}H_{46}N_2O_4B_{10}$: 752.4453 $[M]^+$; found 752.4457 ; elemental analysis (%) calcd for $C_{42}H_{46}N_2O_4B_{10}$: C, 67.16; H, 6.13; N, 3.73; found: C, 67.13; H, 5.99; N, 3.64.

Synthesis of $3^{2+} \cdot 2[SbF_6]^-$: Compound **3** (68 mg, 0.1 mmol) was dissolved in dichloromethane (10 mL), and $AgSbF_6$ (70 mg, 0.22 mmol) was added into the solution of **3**. The resulting solution was filtered and evaporated. The blue crude product was washed by toluene. The blue powder was dissolved in dichloromethane and *n*-hexane was layered over the solution. The turquoise powder was afforded for 1 day. ; elemental analysis (%) calcd for $C_{46}H_{40}N_2O_4Sb_2F_{12}$: C, 47.78; H, 3.49; N, 2.42; found: C, 47.56; H, 3.62; N, 2.34.

Synthesis of $4^{2+} \cdot 2[SbF6]^- \cdot 2[CH_2Cl_2]$: Compound **4** (90 mg, 0.12 mmol) was dissolved in dichloromethane (10 mL), and $AgSbF_6$ (90 mg, 0.29 mmol) was added into the solution of **4**. The resulting solution was filtered and evaporated. The blue crude

product was washed by toluene. The blue powder was dissolved in dichloromethane and *n*-hexane was layered over the solution. The blue polycrystalline solid was afforded for 1 day; elemental analysis (%) calcd for $C_{44}H_{50}N_2O_4B_{10}Sb_2F_{12}Cl_4$: C, 37.96; H, 3.62; N, 2.01; found: C, 37.95; H, 3.58; N, 2.15.

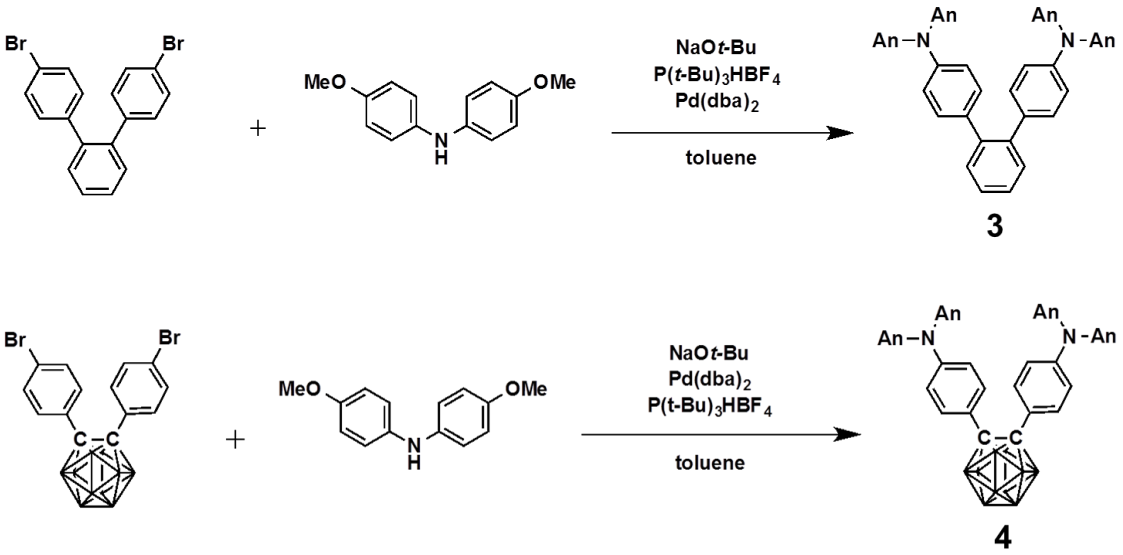

Scheme 1.2. Synthetic route of **3** and **4**.

1.2.2 DFT Calculations

Quantum chemical calculations were performed with using a hybrid Hartree–Fock/density functional theory (HF/DFT) method (B3LYP).[11] Full geometrical optimization for **3**, **4**, $\mathbf{3}^{\cdot+}$, $\mathbf{4}^{\cdot+}$, $\mathbf{3}^{2+}$, and $\mathbf{4}^{2+}$ was carried out, and furthermore, their local minimum structures were confirmed by performing subsequent frequency analyses. Excitation energies were examined on the basis of time-dependent density functional theory (TD-DFT)[12] by using the (U)B3LYP/6-31G* optimized structures. All the computations employed the 6-31G* basis sets.[13] In addition, the symmetric and asymmetric optimized structures for $\mathbf{3}^{\cdot+}$ and $\mathbf{4}^{\cdot+}$ were determined on the basis of

TD-DFT method by using the BLYP35 functional with the SVP basis sets, and their excitation energies were computed at the BLYP35/SVP level of theory.[14] In addition, the solvent effect has been included by the CPCM version of polarizable continuum solvent model for CH_2Cl_2 (ε = 8.93).[15] All these computational approaches are implemented in Gaussian 09 package of ab initio MO calculation.[16]

1.2.3 Electrochemical Measurements

The redox properties were evaluated by cyclic voltammetry (CV) and differential pulse voltammetry (DPV) in CH_2Cl_2 solution at 298 K with 0.1 M tetra-*n*-butylammonium tetrafluoroborate ($TBABF_4$) as supporting electrolyte (scan rate 100 mV s^{-1}) using an ALS/chi Electrochemical Analyzer model 612A. A three-electrode assembly was used, which was equipped with a platinum disk (2 mm^2) and a platinum wire as the working and counter electrodes, respectively, and Ag/0.01 M $AgNO_3$ (acetonitrile) was used as the reference electrode. The redox potential were referenced against a ferrocene/ferrocenium ($Fc^{0/+}$) redox potential measured in the same electrolytic solution.

1.2.4 Spectroelectrochemical Measurements

Spectroelectrochemical measurements were carried out with a custom-made optically transparent thin-layer electrochemical (OTTLE) cell (light pass length = 1 mm) equipped with a platinum mesh and a platinum coil as the working and counter electrodes, respectively, and Ag/0.01 M $AgNO_3$ (acetonitrile) was used as the reference electrode. The potential was applied with an ALS/chi Electrochemical Analyzer model 612A.

1.2.5 ESR Measurements

ESR spectra were recorded on a JEOL JES-TE200 X-band ESR spectrometer, in which temperature was controlled by a JEOL ES-DVT3 variable-temperature unit in the range of 193-293 K. A Mn^{2+}/MnO solid solution was used a reference.

1.2.6 Magnetic susceptibility measurements

The magnetic susceptibility of powder sample of $\mathbf{3^{2+}•2[SbF_6]^-}$ and polycrystalline sample of $\mathbf{4^{2+}•2[SbF_6]^-•2[CH_2Cl_2]}$ were measured by a Quantum Design MPMS-5S SQUID magnetometer in the temperature range 2–350 K at a constant magnetic field of 0.1 T. The raw data were corrected for both the magnetization of the sample holder alone and the diamagnetic contribution of the sample itself. The estimation of the diamagnetic contribution was done by using the Pacault method.[17]

1.3 Results and Discussion

A better understanding of the difference in the electronic structures of BTAs **3** and **4** in their neutral states was gained by DFT calculations (B3LYP/6-31G*). The optimized geometrical parameters, in particular, the separations between two nitrogen atoms for **3** and **4** (8.10 Å for **3** and 7.62 Å for **4**) fall within the experimental data determined by the X-ray diffraction (Figures 1.2 and 1.3). The HOMO of **3** is mainly localized on the triarylamine moieties, but has some contribution from the π-orbital of the *o*-phenylene bridging unit, thus leading to the energy gap of 0.12 eV between the HOMO and HOMO-1 orbitals (Figure 1.4). In contrast, the HOMO of **4** has almost no contribution from the σ-orbital of the *o*-carborane cluster, resulting in the quasi-degeneracy between the HOMO and HOMO-1 orbitals (0.05 eV) (Figure 1.4). These trends suggest a

negligible through-bond electronic coupling between the two triarylamine redox centers in $\mathbf{4}^{\bullet+}$.

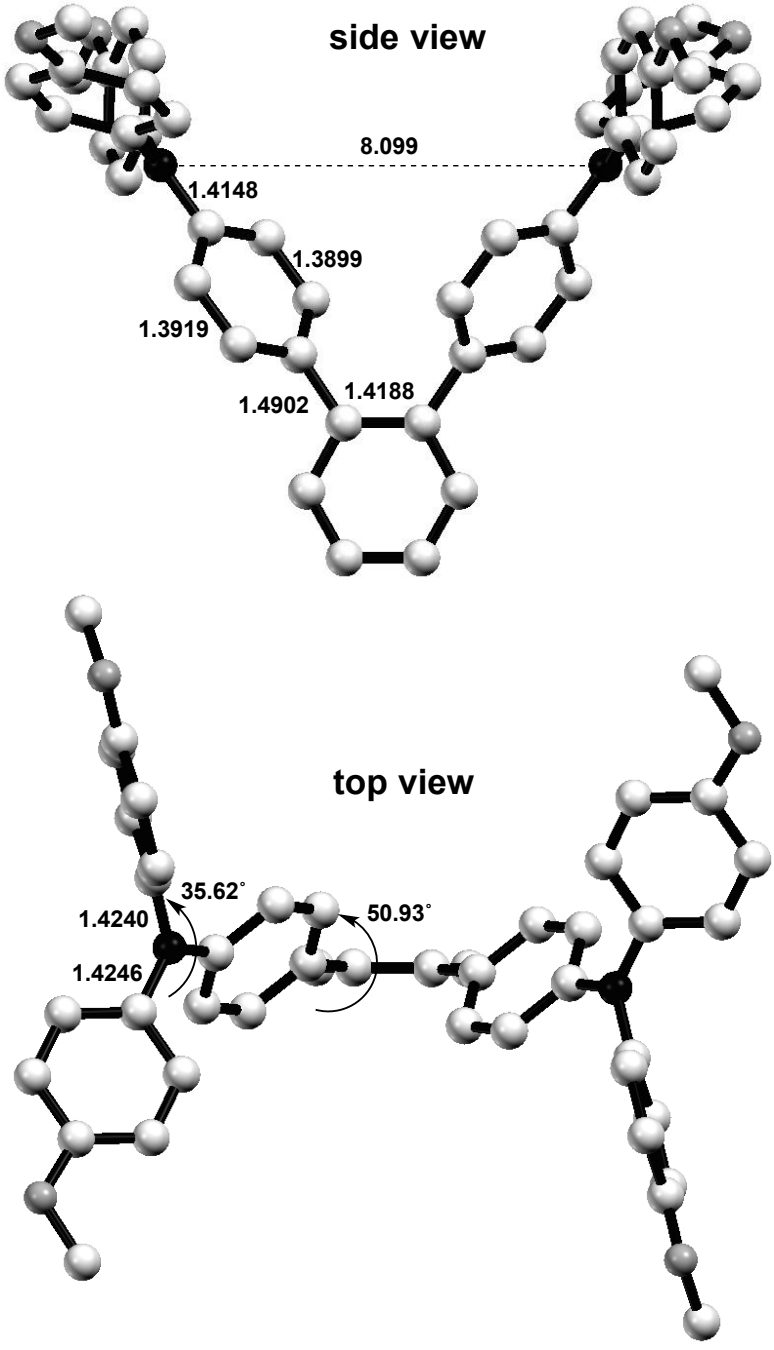

Figure 1.2. DFT-optimized structure (C_2 symmetry) for **3** at B3LYP/6-31G* level of theory. Bond lengths are shown in Å. Total energy is –2187.34090724 hartree.

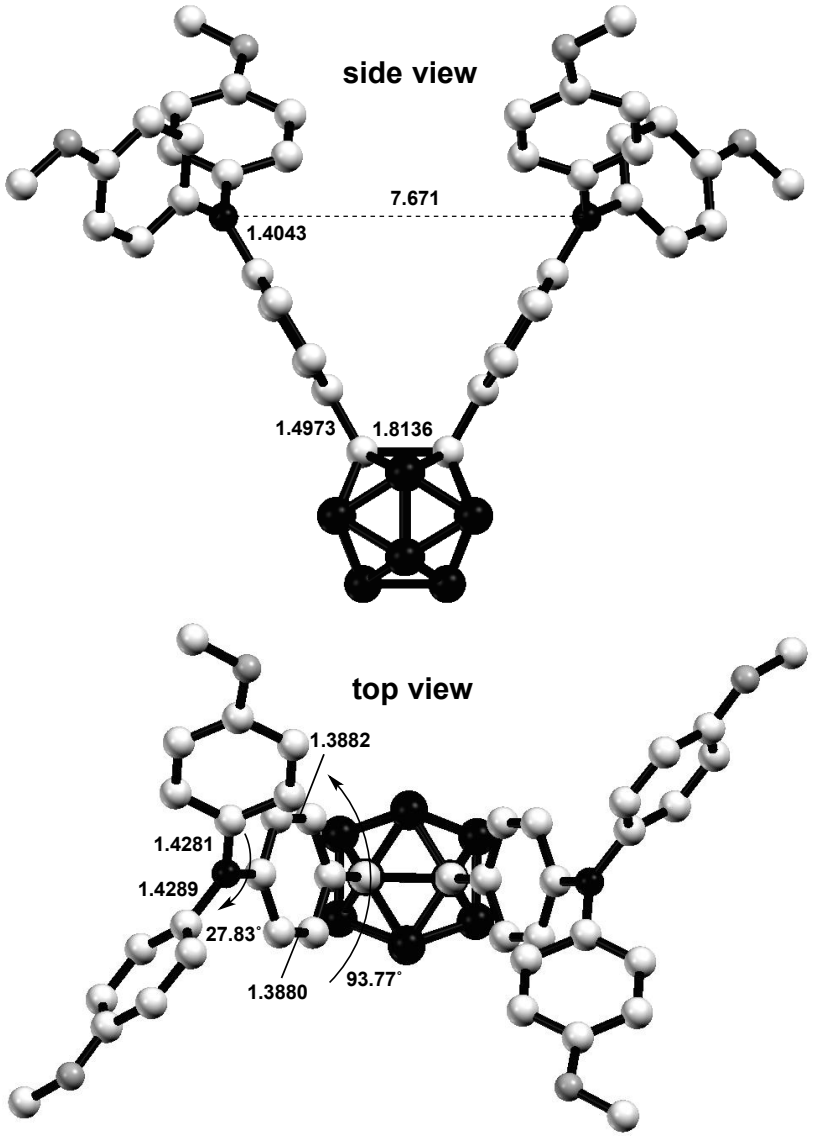

Figure 1.3. DFT-optimized structure (C_2 symmetry) for **4** at B3LYP/6-31G* level of theory. Bond lengths are shown in Å. Total energy is –2287.18837158 hartree.

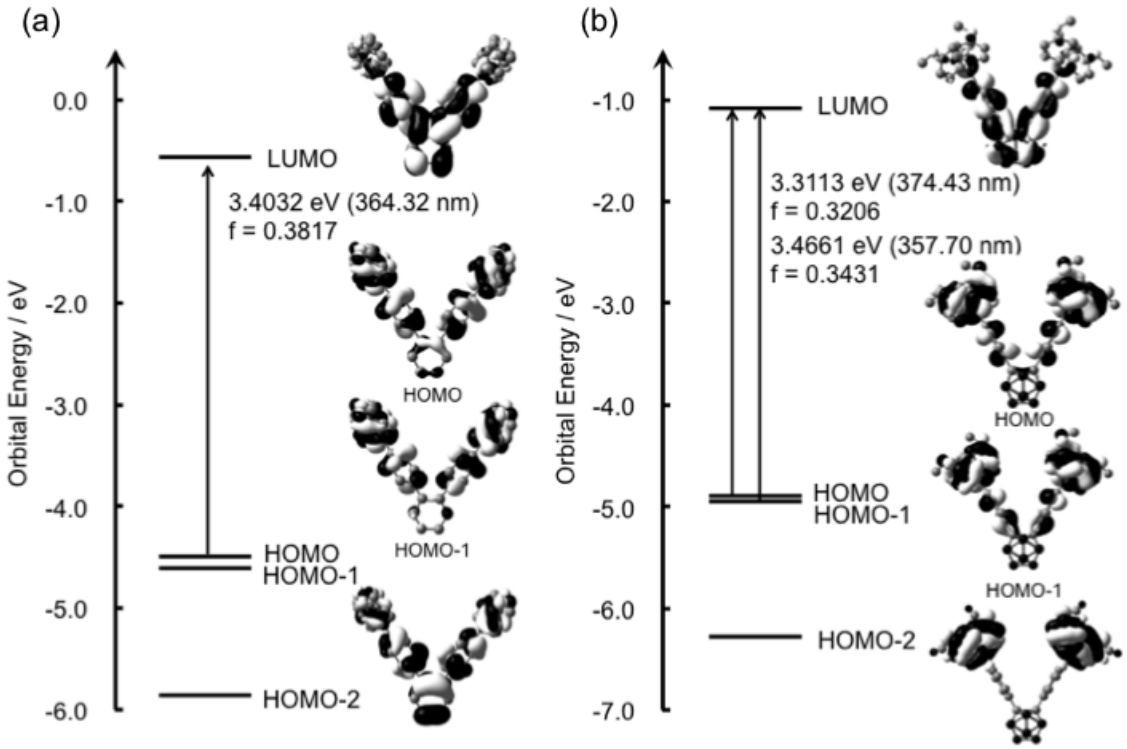

Figure 1.4. Frontier Kohn-Sham orbital energy levels and orbital plots of (a) **3** and (b) **4** at the B3LYP/6-31G* level of theory.

To gain more insight into the strength of the electronic coupling in $\mathbf{3}^{\bullet+}$ and $\mathbf{4}^{\bullet+}$, we examined the redox behaviors of **3** and **4** by cyclic voltammetry in 0.1 M [nBu$_4$N][BF$_4$]/CH$_2$Cl$_2$ at 298 K. A cyclic voltammogram (CV) of **3** showed one quasi-reversible oxidation wave (Figure 1.5a). A closer inspection by the simulation of the observed CV displayed a stepwise oxidation to the dication $\mathbf{3}^{2+}$ via a radical cation $\mathbf{3}^{\bullet+}$, with a small potential splitting [ΔE = 0.09 V] for the first and second oxidation processes [E_1 = +0.20 V (1e) and E_2 = +0.29 V (1e) (vs $Fc^{0/+}$)], thus indicating some degree of charge/spin transfer between the two triarylamine redox centers in $\mathbf{3}^{\bullet+}$ (Figure 1.5a). Similarly, the CV of **4** exhibited one reversible oxidation wave (Figure 1.5b). However, the simulation of the observed CV evaluated that the observed voltammetric

behavior [E_1 = +0.36 V (1e) and E_2 = +0.40 V (1e) (vs $Fc^{0/+}$)] corresponds to the case with two non-interacting redox centers, where the ΔE value is $(2RT/F)\ln 2$ = 0.036 V (at 298 K),[18] again indicating a negligible through-bond electronic coupling between the two triarylamine redox centers in $\mathbf{4}^{\bullet+}$ (Figure 1.5b). The differential pulse voltammetry (DPV) of **3** and **4** was also in line with the above-mentioned CV analysis (Figure 1.6).

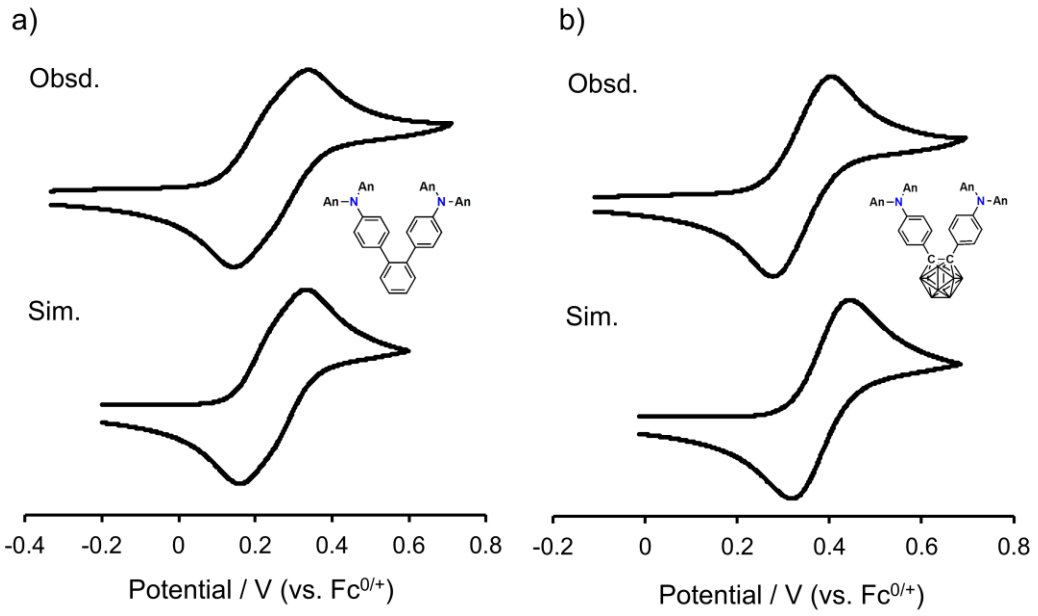

Figure 1.5. Observed and simulated cyclic voltammograms in CH_2Cl_2 (at 1×10^{-3} M) with 0.1 M $[n\mathrm{Bu_4N}]^+[BF_4]^-$ at 298 K (scan rate 0.1 V s^{-1}) for a) **3** and b) **4**; Simulated parameters (standard formal potential, standard rate constant, transfer coefficient): E_1 = +0.20 V, $k_1 = 5.0\times10^{-3}$ cm s^{-1}, α_1 = 0.5, E_2 = +0.29 V, $k_2 = 5.0\times10^{-3}$ cm s^{-1}, α_2 = 0.5 for **3**; E_1 = +0.36 V, $k_1 = 5.0\times10^{-3}$ cm s^{-1}, α_1 = 0.5, E_2 = +0.40 V, $k_2 = 5.0\times10^{-3}$ cm s^{-1}, α_2 = 0.5 for **4**. All diffusion coefficients set equal to 1.0×10^{-5} cm^2 s^{-1}. DigiSim® program[19] was used for digital simulation.

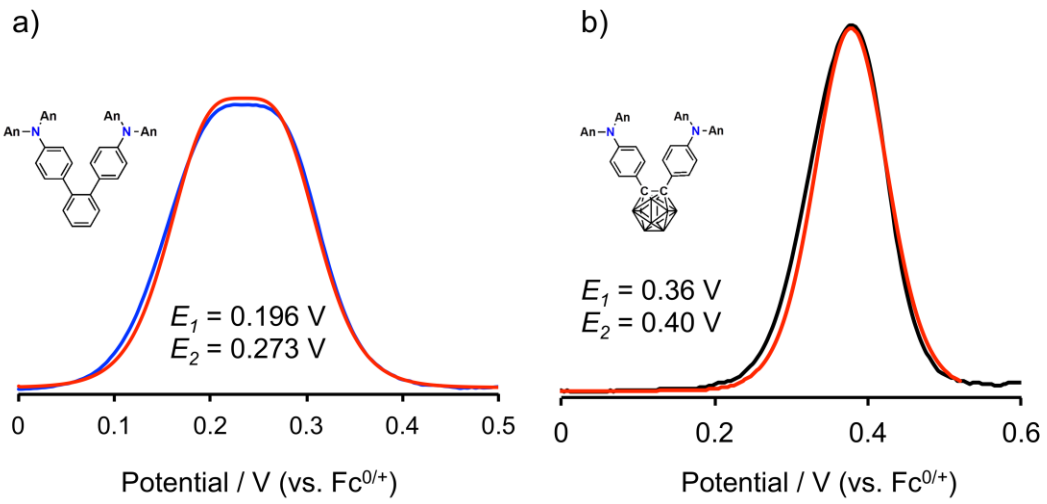

Figure 1.6. Observed and simulated differential pulse voltammograms (DPVs) in CH_2Cl_2 (at 1×10^{-3} M) with 0.1 M $[n\mathrm{Bu_4N}]^+[BF_4]^-$ at 298 K (scan rate 0.1 V s^{-1}) for a) **3** and b) **4**; The simulated DPV is drawn with a red line, and the oxidation potentials were estimated by the DPV simulation.[20]

In general, the lowest-energy absorption band allows us to directly monitor the optically induced intramolecular charge/spin transfer (ICT/IST) in organic MV compounds. Hence, we have recorded the absorption spectral change during stepwise chemical oxidation of **3** and **4** with $AgSbF_6$ in CH_2Cl_2 (Figure 1.7). For **3**, the lowest-energy band at 4.00 eV (310 nm) with shoulder band at 3.56 eV (348 nm) was gradually changed into new bands at 0.76 eV (1630 nm), 1.65 eV (750 nm), and 3.27 eV (379 nm) with an isosbestic point at 3.51 eV (353 nm) during the oxidation process from **3** to $\mathbf{3}^{\bullet+}$ (Figure 1.7a). The weak lowest-energy band is characteristic of the so-called IV-CT band observed for organic MV compounds classified into the Robin and Day's class-II. The lowest-energy transition observed for $\mathbf{3}^{\bullet+}$ was examined by the time-dependent DFT (TD-DFT) calculations. Recently, Kaupp and co-workers pointed

out the fact that the frequently used B3LYP hybrid functional may often lead to erroneous results in organic MV compounds.[14] In fact, the B3LYP/6-31G* geometrical optimization for $\mathbf{3}^{\bullet+}$ gave the symmetrical structure, and the lowest-energy transition energy was computed to be 0.39 eV (3164 nm; f = 0.125). Hence, we have also performed the DFT calculations for $\mathbf{3}^{\bullet+}$ by using the BLYP-based hybrid functional with 35% exact exchange and the SVP basis sets[21] (BLYP35/SVP),[14] including the solvation effect by the CPCM version[15] of polarizable continuum solvent model for CH_2Cl_2 (ε = 8.93). As a result, the asymmetric optimized structure with the spin-density being localized on one of the two triarylamine centers was obtained for $\mathbf{3}^{\bullet+}$, and the lowest-energy transition assignable to the transition from βHOMO to βLUMO was estimated to be 0.69 eV (1804 nm; f = 0.025) in good agreement with the observed IV-CT band. Furthermore, during the oxidation process from $\mathbf{3}^{\bullet+}$ to $\mathbf{3}^{2+}$, the lowest energy IV-CT band disappeared in association with the oxidation of both triarylamine redox centers, and the intensity of the next-lowest-energy band at 1.65 eV (750 nm), which is assignable to π–π* transition within the triarylamine radical cation center,[22] reached up to nearly twice that of $\mathbf{3}^{\bullet+}$ (Figure 1.7b). As shown in Figure 1.7c, turning next to **4**, the lowest-energy band at 3.86 eV (321 nm) was gradually changed into new bands at 1.59 eV (779 nm) and 3.47 eV (357 nm) with an isosbestic point at 3.55 eV (349 nm) during the oxidation process from **4** to $\mathbf{4}^{2+}$. It should be noted that the IV-CT band could not be observed in the NIR region for $\mathbf{4}^{\bullet+}$. The DFT calculations for $\mathbf{4}^{\bullet+}$ at the BLYP35/SVP + CPCM(CH_2Cl_2) level of theory predicted that the lowest-energy transition corresponding to the optically assisted IV-CT event is assignable to a transition from βHOMO to βLUMO (0.93 eV (1334 nm)) with negligibly small oscillator strength (f = 0.0006), thus supporting no observation of the IV-CT band for $\mathbf{4}^{\bullet+}$,

suggesting the very small electronic coupling between the two redox centers in $\mathbf{4}^{\bullet+}$ or the very small transition dipole moment for $\mathbf{4}^{\bullet+}$.[23] Note that the stepwise electrochemical oxidation of **3** and **4** in CH_2Cl_2 reproduced the same spectral changes shown in Figure 1.7.

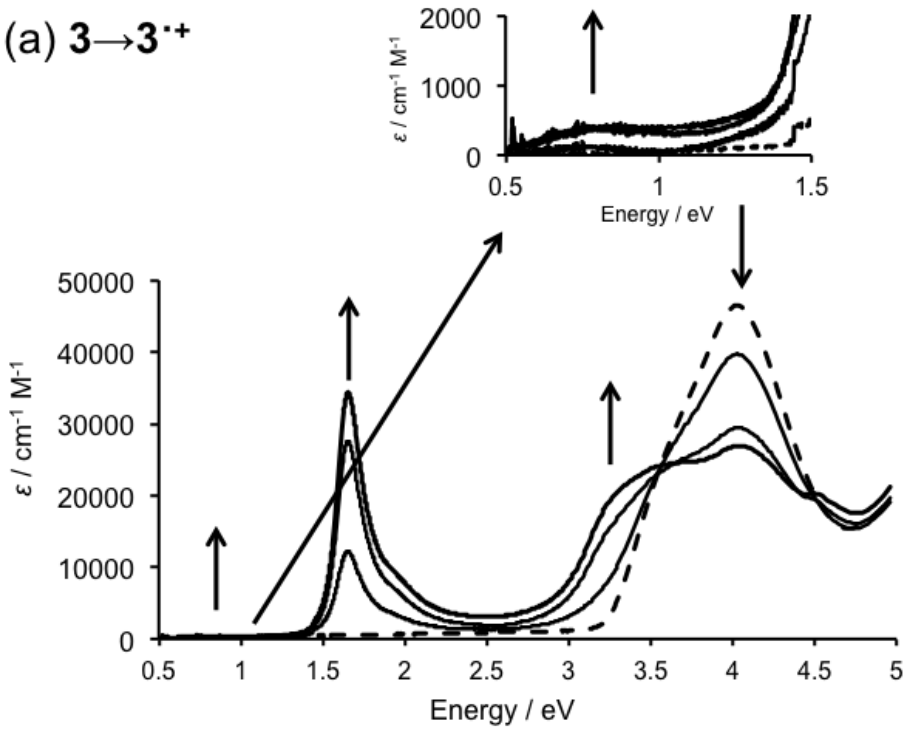

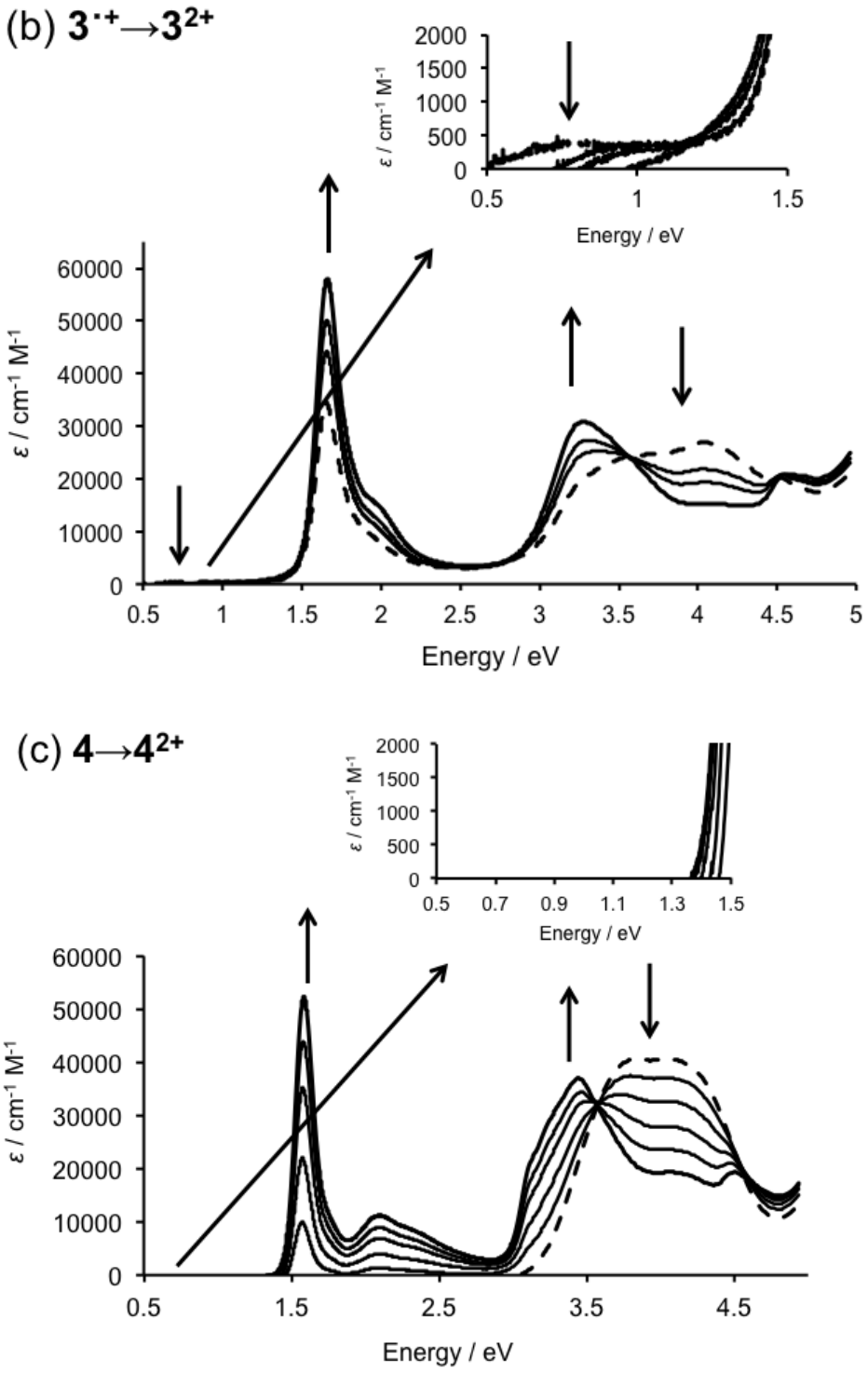

Figure 1.7. UV/Vis-NIR optical absorption spectra of the stepwise chemical oxidation with $AgSbF_6$ (a) from **3** (broken line) to $\mathbf{3}^{\cdot+}$ (solid line), (b) from $\mathbf{3}^{\cdot+}$ (broken line) to $\mathbf{3}^{2+}$ (solid line), (c) from **4** (broken line) to $\mathbf{4}^{2+}$ (solid line), in CH_2Cl_2 (at 1×10^{-4} M) at r.t.

Judging from the fact that the observed IV-CT band is symmetric and the DFT consideration supports the class-II MV character of $\mathbf{3}^{\bullet+}$, the electronic coupling (V) were evaluated by the Mulliken-Hush theory [Eq. (1.1)]:[2b]

$$V = \frac{\mu_{ab}\tilde{\nu}_{\max}}{\Delta\mu_{12}} \qquad (1.1)$$

where μ_{ab} is the transition moment, which is determined by integration of the IV-CT band, $\tilde{\nu}_{\max}$ the energy of the IV-CT band maximum, $\Delta\mu_{12}$ the difference in the diabatic dipole moments between the ground and excited states, which is calculated by Eq. (1.2),

$$\Delta\mu_{12} = \sqrt{(\Delta\mu_{ab})^2 + 4(\mu_{ab})^2} \qquad (1.2)$$

from the difference in the adiabatic dipole moments between the ground and excited states $\Delta\mu_{ab}$. The $\Delta\mu_{ab}$ value is not accessible from the observed IV-CT band analysis, and thus, was estimated to be 37 D by the DFT calculations (BLYP35/SVP + CPCM(CH_2Cl_2)). As a consequence, the electronic coupling for $\mathbf{3}^{\bullet+}$ in CH_2Cl_2 was evaluated to be 794 cm^{-1}. It should be noted here that the optical excitation energy of the IV-CT band for class II MV compounds approximately corresponds to the (total) reorganization energy λ, which is partitioned into solvent-independent inner-sphere (λ_{in}) and solvent-dependent outer-sphere (λ_{out}) contributions, and hence, the IV-CT band should exhibit a blue-shift with an increase of solvent polarity.[2b] In fact, the $\tilde{\nu}_{\max}$ value increased in an increasing solvent polarity order; CH_2Cl_2, PhCN, *n*BuCN, and MeCN.[24] Unfortunately, we could not confirm the existence of the IV-CT band for $\mathbf{4}^{\bullet+}$

in a highly polar solvent such as PhCN, *n*BuCN, and MeCN, simply because of an unexpected chemical instability of $\mathbf{4}^{\bullet+}$ in those polar solvents.

Besides the above-mentioned optical ICT/IST, thermally activated ICT/IST event can be observable by the variable-temperature electron spin resonance (VT-ESR) spectroscopy. The ESR spectra of $\mathbf{3}^{\bullet+}$ and $\mathbf{4}^{\bullet+}$ generated by the chemical oxidation of the neutral species with 0.5 equiv of $AgSbF_6$ in CH_2Cl_2 were successfully detected in the temperature range 193–293 K (Figure 1.8).[25] The signal intensities of the central three lines decreased gradually with the decreasing temperature. Such a temperature dependency clearly indicates that the five-line pattern at room temperature is induced by thermally activated ICT/IST between the two triarylamine redox centers, indicating that both $\mathbf{3}^{\bullet+}$ and $\mathbf{4}^{\bullet+}$ are class II MV systems.[26] The VT-ESR spectra of $\mathbf{4}^{\bullet+}$ show that the spin is fully localized on one triarylamine redox center on the ESR time scale below 233 K. The observed VT-ESR spectra of $\mathbf{3}^{\bullet+}$ and $\mathbf{4}^{\bullet+}$ in CH_2Cl_2 at various temperatures were successfully simulated using the ESR-EXN program, which simulates the ESR line shape when there exists the intramolecular dynamic spin exchange among the multi-redox-active centers.[27] From the simulation, we obtained the first-order rate constants (k_{th}) for the thermally activated ICT/IST process between the two triarylamine redox centers [Eq. (1.3)]:

$$k_{th} = A \exp\left(-\frac{\Delta G^*}{k_B T}\right) \qquad (1.3)$$

The Arrhenius plot gave a clear linear relationship between $\ln(k_{th})$ and $1/T$ for both $\mathbf{3}^{\bullet+}$ and $\mathbf{4}^{\bullet+}$ (Figure 1.9). From this relationship, the activation barrier (ΔG^*) for the

thermally activated ICT/IST was estimated 3.09 kcal mol^{-1} for **3**$^{\bullet+}$ and 5.82 kcal mol^{-1} for **4**$^{\bullet+}$. In the case of degenerate MV states, the ΔG^* value can be related to the electronic coupling (V) and the reorganization energy (λ) by Eq. (1.4).[28]

$$\Delta G^* = \frac{(\lambda - 2V)^2}{4\lambda} \qquad (1.4)$$

Hence, the electronic couplings for **3**$^{\bullet+}$ and **4**$^{\bullet+}$ can be deduced from Eq. (1.4) by using the VT-ESR barrier, ΔG^*, and the optically determined λ, which corresponds to the energy of the IV-CT band maximum; in this way, the electronic coupling for **3**$^{\bullet+}$ was evaluated to be 492 cm^{-1} between the values for **1**$^{\bullet+}$ and **2**$^{\bullet+}$. Judging from the DFT-computed transition energy, even though the IV-CT band was not observed for **4**$^{\bullet+}$, the electronic coupling can be estimated to be a negligibly small value around several tens of cm^{-1}, virtually indicating a class-I MV character of **4**$^{\bullet+}$. The present VT-ESR results are also confirmed by DFT calculations (BLYP35/SVP + CPCM(CH_2Cl_2)), which predict the activation barrier (ΔG^*) in the double well potential is 2.58 kcal mol^{-1} for **3**$^{\bullet+}$ and 4.54 kcal mol^{-1} for **4**$^{\bullet+}$. The author summarized the experimentally determined energy diagram for the self-exchange ICT/IST of **3**$^{\bullet+}$ and **4**$^{\bullet+}$ in Figure 1.10. The present dynamic ESR studies indicate that the through-space pathway dominates the ICT/IST behavior in **4**$^{\bullet+}$, whereas the through-bond pathway prevails over the through-space one in the ICT/IST behavior in **3**$^{\bullet+}$. It may be worth mentioning, in passing, the pre-exponential factor A in Eq. (1.3) in connection with the observed ICT/IST rates for **3**$^{\bullet+}$ and **4**$^{\bullet+}$; the values are estimated to be 8×10^{11} s^{-1} for **3**$^{\bullet+}$ and 1×10^{13} s^{-1} for **4**$^{\bullet+}$, from the Arrhenius fits (Figure 1.9). As has been often discussed in

intramolecular electron transfer reactions in solution,[26b,28,29] the electron transfer processes range from the nonadiabatic ($V \lesssim 50$ cm^{-1}) to adiabatic ($V \gtrsim 200$ cm^{-1}) regimes. In class-II MV systems like $\mathbf{3}^{\bullet+}$, the vibrational motion is slower than the electronic motion, and thus, the prefactor A is comparable to the solvent reorientation frequencies ($10^{11} - 10^{12}$ s^{-1}) to ensure adiabatic electron transfer. Conversely, in class-I MV systems like $\mathbf{4}^{\bullet+}$, the electronic motion is slower than the vibrational motion, thereby leading to the prefactor A as a function of the electronic coupling (Eq. (1.5)):

$$A_{\text{nonadiabatic}} = \frac{V^2}{h}\sqrt{\frac{4\pi^3}{\lambda RT}} \qquad (1.5)$$

where h and R are Planck's and gas constants, respectively. Hence, the prefactor A falls within the range of $10^{12} - 10^{13}$ s^{-1} based on Eq. (1.5). Such a difference in nature of the thermal intramolecular ICT/IST processes in $\mathbf{3}^{\bullet+}$ and $\mathbf{4}^{\bullet+}$ seemingly lead to less than one order of magnitude difference in the k_{th} values determined for both MV compounds, e.g., at 293 K (Figure 1.8).

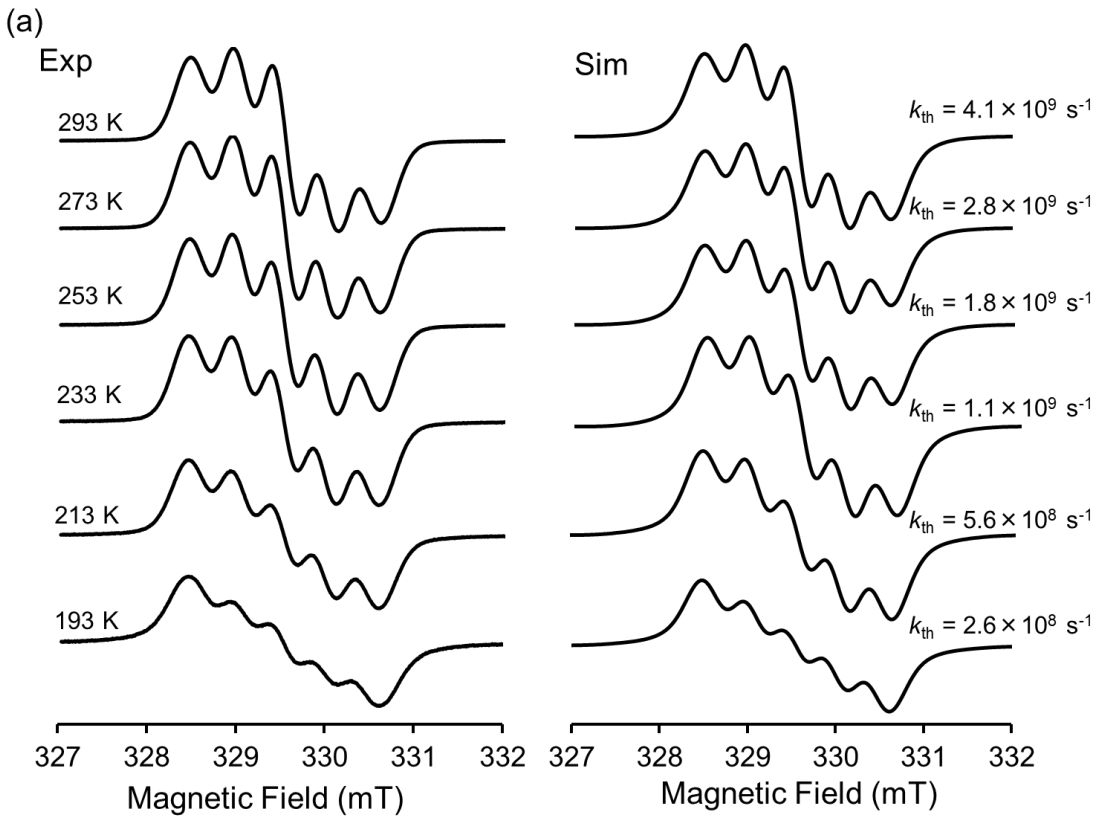
(a)
Exp
293 K
273 K
253 K
233 K
213 K
193 K
327
328
329
330
331
332
Magnetic Field (mT)
Sim
k_{th} = 4.1 × 10^{9} s^{-1}
k_{th} = 2.8 × 10^{9} s^{-1}
k_{th} = 1.8 × 10^{9} s^{-1}
k_{th} = 1.1 × 10^{9} s^{-1}
k_{th} = 5.6 × 10^{8} s^{-1}
k_{th} = 2.6 × 10^{8} s^{-1}
327
328
329
330
331
332
Magnetic Field (mT)

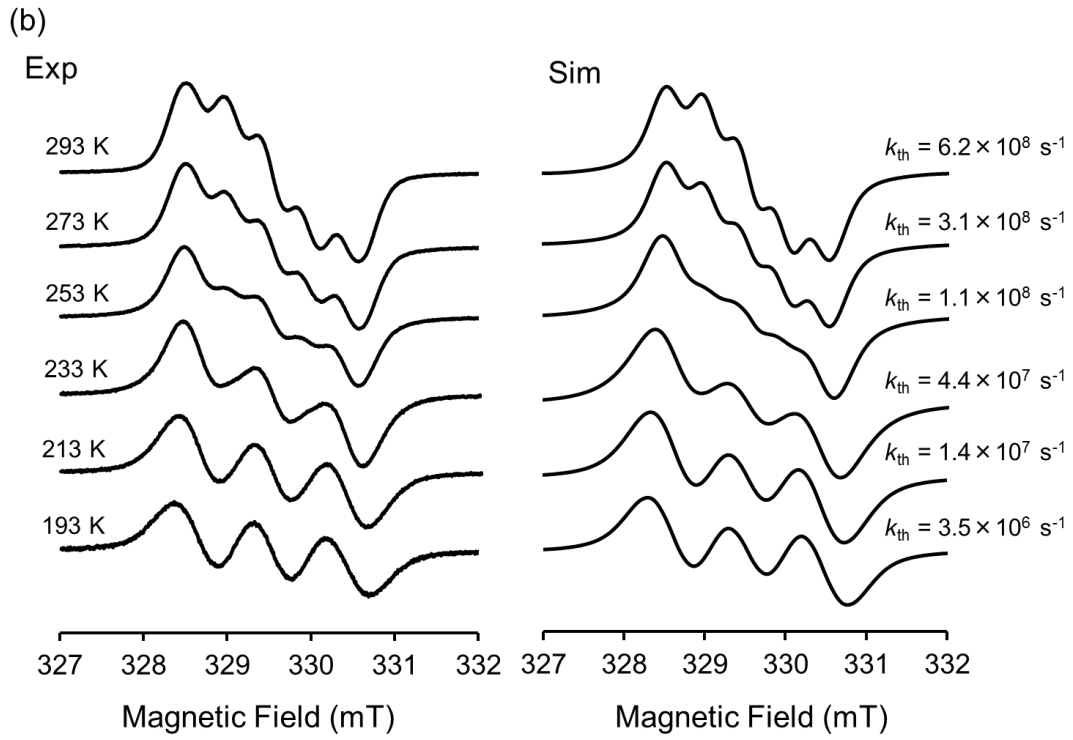

Figure 1.8. Observed X-band VT-ESR spectra (left) and simulated spectra with determined intramolecular ICT/IST rates (k_{th}) (right) of (a) $\mathbf{3}^{\bullet+}$ and (b) $\mathbf{4}^{\bullet+}$ in CH_2Cl_2 (at 1×10^{-4} M).

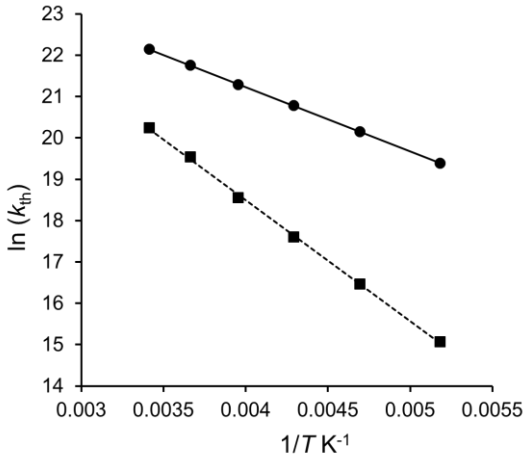

Figure 1.9. Arrehenius plots of the intramolecular ICT/IST rates (k_{th}) for $\mathbf{3}^{\bullet+}$ (●) and $\mathbf{4}^{\bullet+}$ (■) obtained from the simulation of the observed VT-ESR spectrum.

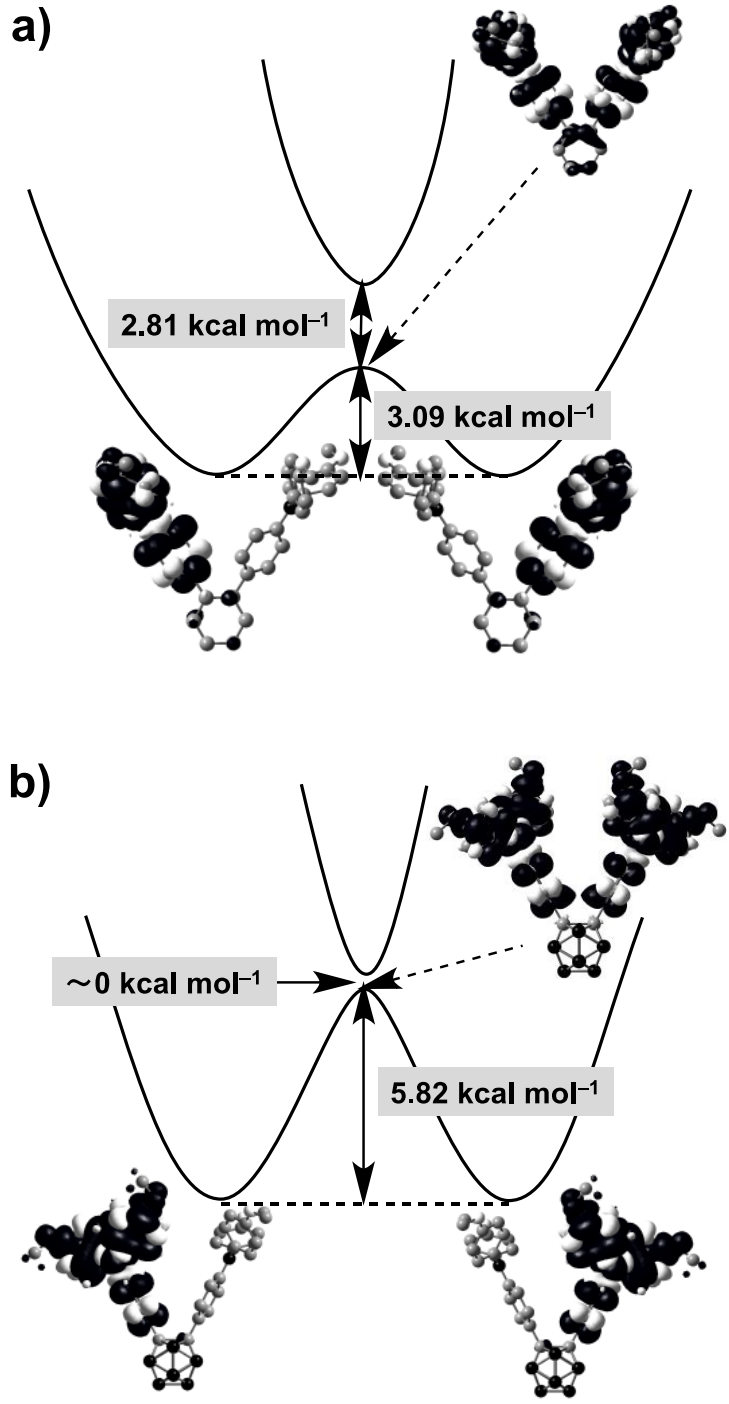

Figure 1.10 Schematic energy diagrams, determined experimentally for the self-exchange ICT/IST of a) $\mathbf{3}^{\bullet+}$ and b) $\mathbf{4}^{\bullet+}$ in CH_2Cl_2. The depicted molecular structures with spin density distribution are the optimized structures at the local minima and the saddle point in double-well potential [BLYP35/SVP + CPCM(CH_2Cl_2) level of theory].

The Heisenberg spin-exchange phenomenon is closely related to the present charge/spin self-exchange phenomenon. The author succeeded in the isolation of analytically pure salts of dications $\mathbf{3}^{2+}$ and $\mathbf{4}^{2+}$, i.e., $\mathbf{3}^{2+}\bullet\mathbf{2[SbF_6]}^{-}$ and $\mathbf{4}^{2+}\bullet\mathbf{2[SbF_6]}^{-}\bullet\mathbf{2[CH_2Cl_2]}$ as powder and crystalline samples, respectively. The molecular structure of $\mathbf{4}^{2+}$ determined by X-ray analysis reveals a shortening of the distance between the two nitrogen atoms and an insertion of one $[SbF_6]^-$ anion between the two triarylaminium radical centers (Figure 1.11).[30] The magnetic susceptibility of these diradical dication salts was measured on a SQUID magnetometer in the temperature range 2–300 K at a constant magnetic field of 1000 G (Figure 1.12a). From the best fitting with the Bleaney-Bowers equation,[21] the singlet–triplet energy gaps (ΔE_{S-T}) were determined to be –0.20 kcal mol^{-1} for $\mathbf{3}^{2+}$ and –0.01 kcal mol^{-1} for $\mathbf{4}^{2+}$.[31] According to the DFT-based broken-symmetry approach,[32] ΔE_{S-T} was estimated to be –0.14 kcal mol^{-1} for $\mathbf{3}^{2+}$ and –0.01 kcal mol^{-1} for $\mathbf{4}^{2+}$. The difference in the ΔE_{S-T} value can be deduced from the conjugation through the bridging units between the two triarylaminium radical centers: in $\mathbf{3}^{2+}$, the antiferromagnetic quinoid form can contribute in addition to the paramagnetic benzenoid form through the *ortho*-phenylene bridge, leading to an intramolecular antiferromagnetic interaction; in $\mathbf{4}^{2+}$, there exists no quinoid contribution like $\mathbf{3}^{2+}$, resulting in virtually no intramolecular magnetic interaction (Figure 1.12b).

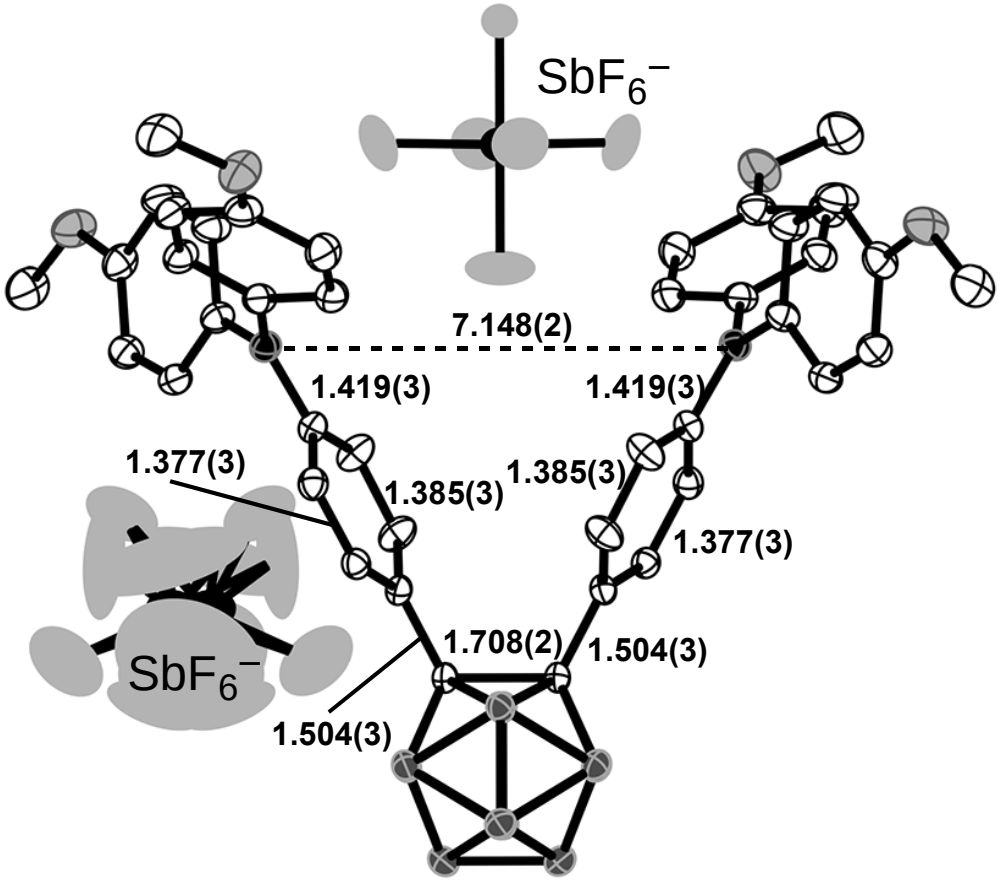

Figure 1.11 Molecular structures and selected bond lengths of $\mathbf{4^{2+}\bullet 2[SbF_6]^-}$ in the solid state at 144(1) K. Ellipsoids are set at 50% probability; hydrogen atoms and CH_2Cl_2 molecules are omitted for clarity; nitrogen atoms are colored in black.

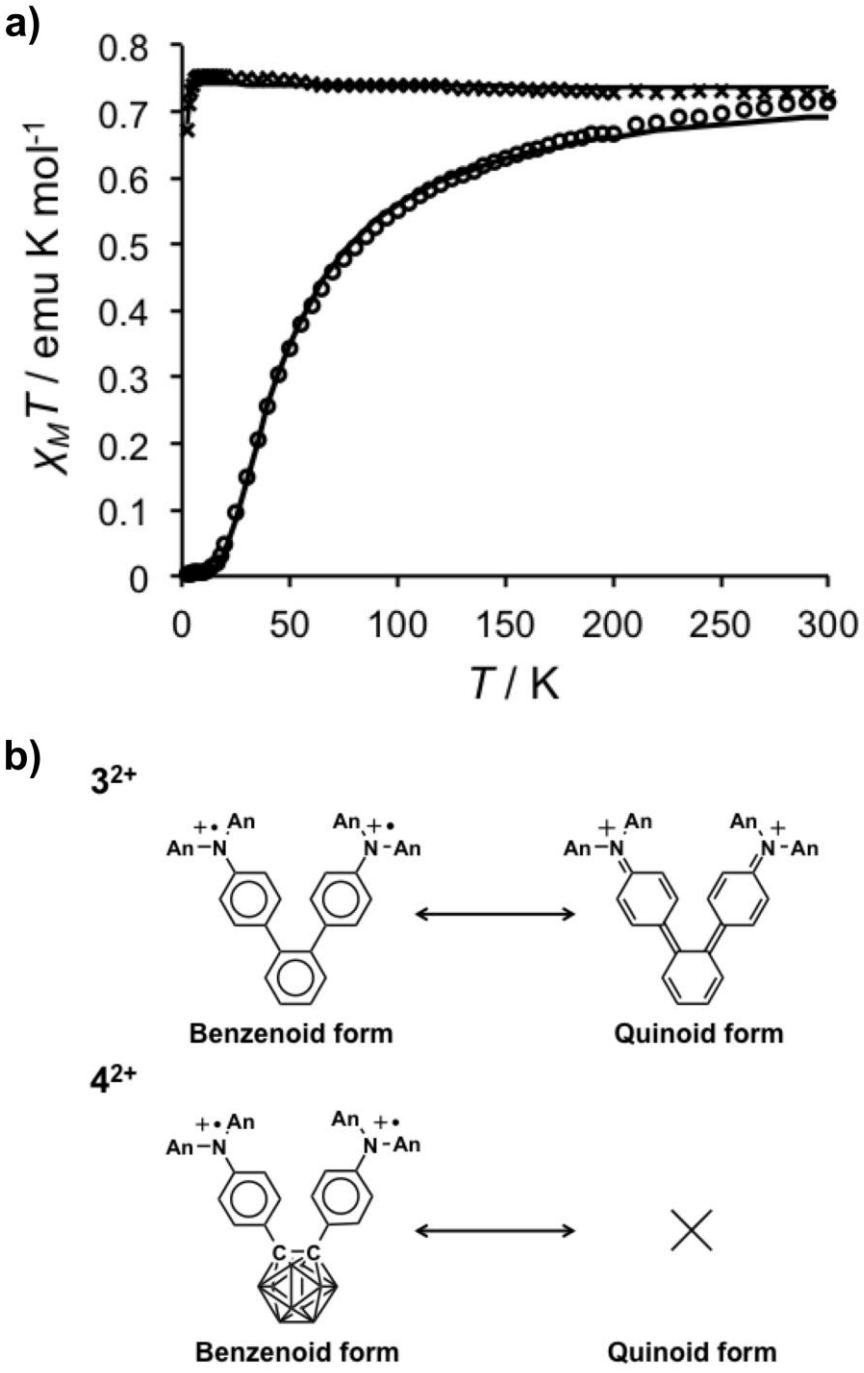

Figure 1.12. a) Plots of $\chi_M T$ versus T for $\mathbf{3^{2+}\bullet 2[SbF_6]^-}$ (◯) and $\mathbf{4^{2+}\bullet 2[SbF_6]^-\bullet 2[CH_2Cl_2]}$ (×) at 0.1 T. The solid lines represent the best theoretical fits, and b) the resonance structures of $\mathbf{3^{2+}}$ and $\mathbf{4^{2+}}$.

1.4 Conclusion

In this work, the comparison between two BTA radical cations, $\mathbf{3}^{\cdot+}$ and $\mathbf{4}^{\cdot+}$, where the triarylamine redox centers have similar geometrical arrangements but they are linked by bridging units (*ortho*-phenylene and *ortho*-carborane) with different conjugation systems, demonstrated that the through-space pathway dominates the intramolecular charge/spin transfer (ICT/IST) in *ortho*-carborane-bridged $\mathbf{4}^{\cdot+}$, whereas the through-bond pathway prevails for *ortho*-phenylene-bridged $\mathbf{3}^{\cdot+}$, and thus, $\mathbf{3}^{\cdot+}$ is a class-II MV compound, whereas $\mathbf{4}^{\cdot+}$ is considered to be a class-I MV compound with negligible electronic coupling. Accordingly, while there can be no doubt about considerably low activation barrier for the toroidal delocalization in the hexaarylbenzene radical cation, $\mathbf{5b}^{\bullet+}$, there must be considerable doubt about the origin of strong electronic coupling by the through-space pathway through the six phenyl rings attached to the central benzene ring.

1.5 References

[1] J. Bonvoisin, J.-P. Launay, W. Verbouwe, M. Van der Auweraer, F. C. De Schryver, *J. Phys. Chem*. **1996**, *100*, 17079-17082.

[2] a) J. Hankache, O. S. Wenger, *Chem. Rev*. **2011**, *111*, 5138-5178; b) A. Heckmann, C. Lambert, *Angew. Chem. Int. Ed.* **2012**, *51*, 326-392.

[3] a) C. Lambert, G. Nöll, J. Schelter, *Nat. Mater*. **2002**, *1*, 69-73; b) C. Lambert, S. Amthor, J. Schelter, *J. Phys. Chem. A* **2004**, *108*, 6474-6486.

[4] a) G. Nöll, M. Avola, *J. Phys. Org. Chem.* **2006**, *19*, 238-241; b) D. Sakamaki, A. Ito, T. Matsumoto, K. Tanaka, *RSC Adv*. **2014**, *4*, 39476-39483.

[5] a) C. Lambert, G. Nöll, *Angew. Chem. Int. Ed.* **1998**, *37*, 2107-2110; b) C. Lambert, G. Nöll, *Chem. Eur. J*. **2002**, *8*, 3467-3477; c) S. V. Rosokha, I. S. Neretin, D. Sun, J. K. Kochi, *J. Am. Chem. Soc*. **2006**, *128*, 9394-9407.

[6] R. N. Grimes, *Carboranes*, 2nd ed., Academic Press, New York, **2011**.

[7] CCDC 1554271 (3), 1554272 (4), and 1554289 (**4^{2+}•2[SbF_6]$^-$•2[CH_2Cl_2]**) contain the supplementary crystalic data for this paper. These data can be obtained free of charge from The Cambridge Crystallographic Data Centre via www.ccdc.cam.ac.uk/data_request/cif.

[8] It should be noted that the favorable geometrical arrangements between the two triarylamine redox centers of **3** are not the same in solution and crystalline states, probably due to the packing effects in the crystal environment (Figure 1.1a); the geometrical arrangement between the two redox centers in the DFT-optimized

[9] Compound **3** has been mentioned previously in a patent paper: Y. Mizuta, A. Kawahara, Jpn. Kokai Tokkyo Koho JPH05117213A, **1993**.

[10] K. Kokado, A. Nagai, Y. Chujo, *Macromolecules* **2010**, *43*, 6463-6468.

[11] K. Ragavachari, *Theor. Chim. Acc*. **2000**, *103*, 361-363 and references cited therein.

[12] A. Dreuw, M. Head-Gordon, Chem. Rev. **2005**, *105*, 4009-4037.

[13] W. J. Hehre, L. Radom, P.v. R. Schleyer, J. A. Pople, *Ab Initio Molecular Orbital Theory*, Wiley, New York, **1986**.

[14] a) M. Renz, K. Theilacker, C. Lambert, M. Kaupp, *J. Am. Chem. Soc*. **2009**, *131*, 16292-16302; b) M. Renz, M. Kess, M. Diedenhofen, A. Klamt, M. Kaupp, *J. Chem. Theory Comput*. **2012**, *8*, 4189-4203; c) M. Parthey, M. Kaupp, *Chem. Soc. Rev*. **2014**, *43*, 5067-5088.

[15] M. Cossi, N. Rega, G. Scalmani, V. Barone, *J. Comput. Chem*. **2003**, *24*, 669-681.

[16] M. J. Frisch, *et al*., Gaussian 09 (Revision D.01), Gaussian, Inc., Wallingford CT, **2013**.

[17] R. R. Gupta, *Landolt-Börnstein, New Series II*; K.-H. Hellwege, A. M. Hellwege, Eds. ; Springer Verlag: Berlin, 1986; Vol. *16* (Diamagnetic Susceptibility).

[18] a) J. B. Flanagan, S. Margel, A. J. Bard, F. C. Anson, *J. Am. Chem. Soc*. **1978**, *100*, 4248-4253; b) K. Hinkelmann, J. Heinze, *Ber. Bunsenges. Phys. Chem*. **1987**, *91*, 243-249: c) R. F. Winter, *Organometallics* **2014**, *33*, 4517-4536.

[19] E. -G. Jäger, M. Rudolph, *J. Electroanal. Chem*. **1997**, *434*, 1-18.

[20] W. Huang, T. L. E. Henderson, A. M. Bond, K. B. Oldham, *Anal. Chim. Acta*, **1995**, *304*. 1-15.

[21] A. Schöfer, H. Horn, R. Ahlrichs, *J. Chem. Phys*. **1992**, *97*, 2571-2577.

[22] C. Lambert, G. Nöll, *J. Am. Chem. Soc*. **1999**, *121*, 8434-8442.

[23] K. Y. Wong, P. N. Schatz, *Prog. Inorg. Chem*. **1981**, *28*, 369-449.

[24] The extrapolation of a linear regression of the data points to gas phase gave the upper limit of inner reorganization energy (λ_{in}) of $\mathbf{3}^{\cdot+}$ as 1980 cm^{-1}. In addition, the

electronic coupling (V) of $\mathbf{3}^{\cdot+}$ in CH_2Cl_2, PhCN, *n*BuCN, and MeCN was roughly estimated to be 790, 460, 206, and 255 cm^{-1}, respectively, on the basis of Hush analysis; N. S. Hush, *Coord. Chem. Rev*. **1985**, *64*, 135-157.

[25] To check the influence of intermolecular CT pathway, we measured the VT-EPR spectra of $\mathbf{3}^{\cdot+}$ and $\mathbf{4}^{\cdot+}$ at lower concentration (5×10^{-5} M). Neither discernible line-narrowing nor change in spectral shape was observed for both $\mathbf{3}^{\cdot+}$ and $\mathbf{4}^{\cdot+}$.

[26] a) Y. Hirao, M. Urabe, A. Ito, K. Tanaka, *Angew. Chem. Int. Ed.* **2007**, *46*, 3300-3303; b) K. Lancaster, S. A. Odom, S. C. Jones, S. Thayumanavan, S. R. Marder, J.-L. Brédas, V. Coropceanu, S. Barlow, *J. Am. Chem. Soc*. **2009**, *131*, 1717-1723; c) D. R. Kattnig, B. Mladenova, G. Grampp, C. Kaiser, A. Heckmann, C. Lambert, *J. Phys. Chem. C* **2009**, *113*, 2983-2995.

[27] J. Heinzer, *Mol. Phys.* **1971**, *22*, 167-177.

[28] B. S. Brunschwig, C. Creutz, N. Sutin, *Chem. Soc. Rev*. **2002**, *31*, 168-184.

[29] K. D. Demadis, C. M. Hartshorn, T. J. Meyer, *Chem. Rev*. **2001**, *101*, 2655-2685.

[30] B. Bleaney, K. D. Bowers, *Proc. R. Soc. London, Ser. A*, **1952**, *214*, 451-465.

[31] Although the ESR analysis of $\mathbf{3}^{2+}$ and $\mathbf{4}^{2+}$ are useful to investigate the singlet/triplet nature of the present dicationic species in solution, we could observe neither definite fine-structure nor forbidden transition for the ESR spectra of a frozen CH_2Cl_2 solution of $\mathbf{3}^{2+}$ and $\mathbf{4}^{2+}$ at 123 K.

[32] V. H. Smith, *Applied Quantum Chemistry*, D. Reidel Publisher, Dordrecht, **1986**.

Chapter 2

Mixed-Valene States of *meta*- or *para*-Phenylene Bridged Bis(triphenylamine) Radical Cation

2.1 Introduction

The understanding of organic mixed-valence (MV) compounds has been at the forefront of research in fundamental intramolecular electron transfer phenomena.[1] In Chapter 1, the comparison between two bis(triarylamine) (BTA) radical cations, where the triarylamine redox centers have similar geometrical arrangements but they are linked by bridging units (*ortho*-phenylene and *ortho*-carborane) with different conjugation systems, demonstrated that the through-space pathway dominates the intramolecular charge/spin transfer (ICT/IST) in *ortho*-carborane-bridged, whereas the through-bond pathway prevails for *ortho*-phenylene-bridged, and thus, *ortho*-phenylene-bridged BTA is a class-II MV compound, whereas *ortho*-carborane-bridged BTA is considered to be a class-I MV compound with negligible electronic coupling. Moreover, *meta*- and *para*-phenylene-bridged BTA $\mathbf{1}^{\cdot+}$ and $\mathbf{2}^{\cdot+}$ and *meta*- and *para*-phenylenediamine $\mathbf{3}^{\cdot+}$ and $\mathbf{4}^{\cdot+}$ are very interesting in MV

state (Scheme 2.1). Actually, It reported that the radical cation of **4** belongs to the class-II just at the border to class-III.[2] Furthermore, it reported that phenyl-substituted-*meta*-phenylene-bridged BTA $\mathbf{5}^{\cdot+}$ are class-II mixed-valence compound.[3] The author revisited non-substituted-meta-phenylene-bridged BTA $\mathbf{1}^{\cdot+}$.

In this work, three radical cations, $\mathbf{1}^{\cdot+}$ and $\mathbf{2}^{\cdot+}$, where the triarylamine redox centers have different bridging units (*meta*- and *para*-phenylene), and $\mathbf{3}^{\cdot+}$, *meta*-phenylenediamine, were investigated by cyclic voltammetry, UV-vis-NIR and ESR spectroscopy, and DFT calculations. $\mathbf{1}^{\cdot+}$ and $\mathbf{2}^{\cdot+}$ are classified into class-II mixed-valence compounds by the observed IV-CT band, TD-DFT calculations and VT-ESR spectra.

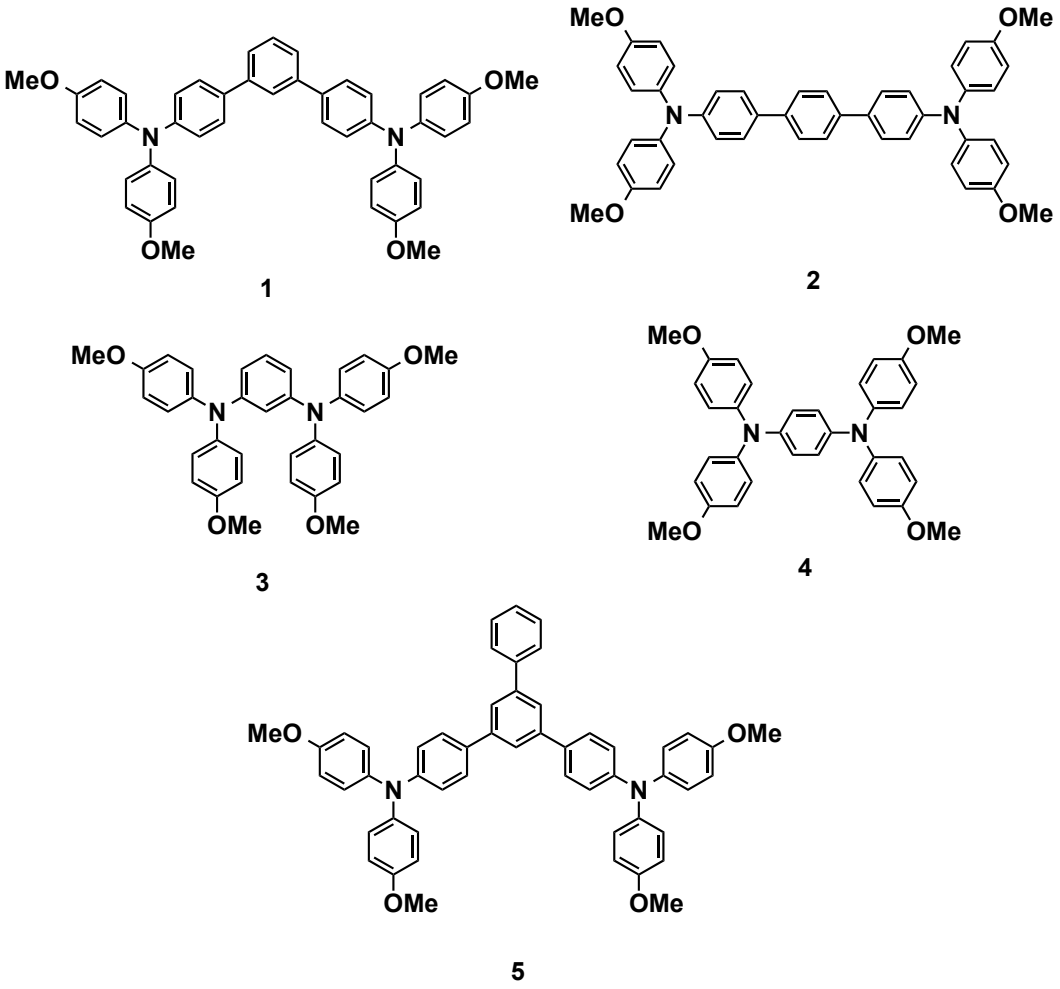

Scheme 2.1. Molecular Structures of **1**-**5**.

2.2 Experimental Section

2.2.1 Synthesis

All the purchased reagents were of standard quality, and used without further purification. All the purchased solvents were purified, dried, and degassed by standard procedures. Column chromatography was performed with silica gel (Kanto Chemical Co., Inc., silica gel 60N, spherical neutral). Elemental analyses were performed by Center for Organic Elemental Microanalysis, Kyoto University. ^{1}H and ^{13}C NMR spectra were measured by a JEOL JNM-AL400 FT-NMR spectrometer. Chemical shifts

of NMR spectra are determined relative to internal tetramethylsilane (TMS) standard (δ), and are given in parts per million (ppm).

Synthesis of 1: A mixture of 4,4'-Dibromo-*p*-terphenyl (194 mg, 0.50 mmol), 4,4'-Dimethoxydiphenylamine (286 mg, 1.25 mmol), $Pd(dba)_2$ (17.3 mg, 0.03 mmol), $P(t\text{-Bu})_3HBF_4$ (14.5 mg, 0.05 mmol), and NaO*t*-Bu (144 mg, 1.50 mmol) in toluene (5 mL) was refluxed under argon atmosphere for 20 h. The reaction mixture was washed with brine and the organic layer was dried over Na_2SO_4. After evaporation of the solvent, the crude product was chromatographed on silica gel with dichloromethane:*n*-hexane = 1:1 to afford **1** (140 mg, 0.20 mmol, 40%) as a yellow solid: mp 97.2-99.8°C; ^{1}H NMR (400 MHz, $CDCl_3$) δ = 3.80 (s, 12H), 6.83 (d, J = 9.0 Hz, 8H), 6.98 (d, J = 8.6 Hz, 4H), 7.08 (d, J = 9.0 Hz, 8H), 7.44 (d, J = 8.8 Hz, 4H), 7.56 (s, 4H); ^{13}C NMR (100 MHz, $CDCl_3$) δ = 55.5, 114.7, 120.7, 126.5, 126.6, 127.3, 132.6, 140.8, 148.0, 155.8; APCI HRMS: *m/z* calcd for $C_{46}H_{40}N_2O_4$: 685.3061 $[M+H]^+$; found 685.3038; Elemental analysis (%) calcd for $C_{46}H_{40}N_2O_4$: C, 80.68; H, 5.89; N, 4.09. Found: C, 80.58; H, 5.97; N, 4.00.

Synthesis of 2: A mixture of 4,4'-Dibromo-*m*-terphenyl (388 mg, 1.0 mmol), 4,4'-Dimethoxydiphenylamine (573 mg, 2.5 mmol), $Pd(dba)_2$ (50 mg, 0.05 mmol), $P(t\text{-Bu})_3HBF_4$ (50 mg, 0.10 mmol), and NaO*t*-Bu (384 mg, 4.0 mmol) in toluene (20 mL) was refluxed under argon atmosphere for 21 h. The reaction mixture was washed with brine and the organic layer was dried over Na_2SO_4. After evaporation of the solvent, the crude product was chromatographed on silica gel with dichloromethane:toluene = 1:1 to afford **2** (491 mg, 0.72 mmol, 72%) as a white solid:

mp 177-179°C; ^{1}H NMR (400 MHz, $CDCl_3$) δ = 3.80 (s, 12H), 6.84 (d, J = 8.8 Hz, 8H), 6.99 (d, J = 8.5 Hz, 4H), 7.08 (d, J = 8.8 Hz, 8H), 7.43-7.45 (m, 8H); ^{13}C NMR (100 MHz, $CDCl_3$) δ = 55.5, 114.7, 120.7, 124.7, 124.8, 126.5, 127.5, 128.9, 133.1, 140.8, 141.2, 148.1, 155.8; APCI HRMS: *m/z* calcd for $C_{46}H_{40}N_2O_4$: 685.3061 $[M+H]^+$; found 685.3041; Elemental analysis (%) calcd for $C_{46}H_{40}N_2O_4$: C, 80.68; H, 5.89; N, 4.09. Found: C, 80.43; H, 5.97; N, 4.04.

Synthesis of 3: A mixture of 1,3-Dibromobenzene (588 mg, 2.5 mmol), 4,4'-Dimethoxydiphenylamine (1.15 g, 5.0 mmol), $Pd(dba)_2$ (144 mg, 0.25 mmol), P(*t*-Bu)$_3$HBF$_4$ (145 mg, 0.50 mmol), and NaO*t*-Bu (720 mg, 7.5 mmol) in Toluene (10 mL) was refluxed under argon atmosphere for 22 h with starring. The reaction mixture was washed with saturated aqueous solution of NaCl and the organic layer was dried over Na_2SO_4. After evaporation of the solvent, the crude product was chromatographed on silica gel with dichloromethane:*n*-hexane = 3:2 to afford **3** (563 mg, 1.1 mmol, 44%) as a yellow solid: mp 52.0-54.2°C; ^{1}H NMR (400 MHz, $CDCl_3$) δ = 3.76 (s, 12H), 6.40 (dd, J = 6.1 Hz and 2.2 Hz, 2H), 6.57 (t, J = 2.2 Hz, 1H), 6.75 (d, J = 9.0 Hz, 8H), 6.92-6.99 (m, 9H); ^{13}C NMR (100 MHz, $CDCl_3$) δ =55.5, 113.7, 114.2, 114.4, 126.0, 129.1, 140.9, 149.1, 155.4; ; Elemental analysis (%) calcd for $C_{34}H_{32}N_2O_4$: C, 76.67; H, 6.06; N, 5.26. Found: C, 76.48; H, 6.21; N, 5.18.

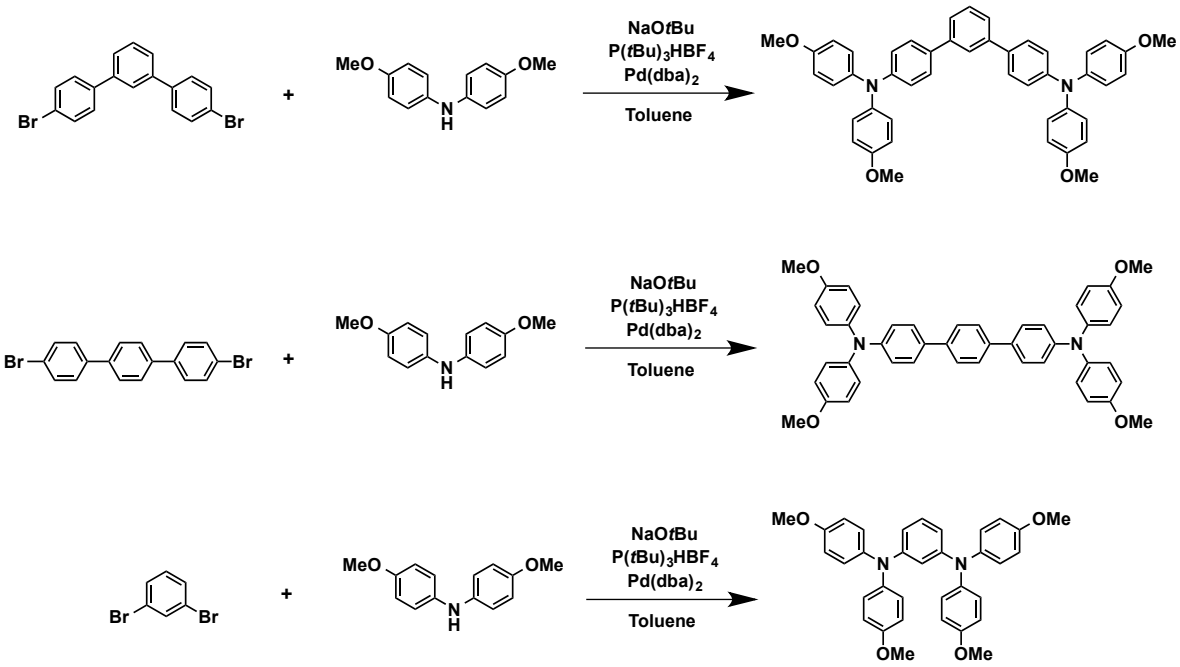

Scheme 2.2. Synthetic route of **1**-**3**.

2.2.2 DFT Calculations

Quantum chemical calculations were performed with using a hybrid Hartree–Fock/density functional theory (HF/DFT) method (B3LYP).[4] Full geometrical optimization for **1**, **2**, **3, 1**$^{\cdot+}$, **2**$^{\cdot+}$, and **3**$^{\cdot+}$ was carried out, and furthermore, their local minimum structures were confirmed by performing subsequent frequency analyses. Excitation energies were examined on the basis of time-dependent density functional theory (TD-DFT)[5] by using the (U)B3LYP/6-31G* optimized structures. All the computations employed the 6-31G* basis sets.[6] In addition, the symmetric and asymmetric optimized structures for **3**$^{\cdot+}$ and **4**$^{\cdot+}$ were determined on the basis of TD-DFT method by using the BLYP35 functional with the SVP basis sets, and their excitation energies were computed at the BLYP35/SVP level of theory.[7] In addition, the solvent effect has been included by the CPCM version of polarizable continuum

solvent model for CH_2Cl_2 (ε = 8.93).[8] All these computational approaches are implemented in Gaussian 09 package of ab initio MO calculation.[9]

2.2.3 Electrochemical Measurements

The redox properties were evaluated by cyclic voltammetry (CV) and differential pulse voltammetry (DPV) in CH_2Cl_2 solution at 298 K with 0.1 M tetra-*n*-butylammonium tetrafluoroborate ($TBABF_4$) as supporting electrolyte (scan rate 100 mV s^{-1}) using an ALS/chi Electrochemical Analyzer model 612A. A three-electrode assembly was used, which was equipped with a platinum disk (2 mm^2) and a platinum wire as the working and counter electrodes, respectively, and Ag/0.01 M $AgNO_3$ (acetonitrile) was used as the reference electrode. The redox potential were referenced against a ferrocene/ferrocenium ($Fc^{0/+}$) redox potential measured in the same electrolytic solution.

2.2.4 Spectroelectrochemical Measurements

Spectroelectrochemical measurements were carried out with a custom-made optically transparent thin-layer electrochemical (OTTLE) cell (light pass length = 1 mm) equipped with a platinum mesh and a platinum coil as the working and counter electrodes, respectively, and Ag/0.01 M $AgNO_3$ (acetonitrile) was used as the reference electrode. The potential was applied with an ALS/chi Electrochemical Analyzer model 612A.

2.2.5 ESR Measurements

Cw-ESR Spectra were recorded on a JEOL JES-TE200 X-band ESR spectrometer, in

which temperature was controlled by a JEOL ES-DVT3 variable-temperature unit in the range of 193-293 K. An Mn^{2+}/MnO solid solution was used as a reference.

2.3 Results and Discussion

A better understanding of the difference in the electronic structures of BTAs **1** and **2** in their neutral states was gained by DFT calculations (B3LYP/6-31G*). Figure 2.1 shows the frontier Kohn-Sham orbitals for **1**, **2**, **3**, and **4**. The HOMO of **1** is delocalized on the *p*-phenylene bridge unit, thus leading to the energy gap of 0.20 eV between the HOMO and HOMO-1 orbitals. In contrast, the HOMO of **2** is mainly localized on the triarylamine moieties, and has little contribution from the π-orbital of center benzene ring of the *m*-phenylene bridge unit, resulting in the quasi-degeneracy between the HOMO and HOMO-1 orbitals (0.02 eV). These trends suggest a negligible through-bond electronic coupling between the two triarylamine redox centers in $\mathbf{2}^{\bullet+}$. On the other hand, the HOMOs of *p*-phenylenediamine **3** and *m*-phenylenediamine **4** are mainly delocalized on the *phenylene* bridge unit, thus leading to the energy gaps of 0.70 eV (**3**) and 0.15 eV (**4**) between the HOMO and HOMO-1 orbitals.

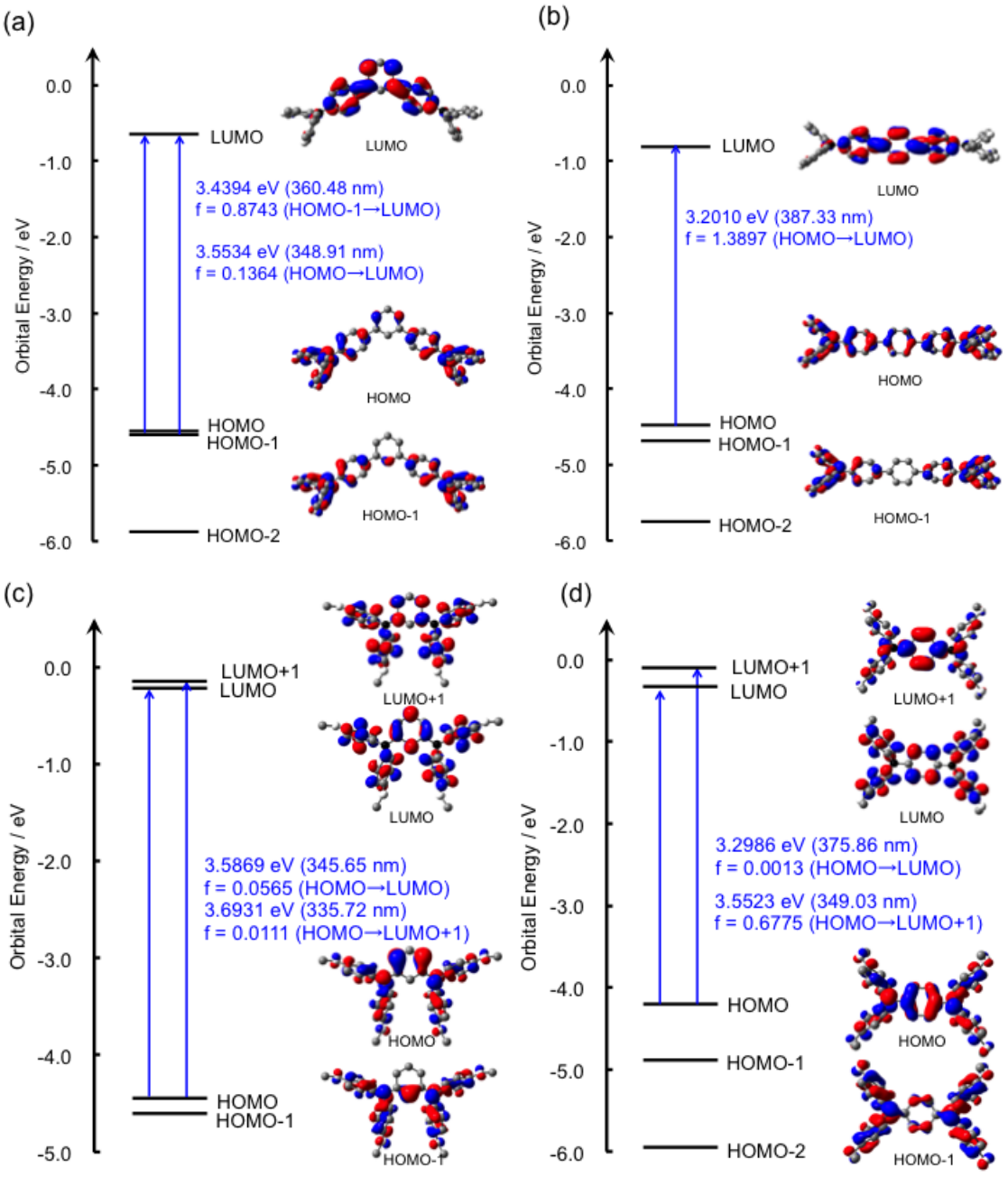

Figure 2.1. Frontier Kohn-Sham orbital energy levels and orbital plots of (a) **1**, (b) **2**, (c) **3**, and (b) **4** at the B3LYP/6-31G* level of theory.

To gain more insight into the strength of the electronic coupling in $\mathbf{1}^{\bullet+}$, $\mathbf{2}^{\bullet+}$, $\mathbf{3}^{\bullet+}$, and $\mathbf{4}^{\bullet+}$, the author examined the redox behaviors of **1, 2**, and **3** by cyclic voltammetry in 0.1 M [nBu$_4$N][BF$_4$]/CH$_2$Cl$_2$ at 298 K (Figure 2.2 and Table 2.1). Lambert et al reported the redox behavior of $\mathbf{4}$[2]. A cyclic voltammogram (CV) of **1** and **2** showed one reversible oxidation wave. For **1**, a closer inspection by the simulation of the observed DPV displayed a stepwise oxidation to the dication $\mathbf{1}^{2+}$ via a radical cation $\mathbf{1}^{\bullet+}$, with a small potential splitting [ΔE = 0.08 V] for the first and second oxidation process [E_1 = +0.18 V (1e) and E_2 = +0.26 V (1e) (vs $Fc^{0/+}$)], thus indicating some degree of charge/spin transfer between the two triarylamine redox centers in $\mathbf{1}^{\bullet+}$. Similarly, the simulation of observed DPV for **2** displayed a stepwise oxidation to the dication $\mathbf{2}^{2+}$ via a radical cation $\mathbf{2}^{\bullet+}$, with a smaller potential splitting [ΔE = 0.07 V] for the first and second oxidation process [E_1 = +0.20 V (1e) and E_2 = +0.27 V (1e) (vs $Fc^{0/+}$)]. The smaller potential spitting indicates lower electronic coupling between two triarylamine redox centers in $\mathbf{2}^{\bullet+}$. On the other hand, the cyclic voltammogram of **3** exhibited two reversible oxidation waves that correspond to the stepwise one-electron oxidation of each arylamino moiety. It is noteworthy that for **3** is larger than **1** and **2**. Similarly, the cyclic voltammogram of **3** exhibited two reversible oxidation waves that have a larger potential splitting [ΔE = 0.48 V] for the first and second oxidation process [E_1 = -0.14 V (1e) and E_2 = +0.34 V (1e) (vs $Fc^{0/+}$)]. This result means a larger electronic coupling in **3** than **4** due to the *meta*- and *para*-phenylene geometrical differences.

Table 2.1. Redox potentials (*E*) and difference between the first and second redox process (ΔE) of **1**-**4**.[a]

Compound	E_1 / V	E_2 / V	ΔE / mV
1[b,c]	0.20	0.27	70
2[b,c]	0.18	0.26	80
3[b,e]	0.17	0.46	290
4[c,e]	-0.14	0.34	480

[a] Potentials are given vs. Fc/Fc^+.

[b] Measured in CH_2Cl_2 with 0.1 M *n*-Bu_4NBF_4 at 298 K (scan rate 0.1 V sec^{-1}).

[c] Determined by DPV simulation.

[d] Measured in CH_2Cl_2 with 0.1 M *n*-Bu_4NPF_6 at 298 K (scan rate 0.25 V sec^{-1}).[2]

[e] Half-wave potentials from CV.

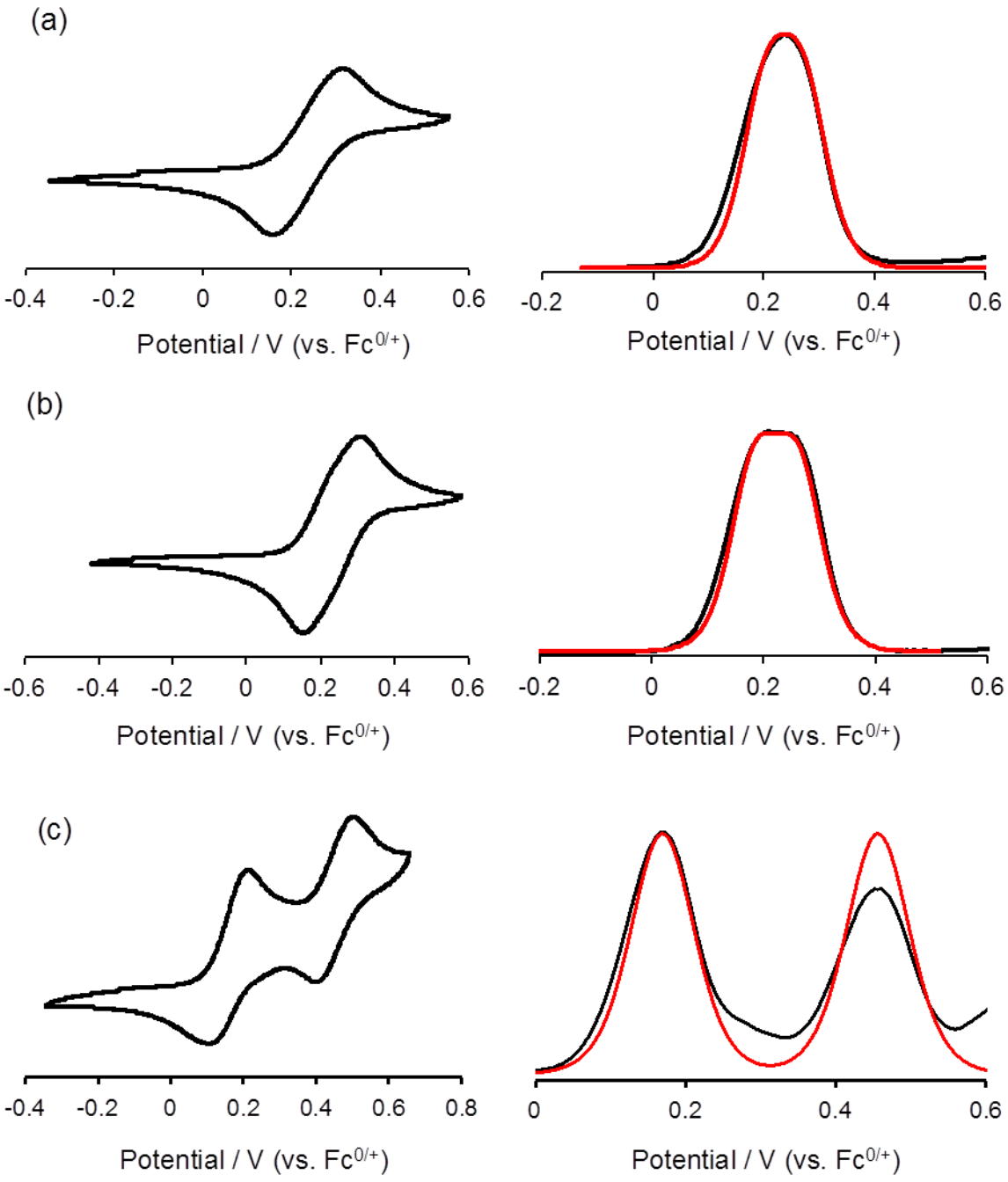

Figure 2.2. Observed cyclic voltammograms (left) and observed (black) and simulated (red) DPV (right) in CH_2Cl_2 (at 1×10^{-3} M) with 0.1 M $[n\mathrm{Bu_4N}]^+[BF_4]^-$ at 298 K (scan rate 0.1 V s^{-1}) for (a) **1**, (b) **2**, and (c) **3**.

In general, the lowest-energy absorption band allows us to directly monitor the optically induced intramolecular charge/spin transfer (ICT/IST) in organic MV compounds. Hence, the author has recorded the absorption spectral change during stepwise chemical oxidation of **1** and **2** with $AgSbF_6$ and electrochemical oxidation of **3** in CH_2Cl_2. For **1**, the lowest-energy band at 3.68 eV (337 nm) was gradually changed into new bands at 1.07 eV (1162 nm) and 1.64 eV (756 nm) with an isosbestic point at 3.43 eV (361 nm) during the oxidation process from **1** to $\mathbf{1}^{\bullet+}$ (Figure 2.3a). The lowest-energy band is characteristic of the so-called IV-CT band observed for organic MV compounds classified into the Robin and Day's class-II. The lowest-energy transition observed for $\mathbf{1}^{\bullet+}$ was examined by the time-dependant DFT (TD-DFT) calculations. Recently, Kaupp and co-workers pointed out the fact that the frequently used B3LYP hybrid functional may often lead to erroneous results in organic MV compounds.[7] In fact, the B3LYP/6-31G* geometrical optimization for $\mathbf{1}^{\bullet+}$ gave symmetrical structure, and the lowest-energy transition energy was computed to be 0.18 eV (6959 nm; f = 0.0551). Hence, the author has also performed the DFT calculations for $\mathbf{1}^{\bullet+}$ by using the BLYP-based hybrid functional with 35% exact exchange and the SVP basis sets[10] (BLYP35/SVP)[7], including the solvation effect by the CPCM version[8] of polarizable continuum solvent model for CH_2Cl_2 (ε = 8.93). As a result, the asymmetric optimized structure with the spin-density being localized on one of the two triarylamine centers was obtained for $\mathbf{1}^{\bullet+}$, and the lowest-energy transition assignable to the transition from βHOMO to βLUMO was estimated to be 0.81 eV (1527 nm; f = 0.0021) in good agreement with the observed IV-CT band. Furthermore, during the oxidation process from $\mathbf{1}^{\bullet+}$ to $\mathbf{1}^{2+}$, the lowest-energy IV-CT band disappeared in association with the oxidation of both triarylamine redox centers, and intensity of the

next-lowest-energy band at 756 nm, which is assignable to π–π* transition within the triarylamine radical cation center[2], reached up to nearly twice that of $\mathbf{1}^{\bullet+}$ (Figure 2.3b)

As Shown in Figure 2.3c, turning next to **2**, the lowest-energy band at 3.42 eV (363 nm) was gradually changed into new bands at 1.13 eV (1100 nm) and 1.66 eV (749 nm) with an isosbestic point at 3.20 eV (388 nm) during the oxidation process from **2** to $\mathbf{2}^{\bullet+}$. The IV-CT band observed for organic MV compounds classified into the Robin and Day's class-II was observed in the NIR region for $\mathbf{2}^{\bullet+}$. The B3LYP/6-31G* geometrical optimization for $\mathbf{2}^{\bullet+}$ gave symmetrical structure, and the lowest-energy transition energy was computed to be 0.58 eV (2143 nm; f = 0.6675) by the TD-DFT calculation. Hence, by using BLYP35/SVP with CPCM for CH_2Cl_2, the asymmetric optimized structure with the spin-density being localized on one of the two triarylamine centers was obtained for $\mathbf{2}^{\bullet+}$, and the lowest-energy transition assignable to the transition from βHOMO to βLUMO was estimated to be 0.79 eV (1565 nm; f = 0.2419) in good agreement with the observed IV-CT band. During the oxidation process from $\mathbf{2}^{\bullet+}$ to $\mathbf{2}^{2+}$, the lowest-energy IV-CT band disappeared in association with the oxidation of both triarylamine redox centers, and intensity of the next-lowest-energy band at 749 nm, which is assignable to π–π* transition within the triarylamine radical cation center, reached up to nearly twice that of $\mathbf{2}^{\bullet+}$ (Figure 2.3d).

The absorbance of the IV-CT band observed for $\mathbf{1}^{\bullet+}$ was very smaller than $\mathbf{2}^{\bullet+}$, and it suggests the small electronic coupling between the two redox centers in $\mathbf{1}^{\bullet+}$ or the small transition dipole moment for $\mathbf{2}^{\bullet+}$. The electronic coupling was evaluated as below.

As Shown in Figure 2.3e, turning next to **3**, the lowest-energy band at 4.09 eV (303 nm) was gradually changed into new bands at 0.69 eV (1810 nm) and 1.65 eV (752 nm) with an isosbestic point at 3.76 eV (330 nm) during the oxidation process from **3** to $\mathbf{3}^{\bullet+}$.

The IV-CT band observed for organic MV compounds classified into the Robin and Day's class-II was observed in the NIR region for $\mathbf{3}^{\bullet+}$. The B3LYP/6-31G* geometrical optimization for $\mathbf{3}^{\bullet+}$ gave symmetrical structure, and the lowest-energy transition energy was computed to be 0.40 eV (3105 nm; f = 0.0763) by the TD-DFT calculation. Hence, by using BLYP35/SVP with CPCM for CH_2Cl_2, the asymmetric optimized structure with the spin-density being localized on one of the two triarylamine centers was obtained for $\mathbf{3}^{\bullet+}$, and the lowest-energy transition assignable to the transition from βHOMO to βLUMO was estimated to be 0.73 eV (1987 nm; f = 0.0267) in good agreement with the observed IV-CT band. This result suggests that the radical cation of *meta*-phenylenediamine **3** is classified into class-II mixed valence compound. During the oxidation process from $\mathbf{3}^{\bullet+}$ to $\mathbf{3}^{2+}$, the lowest-energy IV-CT band disappeared in association with the oxidation of both triarylamine redox centers, and intensity of the next-lowest-energy band at 752 nm, which is assignable to π–π* transition within the triarylamine radical cation center, reached up to nearly twice that of $\mathbf{3}^{\bullet+}$ (Figure 2.3f).

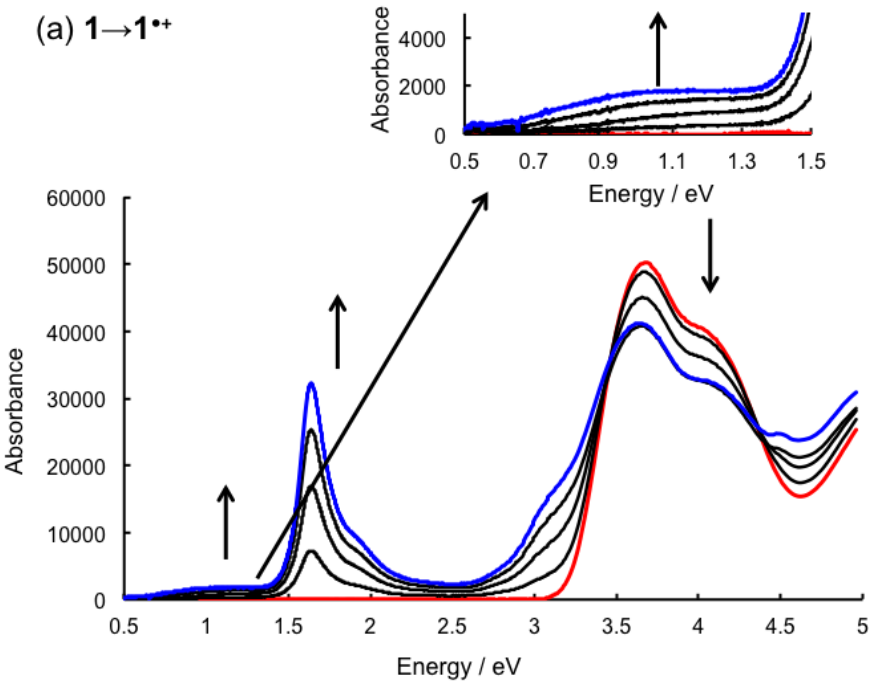
(a) 1→1•+
Absorbance
4000
2000
0
0.5
0.7
0.9
1.1
1.3
1.5
Energy / eV
60000
50000
40000
30000
20000
10000
0
Absorbance
0.5
1
1.5
2
2.5
3
3.5
4
4.5
5
Energy / eV

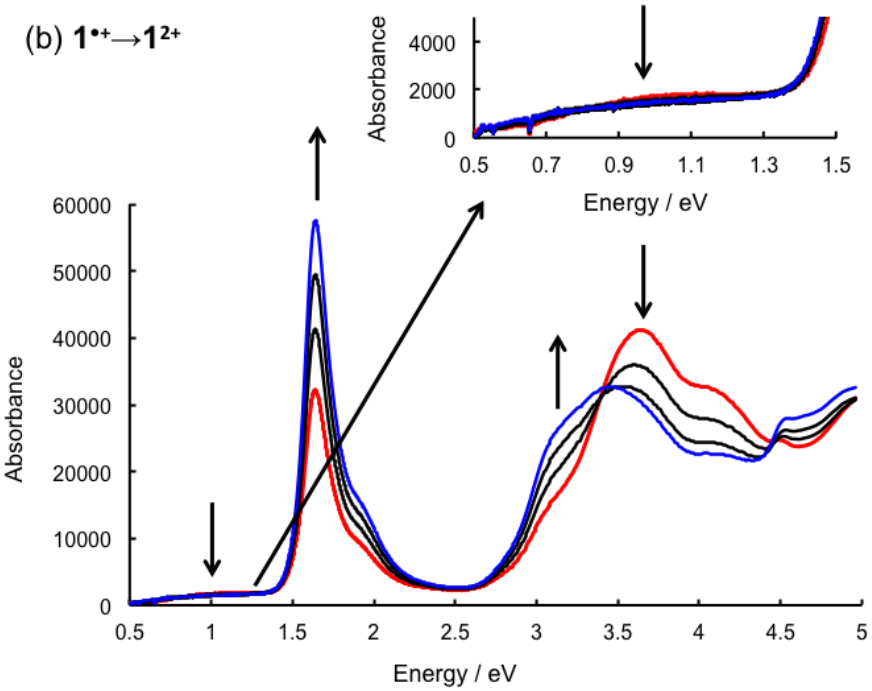
(b) 1•+→12+
Absorbance
4000
2000
0
0.5
0.7
0.9
1.1
1.3
1.5
Energy / eV
60000
50000
40000
30000
20000
10000
0
Absorbance
0.5
1
1.5
2
2.5
3
3.5
4
4.5
5
Energy / eV

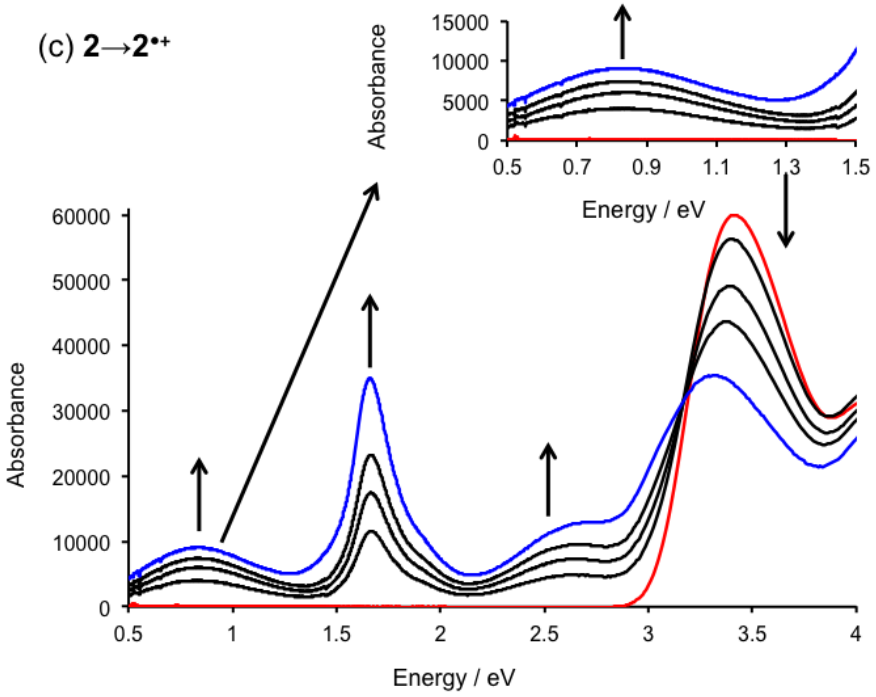
(c) 2→2•+
Absorbance
Energy / eV
60000
50000
40000
30000
20000
10000
0
0.5
1
1.5
2
2.5
3
3.5
4
15000
10000
5000
0.5
0.7
0.9
1.1
1.3
1.5

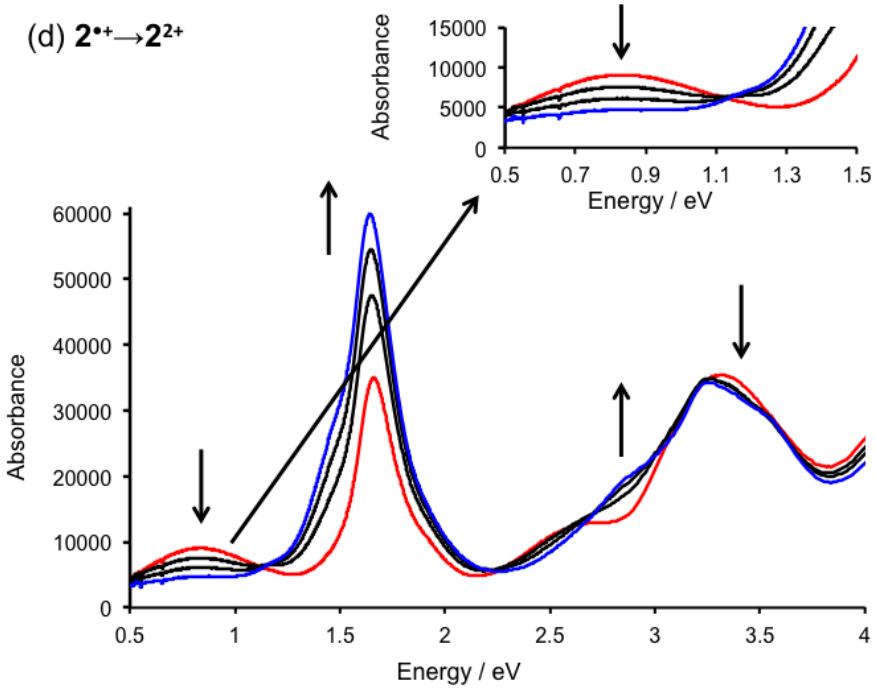
(d) 2•+→2²+
Absorbance
Energy / eV
60000
50000
40000
30000
20000
10000
0
0.5
1
1.5
2
2.5
3
3.5
4
15000
10000
5000
0.5
0.7
0.9
1.1
1.3
1.5

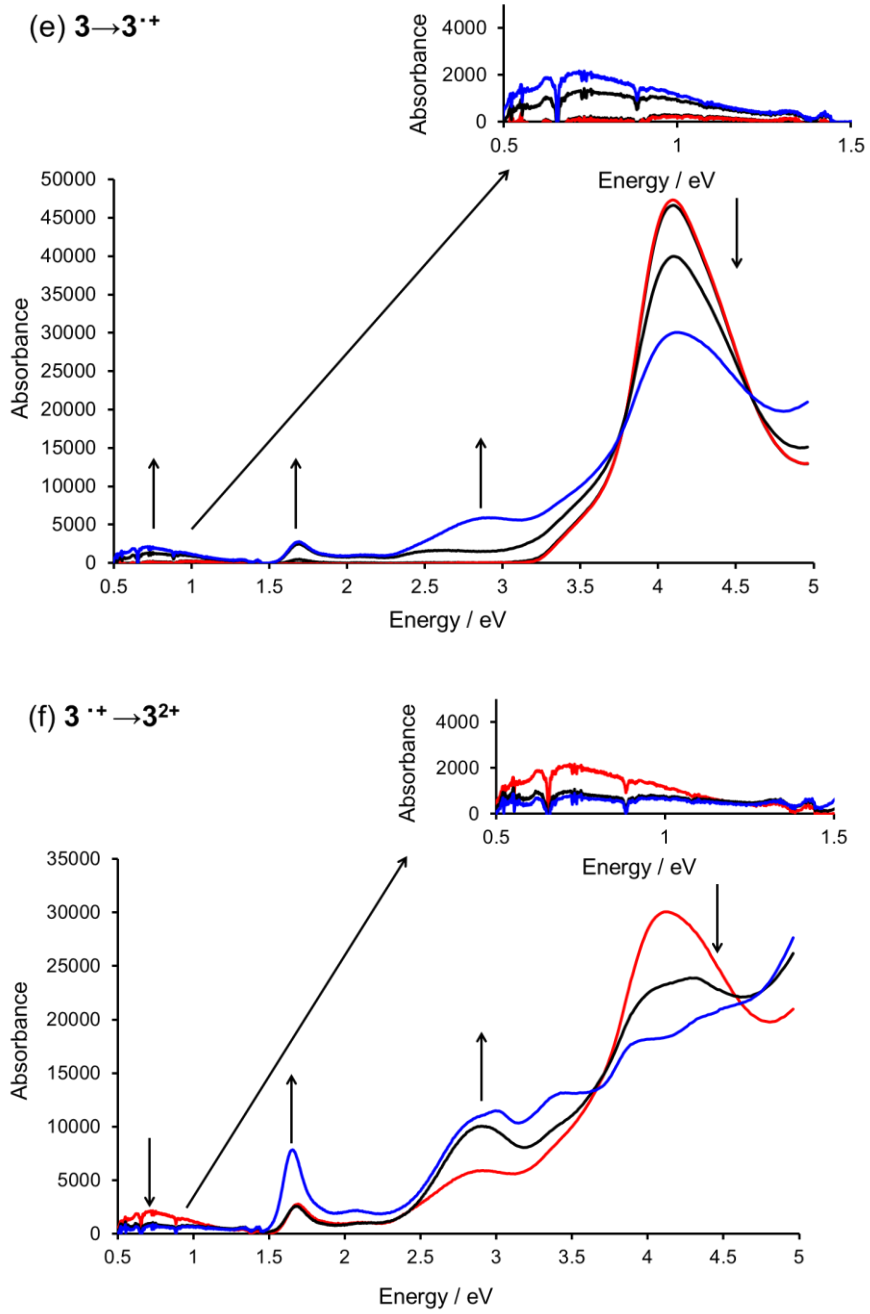

Figure 2.3. UV/Vis-NIR optical absorption spectra of the stepwise chemical oxidation with $AgSbF_6$ (a) from **1** (red line) to $\mathbf{1}^{\cdot+}$ (blue line), (b) from $\mathbf{1}^{\cdot+}$ (red line) to $\mathbf{1}^{2+}$ (blue line), (c) from **2** (red line) to $\mathbf{2}^{\cdot+}$ (blue line), (d) from $\mathbf{2}^{\cdot+}$ (red line) to $\mathbf{2}^{2+}$ (blue line), and electrochemical oxidation (e) from **3** (red line) to $\mathbf{3}^{\cdot+}$ (blue line), (f) from $\mathbf{3}^{\cdot+}$ (red line) to $\mathbf{3}^{2+}$ (blue line) in CH_2Cl_2 (at 1×10^{-4} M) at r.t.

Judging from the fact that the observed IV-CT band is symmetric and the DFT consideration supports the class-II MV character of $\mathbf{1}^{\bullet+}$, $\mathbf{2}^{\bullet+}$ and $\mathbf{3}^{\bullet+}$, the electronic coupling (V) were evaluated by the Mulliken-Hush theory [Eq. (2.1)]:[1b]

$$V = \frac{\mu_{ab}\tilde{\nu}_{\max}}{\Delta\mu_{12}} \qquad (2.1)$$

where μ_{ab} is the transition moment, which is determined by integration of the IV-CT band, $\tilde{\nu}_{\max}$ the energy of the IV-CT band maximum, $\Delta\mu_{12}$ the difference in the diabatic dipole moments between the ground and excited states, which is calculated by Eq. (2.2),

$$\Delta\mu_{12} = \sqrt{(\Delta\mu_{ab})^2 + 4(\mu_{ab})^2} \qquad (2.2)$$

from the difference in the adiabatic dipole moments between the ground and excited states $\Delta\mu_{ab}$. The $\Delta\mu_{ab}$ values are not accessible from the observed IV-CT band analysis, and thus, were estimated to be 13 D (**1**), 65 D (**2**), and 12 D (**3**) by the DFT calculations (BLYP35/SVP + CPCM(CH_2Cl_2)). As a consequence, the electronic coupling for $\mathbf{1}^{\bullet+}$, $\mathbf{2}^{\bullet+}$, and $\mathbf{3}^{\bullet+}$ in CH_2Cl_2 were evaluated to be 299 (**1**), 861 (**2**), and 2031 cm^{-1} (**3**), respectively. The electronic coupling for the radical cation of *para*-Phenylenediamine **4** was reprted to be 3240 cm^{-1}.[2] In this paper, $\mathbf{4}^{\bullet+}$ belongs to the class II just at the border to class III.

Besides the above-mentioned optical ICT/IST, thermally activated ICT/IST event can be observable by the variable-temperature electron spin resonance (VT-ESR) spectroscopy. The ESR spectra of $\mathbf{1}^{\bullet+}$, $\mathbf{2}^{\bullet+}$, and $\mathbf{3}^{\bullet+}$ generated by the chemical oxidation of the neutral species with 0.5 equiv of $AgSbF_6$ in CH_2Cl_2 were successfully detected in the temperature range 193–293 K (Figure 2.4). For $\mathbf{1}^{\bullet+}$ and $\mathbf{2}^{\bullet+}$, the signal intensities of

the central three lines decreased gradually with the decreasing temperature. Such a temperature dependency clearly indicates that the five-line pattern at room temperature is induced by thermally activated ICT/IST between the two triarylamine redox centers, indicating that both $\mathbf{1}^{\bullet+}$ and $\mathbf{2}^{\bullet+}$ are class II MV systems.[11] The VT-ESR spectra of $\mathbf{1}^{\bullet+}$ show that the spin is fully localized on one triarylamine redox center on the ESR time scale below 233 K. The observed VT-ESR spectra of $\mathbf{1}^{\bullet+}$ and $\mathbf{2}^{\bullet+}$ in CH_2Cl_2 at various temperatures were successfully simulated using the ESR-EXN program, which simulates the ESR line shape when there exists the intramolecular dynamic spin exchange among the multi-redox-active centers.[12] From the simulation, we obtained the first-order rate constants (k_{th}) for the thermally activated ICT/IST process between the two triarylamine redox centers [Eq. (2.3)]:

$$k_{th} = A \exp\left(-\frac{\Delta G^*}{k_B T}\right) \qquad (2.3)$$

The Arrhenius plot gave a clear linear relationship between $\ln(k_{th})$ and $1/T$ for both $\mathbf{1}^{\bullet+}$ and $\mathbf{2}^{\bullet+}$ (Figure 2.5). From this relationship, the activation barrier (ΔG^*) for the thermally activated ICT/IST was estimated 1825 cm^{-1} for $\mathbf{1}^{\bullet+}$ and 902 cm^{-1} for $\mathbf{2}^{\bullet+}$. In the case of degenerate MV states, the ΔG^* value can be related to the electronic coupling (V) and the reorganization energy (λ) by Eq. (2.4).[13]

$$\Delta G^* = \frac{(\lambda - 2V)^2}{4\lambda} \qquad (2.4)$$

Hence, the electronic couplings for $\mathbf{1}^{\bullet+}$ and $\mathbf{2}^{\bullet+}$ can be deduced from Eq. (2.4) by using

the VT-ESR barrier, ΔG^*, and the optically determined λ, which corresponds to the energy of the IV-CT band maximum; in this way, the electronic coupling for $\mathbf{1}^{\cdot+}$ and $\mathbf{2}^{\cdot+}$ were evaluated to be 214 (**1**) and 923 cm^{-1} (**2**), respectively. The present VT-ESR results are also confirmed by DFT calculations (BLYP35/SVP + CPCM(CH_2Cl_2)), which predict the activation barrier (ΔG^*) in the double well potential is 1661 cm^{-1} for $\mathbf{1}^{\cdot+}$ and 668 cm^{-1} for $\mathbf{2}^{\cdot+}$. We summarized the experimentally determined energy diagram for the self-exchange ICT/IST of $\mathbf{1}^{\cdot+}$ and $\mathbf{2}^{\cdot+}$ in Figure 2.6.

On the other hand, the ESR spectrum of $\mathbf{3}^{\cdot+}$ showed a single broad line. The observed spectrum at 293 K was reasonably reproduced by the following hyperfine coupling constants: $|a_N|$ = 0.31 mT (2N), $|a_{Ha}|$ = 0.15 mT (2H), $|a_{Hb}|$ = 0.07 mT (1H), $|a_{Hc}|$ = 0.05 mT (8H), and the contributions from the negligible hydrogen nuclei were incorporated in the line width of the spectral simulation (0.24 mT) (Figure 2.4d), with reference to the DFT-computed spin density distribution for the optimized planar structure of $\mathbf{3}^{\bullet+}$. In addition, the ESR spectral shapes remained unchanged in the measured temperature range (193-293 K). It indicates rapid intramolecular electron transfer between two nitrogen atoms on the ESR time scale.

(a)

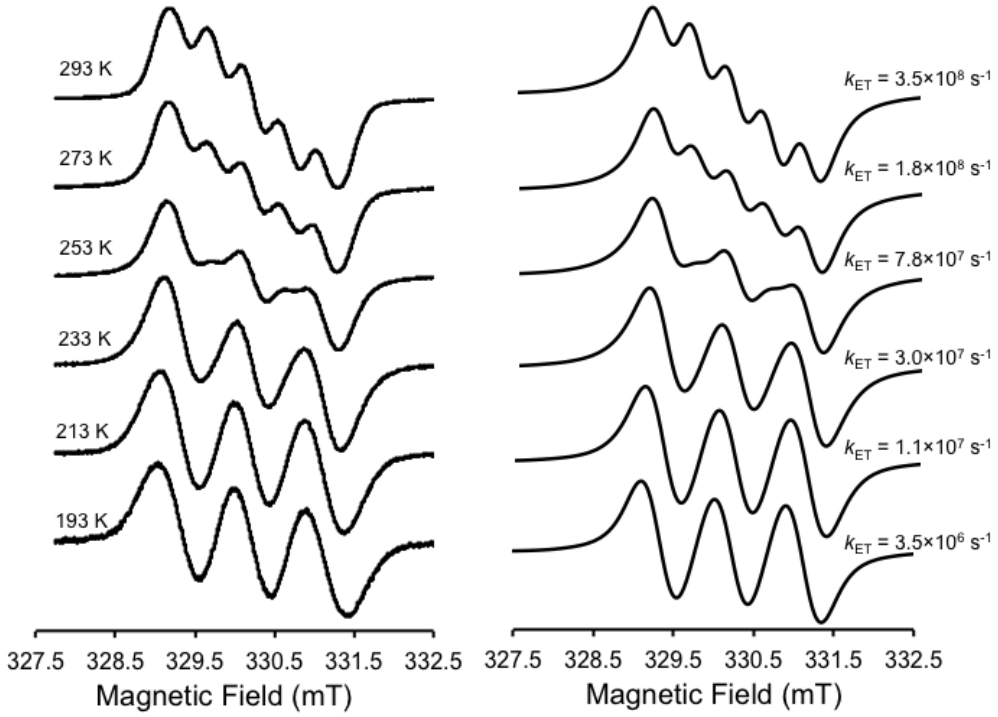
293 K
273 K
253 K
233 K
213 K
193 K
327.5 328.5 329.5 330.5 331.5 332.5
Magnetic Field (mT)
k_{ET} = 3.5×10^{8} s^{-1}
k_{ET} = 1.8×10^{8} s^{-1}
k_{ET} = 7.8×10^{7} s^{-1}
k_{ET} = 3.0×10^{7} s^{-1}
k_{ET} = 1.1×10^{7} s^{-1}
k_{ET} = 3.5×10^{6} s^{-1}
327.5 328.5 329.5 330.5 331.5 332.5
Magnetic Field (mT)

(b)

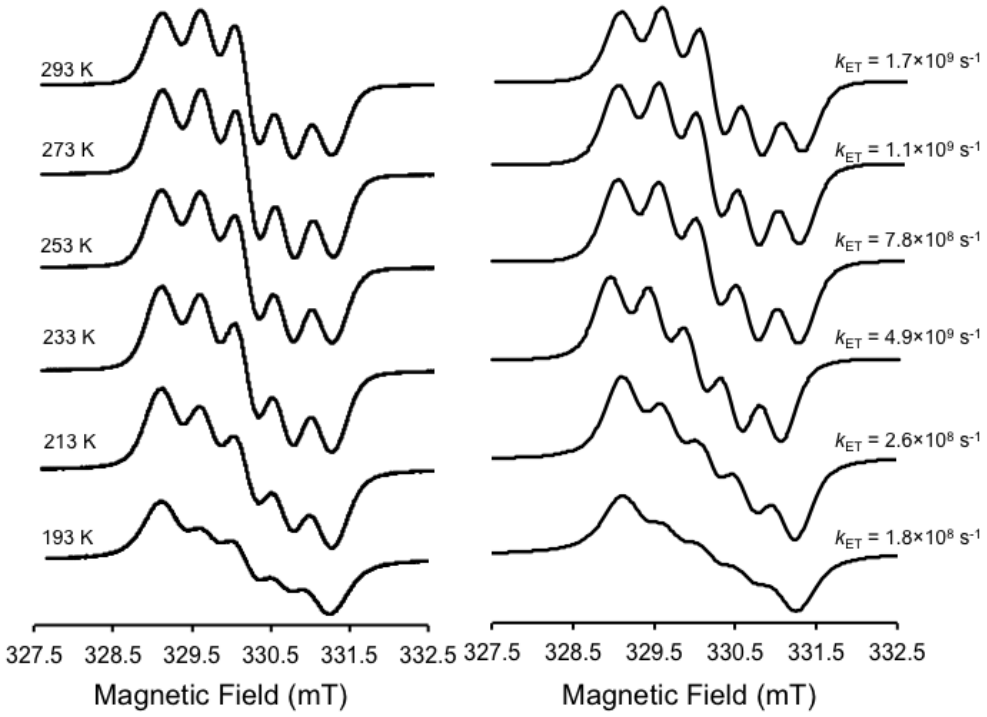
293 K
273 K
253 K
233 K
213 K
193 K
327.5 328.5 329.5 330.5 331.5 332.5
Magnetic Field (mT)
k_{ET} = 1.7×10^{9} s^{-1}
k_{ET} = 1.1×10^{9} s^{-1}
k_{ET} = 7.8×10^{8} s^{-1}
k_{ET} = 4.9×10^{9} s^{-1}
k_{ET} = 2.6×10^{8} s^{-1}
k_{ET} = 1.8×10^{8} s^{-1}
327.5 328.5 329.5 330.5 331.5 332.5
Magnetic Field (mT)

(c) (d)

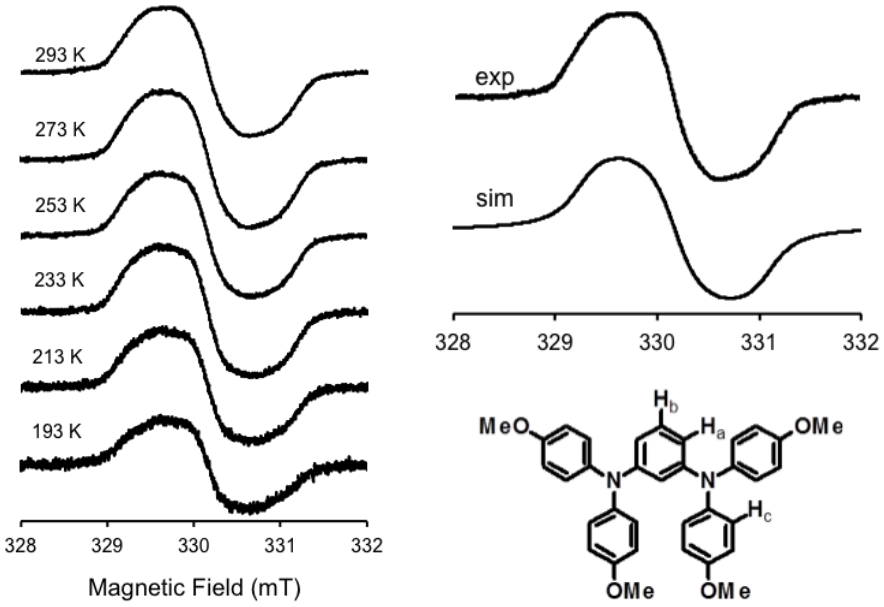

Figure 2.4. Observed X-band VT-ESR spectra (left) and simulated spectra with determined intramolecular ICT/IST rates (k_{th}) (right) of (a) $\mathbf{1}^{\bullet+}$ and (b) $\mathbf{2}^{\bullet+}$, (c) observed X-band VT-ESR spectra of $\mathbf{3}^{\bullet+}$, and (d) observed and simulated ESR spectra of $\mathbf{3}^{\bullet+}$ at 293 K in CH_2Cl_2 (at 5×10^{-4} M).

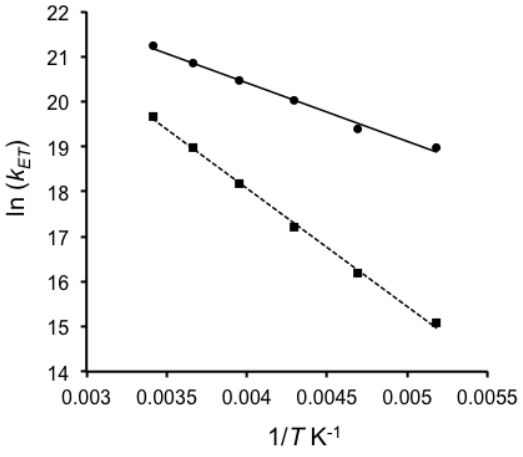

Figure 2.5. Arrehenius plots of the intramolecular ICT/IST rates (k_{ET}) for $\mathbf{1}^{\bullet+}$ (■) and $\mathbf{2}^{\bullet+}$ (●) obtained from the simulation of the observed VT-ESR spectrum.

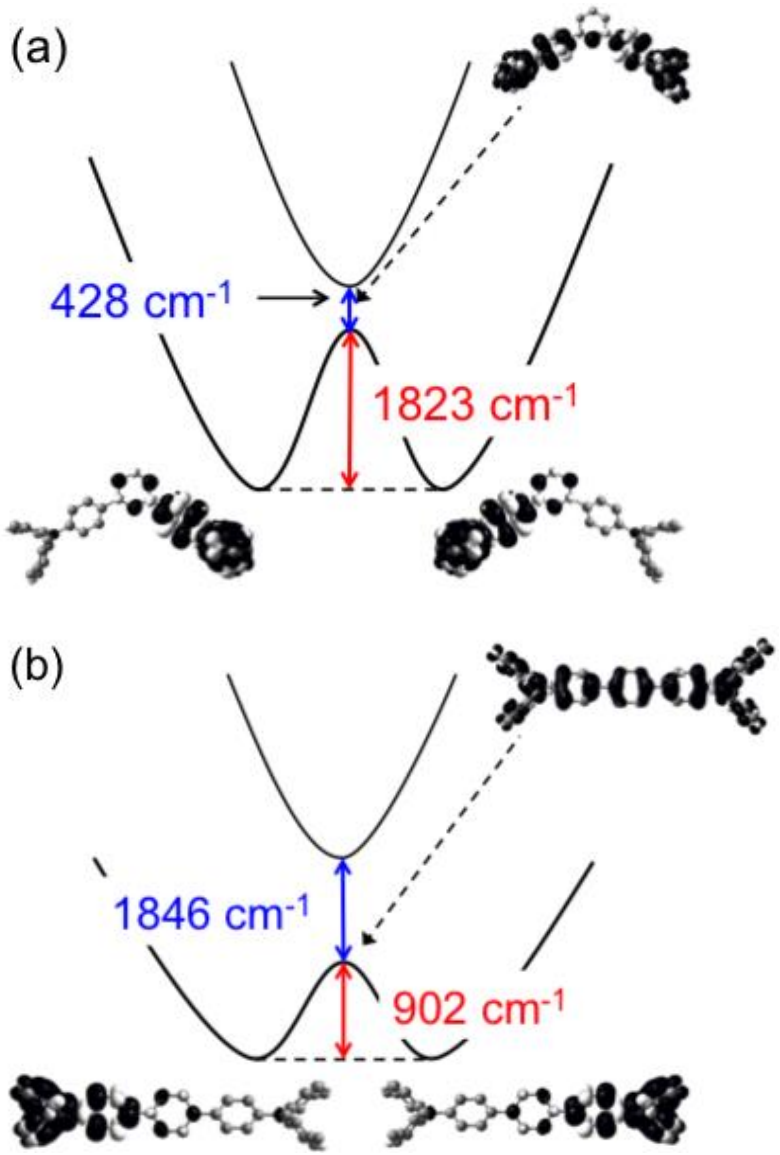

Figure 2.6. Schematic energy diagrams, determined experimentally for the self-exchange ICT/IST of (a) $\mathbf{1}^{\bullet+}$ and (b) $\mathbf{2}^{\bullet+}$ in CH_2Cl_2. The depicted molecular structures with spin density distribution are the optimized structures at the local minima and the saddle point in double-well potential [BLYP35/SVP + CPCM(CH_2Cl_2) level of theory].

2.4 Conclusion

In this work, three radical cations, $\mathbf{1}^{\cdot+}$ and $\mathbf{2}^{\cdot+}$, where the triarylamine redox centers have different bridging units (*meta*- and *para*-phenylene), and $\mathbf{3}^{\cdot+}$, *meta*-phenylenediamine, were investigated by cyclic voltammetry, UV-vis-NIR and ESR spectroscopy, and DFT calculations. $\mathbf{1}^{\cdot+}$ and $\mathbf{2}^{\cdot+}$ are classified into class-II mixed-valence compounds by the observed IV-CT band, TD-DFT calculations and VT-ESR spectra. On the other hand, the radical cation of *meta*-Phenylenediamine **3**, is classified into class-II mixed-valence compounds by the observed IV-CT band and TD-DFT calculations but VT-ESR spectra indicate rapid intramolecular electron transfer between two nitrogen atoms on the ESR time scale.

2.5 References

[1] a) J. Hankache, O. S. Wenger, *Chem. Rev*. **2011**, *111*, 5138-5178; b) A. Heckmann, C. Lambert, *Angew. Chem. Int. Ed.* **2012**, *51*, 326-392.

[2] C. Lambert, G. Nöll, *J. Am. Chem. Soc.* **1999**, *121*, 8434-8442.

[3] J. Bonvoisin, J.-P. Launay, W. Verbouwe, M. Van der Auweraer, F. C. De Schryver, *J. Phys. Chem*. **1996**, *100*, 17079-17082.

[4] K. Ragavachari, *Theor. Chem. Acc*. **2000**, *103*, 361-363 and references cited therein.

[5] A. Dreuw, M. Head-Gordon, *Chem. Rev.* **2005**, *105*, 4009-4037.

[6] W. J. Hehre, L. Radom, P.v. R. Schleyer, J. A. Pople, *Ab Initio Molecular Orbital Theory*, Wiley, New York, **1986**.

[7] a) M. Renz, K. Theilacker, C. Lambert, M. Kaupp, *J. Am. Chem. Soc*. **2009**, *131*, 16302; b) M. Renz, M. Kess, M. Diedenhofen, A. Klamt, M. Kaupp, *J. Chem. Theory Comput*. **2012**, *8*, 4189-4203; c) M. Parthey, M. Kaupp, *Chem. Soc. Rev*. **2014**, *43*, 5067-5088.

[8] M. Cossi, N. Rega, G. Scalmani, V. Barone, *J. Comput. Chem*. **2003**, *24*, 669-681.

[9] M. J. Frisch, *et al*., Gaussian 09 (Revision D.01), Gaussian, Inc., Wallingford CT, **2013**.

[10] A. Schöfer, H. Horn, R. Ahlrichs, *J. Chem. Phys*. **1992**, *97*, 2571-2577.

[11] a) Y. Hirao, M. Urabe, A. Ito, K. Tanaka, *Angew. Chem. Int. Ed.* **2007**, *46*, 3300-3303; b) K. Lancaster, S. A. Odom, S. C. Jones, S. Thayumanavan, S. R. Marder, J.-L. Brédas, V. Coropceanu, S. Barlow, *J. Am. Chem. Soc*. **2009**, *131*, 1717-1723; c) D. R. Kattnig, B. Mladenova, G. Grampp, C. Kaiser, A. Heckmann, C. Lambert, *J. Phys. Chem. C* **2009**, *113*, 2983-2995.

[12] J. Heinzer, *Mol. Phys.* **1971**, *22*, 167-177.

[13] B. S. Brunschwig, C. Creutz, N. Sutin, *Chem. Soc. Rev*. **2002**, *31*, 168-184.

General Conclusion

In this thesis, the author has studied the electronic properties of triphenylamine-based functional materials from the both experimental and theoretical point of view. The new findings in this thesis are summarized as follows.

Part 1 dealt with the electronic structures of triphenylamine-based acene materials. In Chapter 1, Radical cations of synthetically readily accessible acenes: anthracene, tetracene, and pentacene, with moderately bulky mesityl substituents revealed that their photochemical stability in solution under ambient light and air conditions was comparable to that of the corresponding neutral state, thus indicating the possibility of persistent acene radical cations. The reason is because one-electron oxidation of acenes can also lead to stable $4n + 1$ π-electron systems possessing two Clar's aromatic sextets though higher oligoacenes as formal $4n+2$ Hückel aromatic compounds, no matter how long, possessing only one Clar's aromatic sextet. These results suggest that the radical cations of mesityl acenes in solution under ambient light and air conditions satisfactory

for device fabrication by using wet process.

In Chapter 2, the electronic and molecular structures of 9,10-diamino-substituted anthracenes with different *N*-substituents were revisited. In particular, the author investigated how the difference in the *N*-substituent identity influences both the electronic and molecular structures of the oxidized species of 9,10-diaminoanthracenes. The anthrylene moiety of 9,10-bis(*N*,*N*-di(*p*-anisyl)amino)anthracene retains its planarity during the course of two successive one-electron oxidations, while 9,10-bis(*N*,*N*-dimethylamino)anthracene and 9,10-bis(*N*-*p*-anisyl-*N*-methylamino)-anthracene undergo a substantial structural change into a butterfly-like structure via two-electron oxidation process. The structural changes observed for their oxidized states are ascribed to the significant differences in frontier molecular orbitals of the above-mentioned three kinds of 9,10-diaminoanthracenes due to the extent of mixing between the amine-localized and anthrylene-localized orbitals. This study demonstrated the modification of the electronic properties of diaminoanthracene.

In Chapter 3, the author investigated the spin and charge distributions for radical cation and triradical trication of the highly-twisted anthrylene-embedded hexaaza[1_6]paracyclophane. The electrochemical, spectroelectrochemical, and ESR studies revealed the dynamically delocalized spin and charge distribution for the radical cation, despite somewhat segmentation due to the anthrylenes of π-conjugation through the macrocyclic molecular backbone. Furthermore, the author has succeeded in isolation of the stable triradical trication salt of the macrocycle, in which three segmented PD-based radical spins were found to be mutually antiferromagnetically coupled with $J/k_B \simeq -74$ K, leading to a typical spin-frustrated 3-spin system. The present findings provided new insight into the design of troidal multispin molecular systems.

In Chapter 4, the author showed that the influence of *N*-substituents on the electronic states for the neutral and oxidized species of 5,12-diaminotetracenes. In accordance with an increase in the number of *N*-anisyl-substituents, the frontier MOs of 5,12-diaminotetracenes changed from the tetracene-localized type to the amine-localized type. This tendency finally determines whether the significant structural change into the butterfly-like structure takes place in their oxidized species. The fully and partially *N*-alkylated 5,12-diaminotetracens underwent the folding structural change along C5–C12 line in their dicationic state bypassing the generation of radical cation. In contrast, the fully *N*-anisyl-substituted 5,12-diaminotetracene exhibited two-stage redox property with a very small oxidation potential splitting, indicating no significant structural changes throughout all the oxidation processes. The ESR measurements demonstrated that the radical cation of the fully *N*-anisyl-substituted 5,12-diaminotetracene is classified into the class III or the borderline class III/class II mixed-valence state, thus retaining planarity of the tetracene moiety. Moreover, these compounds exhibited fluorescence in nonpolar solvents from charge transfer transition between diphenylamine and tetracene. This study demonstrated the synthesis of diaminotetracene and the modification of their electronic properties.

In Chapter 5, a series of 6,13-diamino-substituted pentacenes were prepared and characterized as a new class of pentacene derivatives with strong donor ability and enhanced solubility in common organic solvents. The (spectro)electrochemical and DFT studies revealed that the two-electron oxidation process was accompanied by the substantial structural change into a “butterfly-like” conformation of the pentacene moiety. More noteworthy is that the extent of deformation from the planar pentacene moiety in the dications of 6,13-diaminopentacene is tunable by varying the kind of

N-substituents. This study showed the synthesis of 6,13-diaminosubstituted pentacenes as a new class of redox-active pentacene derivatives and their electronic properties. This study demonstrated the synthesis of diaminopentacene and the modification of their electronic properties.

Part 2 dealt with the optical properties of triphenylamine-based functional materials. In Chapter 1, carborane-substituted triphenylamines were newly prepared to demonstrate the effective fluorescent enhancement of triphenylamine as a typical non-fluorescent π-conjugated compound on the basis of molecular design to suppress the non-radiative decay by reduced vibronic coupling. Non-fluorescent carborane substituents worked to reduce only the HOMO distribution in the non-fluorescent parent π-conjugated core, thereby leading to increase in fluorescence quantum yield by suppressing internal conversion. These results provided the new concept that light-emitting efficiency of non-fluorescent triphenylamine-based materials can be enhanced.

In Chapter 2, nitrogen-boron donor-accepter anthrancene derivatives synthesized. From the DFT consideration, the HOMO is localized on arylamino moiety and the LUMO localized on arylborane moiety. HOMO-LUMO gap were confirmed by the electrochemical and optical absorption spectroscopic studies. By the spectroelectrochemistry and ESR measurements, this compound was a relatively stable radical cation species and the spin distribution was mainly localized on nitrogen atom and slightly delocalized on anthracene moiety. These compounds exhibited virtually no solvatochromism in the absorption spectra irrespective of increasing solvent polarity due to the small dipole moment in the ground state. In contrast with no solvatohromism in absorption spectra, and displayed a pronounced bathochromism in emission spectra

with increasing solvent polarity due to the large dipole moment in the S_1 excited-state at the FC geometries. These results are characteristic of donor-π-accepter ICT molecules. As has been disclosed by the X-ray structural analysis of the single crystal, it is noteworthy that these compounds exhibited solid-state fluorescence, owing to the fact that steric hindrance of the bulky dianisylamino- and dimesitylboryl-substituents hinders the concentration quenching in the solid-state. These findings show the potential ability of anthracene derivatives to optoelectric applications.

In Chapter 3, the author studied different B(boron)-π-N(nitrogen) embedded patterns to bring about significant different (opto)electronic properties for the same macrocyclic molecular backbone. A series of B-π-N embedded alternate-meta-para-linked cyclophanes have been prepared and characterized as a new class of ambipolar π-conjugated B-π-N macrocycles. These macrocycle molecules revealed the intramolecular charge transfer in the oxidized states and the intriguing photophysical proprerties in accordance with the embedded patterns, suggesting the electronic structures are tunable by introducing multiple B-π-N moieties.

Part 3 dealt with chsrge/spin transfer mechanisms of triphenylamine-based functional materials. In Chapter 1, radical cations of bis(triarylamine)s which are bridged by *ortho*-phenylene and *ortho*-carborane cluster, respectively, were prepared to elucidate the difference in intramolecular charge/spin transfer (ICT/IST) pathway due to the two different bridging units affording similar geometrical arrangements between the redox centers. Electrochemistry, absorption spectroscopy, VT-ESR spectroscopy, and DFT calculations revealed that the radical cations of bis(triarylamine)s bridged by *ortho*-phenylene and *ortho*-carborane cluster were classified into class-II and class-I mixed valence systems, respectively, and therefore, through-bond and through-space

mechanisms were dominant for the ICT/IST phenomena in *ortho*-phenylene and *ortho*-carborane cluster derivatives, respectively. Moreover, SQUID measurements for dicationic species provided the fact that virtually no spin-exchange interaction is observed for the dication of *ortho*-carborane derivative, while the intramolecular antiferromagnetic coupling between spins in the dication of *ortho*-phenylene derivative, in accordance with the existence of conjugation pathway.

Finally, in Chapter 2, three radical cations where the triarylamine redox centers have different bridging units (*meta*- and *para*-phenylene), and *meta*-phenylenediamine, were investigated by cyclic voltammetry, UV-vis-NIR and ESR spectroscopy, and DFT calculations. Bis(triphenylamines) bridged by *meta*- and *para*-phenylene linkers are classified into class-II mixed-valence compounds by the observed IV-CT band, TD-DFT calculations and VT-ESR spectra. On the other hand, the radical cation of *meta*-Phenylenediamine is classified into class-II mixed-valence compounds by the observed IV-CT band and TD-DFT calculations but VT-ESR spectra indicate rapid intramolecular electron transfer between two nitrogen atoms on the ESR time scale.

In this thesis, the author investigated the electronic properties of triphenylamine-based acene materials, optical properties of triphenylamine-based material and intramolecular electron transfer of triphenylamine-based materials. These molecules have their unique electronic properties originating from their structures. The findings in this thesis have demonstrated that the organic materials with various electronic properties can be created by properly designing the molecular structures. The author hopes that the present thesis can contribute to development of the physical organic chemistry, and the concept in this thesis will be helpful in creating new materials.

List of Publications

Part1: Electronic Structures of Triphenylamine-Based Acene Materials

Chapter 1

(1) Mesityl-Substituted Acene Radical Cation: Descent Stability Comparable to Their Neutral States under Ambient Light and Air

M. Uebe, K. Kawashima, K. Takahashi, A. Ito, *Chem. Eur. J.* **2017**, *23*, 278-281.

(Chapter 1 is the unedited Author's version of a Submitted Work that was subsequently accetpted for publication in *Chem. Eur. J.*, copyright © 2017 Wiley-VCH Verlag GmbH & Co. KGaA after peer review. To access the final edited and published work see the following website: http://onlinelibrary.wiley.com/doi/10.1002/chem.201605072/full)

Chapter 2

(2) 9,10-Diaminoanthracenes Revisited: The Influence of *N*-Substituents on Their Electronic States

M. Uebe, T. Kato, K. Tanaka, A. Ito, *Chem. Eur. J.* **2016**, *22*, 18923-18931.

(Chapter 2 is the unedited Author's version of a Submitted Work that was subsequently accetpted for publication in *Chem. Eur. J.*, copyright © 2017 Wiley-VCH Verlag GmbH & Co. KGaA after peer review. To access the final edited and published work see the following website: http://onlinelibrary.wiley.com/doi/10.1002/chem.201602490/full)

Chapter 3

(3) Isolable Triradical Trication of Hexaaza[1_6]paracyclophane with Embedded

9,10-Anthrylene: Frustrated Three-Spin System

R. Kurata,, D. Sakamaki, M. Uebe, M. Kinoshita, T. Iwanaga, T. Matsumoto, A. Ito, *Org. Lett.* **2017**, *19*, 4371-4374.

(Chapter 3 is the unedited Author's version of a Submitted Work that was subsequently accetpted for publication in *Org. Lett.*, copyright © American Chemical Society after peer review. To access the final edited and published work see the following website: http://pubs.acs.org/doi/10.1021/acs.orglett.7b02088)

Chapter 4

(4) Synthesis and Characterization of 5,12-Diamino-Substituted Tetracenes

M. Uebe, K. Kawashima, A. Ito, *to be submitted*.

(Chapter 4 is the author's version of an Unsubmitted Work that will be submitted for publication.)

Chapter 5

(5) Synthesis and Characterization of 6,13-Diamino-Substituted Pentacenes

A. Ito, M. Uebe, K. Takahashi, H. Ishikawa, D. Sakamaki, H. Sato, T. Matsumoto, K. Tanaka, *Chem. Eur. J.* **2016**, *22*, 2165-2170.

(Chapter 5 is the unedited Author's version of a Submitted Work that was subsequently accetpted for publication in *Chem. Eur. J.*, copyright © 2017 Wiley-VCH Verlag GmbH & Co. KGaA after peer review. To access the final edited and published work see the following website: http://onlinelibrary.wiley.com/doi/10.1002/chem.201503996/full)

Part 2: Optical Properties of Triphenylamine-Based Functional Materials

Chapter 1

(6) Fluorescence Enhancement of Non-fluorescent Triphenylamine: A Recipe to Utilize Carborane Cluster Substituents

M. Uebe, A. Ito, Y. Kameoka, T. Sato, K. Tanaka, *Chem. Phys. Lett.* **2015**, *633* 190-194.

(Chapter 1 is the unedited Author's version of a Submitted Work that was subsequently accetpted for publication in *Chem. Phys. Lett.*, copyright © Elsevier after peer review. To access the final edited and published work see the following website: https://doi.org/10.1016/j.cplett.2015.05.038)

Chapter 2

(7) Electronic and Photophysical Properties of anthraceneamines Substituted by Organoboron

M. Uebe, D. Sakamaki, A. Ito, K. Tanaka, *to be submitted*.

(Chapter 2 is the author's version of an Unsubmitted Work that will be submitted for publication.)

Chapter 3

(8) Diazadibora[1.1.1.1]*m*,*p*,*m*,*p*-cyclophanes:Ambipolar Conjugated Macrocycles with Different B–π–N Embedded Patterns

A. Ito, M. Uebe, K. Kurata, S. Yano, H. Fueno, T. Matsumoto, *to be submitted*.

(Chapter 3 is the author's version of an Unsubmitted Work that will be submitted for

publication.)

Part 3: Charge/Spin Transfer Mechanisms of Triphenylamine-Based Functional Materials

Chapter 1

(9) Recognizing Through-Bond and Through-Space Self-Exchange Charge/Spin Transfer Pathways in Bis(triarylamine) Radical Cations with Similar Geometrical Arrangements

M. Uebe, T. Kazama, R. Kurata, D. Sakamaki, A. Ito, *Angew. Chem. Int. Ed* .**2017**, *56*, 15712-15717.

(Chapter 1 is the unedited Author's version of a Submitted Work that was subsequently accetpted for publication in *Angew. Chem. Int. Ed*, copyright © 2017 Wiley-VCH Verlag GmbH & Co. KGaA after peer review. To access the final edited and published work see the following website:

http://onlinelibrary.wiley.com/doi/10.1002/anie.201709874/full)

Chapter 2

(10) Mixed-Valence States of *meta*- or *para*-Phenylene Bridged Bis(triphenylamine) Radical Cation

M. Uebe, K. Kaneda, A. Ito, *to be submitted*.

(Chapter 2 is the author's version of an Unsubmitted Work that will be submitted for publication.)

The following paper is not included in this thesis:

(11) Fluorescent Triphenylamine Derivative: Theoretical Design Based on Reduced Vibronic Coupling

Y. Kameoka, M. Uebe, A. Ito, T. Sato, K. Tanaka, *Chem. Phys. Lett.* **2014**, *615*, 44-49.